DELOS
Environmental DEsign of LOw Crested Coastal Defence Structures

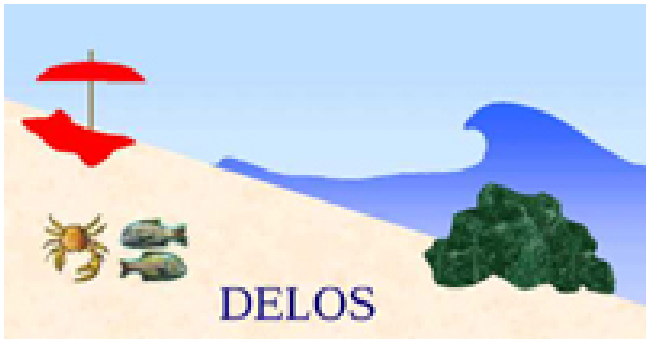

WP 2.1: Flow description

D42: Final phase-resolving Boussinesq-type models

Ioannis Avgeris, Theophanis Karambas, Panayotis Prinos, Christoforos Koutitas

Aristotle University of Thessaloniki (AUTh)

Giorgio Belloti, Riccardo Briganti, Maurizio Brocchini

University Roma 3 (UR3)

AUGUST 2003

GENERAL INTRODUCTION

The design of structures to be built in the nearshore region generally involves the evaluation of different possible layouts, under the effects of local wave and currents conditions, with the aim of minimizing costs and maximizing the desired results. In particular the design of low-crested structures involves optimisation of several parameters, which influence both the position, and the shape of the structures.
The possible layout of the structures to be designed can be tested experimentally in wave tanks and wave flumes using adequate scale models. An alternative and attractive procedure is to employ suitable numerical and mathematical models. In principle, a very advanced numerical model, able to correctly simulate all the nearshore phenomena (turbulence, waves, currents, sediment transport, etc.) could be equivalent or even superior to a physical model. In practice, the numerical models currently employed in engineering activities, use several assumptions and simplifications: the phenomena that can be simulated strictly depend on the governing equations solved by the model. Indeed, the great advantage of numerical and mathematical models is that their application is usually much less expensive than physical ones: it is certainly more economic to modify a computer file describing the bathymetry of the area under investigation than rebuild a physical model layout.
The following report is structured into two discrete sections, the first one contributed by AUTh and the second one by UR3. In the first section a 2DH higher-order Boussinesq-type model combined with a porous flow model, developed for simulating flow around porous submerged structures is presented. On the other hand, in the second section enhancements on the applicability of Boussinesq-type equations (BTE) into the surf and swash zone are described.

INTRODUCTION TO AUTh's CONTRIBUTION

In the present report the performance of the final version of a 2DH Boussinesq-type model is analysed. The final version of the model, in comparison with the preliminary one, encounters modified equations in order to simulate with higher accuracy the effects of wave propagation in a coastal region where porous submerged structures are present. The Boussinesq model incorporates (a) higher-order non-linear terms, (b) additional dispersion terms, extending the applicability of the model into a wider range of depths and (c) extra terms accounting for the interaction between the waves over the structure and the flow within the porous structure. A depth-averaged Darcy equation, extended with Forchheimer terms, is used for calculating the flow inside the porous structure. Initially, the results of the 1D version of the model are evaluated against experimental data for wave propagation over a rubble mound trapezoidal breakwater on a sloping beach. Regular and irregular waves with ratio of water depth to wave height lower than 0.2 are considered. Comparisons show that the model is capable of predicting quite accurately the wave pattern over submerged structures with ratio of freeboard to water depth as low as 1/8 and ratio of wave height to freeboard up to 1/2. Also, the model reproduces with reasonable accuracy the phenomenon of high frequency energy generation behind the structure. Finally, the 2D version of the model is used for simulating wave transformation around a system of porous submerged breakwaters. The performance of the model is compared with experimental data for regular wave cases, obtaining satisfactory results.

INTRODUCTION TO UR3's CONTRIBUTION

We consider in details two main features of Boussinesq-type models, which require improvement: the extension of the model to swash zone flows and the parameterisation of surf zone turbulence in order to simulate wave breaking.
The first line of research finds motivation in the fact that considerable efforts have been spent in the recent past by several researchers in extending the applicability of BTE models to the intermediate depths. On the contrary, much less work has been done in studying the problems that arise in very shallow water, in proximity and into the swash zone. However, it is now clear that swash zone motions are a fundamental source of low frequency waves (LFW).
These, radiating offshore, contribute to the transport of the bottom sediment, which is locally, i.e. close to the low-crested structures, put into suspension by waves and other organized structures like splash-down vortices but is transported mainly by LFW which deeply modify the bottom morphology over relatively large scales. It is then clear that a poor representation of swash zone flows is not only essential to the quantification of the LFW emitted but also to the large-scale sediment transport which, in turn, can influence the stability of man-made structures.
The second motivation of our works comes from the observation that the modes and extent of transport of suspended sediment are greatly influenced by the velocity profile within the whole water column. In shallow water this is almost uniform, however, this is not the case of the flow in intermediate waters, where submerged structures are often placed. Detailed knowledge of the flow structure over the vertical has been the focus of recent research on BTEs. Of particular interest is the work of Veeramony and Svendsen (2000, VS hereinafter), who developed a rather sophisticated BTE model capable of representing the features of breaking waves by modeling the dynamics of vorticity injected in the flow by a wave roller.
In VS's model the breaking terms are derived directly by a decomposition of the velocity into a potential and a rotational part. This was computed by solving the vorticity transport equation (VTE hereinafter). For closing the turbulence problem, VS assumed a simple eddy viscosity model, i.e. a uniform distribution over the depth. Such an assumption allowed to solve the VTE through an analytical approach.
Although rather successful VS's approach is somehow simplistic and not flexible as it does not allow for a detailed description of the vertical structure of turbulence. Hence, in the present work the limiting hypothesis of uniform eddy viscosity has been removed and a numerical solution of the VTE is proposed. Such an approach is an improvement, since it permits investigation of the effects of different eddy viscosity profiles.

DELOS
Environmental DEsign of LOw Crested Coastal Defence Structures

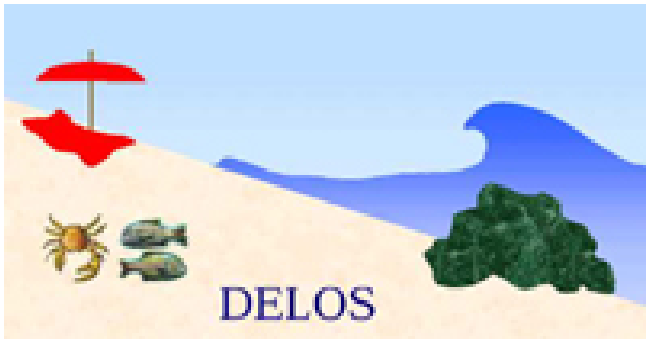

WP 2.1: Flow description

D42: 2DH final Boussinesq-type model

Ioannis Avgeris[1], *Theophanis Karambas*[1], *Panayotis Prinos*[2], *Christoforos Koutitas*[2]

[1] Research Associate, [2] Professor,
Hydraulics Lab., Dept. of Civil Engrg., AUTh - Aristotle University of Thessaloniki,
Thessaloniki 541 24, GREECE

AUGUST 2003

CONTENTS

SYMBOL INDEX

a) Greek Symbols

α : empirical coefficient

α_0 : wave amplitude (1/2 of wave height)

α_1 : porous resistance coefficient (viscous forces)

α_2 : porous resistance coefficient (inertial forces)

β : empirical coefficient

β_s : source shape coefficient

γ : empirical coefficient

δ_β : mixing length coefficient

Δx : spatial step

Δt : time step

η : free surface elevation

ν : kinematic viscosity

ν_e : eddy viscosity coefficient

φ : porosity

ω : angular frequency, $\omega = 2\pi/T$

b) Latin Symbols

B : dispersion coefficient

C_f : dimensionless parameter

c_r : inertial coefficient

c_m : added mass coefficient

D_s = source function magnitude

d_{50} : porous material mean size

f : frequency, $f = 1/T$

g : gravitational acceleration

H : wave height

h : water depth

h_s : porous medium thickness

k : wave number, $k = 2\pi/L$

K : intrinsic permeability

KC : Keulegan-Carpenter number for porous media

L : wave length

T : wave period

x_s : source function centre

$\mathbf{u}$: depth-averaged, horizontal velocity vector

$\mathbf{u_D}$: depth-averaged, Darcy velocity vector

$\mathbf{u_s}$: depth-averaged, seepage velocity vector

u : horizontal velocity in x direction

u_s : horizontal seepage velocity in x direction

1. Introduction

In the last few decades, submerged breakwaters have been extensively used in costal zones for shoreline protection and to prevent beach erosion. Their presence results primarily in wave energy dissipation through the physical mechanisms of wave breaking and friction. In most of the cases these breakwaters are rubble mound porous structures whose design is based on empirical rules.

Unquestionably, the ability to simulate accurately wave transformation over these structures is of major importance in achieving effective coastal design. Several researchers have presented a number of models addressing this problem. Sollitt and Cross (1972, 1976) in their pioneering work presented an analytical approach having as a starting point the unsteady equations for flow in the pores of a coarse granular media. Madsen (1974) also included in his linear wave model, inertia and resistance forces due to the presence of a rectangular porous structure. Wave propagation over porous seabeds was investigated theoretically and experimentally by Gu and Wang (1991), extending Sollitt and Cross (1972). Losada et al. (1995), examined experimentally the validity of the theory of Sollitt and Cross (1972), while Losada et al. (1996) presented a numerical model in order to describe regular wave interaction with submerged breakwaters. In his dissertation, van Gent (1995) simulated wave interaction with permeable coastal structures by developing a one-dimensional model based on the non-linear shallow-water wave equations and a two-dimensional (2DV) model based on the Reynolds-averaged Navier-Stokes equations. As part of his work porous media flow was studied both theoretically and experimentally with emphasis on the resistance of porous media to oscillatory wave motion. Incorporation of porous flow equations into Boussinesq-type models was recently achieved by Cruz et al. (1997) and Liu and Wen (1997). Cruz et al. (1997), derived a set of a 2D-Boussinesq equations over a porous bed of arbitrary thickness and tested their applicability on a plane porous slope and for refraction, diffraction and reflection around a submerged porous breakwater with an opening. Recently, Hsiao et al. (2002) presented a fully non-linear 2D-Boussinesq-type model for waves propagating over a permeable bed and compared model results with experimental data for the case of regular waves passing over a porous submerged breakwater.

In this study wave evolution over porous submerged breakwaters is investigated with the use of a 2DH-Boussinesq-type model, following a procedure similar to that of Cruz et al. (1997). Computed results are compared with experimental measurements provided by Vidal et al. (2002), Gironella and Sánchez-Arcilla (2002) and Zanuttigh and Lamberti (2003).

2. Description of the model

2.1.Governing equations

A higher-order Boussinesq-type model, with improved linear dispersion characteristics is used to describe wave motion in the regions upstream and downstream of the breakwater (Karambas and Koutitas, 2002). Above the breakwater the model incorporates two extra terms accounting for the interaction between the waves over the structure and the flow within the porous structure, one in the continuity equation and one in the momentum equation respectively, following the approach of Cruz et al. (1997). In two-dimensional depth-averaged form the governing equations (continuity and momentum equations) are:

$$\eta_t + \nabla\left[(h+\eta)\mathbf{u}\right] + \varphi\nabla\left(h_s\mathbf{u_s}\right) = 0 \tag{1}$$

$$\begin{aligned}\mathbf{u}_t + \mathbf{u}\nabla\mathbf{u} + g\nabla\eta = &\left(\frac{h^2+2h\eta}{3}\right)\nabla^2\mathbf{u}_t + \nabla h\nabla^2\mathbf{u}_t + \nabla h_x\mathbf{u}_t \\ &+ \frac{h^2}{3}\left(\mathbf{u}\nabla^3\mathbf{u} - \nabla\mathbf{u}\nabla^2\mathbf{u}\right) + \left(h\nabla\eta\nabla\mathbf{u}_t + h\nabla h\mathbf{u}\nabla^2\mathbf{u}\right) \\ &+ Bh^2\left[\nabla^2\mathbf{u}_t + \nabla^3\eta + \nabla^2\left(\mathbf{u}\nabla\mathbf{u}\right)\right] + 2Bh\nabla h\left(\nabla\mathbf{u}_t + \nabla^2\eta\right) \\ &+ \frac{\varphi}{2}h\nabla^2\left(h_s\mathbf{u_{s_t}}\right)\end{aligned} \tag{2}$$

where $\mathbf{u}$ = depth-averaged, horizontal velocity vector, η = surface elevation, h = water depth, B = dispersion coefficient, $\mathbf{u_s}$ = depth-averaged, seepage (fluid) velocity vector inside the porous medium, h_s = porous medium thickness and φ = porosity.

The above variables are shown in Figure 1.

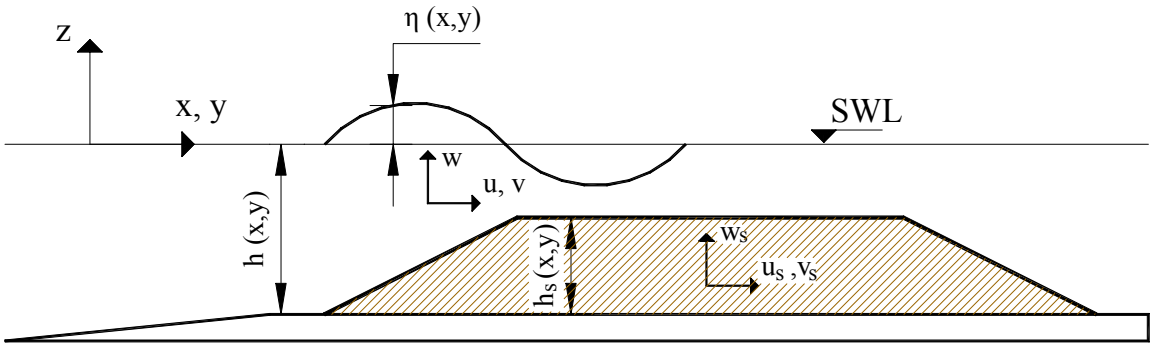

Figure 1. Definition of variables

The additional dispersion terms proportional to B extend the applicability of the model into a wider range of depths. As suggested by Madsen and Sørensen (1992), B is set equal to 1/15, value that gives the closest match to linear theory dispersion relation for h/L_0 as large as 0.5.

Equations (1) and (2) are solved in the region of the breakwater in conjunction with a depth-averaged Darcy-Forchheimer (momentum) equation describing the flow inside the porous medium. Assuming that $O[(h_s/L)^2] << 1$ the two-dimensional, depth-averaged momentum equation written in terms of the fluid velocity $\mathbf{u_s}$ ($\mathbf{u_D} = \varphi\,\mathbf{u_s}$, $\mathbf{u_D}$ = Darcy velocity) reduces to (Cruz et al., 1997)

$$c_r \mathbf{u_s}_t + \mathbf{u_s}\nabla\mathbf{u_s} = -g\nabla\eta + \varphi\alpha_1\mathbf{u_s} + \varphi^2\alpha_2\mathbf{u_s}|\mathbf{u_s}| \tag{3}$$

which is refered as the non-linear long wave equation for porous medium. The fourth term in equation (3) is the Darcy term, while the fifth term is the Forchheimer term accounting for viscous and inertia forces respectively. In equation (3), c_r = inertial coefficient, given by (van Gent, 1995)

$$c_r = \frac{1+c_m}{\varphi} = \frac{1+\gamma\dfrac{1-\varphi}{\varphi}}{\varphi} \tag{4}$$

where c_m = added mass coefficient and γ = empirical coefficient that accounts for the added mass.

The porous resistance coefficients α_1 and α_2, are estimated from the following relationships (Ward, 1964, Sollitt & Cross, 1972, Losada et al., 1995, Cruz et al.,1997)

$$\alpha_1 = \frac{\nu}{K}, \quad \alpha_2 = \frac{C_f}{\sqrt{K}} \tag{5}$$

where ν = kinematic viscosity ($1.0\cdot10^{-6}$ m^2/sec), C_f = dimensionless parameter and K = intrinsic permeability (m^2) given by (van Gent, 1994, 1995, Burcharth and Andersen, 1995)

$$K = \frac{{d_{50}}^2 \cdot \varphi^3}{\alpha(1-\varphi)^2} \tag{6}$$

where α = empirical coefficient and d_{50} = the mean size of the porous material.

Burcharth and Andersen (1995), provide after Engelund (1953), a similar formula for calculating the intrinsic permeability, K

$$K = \frac{{d_{50}}^2 \cdot \varphi^2}{\alpha(1-\varphi)^3} \tag{7}$$

According to Ward (1964), the parameter C_f is a constant, equal to 0.55, however, van Gent (1995) proposes the following expression for calculating C_f

$$C_f = \beta \frac{1-\varphi}{\varphi} \frac{\sqrt{K}}{d_{50}} \tag{8}$$

where β = empirical coefficient.

An alternative expression for the coefficient α_2 is (van Gent, 1995)

$$\alpha_2 = \beta\left(1 + \frac{7.5}{KC}\right)\frac{(1-\varphi)}{d_{50} \cdot \varphi^3} \tag{9}$$

where KC = $(\hat{U}T)/(d_{50} \cdot \varphi)$ is a Keulegan-Carpenter number for porous media flow ($\hat{U}$ = the maximum velocity in the porous medium).

A number of studies (Madsen, 1974, Vidal et al., 1988, van Gent, 1995) propose values for the non-dimensional coefficients α, β and γ depending on the material type and the length scale of the solid particles. In the following table (Table 1) values for the coefficients α and β obtained by van Gent (1995) after his experimental work are listed

Table 1. Material tested and corresponding coefficients (van Gent, 1995)

Material	D_{50}	φ	α	β
Irregular rock	0.0610	0.442	1791	0.55
Semi round rock	0.0487	0.454	0	0.88
Very round rock	0.0488	0.393	1066	0.29
Irregular rock	0.0202	0.449	1662	1.07
Irregular rock	0.0310	0.388	1007	0.63
Spheres	0.0460	0.476	2070	0.69

For the present model the value of 1000, 1.1 and 0.34 is chosen for α, β and γ respectively, as recommended by van Gent (1995). In contrast with the preliminary version of the model (Avgeris et al., 2003), where C_f was considered equal to 0.55, in the present, final version C_f is treated as a variable. The corresponding values of K, C_f, α_1, α_2 and c_r assuming that φ = 0.5, are calculated from equations (6), (8), (5) and (4) and are equal to $0.0005 \cdot d_{50}^2$, 0.0246, $0.002/d_{50}^2$, $1.1001/d_{50}$ and 2.68 respectively.

The one-dimensional form of equations (1) – (3) is written

$$\frac{\partial \eta}{\partial t} + \frac{\partial \left[(h+\eta) u \right]}{\partial x} + \varphi \frac{\partial \left(h_s \cdot u_s \right)}{\partial x} = 0 \tag{10}$$

$$\begin{aligned} &\frac{\partial u}{\partial t} + u\frac{\partial u}{\partial x} + g\frac{\partial \eta}{\partial x} = \frac{\left(h^2 + 2h\eta\right)}{3}\frac{\partial^3 u}{\partial x^2 \partial t} + h\frac{\partial h}{\partial x}\frac{\partial^2 u}{\partial x \partial t} + \frac{\partial h}{\partial x}\frac{\partial \eta}{\partial x}\frac{\partial u}{\partial t} \\ &+ \frac{h^2}{3}\left(u\frac{\partial^3 u}{\partial x^3} - \frac{\partial u}{\partial x}\frac{\partial^2 u}{\partial x^2} \right) + h\frac{\partial \eta}{\partial x}\frac{\partial^2 u}{\partial x \partial t} + h\frac{\partial h}{\partial x}u\frac{\partial^2 u}{\partial x^2} \\ &+ Bh^2\left[\frac{\partial^3 u}{\partial x^2 \partial t} + g\frac{\partial^3 \eta}{\partial x^3} + \frac{\partial^2 \left(u\partial^2 u / \partial x^2 \right)}{\partial x^2} \right] \\ &+ 2Bh\frac{\partial h}{\partial x}\left(\frac{\partial^2 u}{\partial x \partial t} + g\frac{\partial^2 \eta}{\partial x^2} \right) + \varphi h\left(\frac{\partial h_s}{\partial x}\frac{\partial^2 u_s}{\partial x \partial t} + \frac{1}{2}h_s\frac{\partial^3 u_s}{\partial x^2 \partial t} \right) \end{aligned} \tag{11}$$

$$c_r \frac{\partial u_s}{\partial t} + u_s \frac{\partial u_s}{\partial x} = -g\frac{\partial \eta}{\partial x} + \varphi\alpha_1 u_s + \varphi^2 \alpha_2 u_s |u_s| \tag{12}$$

2.2. Numerical scheme

The governing equations are finite-differenced utilizing a high-order predictor-corrector scheme that employs a third-order explicit Adams-Bashforth predictor step and a fourth-order implicit Adams-Moulton corrector step (Wei and Kirby, 1995). The corrector step is iterated until the desirable convergence is achieved. First order spatial derivatives are discretized to fourth-order accuracy.

2.3. Wave generation

Wave generation is implemented inside the computational domain using the source function method as described by Wei et al. (1999). This method employs a mass source term in the continuity equation (1) that acts on a limited 'source region' while it is combined with wave damping sponge layers at the boundaries. The method is adapted to be consistent with the

Karambas and Koutitas (2002) equations, used in the present work, instead of the Nwogu type of equations, used by Wei et al. (1999).

For random wave generation in a two-dimensional field where wave propagation direction forms an angle θ with the x-axis, the expression for the source function term reads

$$f_s(x, y, t) = \frac{1}{4\pi^2} \iint D_s(\lambda, \omega) \exp\left[-\beta_s (x - x_s)^2\right] \exp[i(\lambda y - \omega t)] \, d\omega \, d\lambda \qquad (13)$$

where $\lambda = k\sin(\theta)$ = wavenumber in y direction, x_s = centre of source function, β_s = source shape coefficient and D_s = magnitude of the source function.

In the case of regular waves with angular frequency ω that propagate across the x-axis the above expression simplifies

$$f_s(x, t) = D_s \exp[-\beta_s (x - x_s)]^2 \sin(\omega t) \qquad (14)$$

The value of β_s is calculated from the following relationship

$$\beta_s = \frac{80}{\delta^2 L^2} \qquad (15)$$

where $\delta = 0.3$, while

$$D_s = \frac{2\alpha_0 \cos(\theta)\left(\omega^2 - \alpha_{s1} g k^4 h^3\right)}{\omega k I_1 \left[1 - \alpha_s (kh^2)\right]} \qquad (16)$$

where $\alpha_s = -0.4$, $\alpha_{s1} = \alpha_s + 1/3$ and

$$I_1 = \sqrt{\frac{\pi}{\beta_s}} \exp\left(\frac{-l^2}{4\beta_s}\right) \qquad (17)$$

where $l = k\cos(\theta)$ = wavenumber in x direction.

Figure 2 depicts oblique, irregular waves generated inside a 2D computational field, applying the source function method.

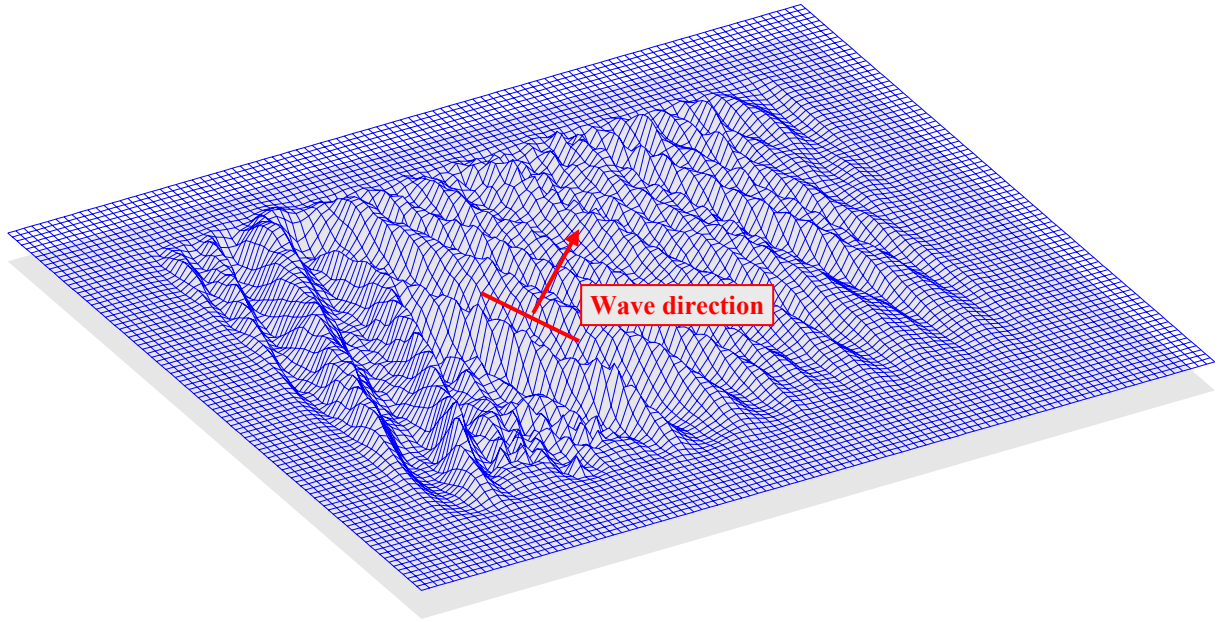

Figure 2. Oblique, irregular waves (Jonswap spectrum, H_s = 0.09 m, T_p = 1.2 sec) generated inside a 2D computational field

2.4. Wave breaking

An eddy viscosity formulation is adopted in order to simulate wave breaking (Kennedy et al., 2000) by introducing an eddy viscosity term in the right-hand-side of the momentum equation (2)

$$\mathbf{u}_t + \ldots = \left(\frac{h^2 + 2h\eta}{3}\right)\nabla^2\mathbf{u}_t + \ldots + \mathbf{E}_b \tag{18}$$

This term is analysed (subscripts of (x, y) and t denote spatial and temporal differentiation respectively) as

$$\mathbf{E}_{b_x} = \frac{1}{h+\eta}\left\{\left(\nu_e\left[(h+\eta)u\right]_x\right)_x + \frac{1}{2}\left(\nu_e\left[(h+\eta)u\right]_y + \left[(h+\eta)v\right]_x\right)_y\right\} \tag{19}$$

$$\mathbf{E}_{b_y} = \frac{1}{h+\eta}\left\{\left(\nu_e\left[(h+\eta)v\right]_y\right)_y + \frac{1}{2}\left(\nu_e\left[(h+\eta)v\right]_x + \left[(h+\eta)u\right]_y\right)_x\right\} \tag{20}$$

The eddy viscosity ν_e, is a function of both space and time and is given by

$$\nu_e = B_b\delta_b{}^2(h+\eta)\eta_t \tag{21}$$

where δ_b = mixing length coefficient equal to 1.2. The quantity B_b controls the occurrence of breaking and varies from 0 to 1 as follows

$$B_b = \begin{cases} 1, & \eta_t \geq 2\eta_t^* \\ \dfrac{\eta_t}{\eta_t^*} - 1, & \eta_t^* < \eta_t \geq 2\eta_t^* \\ 0, & \eta_t \leq \eta_t^* \end{cases} \tag{22}$$

The parameter η_t^* determines the onset and cessation of breaking and is defined as

$$\eta_t^* = \begin{cases} \eta_t^{(F)}, & t \geq T^* \\ \eta_t^{(I)} + \dfrac{t - t_0}{T^*}\left(\eta_t^{(F)} - \eta_t^{(I)}\right), & 0 < t - t_0 \geq T^* \end{cases} \tag{23}$$

where T^* = transition time $\left(= 5\sqrt{g/h}\right)$, t_0 = time that breaking was initiated ($\eta_t > \eta_t^{(I)}$), and thus $t-t_0$ = age of the breaking event. The values of $\eta_t^{(I)}$ and $\eta_t^{(F)}$ are $0.35\sqrt{gh}$ and $0.15\sqrt{gh}$ respectively.

3. 1D Model – Comparison with UCA experiments

Initially, model results were evaluated using data collected during the experiments that took place in the wave and current flume of the Coastal Laboratory of the University of Cantabria (UCA), Spain as part of the research carried out for DELOS project. The experimental set-up is described in detail by Vidal et al. (2002). Several data sets corresponding to different regular and irregular wave conditions were used for model verification.

3.1. Experimental set–up

The wave and current flume of the UCA Coastal Laboratory is 24 m long, 0.60 m wide and 0.80 m high. The piston–type wavemaker has two attached free surface wave gauges integrated in a wave absorption system that allows the absorption of reflected waves from the experimental model.

Wave propagation over a rubble mound breakwater on a sloping beach was tested. The breakwater had a trapezoidal shape, while its crest width ranged between 0.25 and 1.0 m. Crest elevation from the bottom (0.25 m), front and back slope angles (1:2) and rubble

characteristics were maintained constant. The model had two-layer armour of selected gravel and a gravel core. Armour and core characteristics are shown in Table 2.

Table 2. Characteristics of the gravels used for the experimental model

	W_{50} (g)	D_{50} (cm)	Porosity -	Density (Kg/m^3)
Armour	153	3.94	0.53	2647
Core	4.31	1.18	0.49	2607

The rubble mound breakwater was built over a horizontal false bottom, 0.10 m over the bottom of the flume. In the frontal foot of the rubble, a Plexiglas ramp with 1:20 slope connected the false bottom with the bottom of the flume. In the rear end, another 8 m 1:20 Plexiglas ramp simulated the rear beach. A sketch of the wave flume is illustrated in Figure 3. During the experiments water depth at the paddle was either 0.30 m, or 0.35 m, or 0.4 m resulting in a freeboard of 0.05 m, 0.00 and –0.05 m respectively.

To assess free surface evolution and run-up on the beach, 15 resistive free surface gauges were installed along the flume. Three free surface gauges were installed in the slope in front of the breakwater to separate incident and reflected waves. Another two free surface gauges were located over the front slope of the structure. Six free surface gauges measured transmitted waves over the crest and in the flat bottom behind the structure.

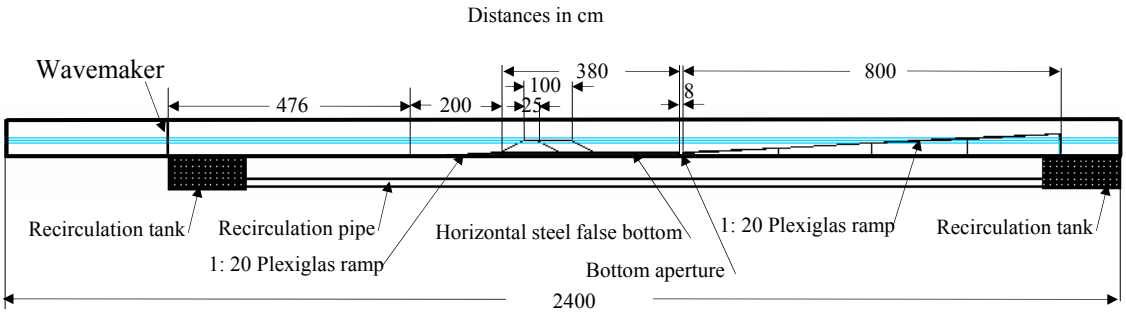

Figure 3. UCA experimental set-up

3.2. Implementation of the model

Evaluation of the numerical model was performed for the case of the submerged breakwater (freeboard = –5 cm) with 1 m crest width.

There were several data sets available, involving regular and irregular waves of TMA spectrum, respective to this layout. In this report the comparison of model results with the

experimental data of 2 regular tests (two out of the four chosen for comparison with the preliminary version of the model) and 3 irregular tests indexed with code numbers 215, 219, 230, 243, 255, 263 and 275 (cases (a), (b), (c), (d), (e), (f) and (g)) is presented. For each case the target wave characteristics were: (a) H = 0.10 m, T = 1.6 sec, (b) H = 0.05 m, T = 3.2 sec, (c) H_s = 0.04 m, T_p = 1.6 sec, (d) H_s = 0.07 m, T = 1.6 sec and (e) H_s = 0.07 m, T_s = 2.4 sec.

For the regular wave tests, the location of the wavemaker was defined as the centre of the source function. On the other hand, in the case of irregular waves the centre of the source function coincided with gauge 1 in order to use the free surface time series at this gauge as an input for the derivation of the source function record. The time step used was either Δt = 0.0025 sec (regular waves) or Δt = 0.002083 sec (irregular waves) and the grid size Δx = 0.05 m. The layout of the computational domain is depicted in Figure 4. In this figure, the numbered vertical lines indicate the location of the wave gauges for which computed results are compared with experimental measurements.

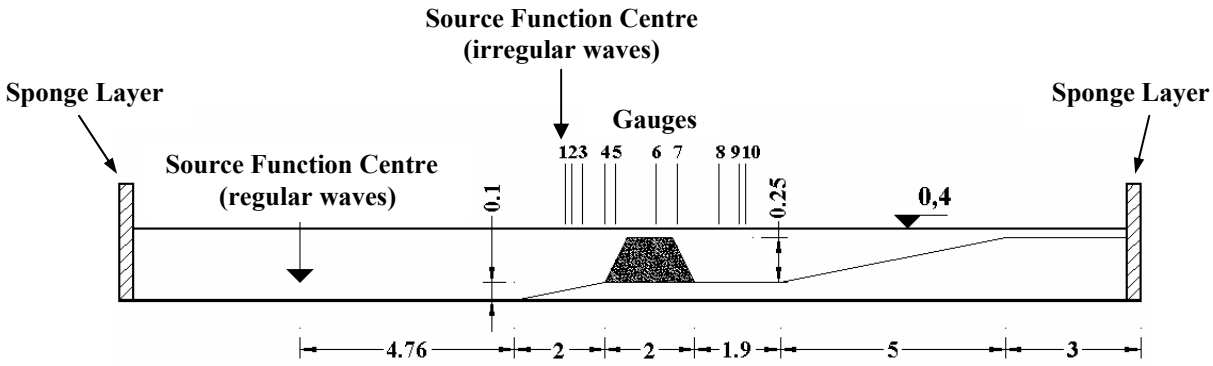

Figure 4. Layout of the computational domain

The porosity of the rubble mound was set equal to 0.5 while the characteristic diameter d_{50} of the gravel was set equal to 2 cm, resulting in a permeability K equal to $2 \cdot 10^{-7}$ m^2 (equation 6). Hence, the respective values of α_1 and α_2 are 5.0 and 55.0.

For all the regular wave cases considered, incident wave height was calculated by employing the Funke and Mansard incident-reflection analysis method, using the free surface elevation time series of wave gauges 1, 2 and 3.

In Figures 8 – 15 comparison between computed results and experimental data are shown for case (a). Figures 8 – 13 present surface elevation time series at 6 wave gauges, (1) Figure 8 seaward of the breakwater, over the sloping bed (gauge 2 or 3) (2) Figure 9 over the frontal slope of the breakwater (gauge 4 or 5), (3) Figure 10 over the breakwater crest (gauge 6),

(4) Figure 11 over the shoreward slope of the structure (gauge 7) and (5&6) Figure 12 and Figure 13 behind the breakwater (gauge 8 and gauge 9). Figures 14 and 15 illustrate comparatively for the same case the computed and experimental incident and transmitted spectra respectively. Figures 16 – 23, are analogous to Figures 8 – 15 for test case (b). Figures 24 – 28, 29 – 33 and 34 – 38 present comparatively, computed and recorded free surface elevation time series at wave gauges 4 – 8 for cases (c), (d) and (e) respectively. Finally, Figure 45 shows the values of the transmission coefficient K_{trans} as calculated from model results and the experimental data for cases (a) – (d).

4. 1D Model – Comparison with UPC experiments

Further evaluation of the model results was performed with the use of the experiments that were carried out in the wave flume of the Maritime Engineering Laboratory of UPC, Spain. These experiments in comparison to the UCA experiments provide a helpful tool in order to assess scale effects.

4.1. Experimental set–up

The experimental layout is depicted in Figure 5 and was quite similar to that of the University of Cantabria. A rubble mound breakwater with 1:2 slopes that consisted of an armour layer (d_{50} = 10.5 cm) and a core (d = 20–40 mm) of selected gravel was built over a horizontal plane approximately in the middle of the wave flume. The crest width of the structure was either 1,225 m or 2,345 m and rose 2,705 m over the bottom of the flume. In front of the breakwater lied an inclined bed with two different successive slopes (1/9.35 and 1/28). Similarly to the UCA experiments, water depth at the wavemaker ranged between three levels (2.82 m, 2.62 m and 2.42 m), thus the breakwater was either submerged (freeboard = –11.5 cm) or emerged (freeboard = 8.5 cm and 28.5 cm). At the rear end of the flume an absorbing inclined beach, constructed of irregular rock dissipated the forthcoming wave energy. Free surface elevation was measured with seven gauges, from which five were installed at the seaward region, in front of the breakwater and the rest behind it. For more details see Gironella and Sánchez-Arcilla (2002).

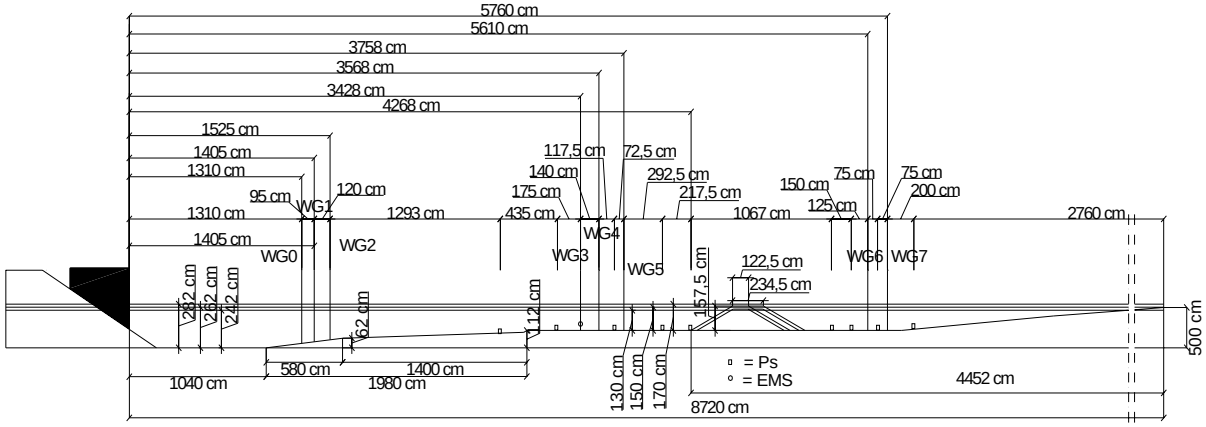

Figure 5. Sketch of the UPC experimental layout

4.2. Implementation of the model

In order to evaluate the performance of the numerical model against scale effects, comparison was carried out for the case of the submerged breakwater (freeboard = –11.5 cm) with 2,345 m crest width.

Considering regular wave tests, there were 3 data sets available, according to this layout. However, only 1 test out of the 3, was appropriate for model testing, since the incident wave characteristics of the other tests resulted in a ratio of wave height to freeboard far greater than 1/2. For this test (index number R6F3C2) comparison of model results with the experimental data (case (a)) is presented. The target wave characteristics for this case were: (a) H = 0.28 m, T = 3.11 sec.

The values used for the time step and the grid size were Δt = 0.005 sec and Δx = 0.10 m. Considering a uniform porosity for the breakwater equal to 0.4 and a mean diameter d_{50} of the porous material equal to 7 cm the corresponding values for K, C_f, α_1, α_2 and c_r are $8.71 \cdot 10^{-7}$, 0.022, 1.148, 23.571 and 3.775.

Similarly to the UCA test cases, incident wave height was calculated analysing the time series of wave gauges 3, 4 and 5 with the Funke and Mansard method.

Figures 39 – 44 show in comparison, computed results and experimental measurements for case (a). Figures 39 – 42 present surface elevation time series at 4 wave gauges, (1) Figures 39, 40 and 41 in front of the breakwater, over the sloping bed (gauge 3, 4 and 5) and (2) Figure 42 at the shoreward horizontal plane behind the structure (gauge 6). Figures 43 and 44 depict comparatively the computed and experimental incident and transmitted spectra

respectively for case (a). Finally, Figure 45 shows the values of the transmission coefficient K_{trans} as calculated from model results and the experimental data for the same case.

5. 2D Model – Wave transformation around a system of porous submerged breakwaters – Comparison with Aalborg experiments

Waves travelling over porous breakwaters are subject to transformation due to combined physical effects, including refraction, diffraction, shoaling and damping. Apparently, the simulation of such complicated processes is quite a demanding task. The 2D version of the model is firstly applied to simulate wave transformation around a system of porous submerged breakwaters that consists of two (or infinite in a generic sense) trapezoidal rubble mounds with 1:6.66 forward slope, 1:20 backward slope and 1 m crest width. The structures are located on a 1:30 sloping bed. The depth of the water on the horizontal bottom is 0.5 m and the freeboard –0.2 m. Breakwater width and length are 3 and 4 m respectively, while the opening between the structures is 4 m. The mean diameter of the breakwater material (d_{50}) is considered equal to 4 cm and the porosity equal to 0.4. Figure 6 shows the bathymetry of the 2D field. The computational domain is restricted to the half of the field, considering that there is a symmetry line along the middle of the opening. Both at the left and the right boundaries of the computational domain, wave-reflecting (symmetry) boundary conditions are imposed. A regular (case (a)) and an irregular (JONSWAP spectrum, (case (b)) wave cases are considered, with incident wave characteristics H = 0.1 m, T = 1.6 sec and H_s = 0.1 m, T_p = 1.6 sec, respectively.

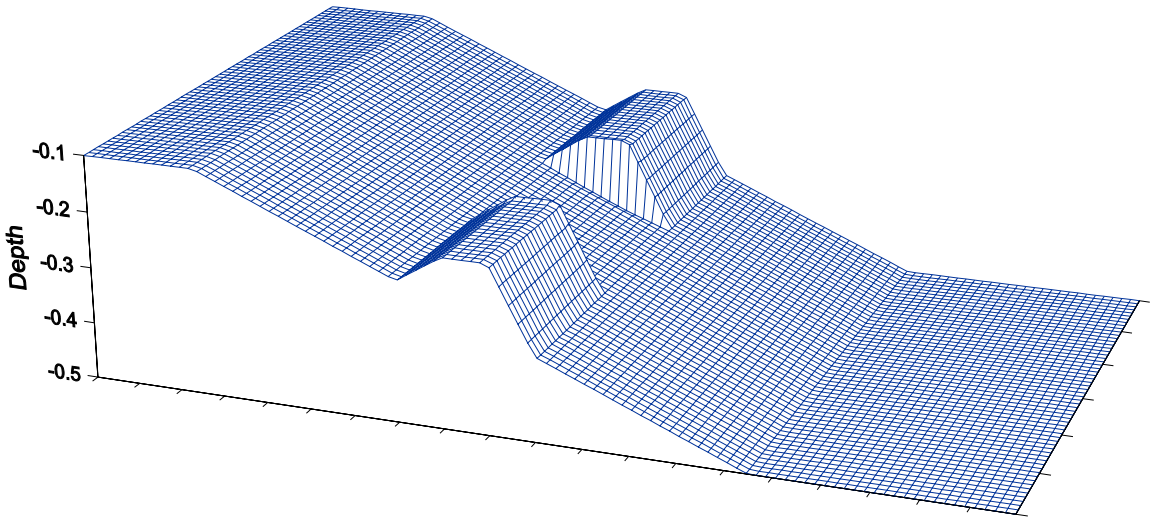

Figure 6. Bathymetry of the 2D computational field

In Figure 46 and Figure 47, snapshots of free surface elevation for case (a) and case (b) respectively are depicted, while Figures 48 and 49 show the wave-induced current fields averaged over two (case (a)) and thirty (case (b)) wave periods.

Further, preliminary tests of the present model against the 3D hydrodynamic experiments carried out under the framework of the DELOS project at the 9.7 x 12.5 basin of Aalborg University, Denmark were performed. Two different layouts were considered during these experimental tests. The first one was a symmetrical layout, composed by two detached porous breakwaters forming a rip channel in the middle. The second layout consisted of a single breakwater inclined at 30^0 with respect to the beach. Detailed description of the experimental layouts and the characteristics of the tests is provided by Zannutigh and Lamberti (2003). Here the numerical results of a single regular wave test (test 19) corresponding to the symmetrical layout with the submerged (freeboard = –0.07m) narrow crest structures are presented. A plan view of this layout is shown in Figure 7. For this test the target wave characteristics were: H = 0.1026 m, T = 1.81 sec. In the model, the porosity of the rubble mound was set equal to 0.5 while the characteristic diameter d_{50} of the gravel was set equal to 3.5 cm.

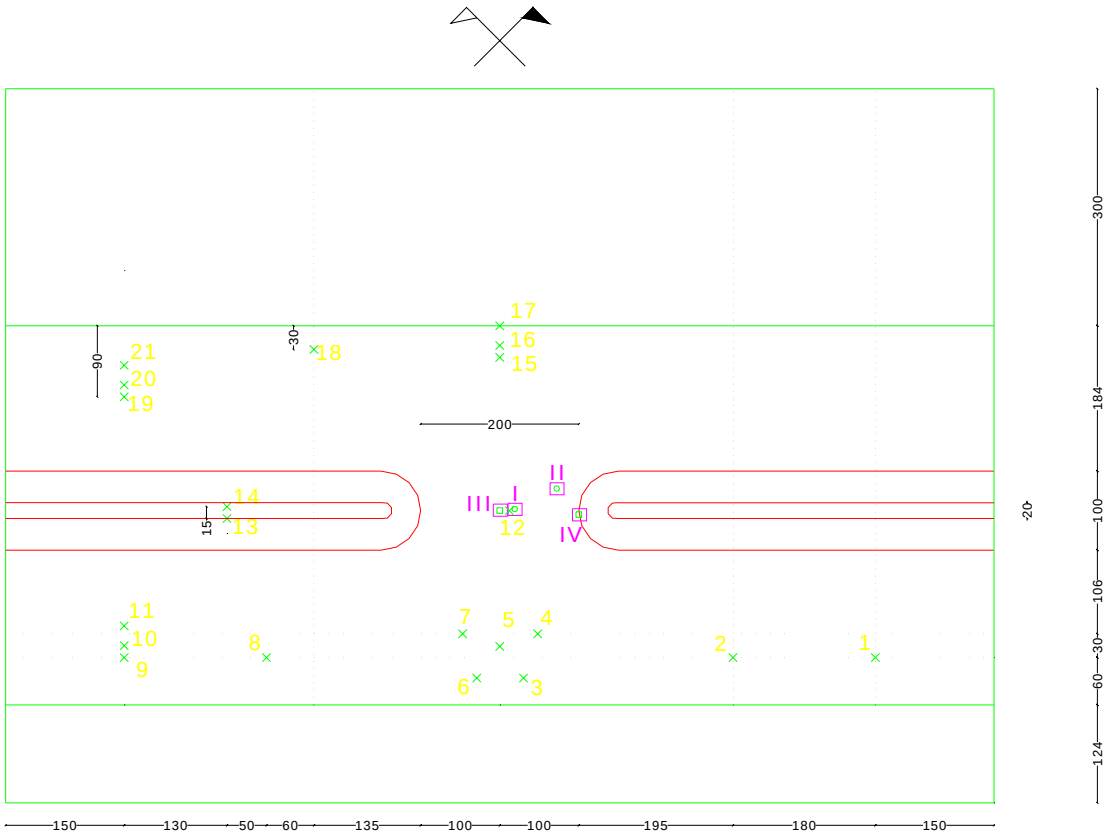

Figure 7. Plan view of Aalborg experimental layout 1 (narrow crest structures)

Figures 50 – 51 present a comparison of surface elevation time series between model results and experimental data at 2 wave gauges, Figure 50 seaward of the breakwater, over the horizontal bed (gauge 11) and Figure 51 behind the breakwater (gauge 19). Finally, Figure 52 depicts the wave-induced current field averaged over two wave periods for the same test.

6. Evaluation of model performance

The comparisons indicate that the model simulates quite well wave evolution at the regions before and over the breakwater. Behind the breakwater the decomposition of the leading wave component into higher frequency waves, comparatively to the preliminary version of the model, is predicted with higher accuracy due to the additional higher-order terms. A deficiency of the model affecting the results is that the linear dispersion relationship is not accurate, although improved. According to Gobbi and Kirby (1999) this deficiency seems to be important. Apparently, model performance is also influenced by the fact that the wave energy dissipation rate due to porous resistance and wave breaking is not exactly predicted. Present model behaviour is enhanced, compared with the behaviour of weakly non-linear Boussinesq-type models applied in the simulation of wave evolution over impermeable and permeable submerged bars (Gobbi and Kirby, 1999, Hsiao et al., 2002). Thought, it should be emphasised that in the present study the model was tested for rather extreme geometrical conditions as far as the ratios of wave height and water depth to freeboard of the submerged breakwater are concerned. Also, the successive, comparative evaluation of model results with the UCA and UPC experimental data, demonstrates that the model is quite insensitive to scale effects.

7. Conclusions

A 2DH-Boussinesq-type model combined with a depth-averaged Darcy-Forchheimer equation is applied in this study for simulating wave propagation over submerged porous breakwaters. The model was tested against experimental measurements for the case of a rubble mound trapezoidal breakwater on a sloping beach. Both regular and irregular wave cases were used in order to assess model performance. The comparative analysis demonstrates that the model predicts quite accurately the wave pattern over and behind the structure. Additional higher order non-linear terms improve the ability of the model to describe the process of non-linear harmonic generation behind the structure.

8. Figures

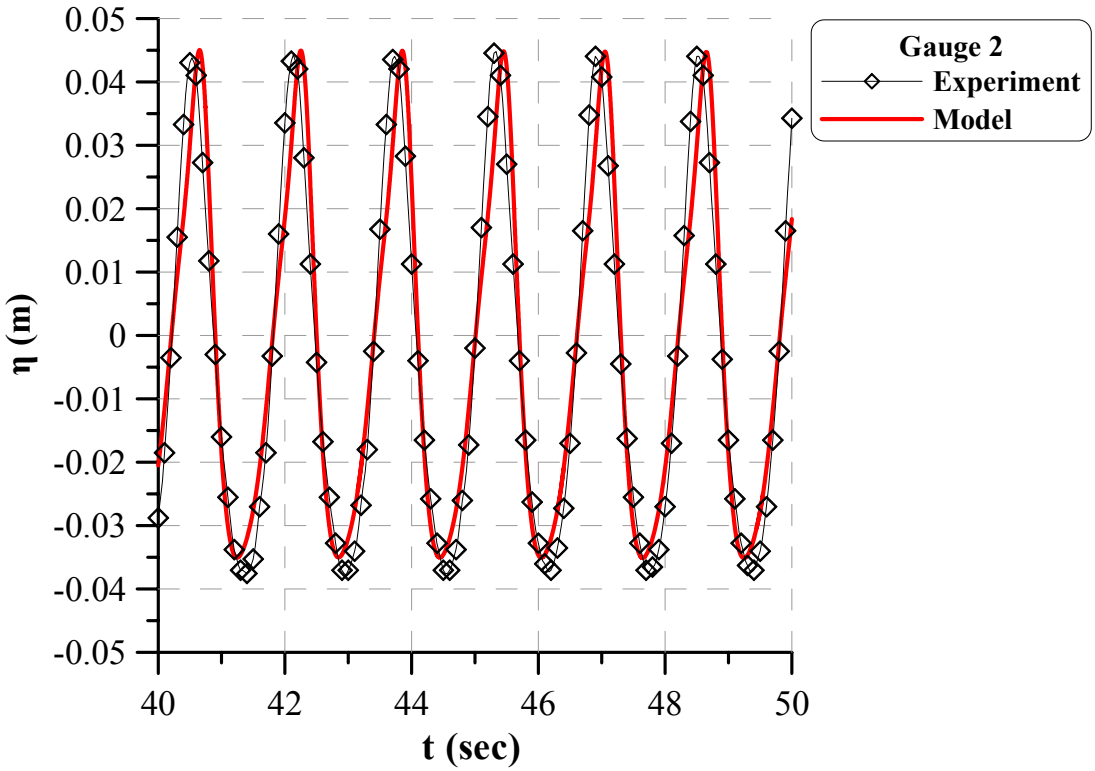

Figure 8.Computed and experimental free surface elevation (UCA, H=0.10, T=1.6).

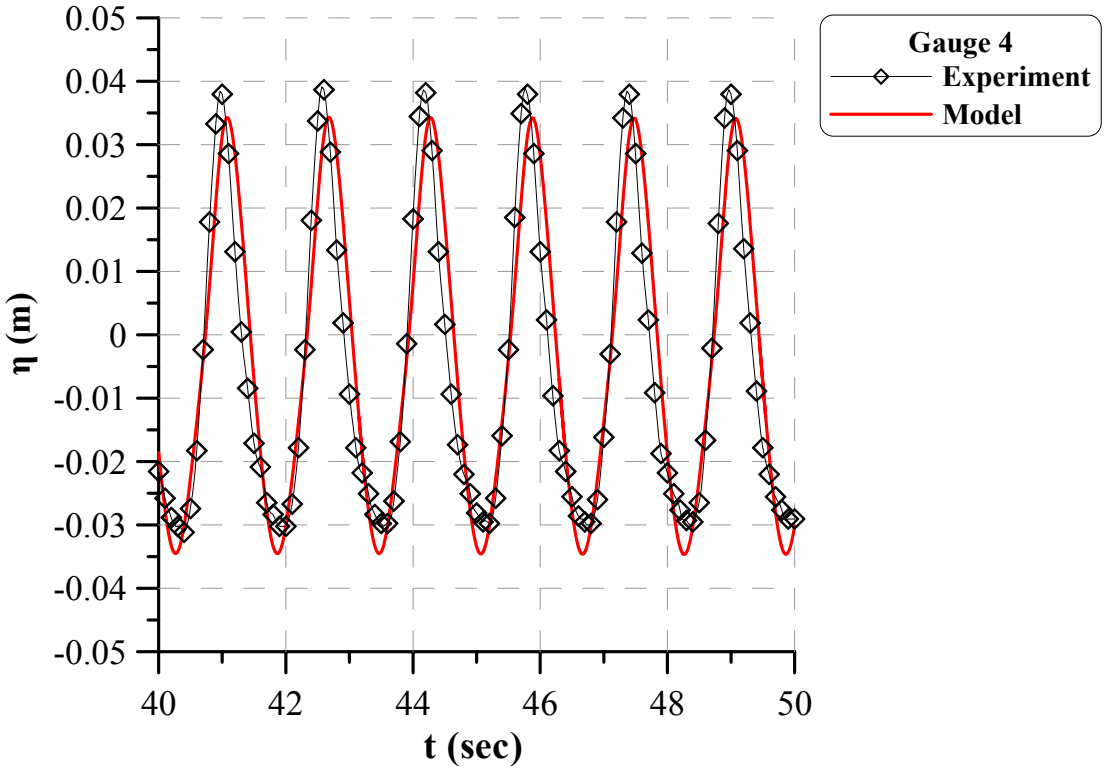

Figure 9.Computed and experimental free surface elevation (UCA, H=0.10, T=1.6).

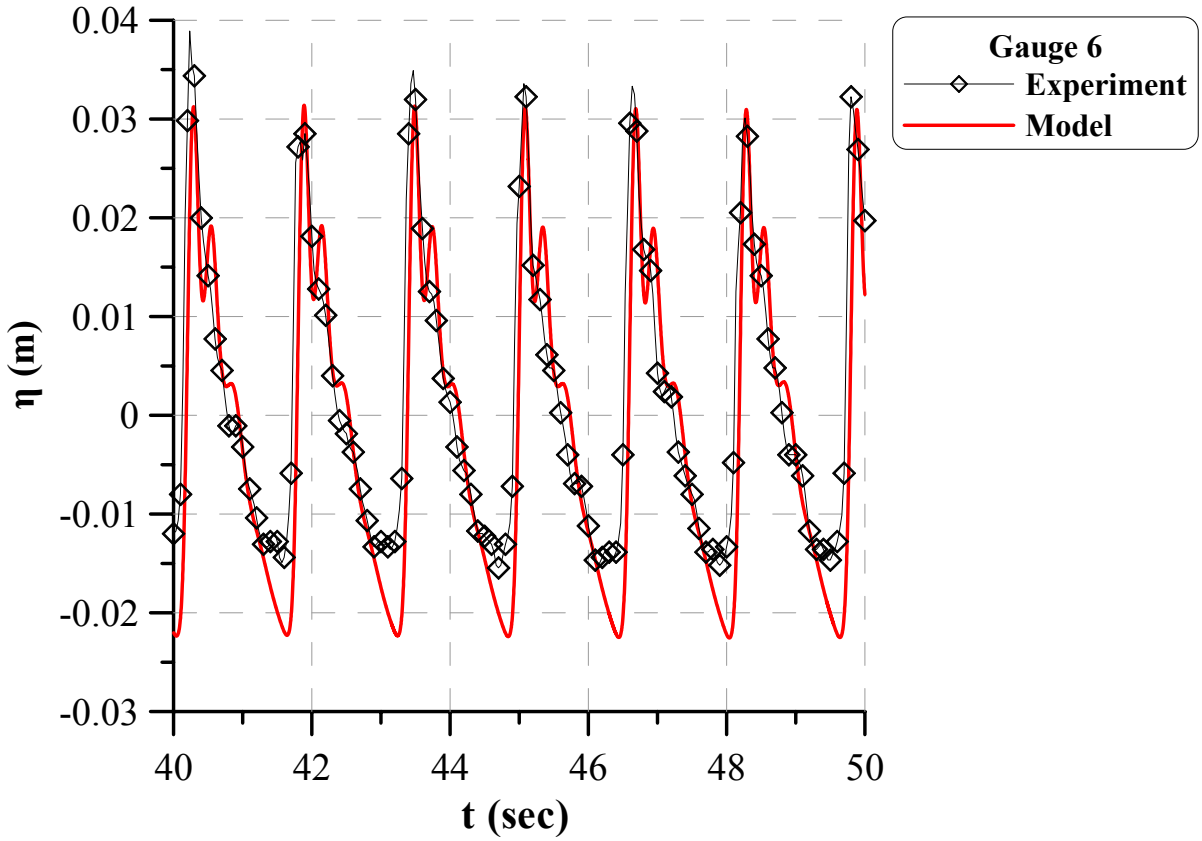

Figure 10.Computed and experimental free surface elevation (UCA, H=0.10, T=1.6).

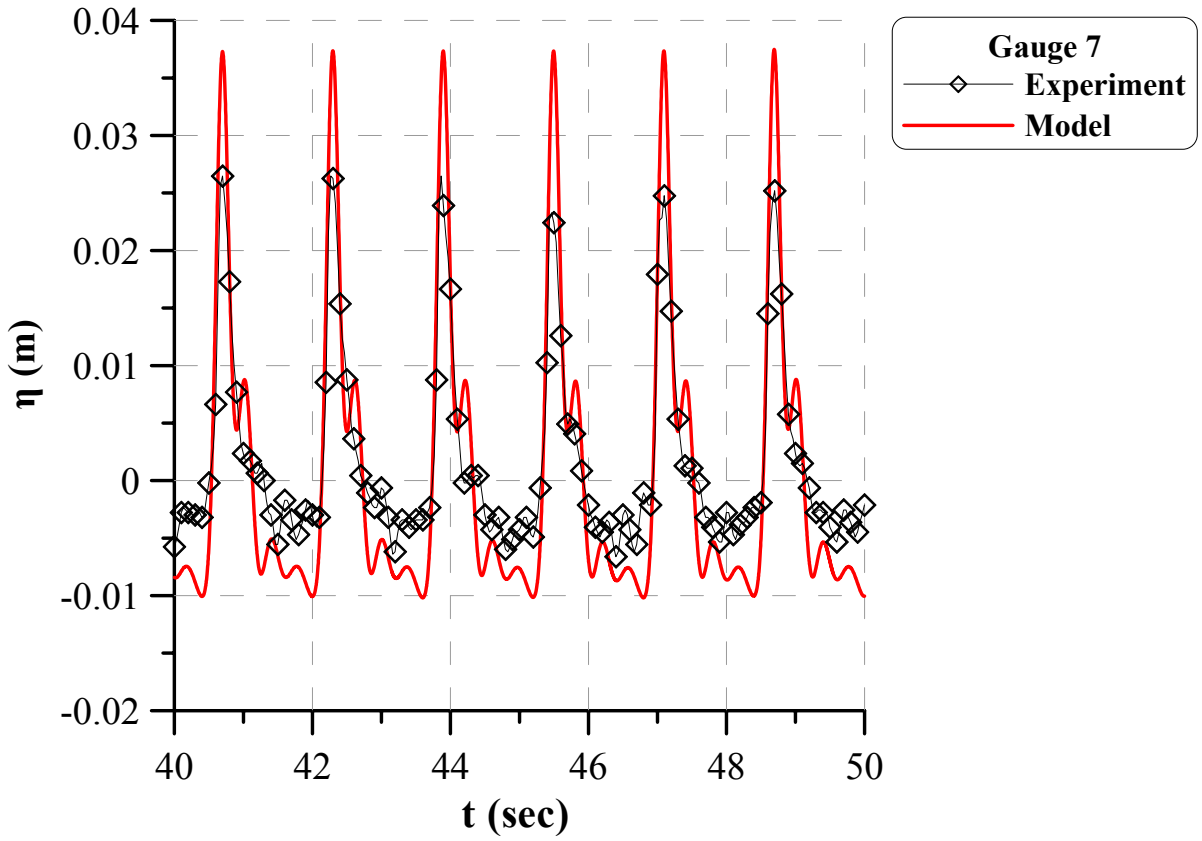

Figure 11.Computed and experimental free surface elevation (UCA, H=0.10, T=1.6).

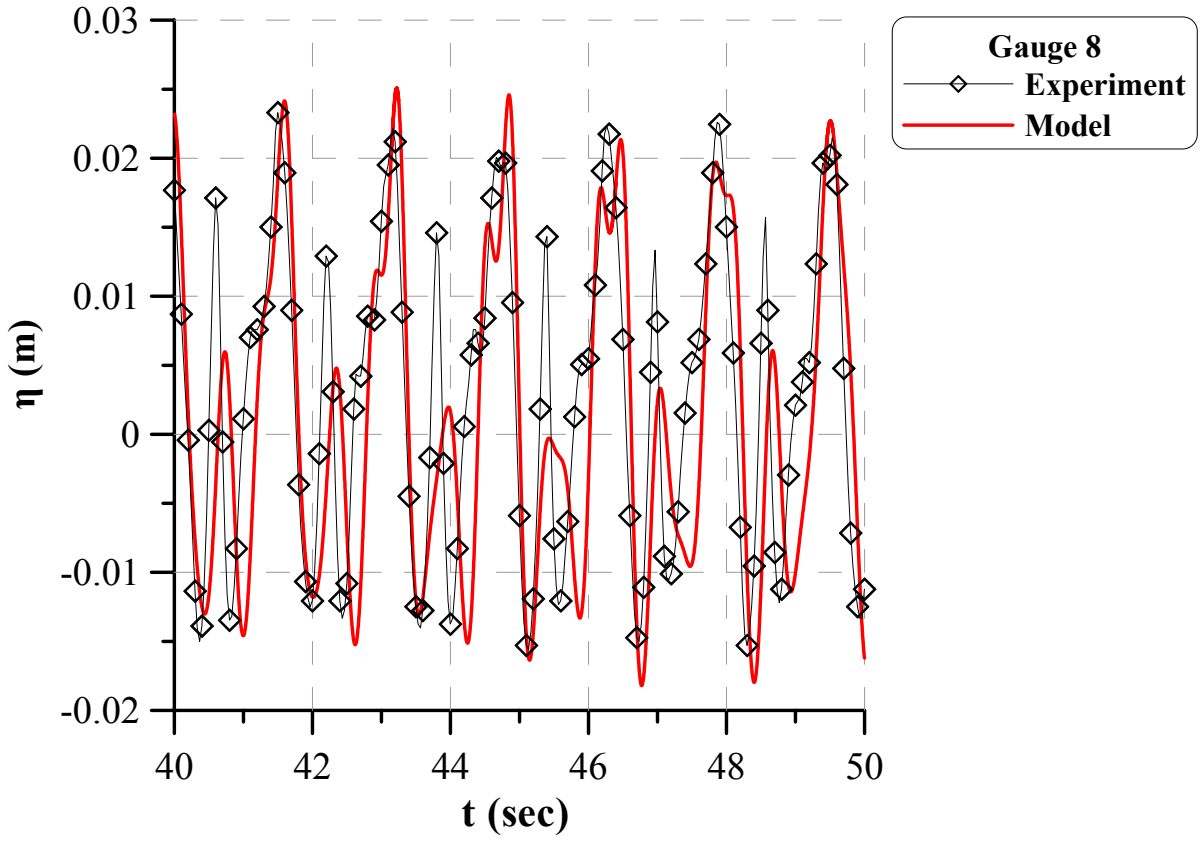

Figure 12.Computed and experimental free surface elevation (UCA, H=0.10, T=1.6).

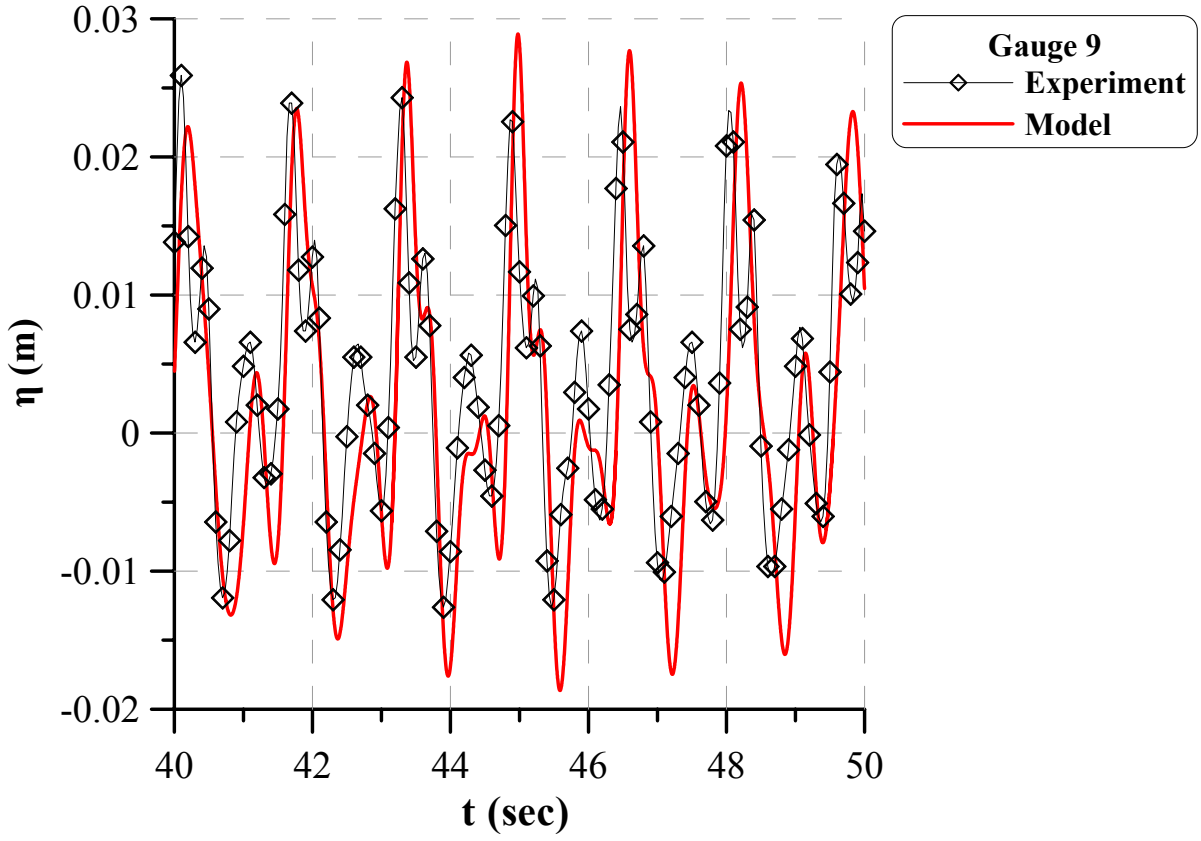

Figure 13.Computed and experimental free surface elevation (UCA, H=0.10, T=1.6).

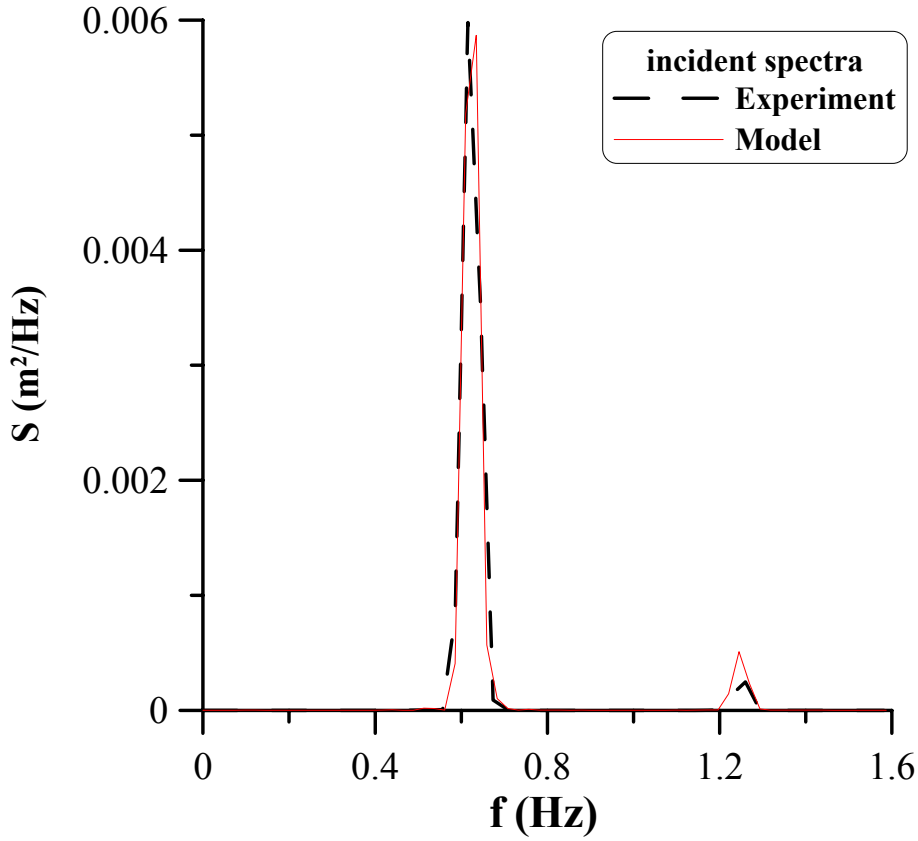

Figure 14.Computed and experimental incident spectra (UCA, H=0.10, T=1.6).

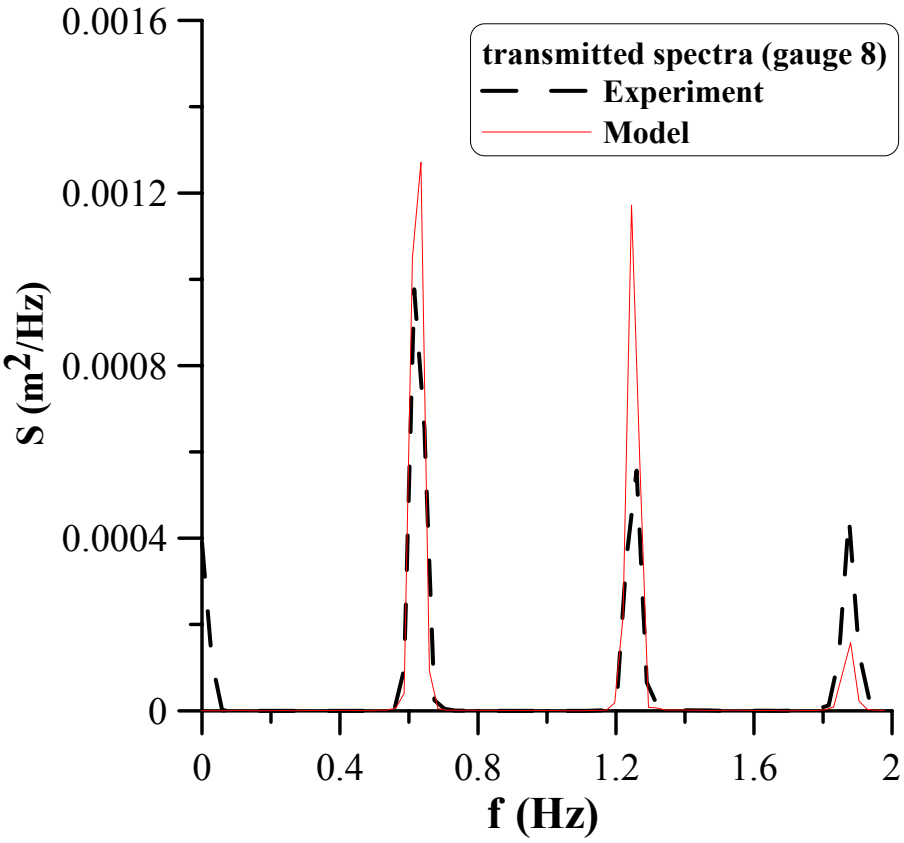

Figure 15.Computed and experimental transmitted spectra (UCA, H=0.10, T=1.6).

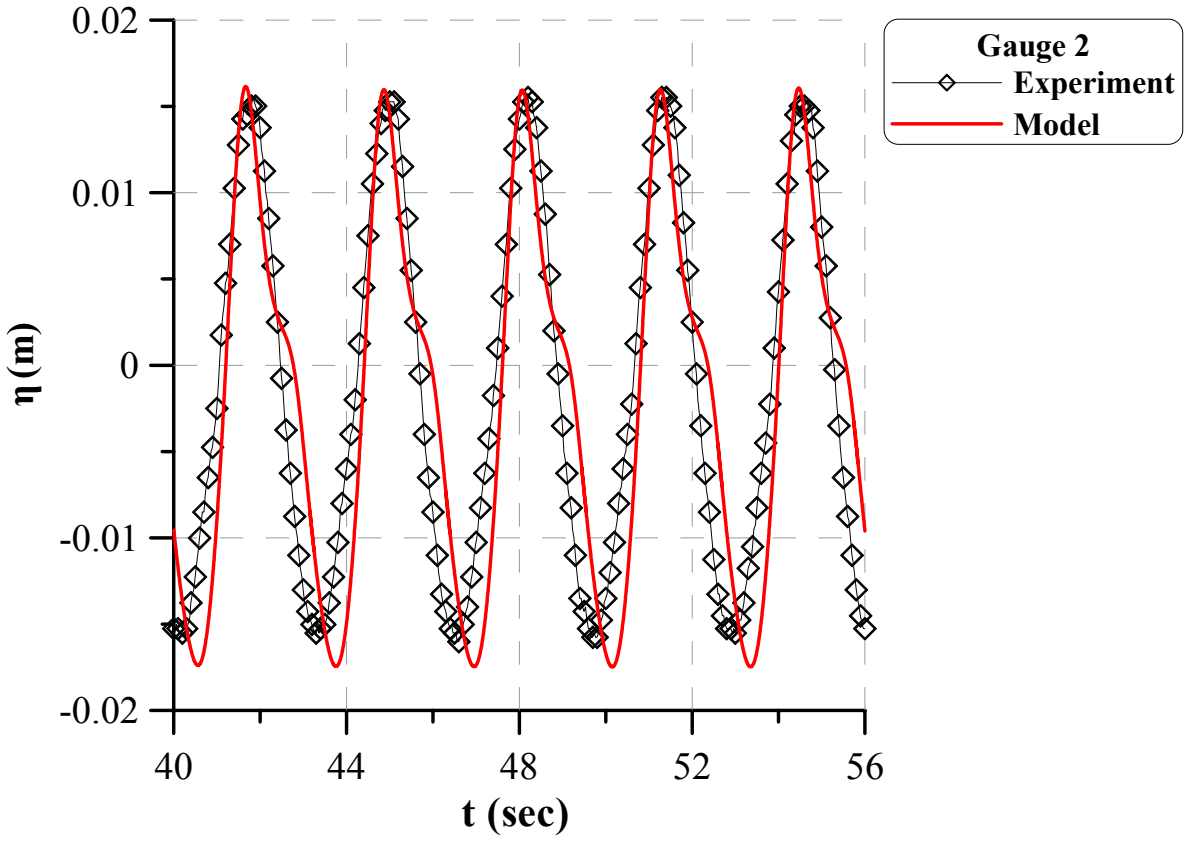

Figure 16.Computed and experimental free surface elevation (UCA, H=0.05, T=3.2).

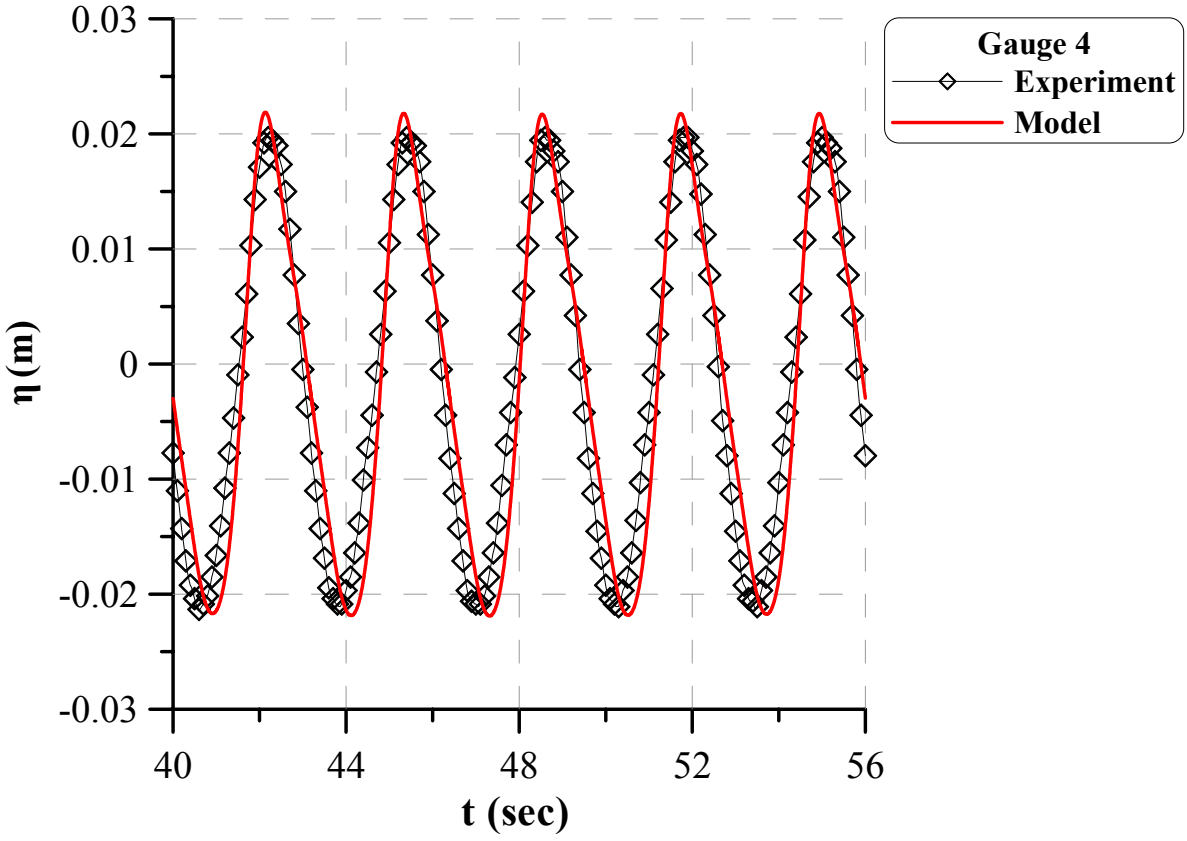

Figure 17.Computed and experimental free surface elevation (UCA, H=0.05, T=3.2).

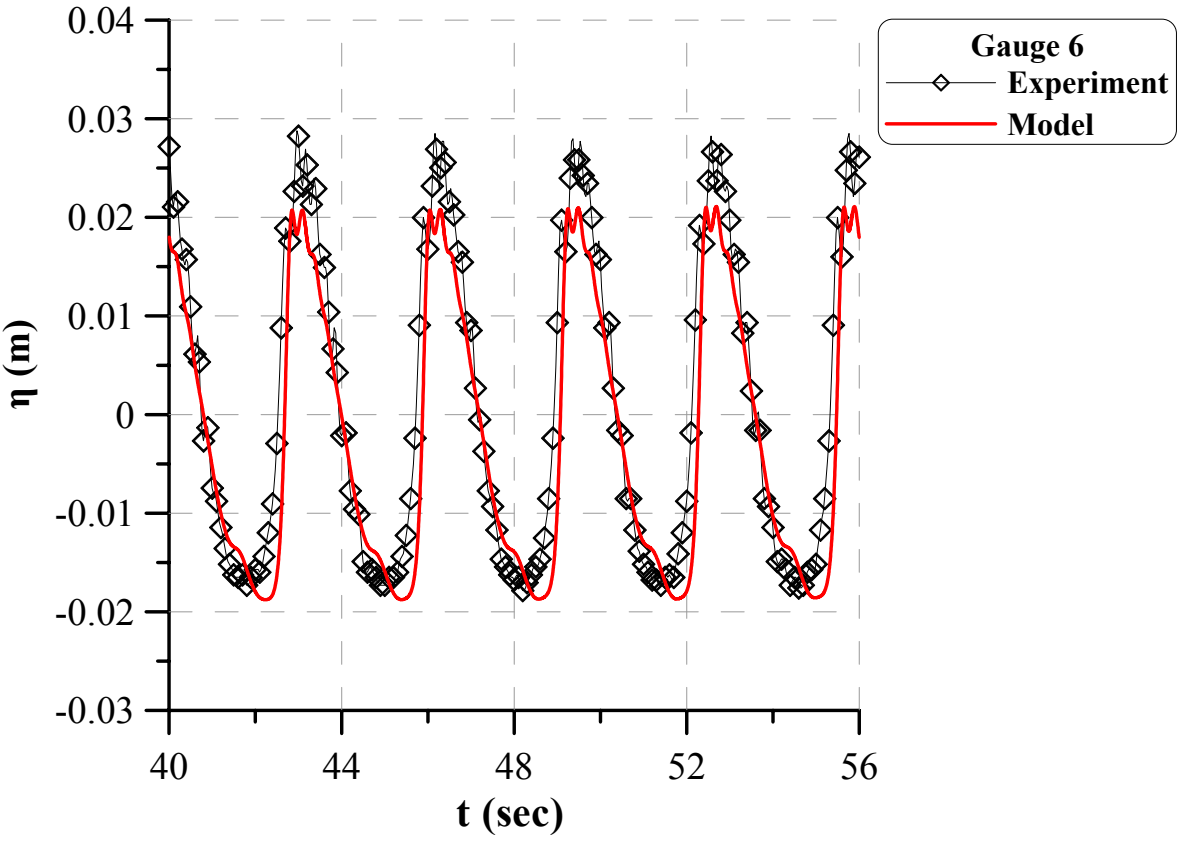

Figure 18.Computed and experimental free surface elevation (UCA, H=0.05, T=3.2).

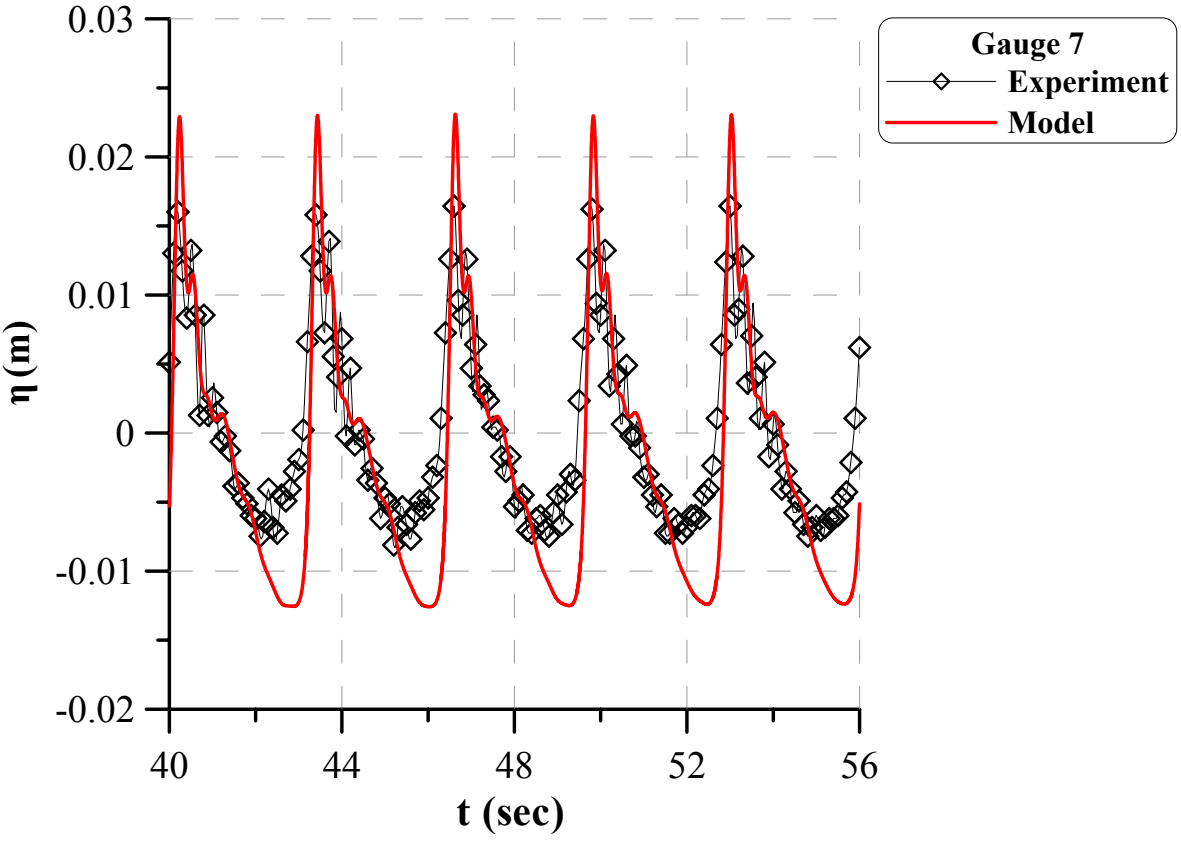

Figure 19.Computed and experimental free surface elevation (UCA, H=0.05, T=3.2).

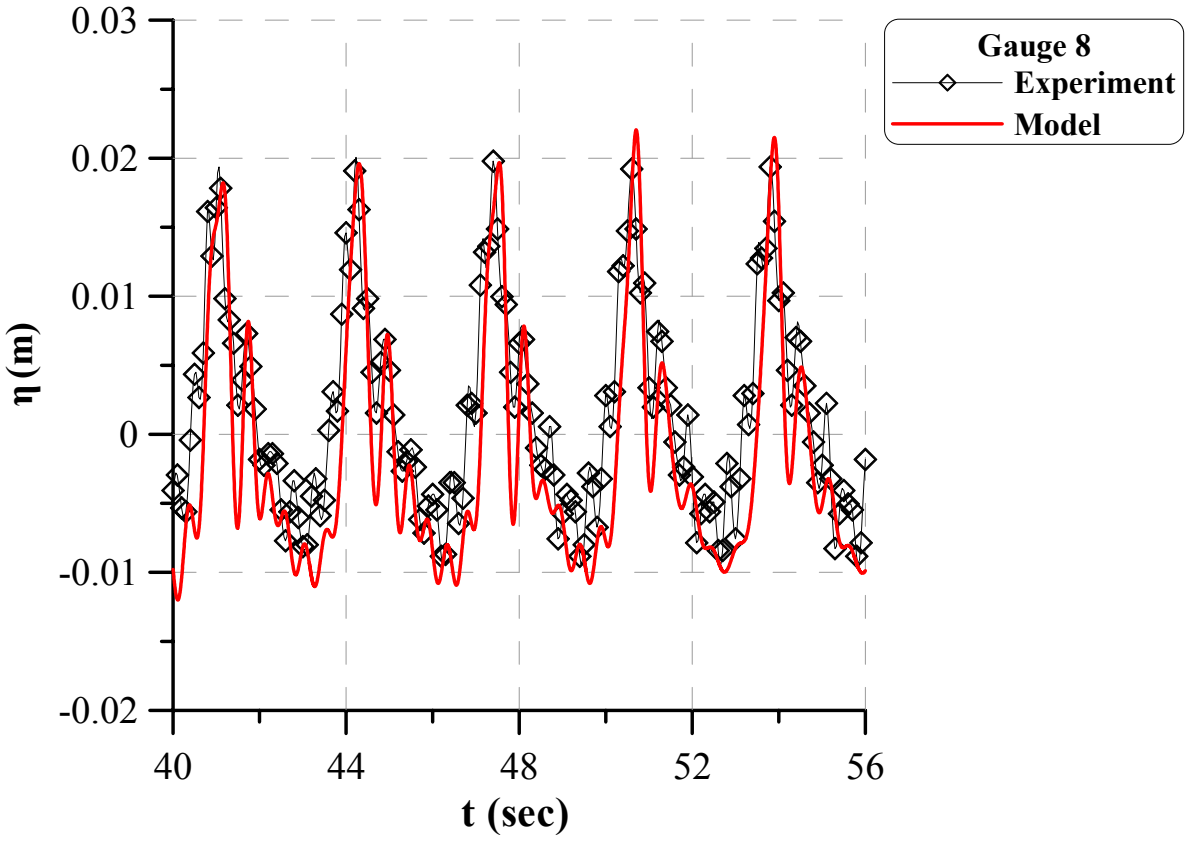

Figure 20.Computed and experimental free surface elevation (UCA, H=0.05, T=3.2).

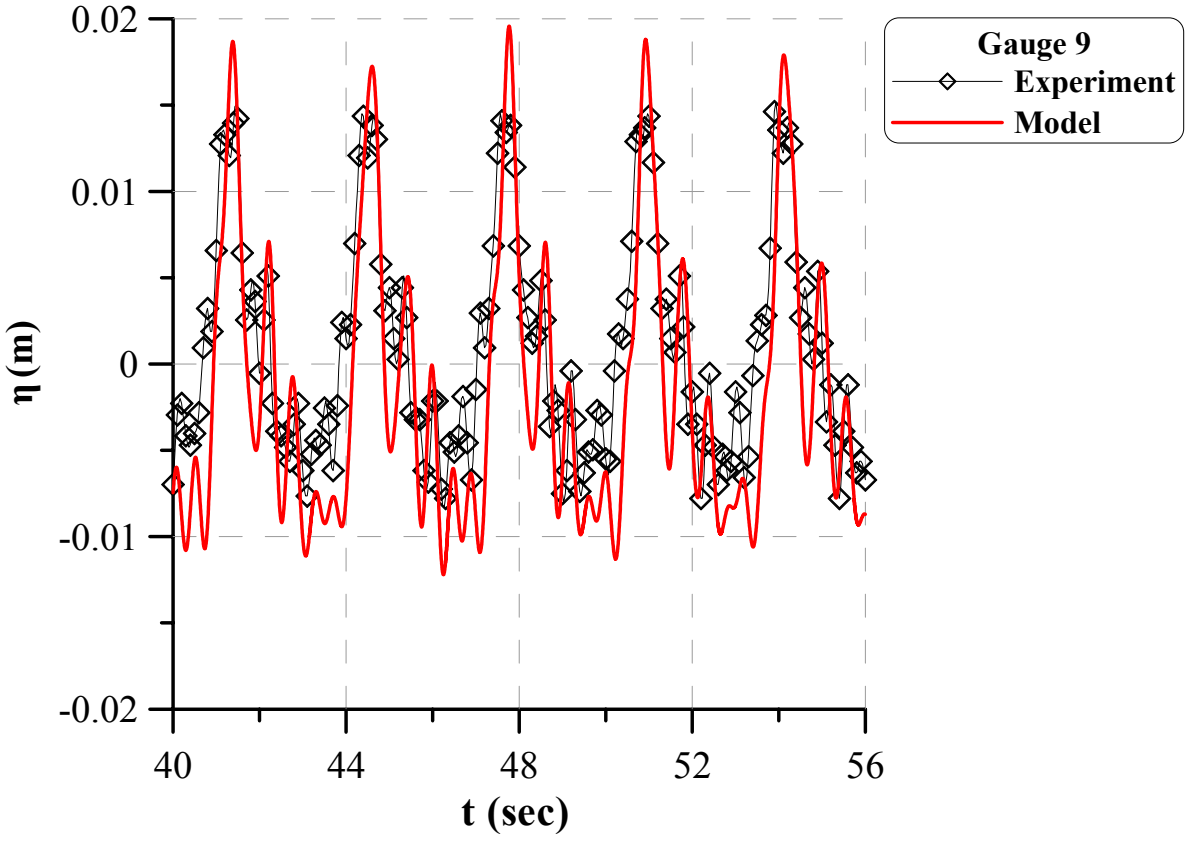

Figure 21.Computed and experimental free surface elevation (UCA, H=0.05, T=3.2).

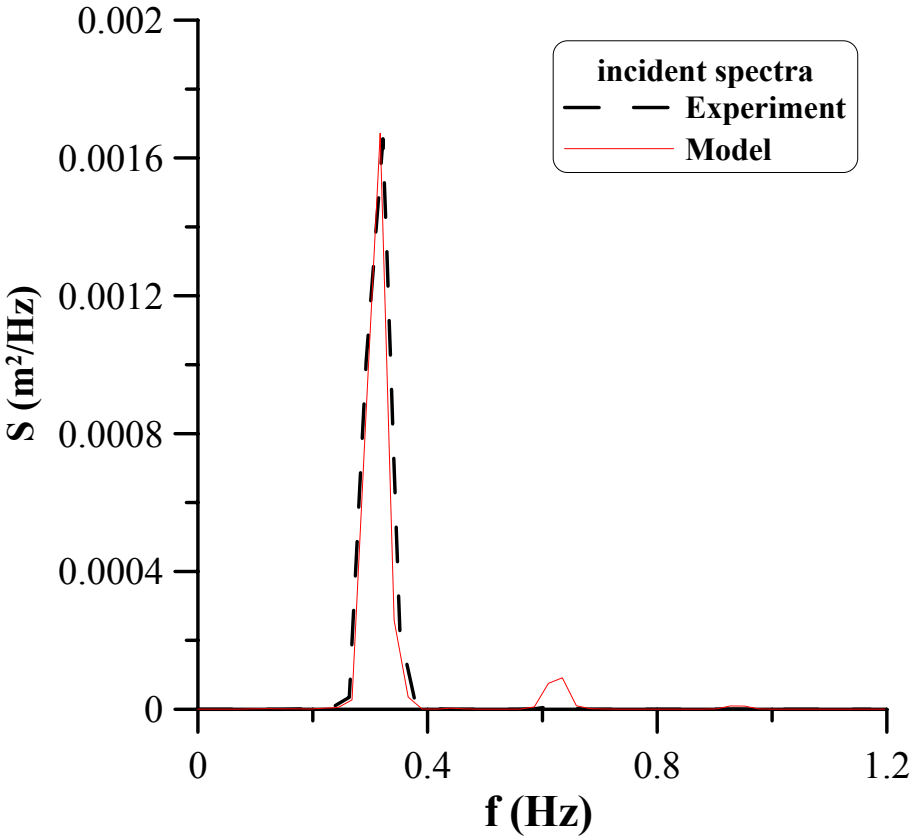

Figure 22.Computed and experimental incident spectra (UCA, H=0.05, T=3.2).

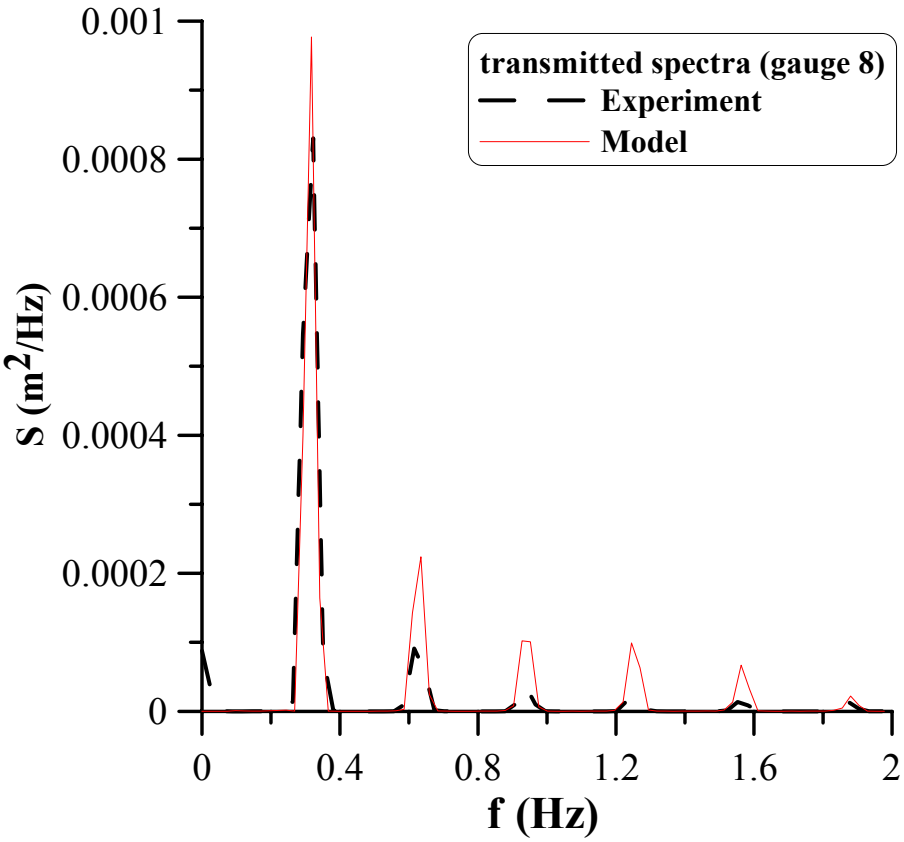

Figure 23.Computed and experimental transmitted spectra (UCA, H=0.05, T=3.2).

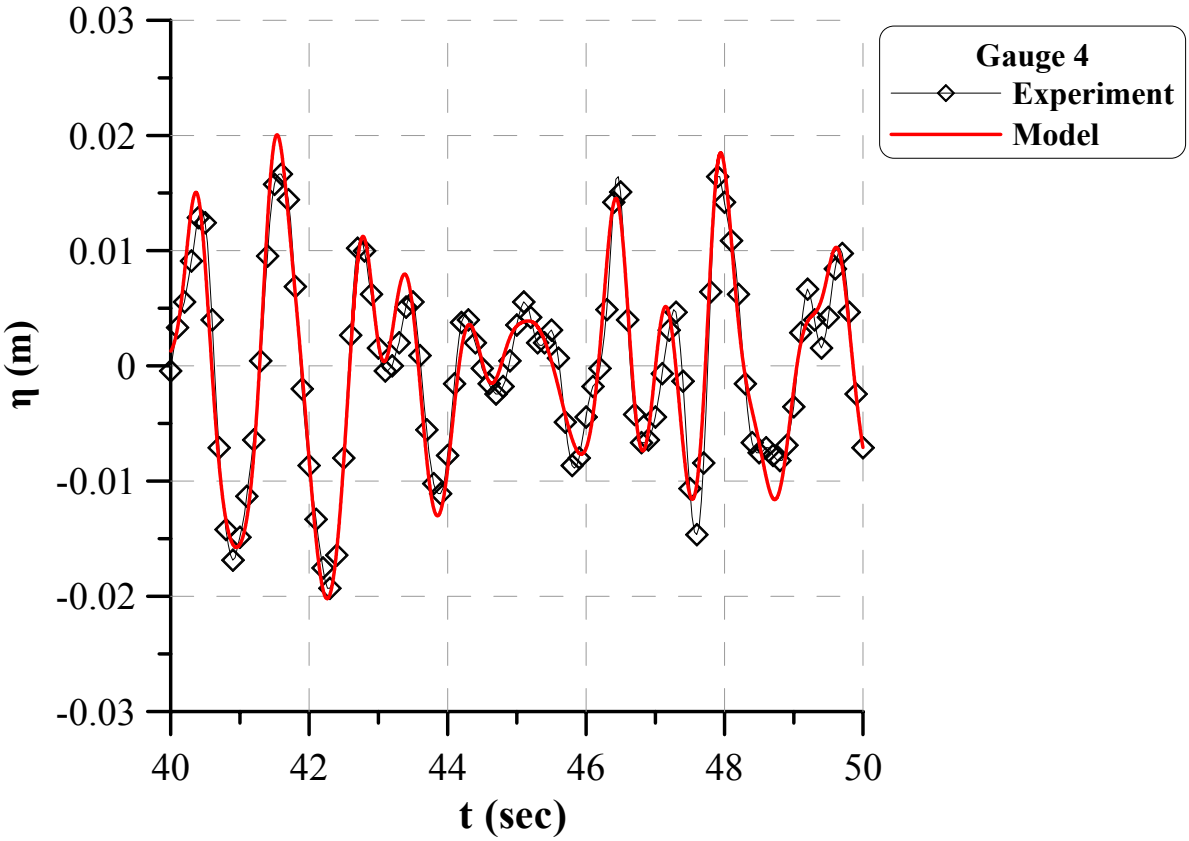

Figure 24. Computed and experimental free surface elevation (UCA, H_s=0.04, T_p=1.6).

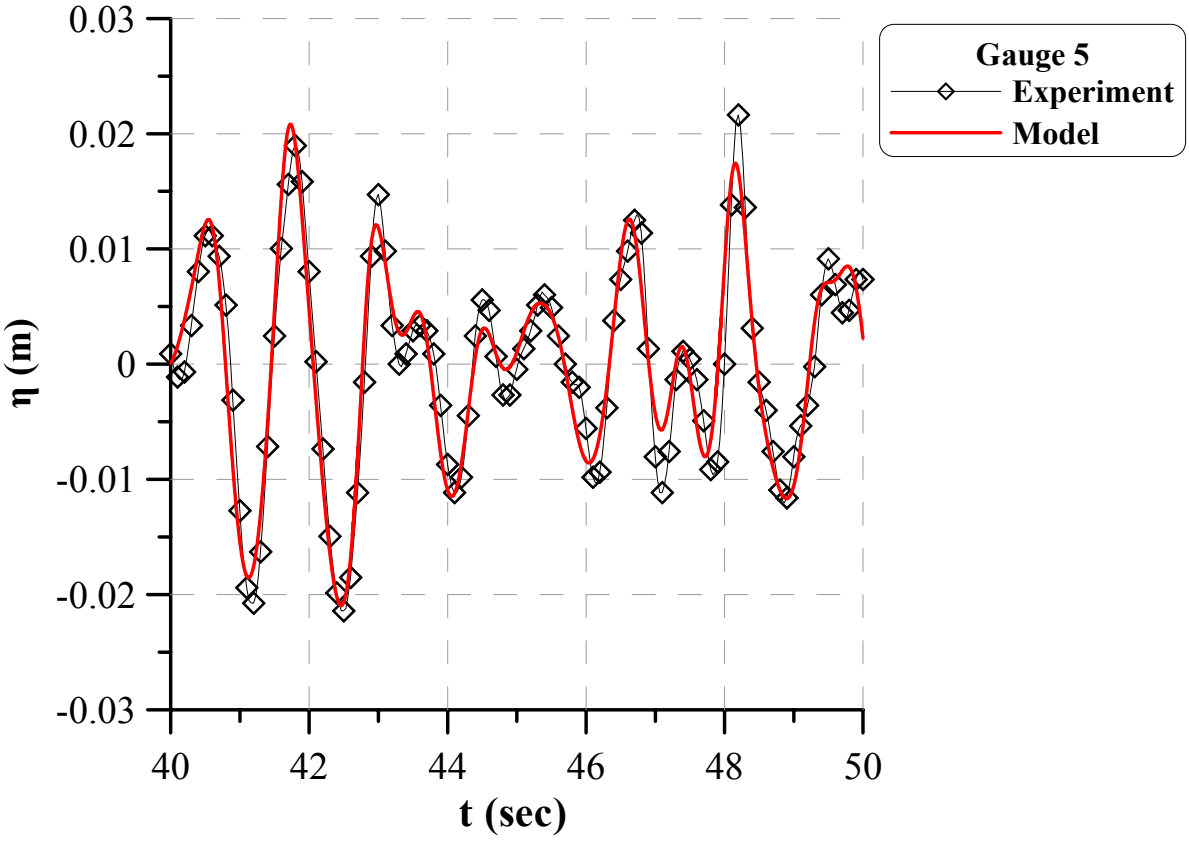

Figure 25. Computed and experimental free surface elevation (UCA, H_s=0.04, T_p=1.6).

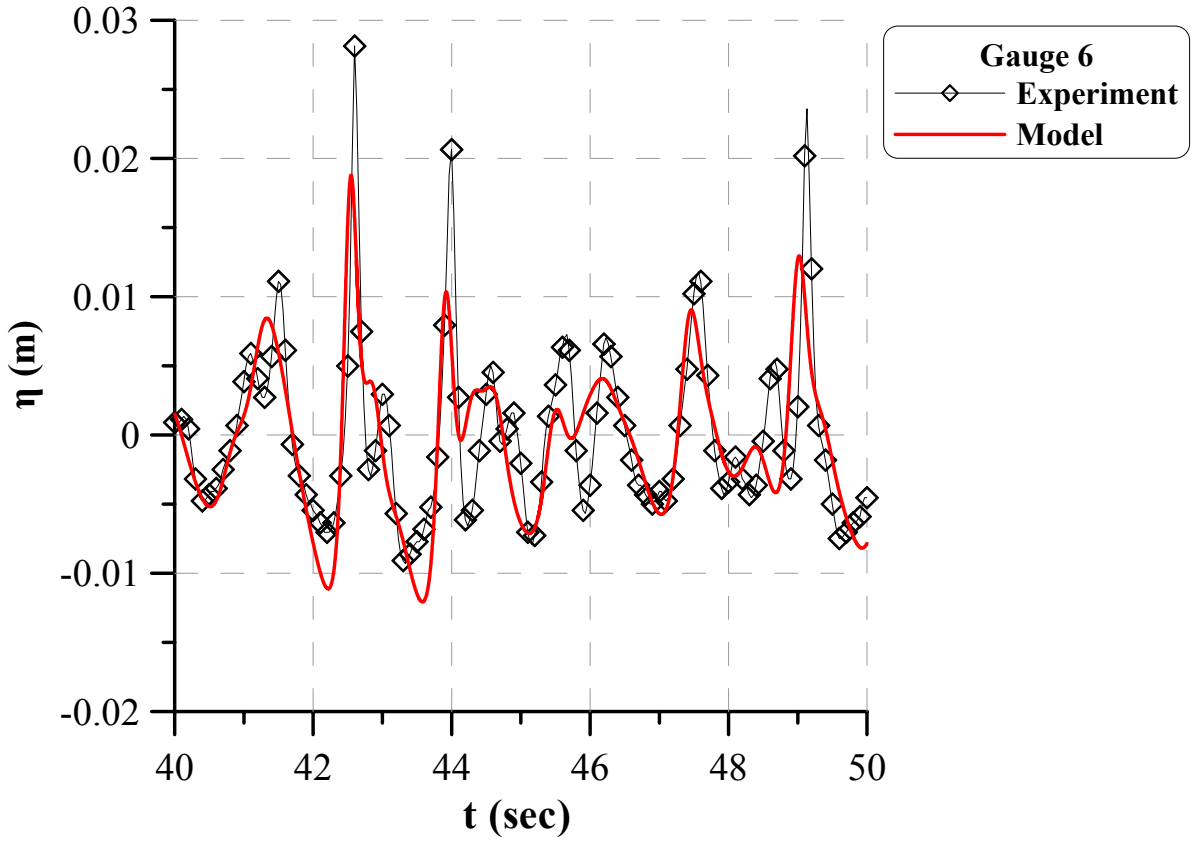

Figure 26. Computed and experimental free surface elevation (UCA, H_s=0.04, T_p=1.6).

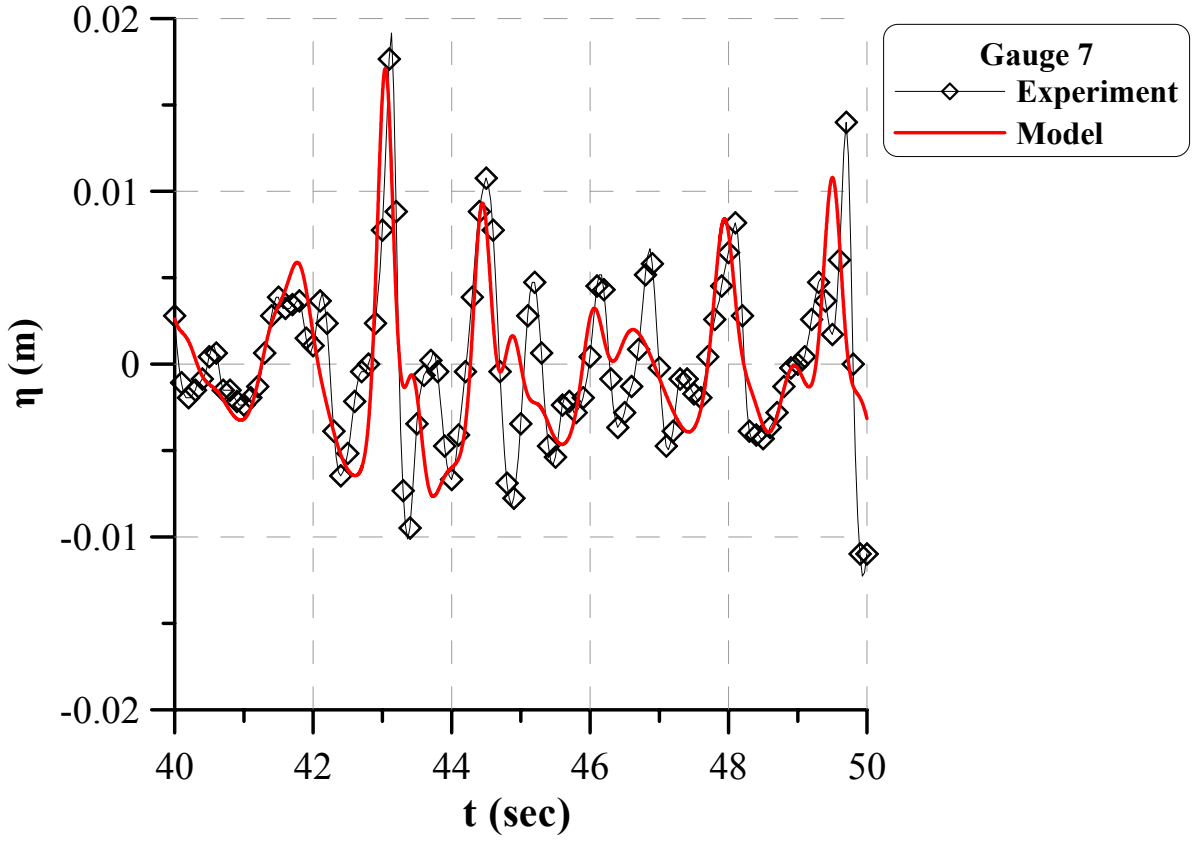

Figure 27. Computed and experimental free surface elevation (UCA, H_s=0.04, T_p=1.6).

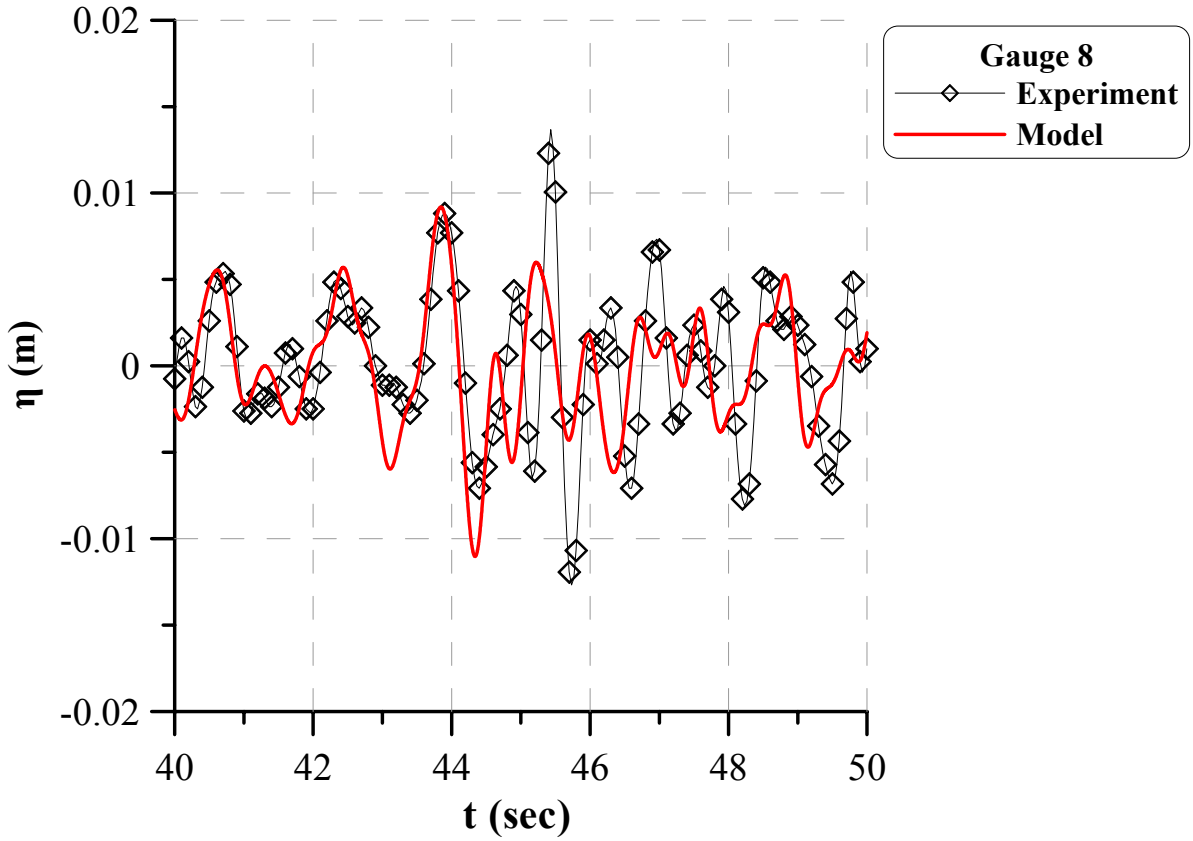

Figure 28. Computed and experimental free surface elevation (UCA, H_s=0.04, T_p=1.6).

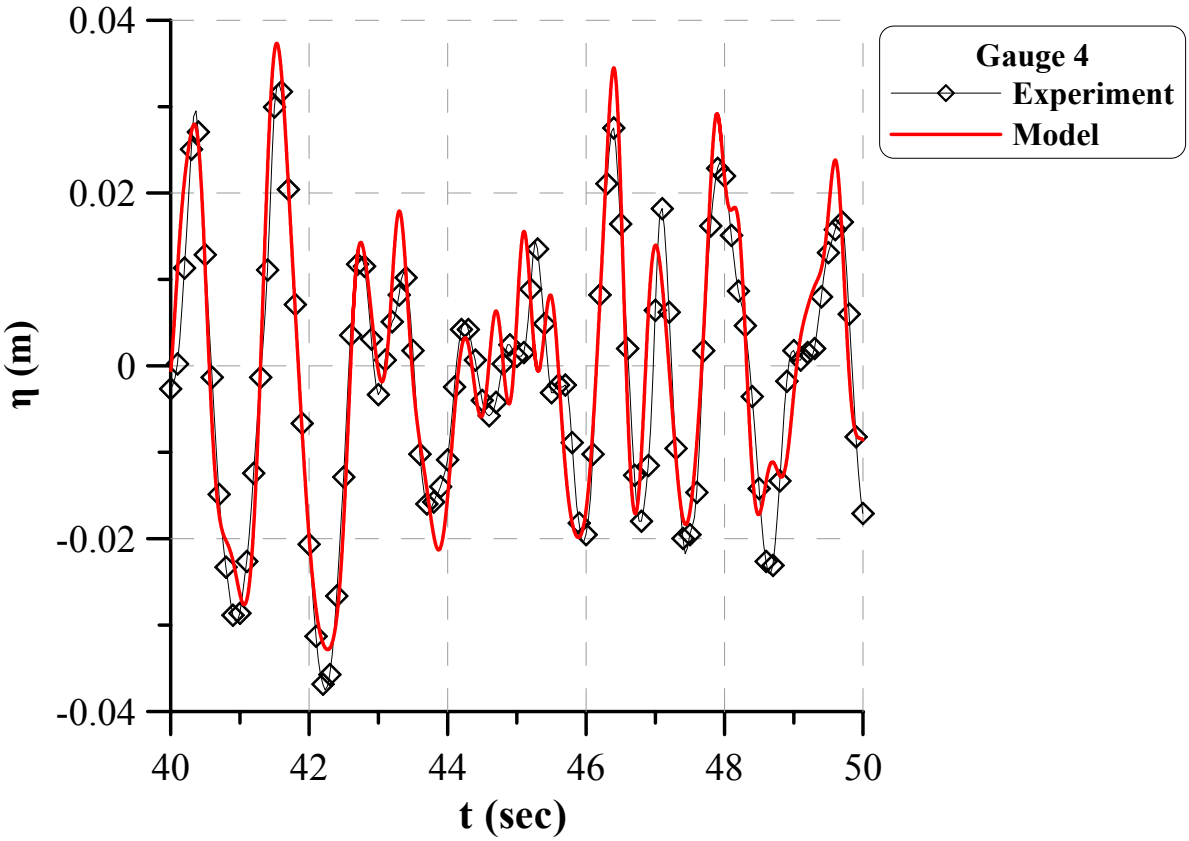

Figure 29. Computed and experimental free surface elevation (UCA, H_s=0.07, T_p=1.6).

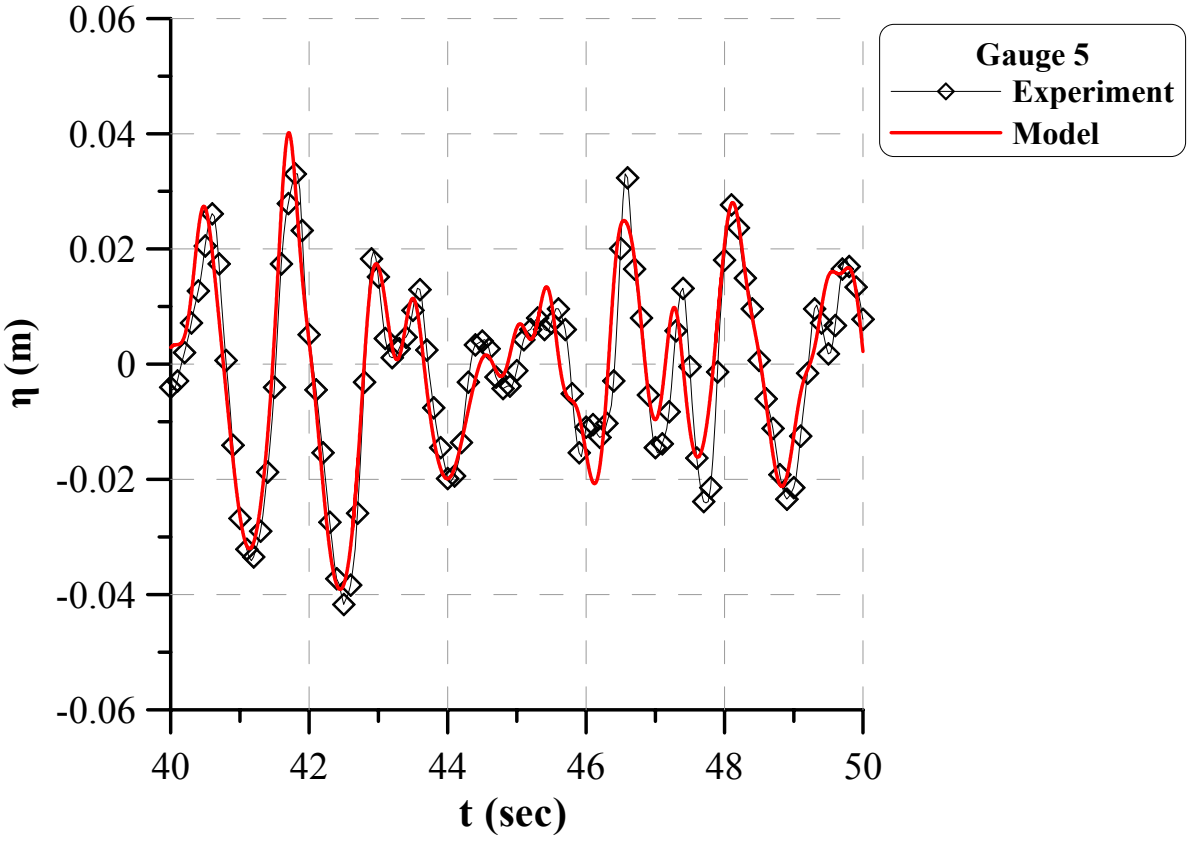

Figure 30. Computed and experimental free surface elevation (UCA, H_s=0.07, T_p=1.6).

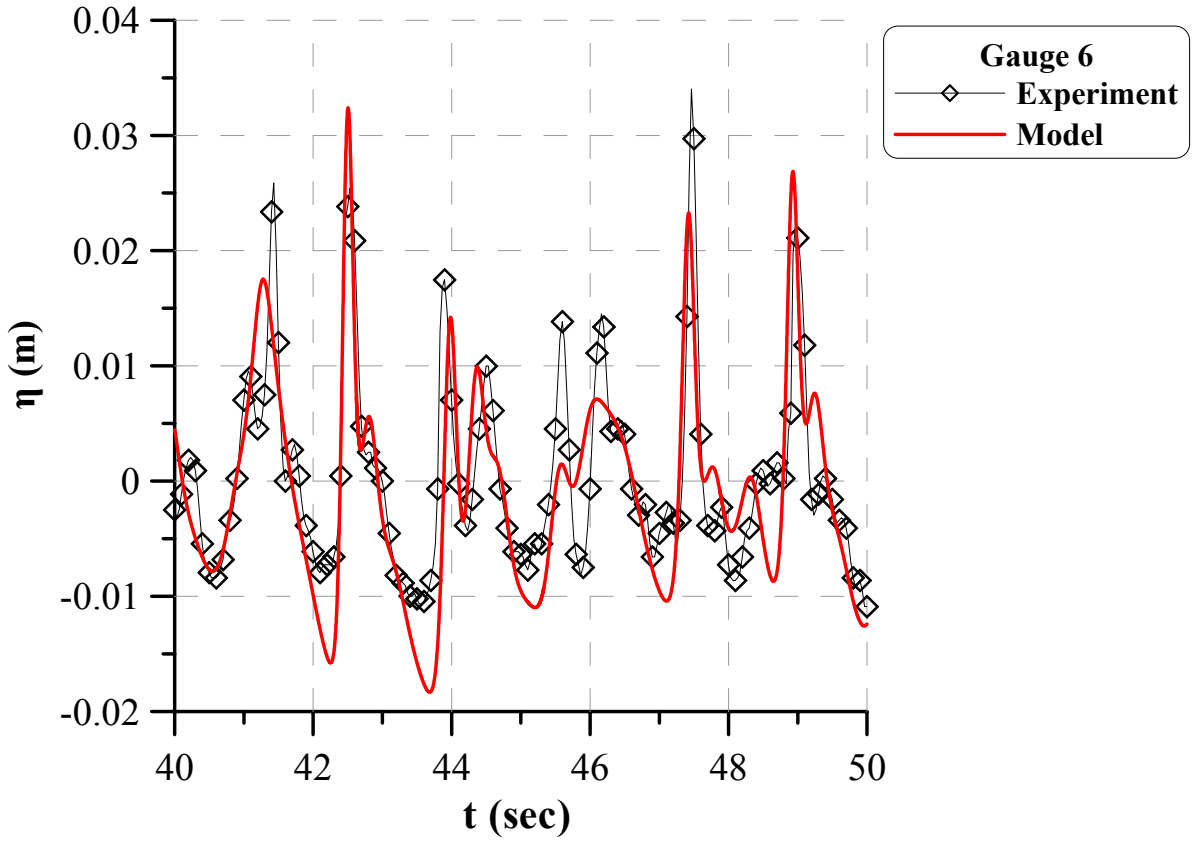

Figure 31. Computed and experimental free surface elevation (UCA, H_s=0.07, T_p=1.6).

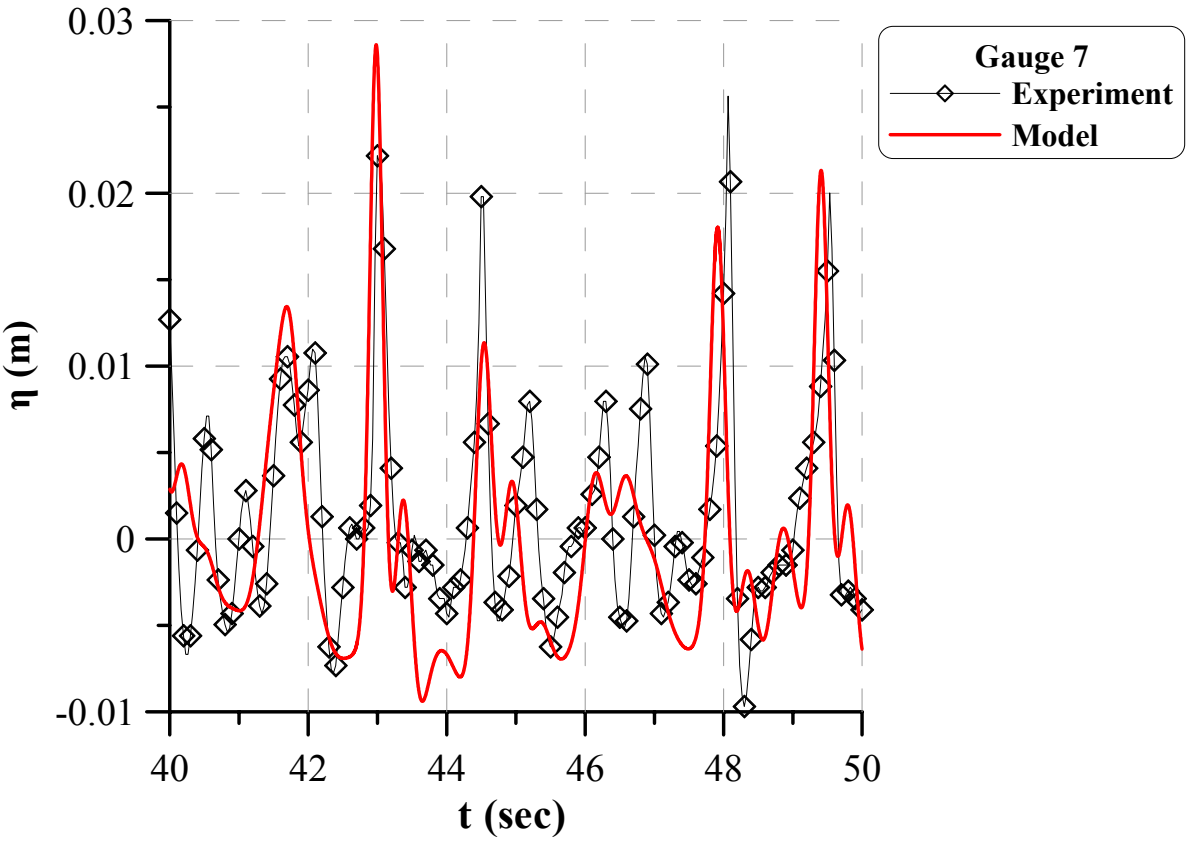

Figure 32. Computed and experimental free surface elevation (UCA, H_s=0.07, T_p=1.6).

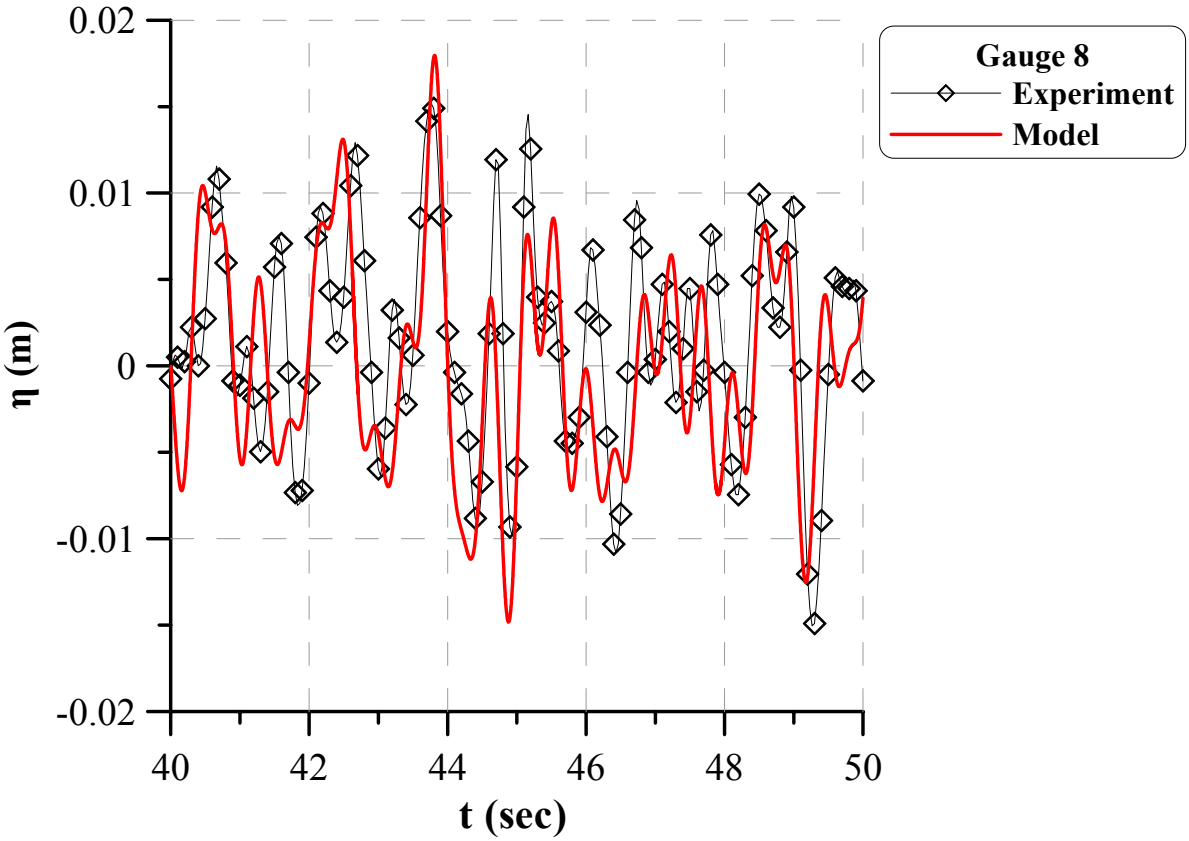

Figure 33.Computed and experimental free surface elevation (UCA, H_s=0.07, T_p=1.6).

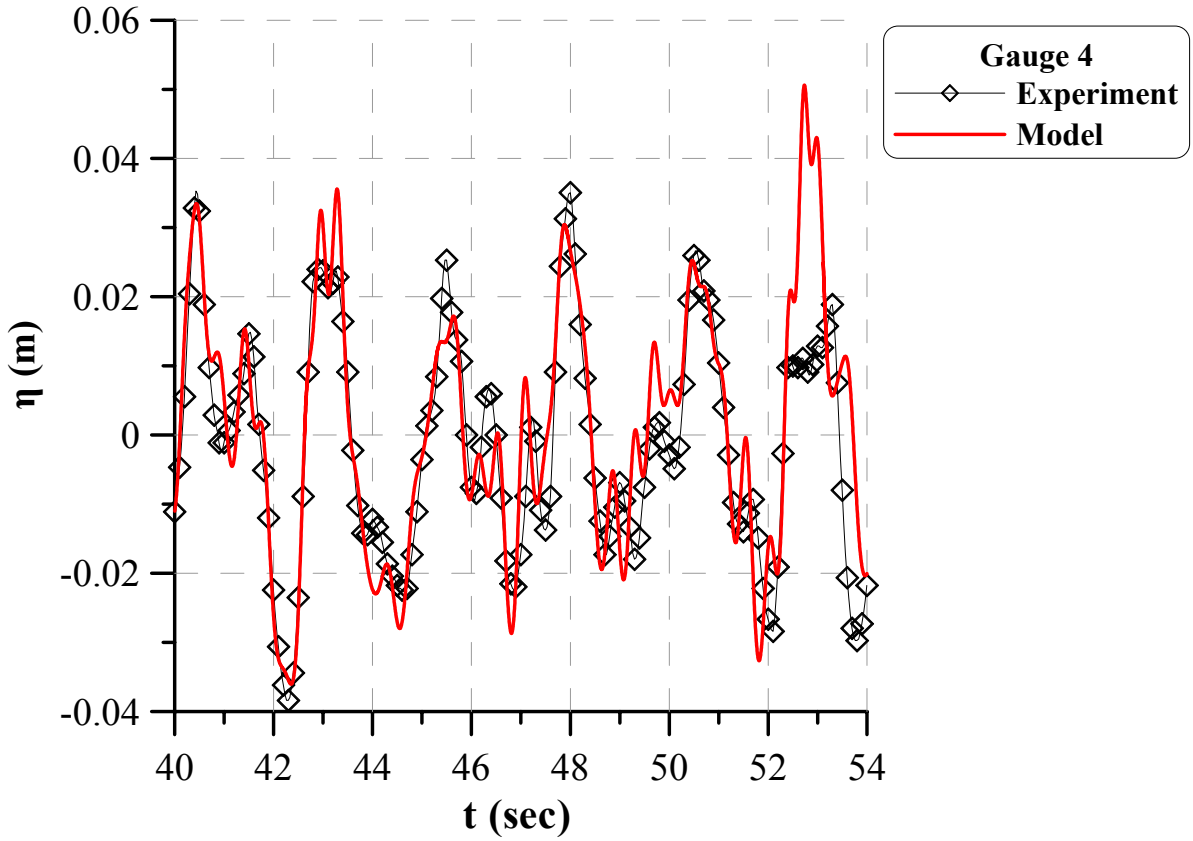

Figure 34. Computed and experimental free surface elevation (UCA, H_s=0.07, T_p=2.4).

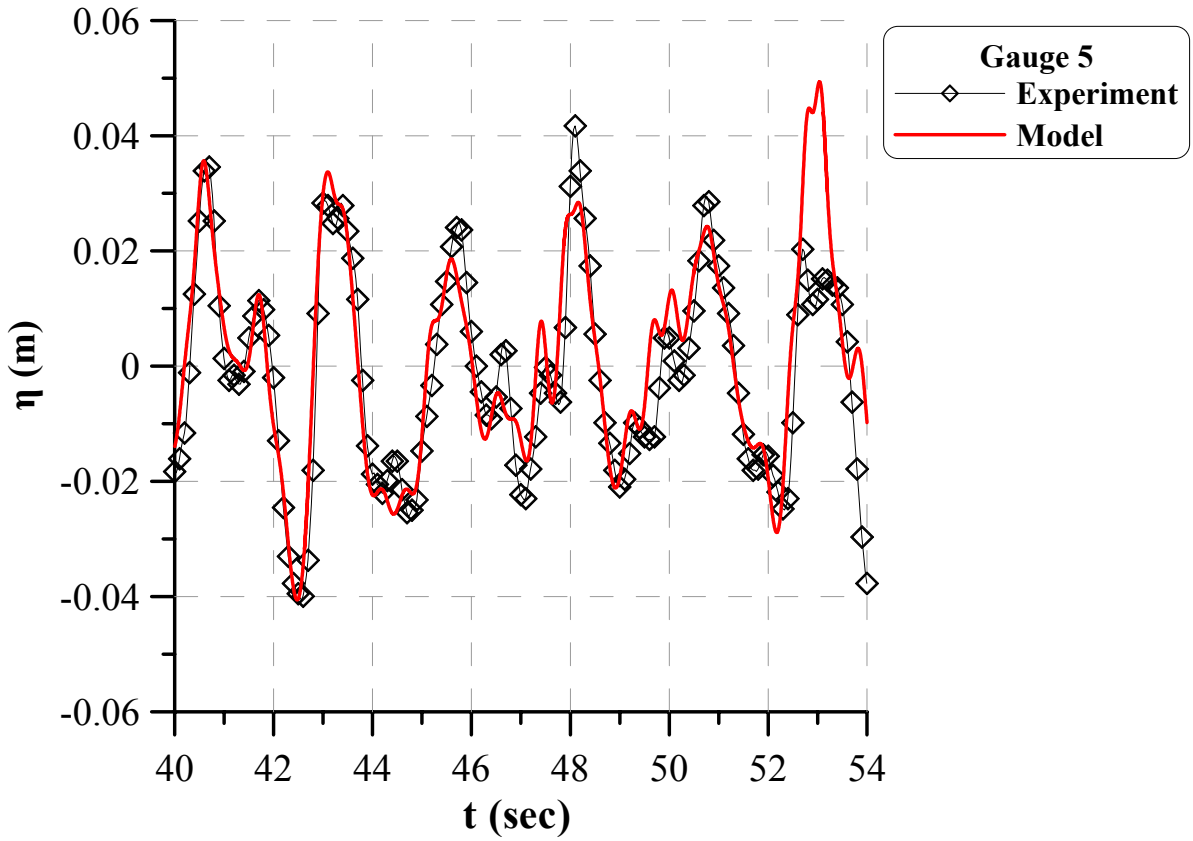

Figure 35. Computed and experimental free surface elevation (UCA, H_s=0.07, T_p=2.4).

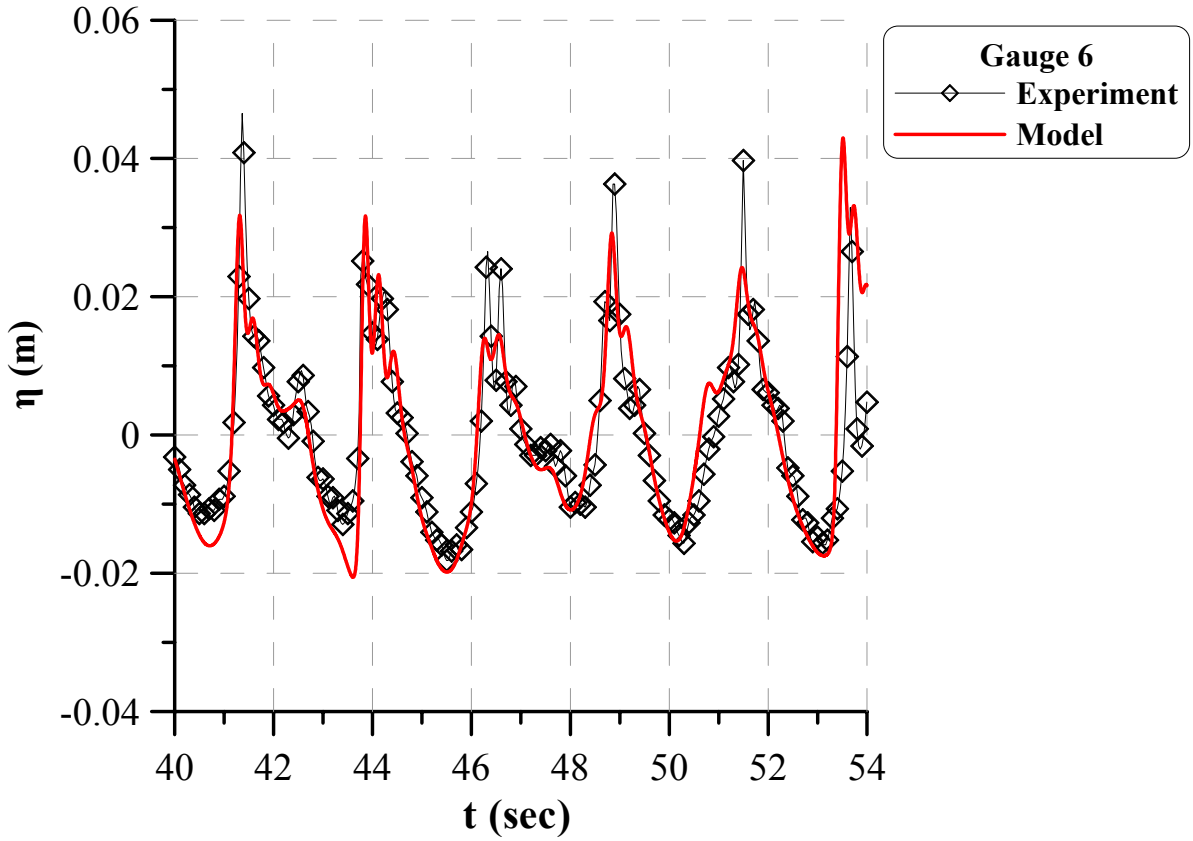

Figure 36. Computed and experimental free surface elevation (UCA, H_s=0.07, T_p=2.4).

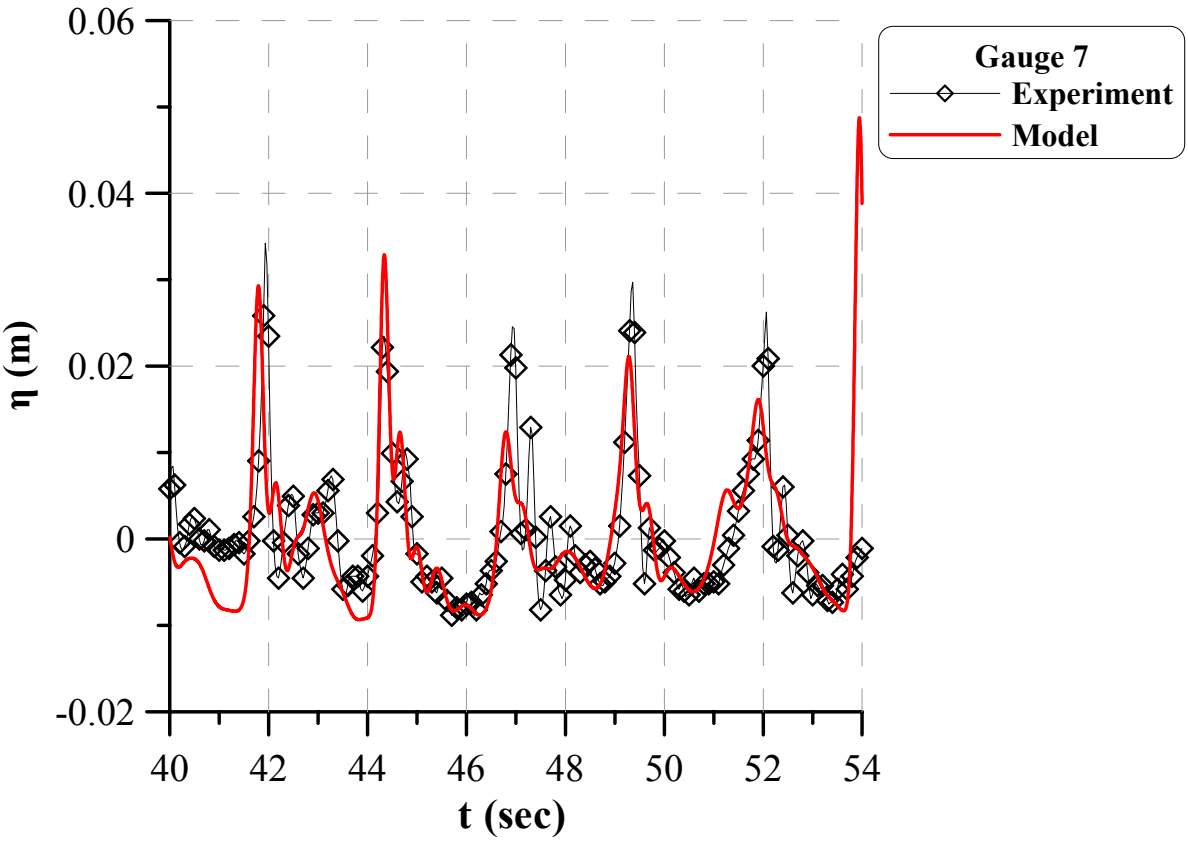

Figure 37. Computed and experimental free surface elevation (UCA, H_s=0.07, T_p=1.6).

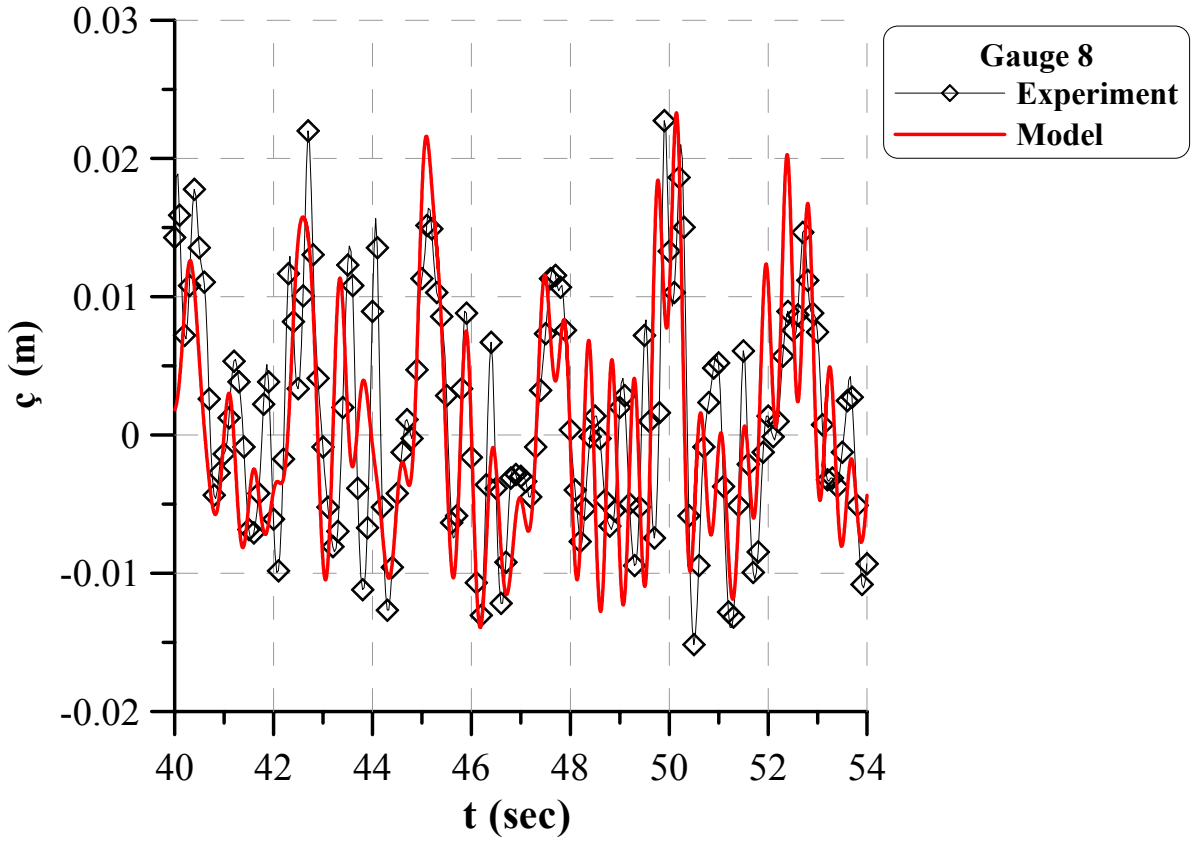

Figure 38. Computed and experimental free surface elevation (UCA, H_s=0.07, T_p=2.4).

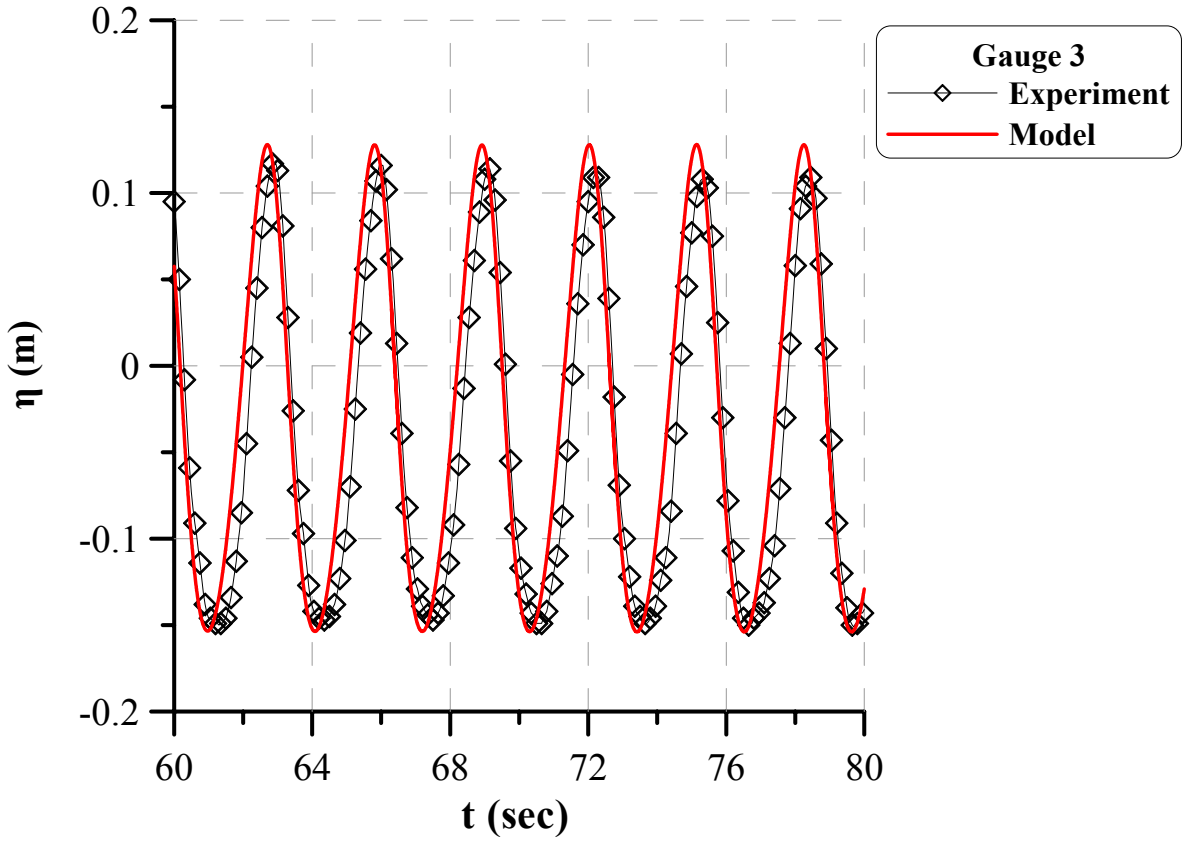

Figure 39.Computed and experimental free surface elevation (UPC, H=0.28, T=3.11).

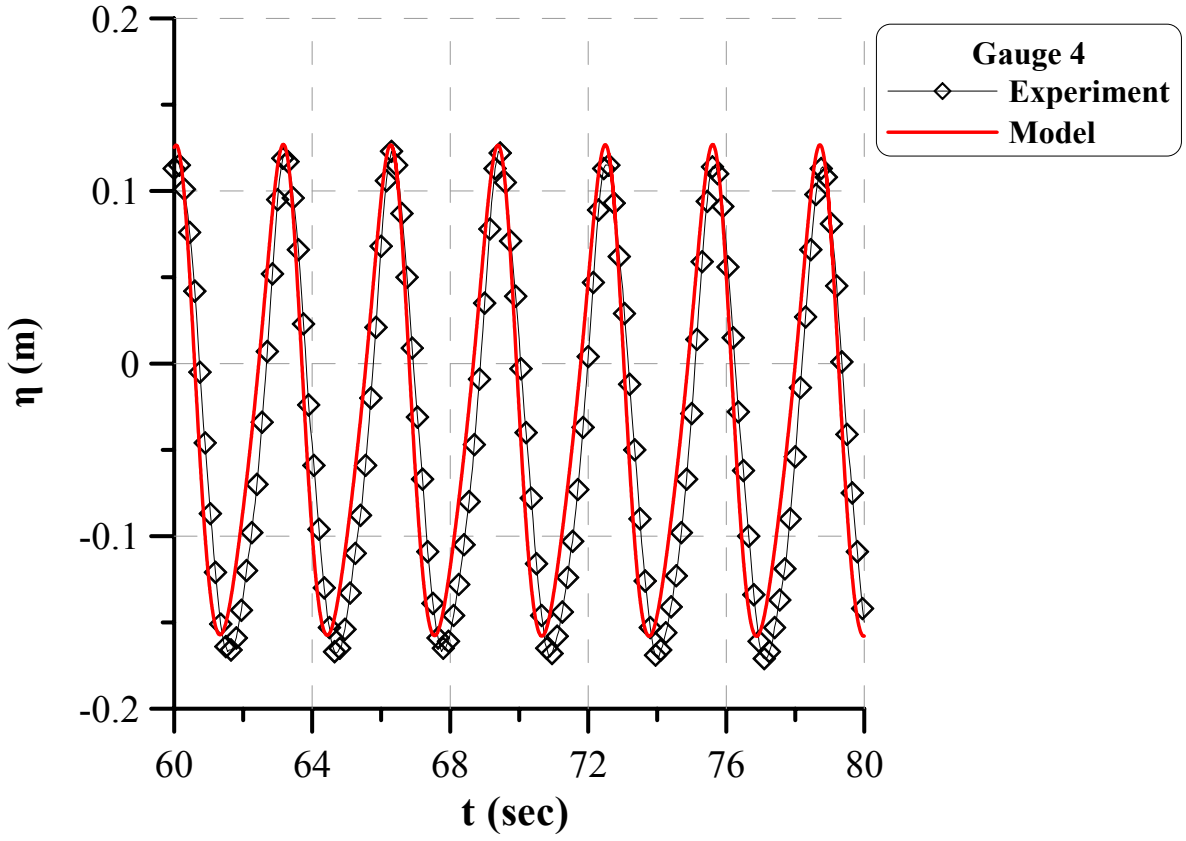

Figure 40.Computed and experimental free surface elevation (UPC, H=0.28, T=3.11).

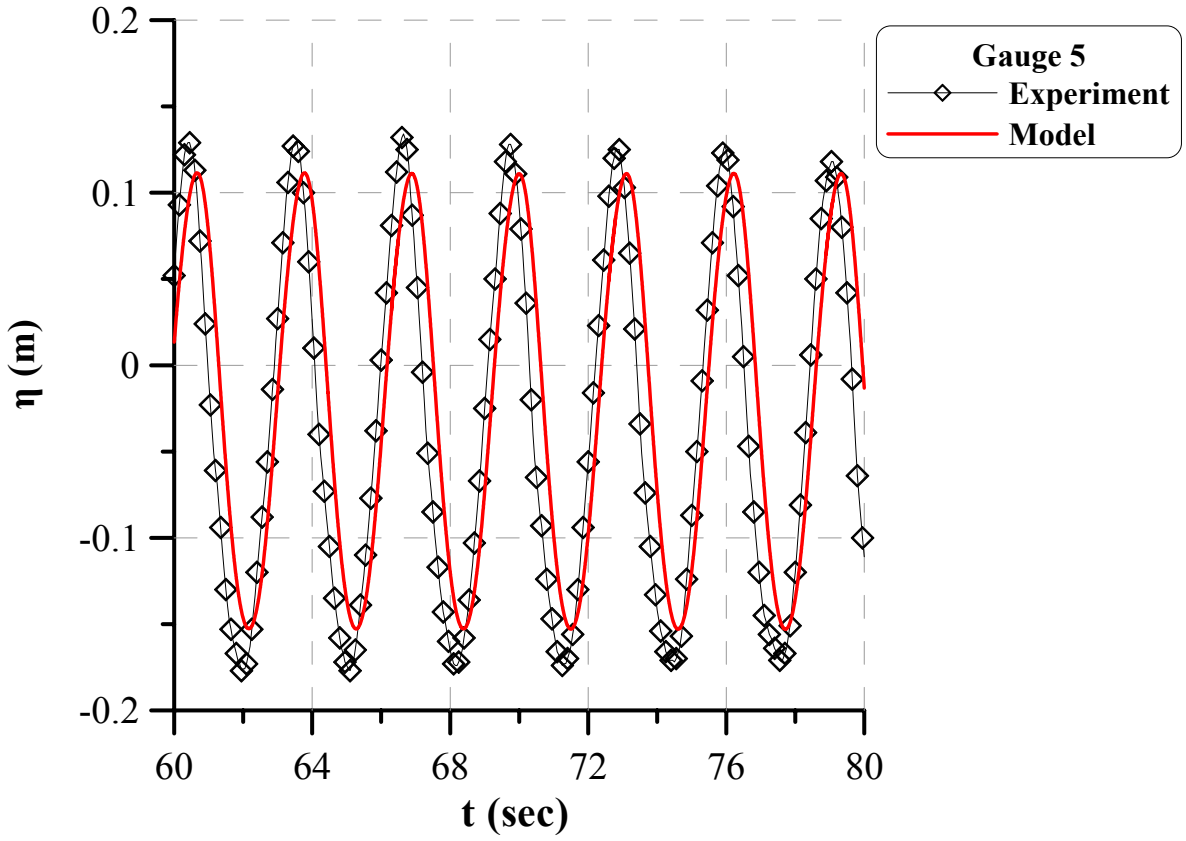

Figure 41.Computed and experimental free surface elevation (UPC, H=0.28, T=3.11).

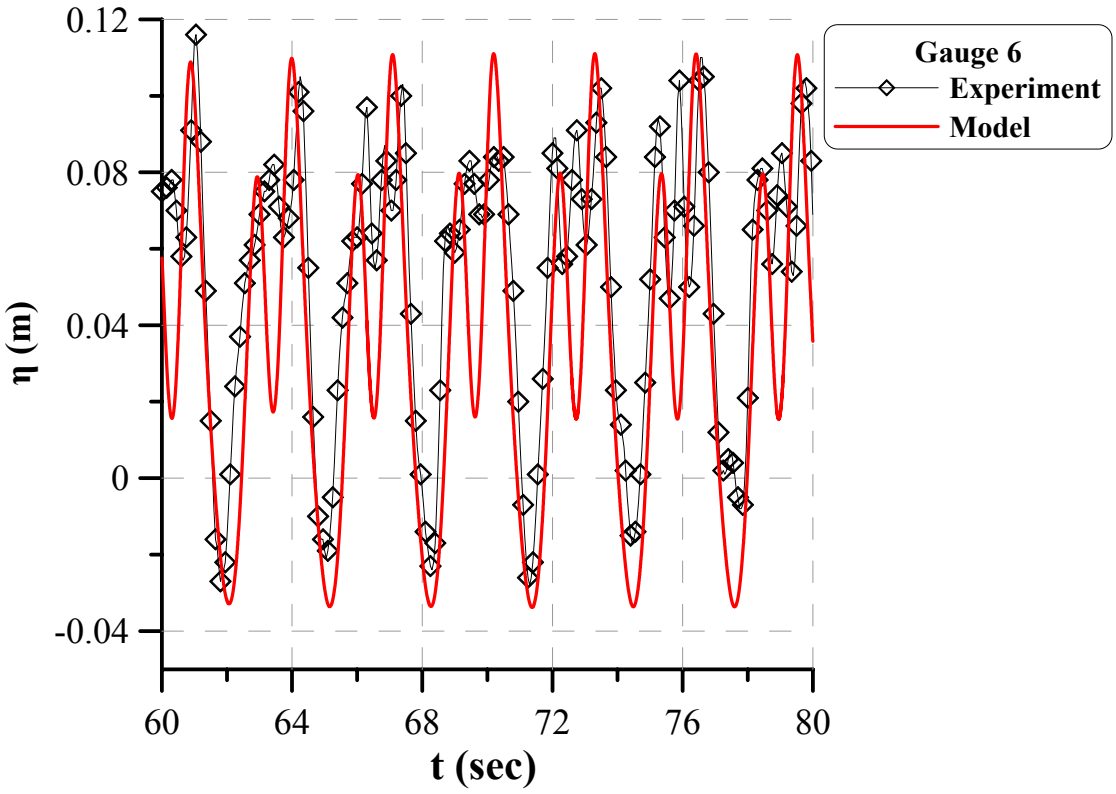

Figure 42. Computed and experimental free surface elevation (UPC, H=0.28, T=3.11).

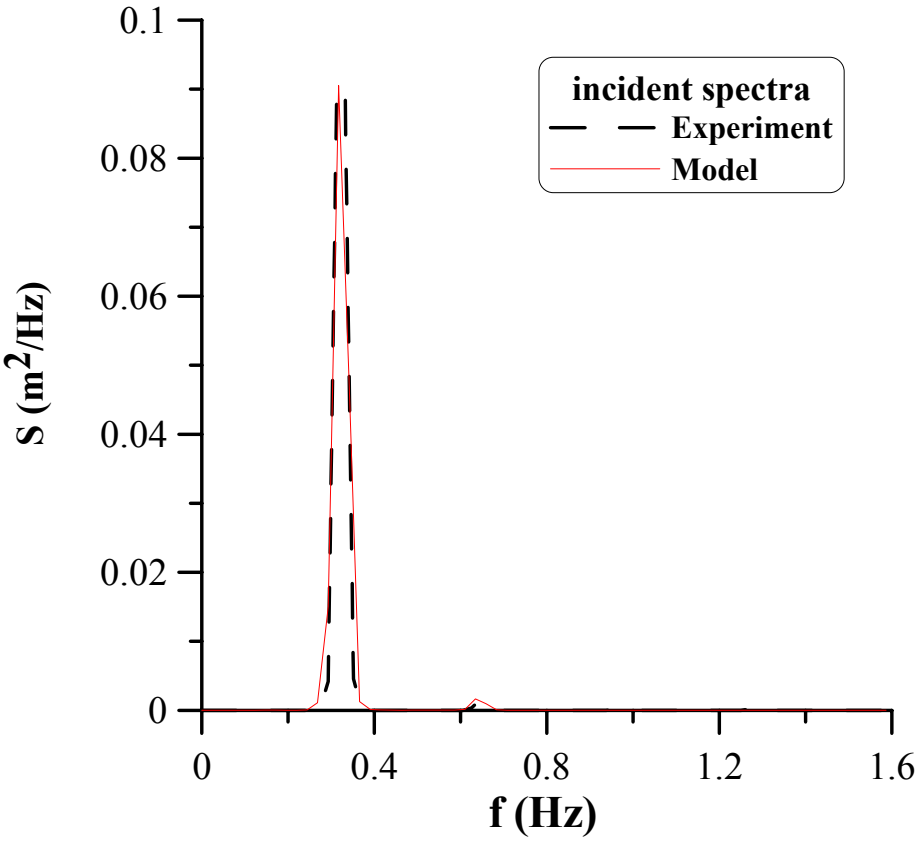

Figure 43.Computed and experimental transmitted spectra (UPC, H=0.28, T=3.11).

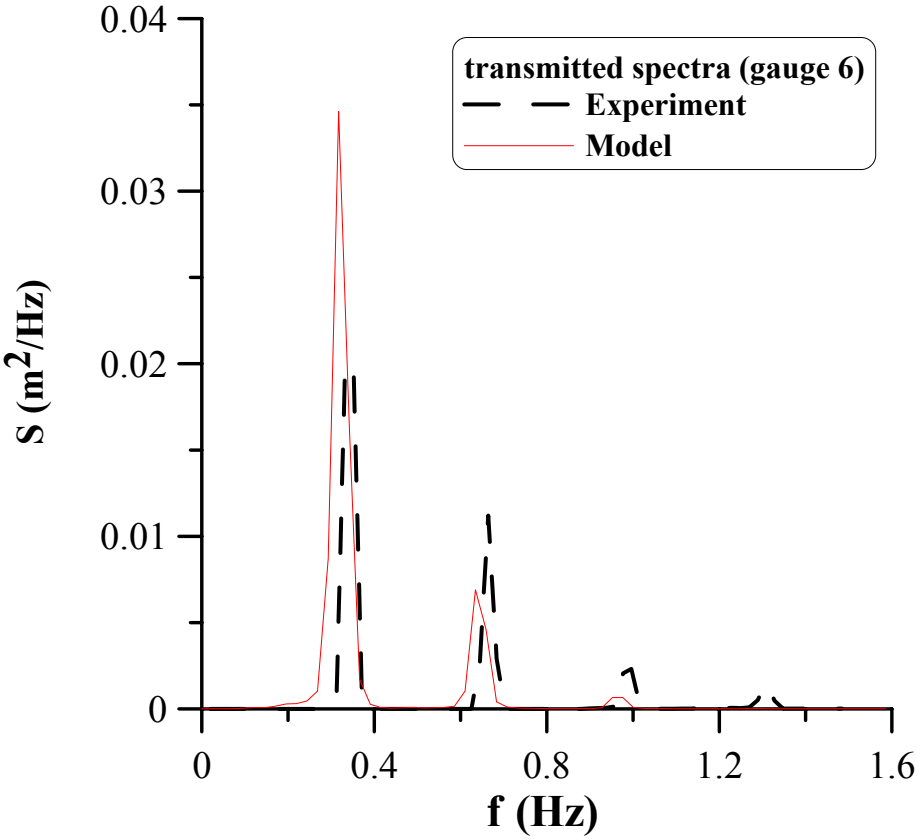

Figure 44.Computed and experimental transmitted spectra (UPC, H=0.28, T=3.11).

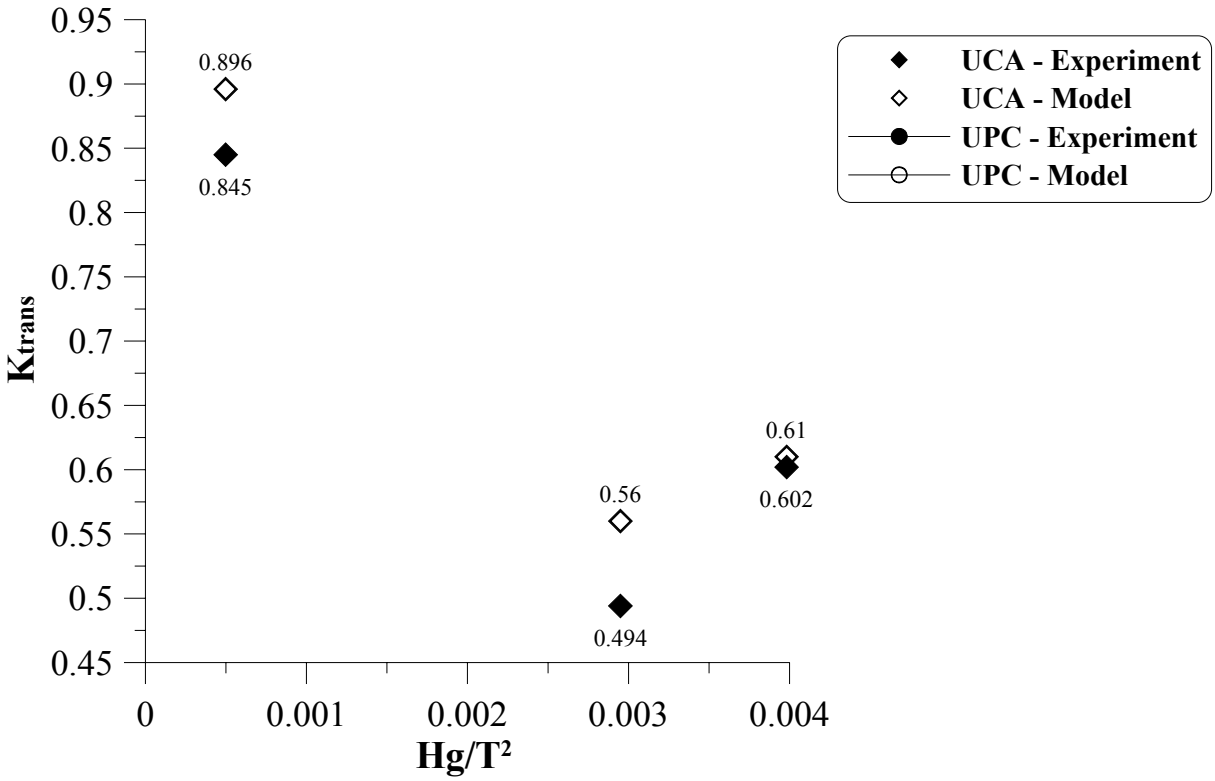

Figure 45. Computed and experimental transmission coefficient K_{trans} (UCA and UPC).

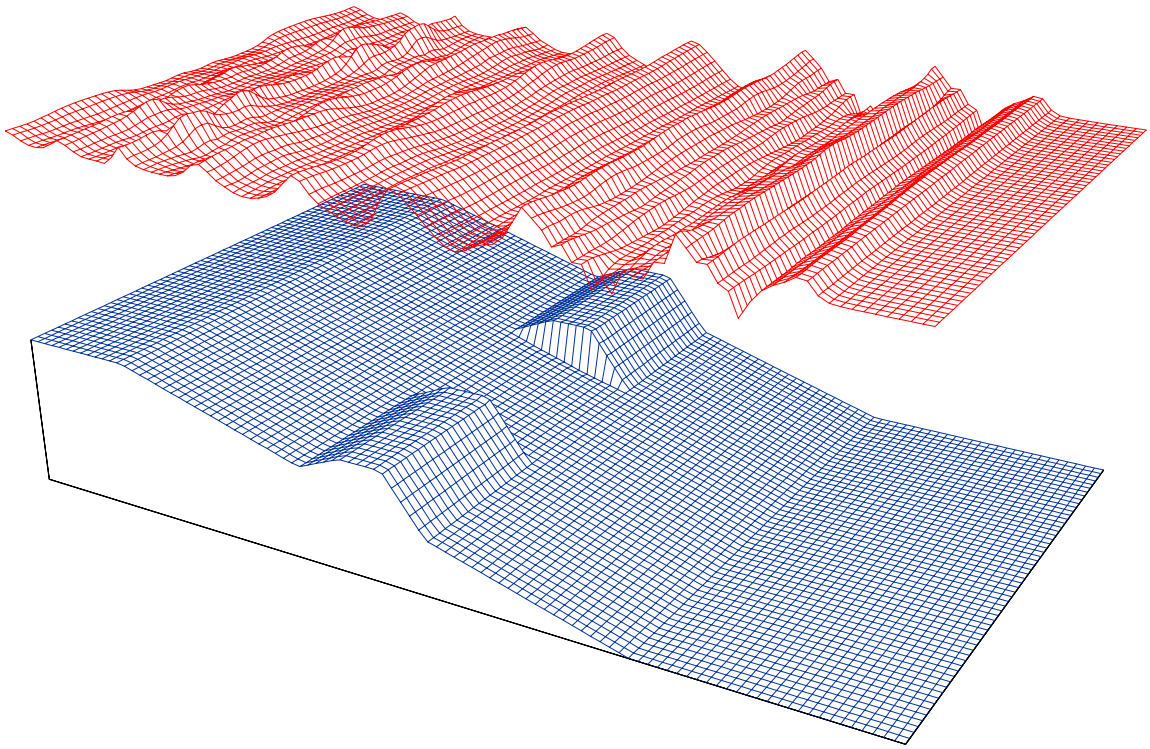

Figure 46. Snapshot (t = 40 sec) of free surface elevation (Case (a), H=0.1, T=1.6)

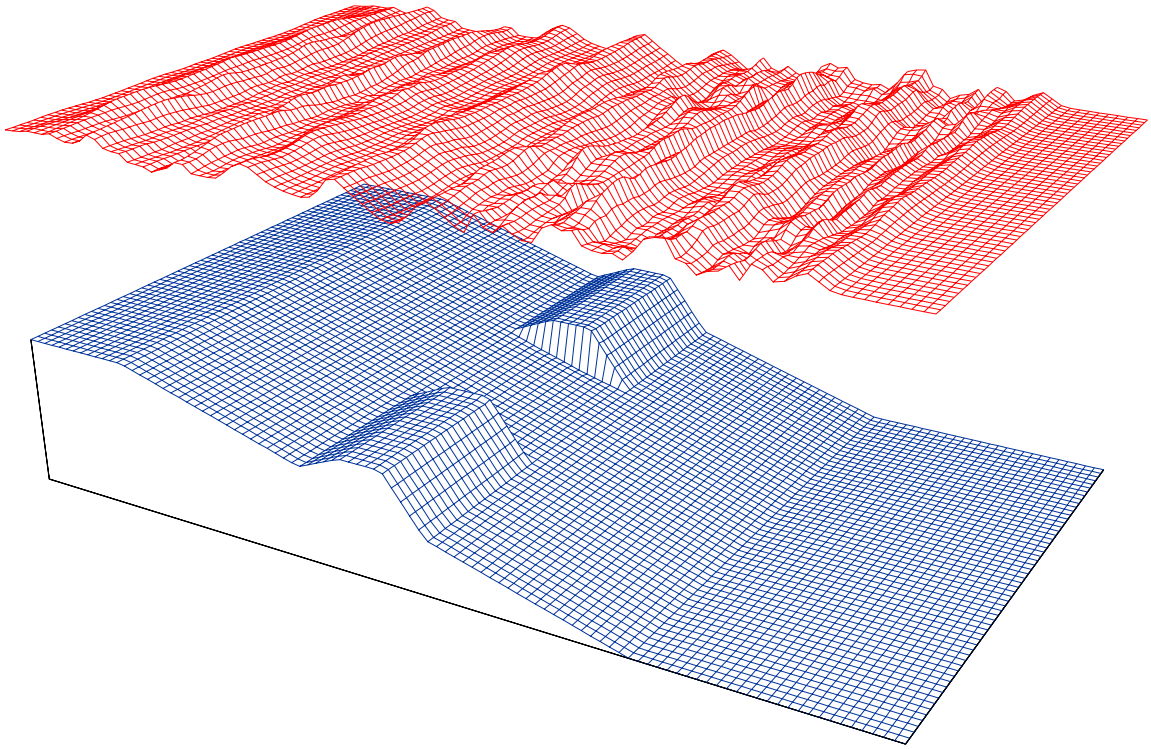

Figure 47. Snapshot (t = 40 sec) of free surface elevation (Case (b), H_s=0.1, T_p=1.6)

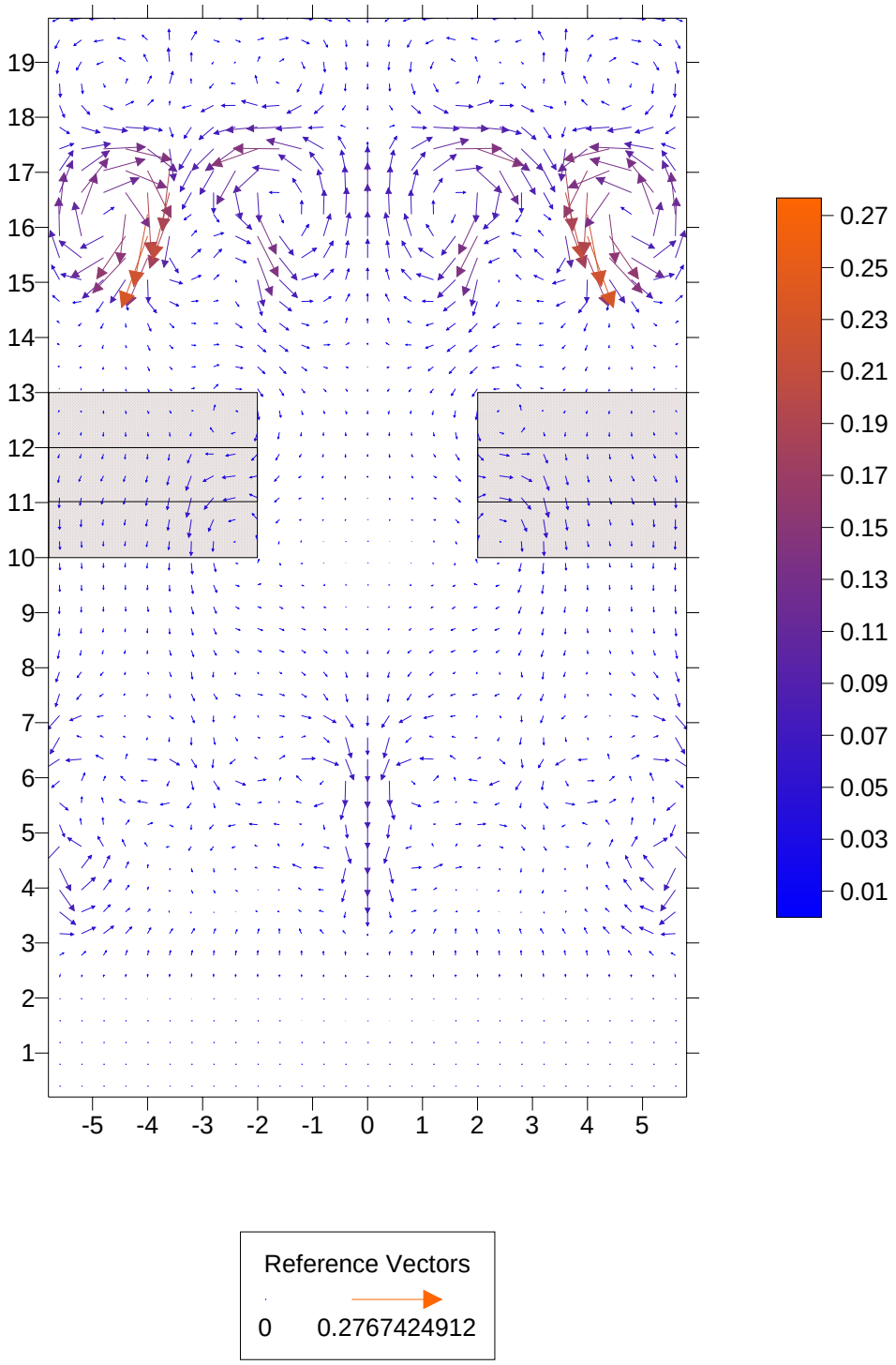

Figure 48. Mean wave-induced current field (Case (a), H=0.1, T=1.6)

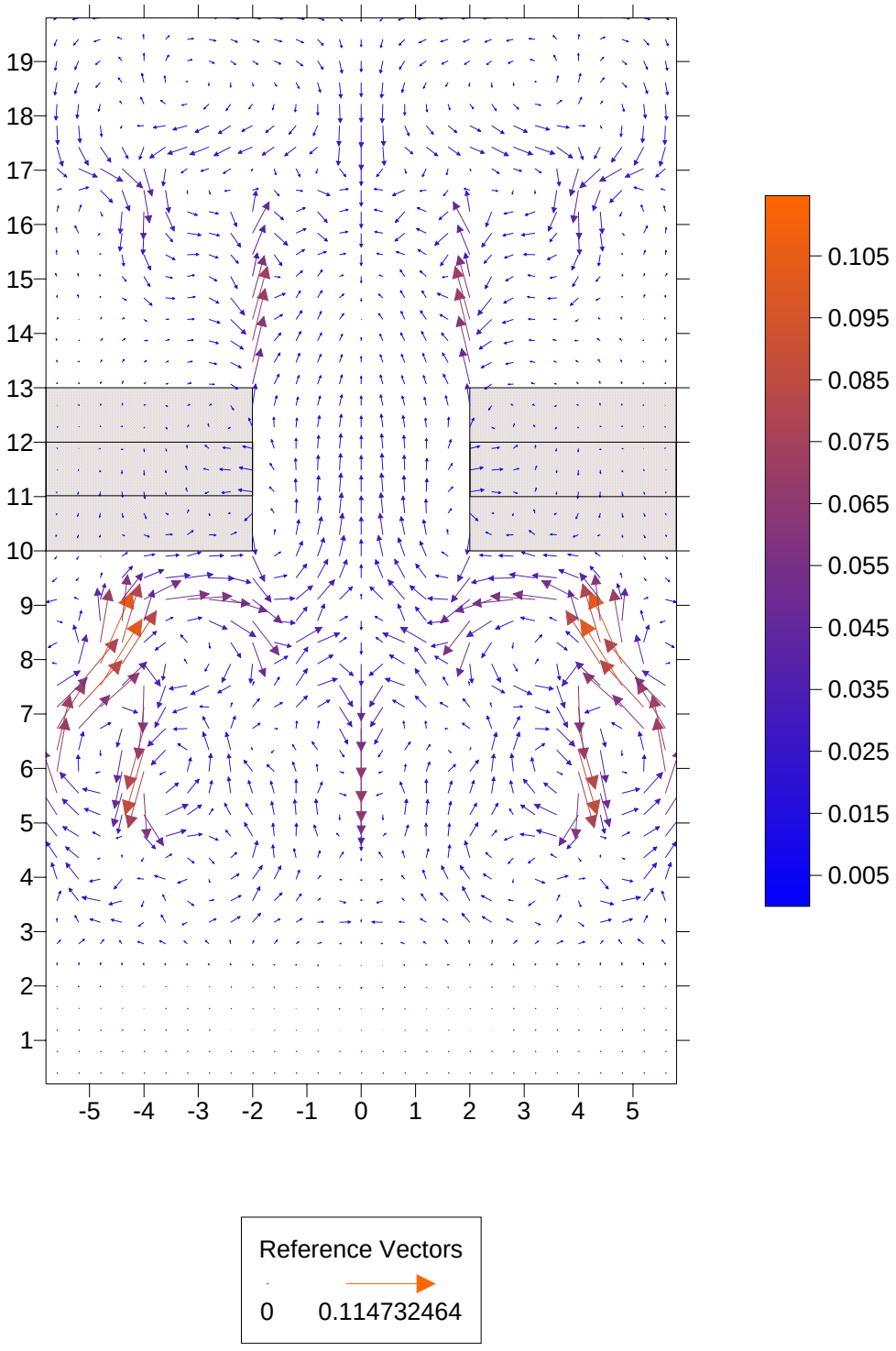

Figure 49. Mean wave-induced current field (Case (b), H_s=0.1, T_p=1.6)

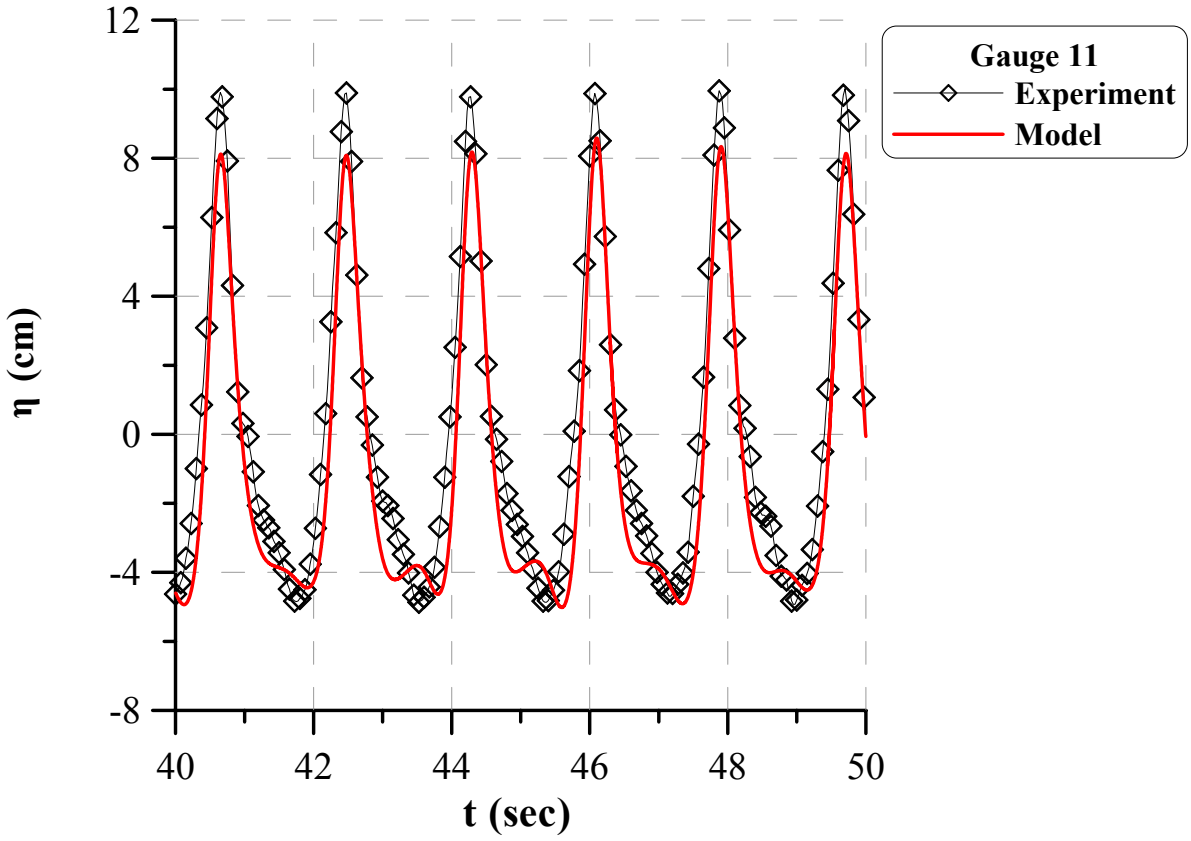

Figure 50.Computed and experimental free surface elevation (Aalborg, H=0.1026, T=1.81).

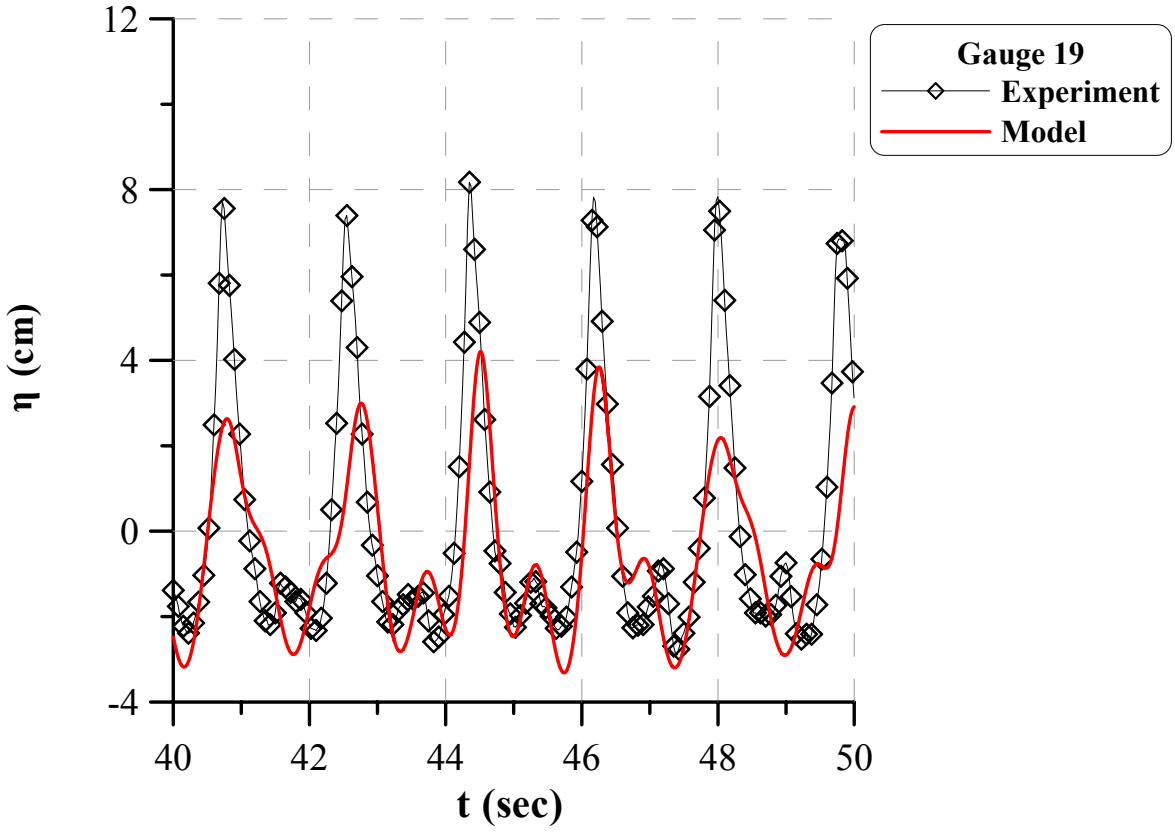

Figure 51.Computed and experimental free surface elevation (Aalborg, H=0.1026, T=1.81).

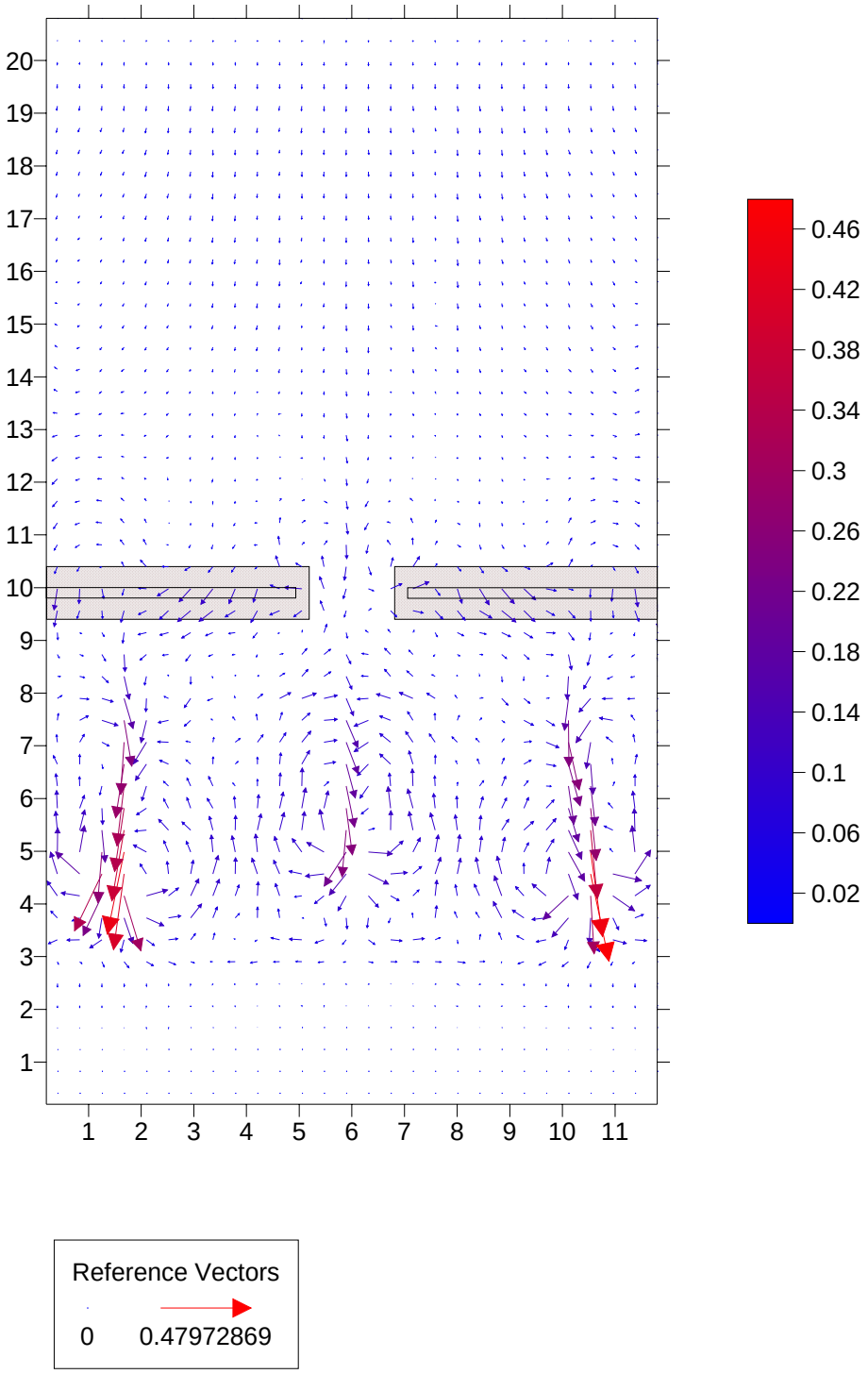

Figure 52. Mean wave-induced current field (Aalborg, H=0.1026, T=1.81)

9. References

Avgeris, I., Karambas, Th., Prinos, P., Koutitas, C., 2003. D27: 2DH preliminary Boussinesq-type model. DELOS Internal Report, pp. 34.

Burcharth, H. F., Andersen, O. H., 1995. On the one-dimensional steady and unsteady porous flow equations. Coastal Engineering, 24, 233-257.

Cruz, E. C., Isobe, M., Watanabe, A., 1997. Boussinesq equations for wave transformation on porous beds. Coastal Engineering, 30, 125-156.

Engelund, F. A., 1953. On the laminar and turbulent flows of ground water through homogeneous sand. Danish Academy of Technical Sciences.

Gironella, X., Sánchez-Arcilla, A., 2002. DELOS Internal presentation.

Gobbi, M. F., Kirby, J.T., 1999. Wave evolution over submerged sills: tests of high-order Boussinesq model. Coastal Engineering, 37, 57-96.

Gu, Z., Wang, H., 1991. Gravity waves over porous bottoms. Coastal Engineering, 15, 497-524.

Hsiao, S.-C., Liu, P. L.-F., Chen, Y., 2002. Nonlinear water waves over a permeable bed. Proceedings R. Soc. Lond. A (2002), 458, 1291-1322.

Karambas, Th. V., Koutitas, C., 2002. Surf and Swash Zone Morphology Evolution Induced by Nonlinear Waves. Journal of Waterway, Port, Coastal and Ocean Engineering, 128 (3), 102-113.

Kennedy, A.B., Chen, Q., Kirby, J.T., Darlymple, R.A., 2000. Boussinesq modeling of wave transformation, breaking, and runup. I: 1D. Journal of Waterway, Port, Coastal and Ocean Engineering 121 (5), 251-261.

Liu, P. L.-F., Wen, J., 1997. Nonlinear diffusive surface waves in porous media. Journal of Fluid Mechanics, 347, 26, 119-139.

Losada, I. J., Losada, M. A., Martín, A., 1995. Experimental study of wave-induced flow in a porous structure. Coastal Engineering, 26, 77-98.

Losada, I. J., Silva, R., Losada, M. A., 1996. 3-D non-breaking regular wave interaction with submerged breakwaters. Coastal Engineering, 28, 229-248.

Madsen, O. S., 1974. Wave transmission through porous structures. Journal of Waterway, Harbour, Coastal and Ocean Engineering, Div., ASCE, 100 (3), 169-188.

Madsen, P.A., Sørensen, O.R., 1992. A new form of the Boussinesq equations with improved linear dispersion characteristics. Part 2: A slowly varying bathymetry. Coastal Engineering, 18, 183-204.

Sollitt, C. K., Cross, R. H., 1972. Wave transmission through permeable breakwaters. In: Proceedings of 13th International Conference on Coastal Engineering, ASCE, New York, 1827-1846.

Sollitt, C. K., Cross, R. H., 1976. Wave reflection and transmission at permeable breakwaters. Technical Paper No. 76-8, CERC.

van Gent, M. R. A., 1994. The modelling of wave action on and in coastal structures. Coastal Engineering, 22, 311-339.

van Gent, M. R. A., 1995. Wave interaction with permeable coastal structures. PhD Thesis, Delft University, Delft, The Netherlands.

Vidal, C., Losada, M. A., Medina, R., Rubio, J., (1988). Solitary wave transmission through porous breakwaters. In: Proceedings of 21st International Conference on Coastal Engineering, ASCE, New York, 1073-1083.

Vidal, C., Lomonaco, P., Migoya, L., Archetti R., Turchetti M., Sorci, M., Sassi, G., (2002). Laboratory experiments on flow around and inside LCS structures. Description of tests and data base. DELOS Project Internal Report, pp. 19.

Ward, J. C., 1964. Turbulent flow in porous media. Journal of Hydraulic Division, ASCE, 90 (HY5), 1-12.

Wei, G., Kirby, J.T., 1995. Time-dependent numerical code for extended Boussinesq equations. Journal of Waterway, Port, Coastal and Ocean Engineering, 121 (5), 251-261.

Wei G., Kirby, J.T., Sinha, A., 1999. Generation of waves in Boussinesq models using a source function method. Coastal Engineering, 36, 271-299.

Zanuttigh B., Lamberti A., 2003. Wave basin experiment final form: 3D Hydrodynamic tests at Aalborg University, DK. DELOS Project Deliverable D 31, pp. 76.

DELOS PROJECT

by
Giorgio Bellotti, Riccardo Briganti and Maurizio Brocchini

Contents

List of Figures

List of Tables

Chapter 1

Introduction

The design of structures to be built in the nearshore region generally involves the evaluation of different possible layouts, under the effects of local wave and currents conditions, with the aim of minimizing costs and maximizing the desired results. In particular the design of low-crested structures involves optimization of several parameters which influence both the position and the shape of the structures.

The possible layout of the structures to be designed can be tested experimentally in wave tanks and wave flumes using adequate scale models. An alternative and attractive procedure is to employ suitable numerical and mathematical models. In principle, a very advanced numerical model, able to correctly simulate *all* the nearshore phenomena (turbulence, waves, currents, sediment transport, etc.) could be equivalent or even superior to a physical model. In practice, the numerical models currently employed in engineering activities, use several assumptions and simplifications: the phenomena that can be simulated strictly depend on the governing equations solved by the model. Indeed, the great advantage of numerical and mathematical models is that their application is usually much less expensive than physical ones: it is certainly more economic to modify a computer file describing the bathymetry of the area under investigation than rebuild a physical model layout.

The development of numerical models to be applied for nearshore flows has, therefore, received great attention in the last fourty years. The interest in numerical models increases as much as computer speed and diffusion do. This work is aimed at improving *Boussinesq Type Equations* (BTE hereinafter) models, which belong to a specific category of numerical models applicable to nearshore flows and can be used to simulate wave transformation and currents generation. We consider in details two main features of BTE models which require improvement: the extesion of the model to swash zone flows and the parametrization of surf zone turbulence.

The first line of research finds motivation in the fact that considerable efforts have been spent in the recent past by several researchers in extending the applicability of BTE models to the intermediate depths. On the contrary, much less work has been done in studying the problems that arise in very shallow water, in proximity and into the swash zone. However, it is now clear that swash zone motions are a fundamental source of low frequency waves (LFW hereinafter) (e.g. Watson et al. 1994; Mase 1995; Baldock et al. 1997). These, radiating offshore, contribute to the transport of the bottom sediment which is locally, i.e. close to the low-crested structures, put into suspension by waves and other organized structures like splash-down vortices (e.g. Fredsoe and Sumer 1997; Chang et al. 2001) but is transported mainly by LFW which deeply modify the bottom morphology over relatively large scales (a.o. Holman and Bowen 1982; Beach and Sternberg

1991; O'Hare and Huntley 1994; Aagaard and Greenwood 1994). It is then clear that a poor representation of swash zone flows is not only essential to the quantification of the LFW emitted but also to the large-scale sediment transport which, in turn, can influence the stability of man-made structures. Research in providing suitable shoreline boundary conditions for BTE models is very new (e.g. Madsen et al. 1997; Lynnet et al. 2002) and until recently the swash zone was modelled either as a perfecly reflecting wall or as a perfectly absorbing boundary. None of these methods, however, can describe the generation of LFW due to swash motions. On the contrary, they act in a different, unphysical way. The perfectly absorbing boundary is such that not even the free LFW propagating towards the shore can be reflected out to sea. Hence, the energy content in the LFW range is always too small. The perfectly reflecting wall, though reflecting all the LFW generated during the propagation of waves towards the shore, cannot account for local generation within the swash zone. Hence, the energy content in the LFW range can either be too large or too small with respect to natural conditions.

The second motivation of our works comes from the observation that the modes and extent of transport of suspended sediment are greatly influenced by the velocity profile within the whole water column. In shallow water this is almost uniform, however, this is not the case of the flow in intermediate waters, where submerged structures are often placed. Detailed knowledge of the flow structure over the vertical has been the focus of recent research on BTEs (e.g. Rakha et al. 1997; Ozanne et al. 2000; Veeramony and Svendsen 2000). Of particular interest is the work of Veeramony and Svendsen 2000 (VS hereinafter) who developed a rather sophisticated BTE model capable of representing the features of breaking waves by modeling the dynamics of vorticity injected in the flow by a wave roller.

In VS's model the breaking terms are derived directly by a decomposition of the velocity into a potential and a rotational part. This was computed by solving the vorticity transport equation (VTE hereinafter). For closing the turbulence problem, VS assumed a simple eddy viscosity model, i.e. a uniform distribution over the depth. Such an assumption allowed to solve the VTE through an analytical approach.

Although rather succesful VS's approach is somehow simplistic and not flexible as it does not allow for a detailed description of the vertical structure of turbulence. Hence, in the present work the limiting hypotesis of uniform eddy viscosity has been removed and a numerical solution of the VTE is proposed. Such an approach is an improvement, since it permits investigation of the effects of different eddy viscosity profiles.

The rest of this report is organized as follows. In chapter 2 depth-integrated wave-resolving models are introduced. The procedure for obtaining both NSWEs and BTEs is illustrated. A specific numerical model, coded by the present Authors for solving the BTEs, is described. A detailed analysis of the problems related to using BTE in very shallow water is finally carried out. This chapter is a review of works published during the course of DELOS project.

In chapter 3 new shoreline boundary conditions for Boussinesq-type models are derived. These boundary conditions are then implemented in the numerical model described in chapter 2, with the aim of verifying their capability in simulating swash zone hydrodynamics. The comparison of the results obtained by means of the numerical model against analytical solutions shows the very good performance of the new shoreline boundary conditions. Also results reported in this chapter have been published under the patronage of DELOS.

In chapter 4 a new method for simulating wave-breaking into BTE models is presented and verified. According to the proposed method the governing equations are derived dropping the

assumption of irrotationality of the flow. The resulting equations present extra terms in comparison with the classical BTEs that take into account wave-breaking generated vorticity. The new method allows wave-averaged vertical profiles of the horizontal velocity to be not self-similar and is capable of simulating important features of nearshore flows such as the undertow. Comparison of the model results with available experimental data suggests good performance of the model. Results of this chapter form the basis for a couple of papers in cours of completion.

Conclusions and some remarks on ongoing research are summarized in chapter 5.

Chapter 2

Depth-integrated wave-resolving models

In this chapter the depth-integrated wave-resolving models for simulating the nearshore hydrodynamics are introduced. In section 2.1 a derivation of the typical model equation is presented, obtaining the NSWE and the BTE. Emphasis is posed on the differences between the two formulations and on the advantages and disadvantages of each. A numerical model, coded by the present Authors for solving the BTE is described in section 2.2. This model was used to test the shoreline boundary conditions (SBCs hereinafter) derived in chapter 3 and the wave-breaking method presented in chapter 4. In section 2.3 the applicability of BTE in very shallow waters is investigated on the basis of the analytical solution of Carrier and Greenspan (1958), valid for periodic waves propagating on a sloping beach. Notice that in order to simplify the derivation of the equations we limit our presentation to one horizontal dimension. Therefore instead of obtaining 2DH equations, in this chapter and more generally in the rest of this report we deal with 1DH equations.

The results presented in section 2.3 are innovative since before this work no careful investigation was carried out in order to understand the role of dispersive-nonlinear terms of BTE in very shallow water. The analysis shows that, if not properly handled, BTE may become extremely unstable in the swash zone, leading to diverging solutions.

2.1 The BTE and the NSWE

In this section a derivation of the NSWE and of the BTE is presented. Several possible approaches have been followed in the past. We decided to follow the derivation by Veeramony and Svendsen (1999), which is based on the direct integration over the water depth of the Reynolds equations. The aim of this section is not to provide the reader with a very detailed derivation of the equations, but to briefly illustrate the basic steps, the simplifications and the assumptions that lead to NSWE and BTE.

2.1.1 Scaling parameters, reference frame and variable used

Two independent non-dimensional parameters are used during the derivation for estimating the order of magnitude of each term appearing in the equations. These parameters are obtained as ratios of the length scales associated with the wave motion: the wave amplitude a_0, the wave number $k_0 = 2\pi/L$ (L being the wavelength) and the water depth h_0. The first non-dimensional

parameter $\delta = a_0/h_0$ measures the nonlinearity of the wave. The second parameter $\mu = k_0 h_0$ measures the frequency dispersiveness of the waves. Large values of μ characterize the motion of waves in deep water, while small values of μ are typical of long waves in very shallow water where wave celerity depends on the water depth rather than on the wave frequency.

On figure 2.1 a typical problem geometry and the employed reference frame are shown. The origin of the cartesian reference frame is at the undisturbed free surface, x is the horizontal coordinate, positive shoreward; z is the vertical coordinate, measured positive upwards. h is the undisturbed water depth, ζ the water elevation with respect to the undisturbed level. d is the total water depth, given by the sum of h and ζ. In the following sections u' indicates the horizontal component of the velocity (measured positive rightward in the adopted reference frame),w' the vertical one (positive upwards).

Nondimensional variables are widely used in the following. These are defined by the following relationships (superscript * represents hereinafter non dimensional quantities)

$$\begin{array}{cc} x^* = k_0 x, & z^* = \frac{z}{h_0}, \qquad t^* = k_0\sqrt{g h_0}\; t \\ u'^* = \delta\sqrt{g h_0}\; u', & w'^* = \delta\mu\sqrt{g h_0}\; w' \end{array} \tag{2.1.1}$$

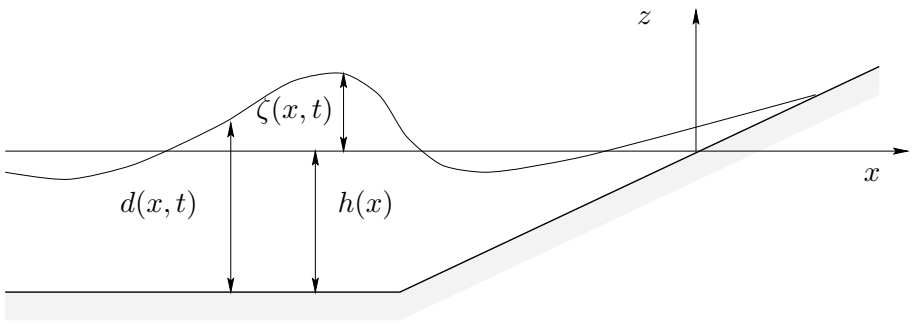

Figure 2.1: Sketch of the typical problem geometry.

2.1.2 Boundary conditions and preliminary assumptions

In order to integrate the Reynolds equations over the water depth proper boundary conditions should be imposed at the limits of the domain of interest. At the free surface it is assumed that a particle originally on the surface stays at the surface during wave propagation. From a mathematical point of view this kinetic boundary condition can be expressed as

$$w'(\zeta) = \frac{\partial \zeta}{\partial t} + u'(\zeta)\frac{\partial \zeta}{\partial x}. \tag{2.1.2}$$

At the free surface is, furthermore, assumed that atmospheric pressure is constant and equal to zero:

$$p(\zeta) = 0. \tag{2.1.3}$$

An impermeable bottom is assumed in the derivation. Thus the kinematic condition at the bottom can be expressed as

$$w'(-h) = -u'(-h)\frac{\partial h}{\partial x}. \tag{2.1.4}$$

Several assumptions and simplifications are used during the derivation of the equations. These are reported here below and briefly discussed. The fluid is assumed to be of constant density and inviscid. The motion of the bulk fluid is non-rotational and a velocity potential exists. The shear stress at the bottom and at the free surface is neglected. This coincides with imposing a free slip condition at the bottom and to neglect any wind force acting on the water.

2.1.3 The depth-integrated continuity equation

We start the derivation from the two-dimensional differential form of the continuity equation

$$\frac{\partial u'}{\partial x} + \frac{\partial w'}{\partial z} = 0. \tag{2.1.5}$$

Integration of (2.1.5) from the free surface ($z = \zeta$) to the bottom ($z = -h$) gives

$$\int_{-h}^{\zeta} \frac{\partial u'}{\partial x} dz + w'(\zeta) - w'(-h) = 0. \tag{2.1.6}$$

Use of the boundary conditions (2.1.2) and (2.1.4) allows to eliminate vertical velocities at the boundaries and application of the Leibniz rule gives

$$\frac{\partial \zeta}{\partial t} + \frac{\partial}{\partial x} \int_{-h}^{\zeta} u' \, dz = 0 \tag{2.1.7}$$

that is the general, dimensional form of the depth-integrated continuity equation.

2.1.4 The depth-integrated momentum equation

We start from the horizontal and vertical momentum equation, which read respectively

$$\frac{\partial u'}{\partial t} + \frac{\partial u'^2}{\partial x} + \frac{\partial u'w'}{\partial z} = -\frac{1}{\rho}\frac{\partial p}{\partial x} + \frac{1}{\rho}\left(\frac{\partial \tau_{xx}}{\partial x} + \frac{\partial \tau_{xz}}{\partial z}\right), \tag{2.1.8}$$

$$\frac{\partial w'}{\partial t} + \frac{\partial u'w'}{\partial x} + \frac{\partial w'^2}{\partial z} = g - \frac{1}{\rho}\frac{\partial p}{\partial z} + \frac{1}{\rho}\left(\frac{\partial \tau_{xz}}{\partial x} + \frac{\partial \tau_{zz}}{\partial z}\right) \tag{2.1.9}$$

where τ_{xx} and τ_{zz} are the normal deviatoric stresses and τ_{xz} is the turbulent stress. Integration of (2.1.8) over the water depth, use of boundary conditions, Leibniz rule and of assumptions about the forces acting on the fluid at the free surface give

$$\frac{\partial}{\partial t}\int_{-h}^{\zeta} u' \, dz + \frac{\partial}{\partial x}\int_{-h}^{\zeta} u'^2 \, dz = \frac{p(-h)}{\rho}\frac{\partial h}{\partial x} + \frac{\partial}{\partial x}\int_{-h}^{\zeta} (-p + \tau_{xx}) \, d\hat{z}. \tag{2.1.10}$$

The expression for the pressure p can be obtained by integrating (2.1.9) from the surface to a generic level z, using both the boundary conditions and the Leibniz rule:

$$\frac{p(z)}{\rho} = g(\zeta - z) - w'^2 + \frac{\partial}{\partial t}\int_{z}^{\zeta} w' \, dz + \frac{\partial}{\partial x}\int_{z}^{\zeta} \left(u'w' - \frac{\tau_{xz}}{\rho}\right) \, dz. \tag{2.1.11}$$

In order to write (2.1.11) in non-dimensional variables, a scaling for the turbulent stress term is to be introduced. Veeramony and Svendsen (1999) proposed the following scaling by assuming an eddy viscosity representation of τ_{xz}

$$\tau_{xz} = \delta\mu\rho g h_0 \nu_t \left(\frac{\partial u'}{\partial z} + \mu^2 \frac{\partial w'}{\partial x} \right) \tag{2.1.12}$$

where ν_t is the eddy viscosity.

By replacing the dimensional variables with the non-dimensional ones given in section 2.1.1 and making use of (2.1.12), equation (2.1.11) becomes

$$\begin{aligned} p^*(z^*) = \left(\zeta^* - \frac{z^*}{\delta} \right) - \delta\mu^2 w'^{*2} + \mu^2 \frac{\partial}{\partial t^*} \int_{z^*}^{\delta\zeta^*} w'^* \, dz^* \\ + \delta\mu^2 \frac{\partial}{\partial x^*} \int_{z^*}^{\delta\zeta^*} u'^* w'^* \, dz^* - \mu^2 \frac{\partial}{\partial x^*} \int_{z^*}^{\delta\zeta^*} \nu_t \frac{\partial u'^*}{\partial z^*} w'^* \, dz^* + O\left(\mu^4\right). \end{aligned} \tag{2.1.13}$$

Equation (2.1.13) is suitable to illustrate the effects of frequency dispersiveness on the pressure distribution over the water depth. The first term of the right hand side of (2.1.13) represents the hydrostatic pressure component. The other terms, of order $O\left(\mu^2\right)$ and $O\left(\delta\mu^2\right)$ deviate the pressure distribution from the hydrostatic, thus allowing for frequency dispersion. Neglecting all these smaller terms coincides with treating non dispersive nonlinear waves, i.e. very long waves. As shown in the following sections neglecting terms of order equal or smaller than $O\left(\mu^2\right)$ leads to obtain the NSWE, while retaining these terms leads to the BTE, which can simulate frequency dispersion.

By inserting non-dimensional variables into (2.1.10), then using both the expression for the pressure (2.1.13) and the following form of the continuity equation integrated from $-h$ to the generic level z

$$w'^*(z) = -\frac{\partial}{\partial x^*} \int_{-h^*}^{z^*} u'^* \, dz^* \tag{2.1.14}$$

gives the following combined momentum equation in terms of horizontal velocity integrals and water surface elevation

$$\begin{aligned} \frac{\partial}{\partial t^*} \int_{-h^*}^{\delta\zeta^*} u'^* \, dz^* + \left(h^* + \delta\zeta^*\right) \zeta_{x^*}^* + \delta \frac{\partial}{\partial x^*} \int_{-h^*}^{\delta\zeta^*} u'^{*2} \, dz^* + \\ - \mu^2 \int_{-h^*}^{\delta\zeta^*} \frac{\partial^2}{\partial x^* \partial t^*} \int_{z^*}^{\delta\zeta^*} \frac{\partial}{\partial x^*} \int_{-h^*}^{z^*} u'^* \, dz^* \, dz^* \, dz^* + \\ - \mu^2 \int_{-h^*}^{\delta\zeta^*} \frac{\partial^2}{\partial x^{*2}} \int_{z^*}^{\delta\zeta^*} \nu_t \frac{\partial u'^*}{\partial z^*} \, dz^* \, dz^* + -\delta\mu^2 \int_{-h^*}^{\delta\zeta^*} \frac{\partial}{\partial x^*} \left(\frac{\partial}{\partial x^*} \int_{-h^*}^{z^*} u'^* \, dz^* \right)^2 dz^* + \\ - \delta\mu^2 \int_{-h^*}^{\delta\zeta^*} \frac{\partial^2}{\partial x^{*2}} \int_{z^*}^{\delta\zeta^*} u'^* \frac{\partial}{\partial x^*} \int_{-h^*}^{z^*} u'^* \, dz^* \, dz^* \, dz^* = 0. \end{aligned} \tag{2.1.15}$$

2.1.5 An approximate expression for the horizontal velocity

The depth-integrated continuity and momentum equations (2.1.7) and (2.1.15) can be solved analytically provided that a vertical profile of the horizontal velocity u' is assumed. By assuming

irrotationality of the fluid motion such profile can be obtained by solving the Laplace equation approximately, imposing the proper boundary conditions at the free surface and at the bottom. In classical Boussinesq models this approximate solution is achieved by expressing the velocity potential as an infinite polynomial series. In the original work that is followed in this section (Veeramony and Svendsen 1999) a very original approach was presented. Those Authors assumed that the wave-breaking process generates vorticity. Therefore the fluid motion cannot be tread as irrotational and approximate solution for the horizontal velocity was obtained by using the streamfunction instead of a velocity potential. In this approach the final expression for the velocity contains terms that represent the influence of the wave-breaking generated vorticity on the fluid motion. The final Boussinesq equations obtained by using this expression for the velocity can naturally simulate the dissipative effects of wave-breaking. Furthermore, since the horizontal velocity depends on the vorticity generated by wave-breaking the vertical profile of the velocity is not self-similar: it depends on both wave propagation and transformation, while models based on the classical approach of irrotational flow present a self-similar vertical profile. It is to be mentioned that very recently Rego et al. (2001) used the same approach for simulating waves over flows with arbitrary vorticity, thus extending in some sense the work of Veeramony and Svendsen (1999) which focussed on wave-breaking generated vorticity.

In this section the final expression for the velocity u' employed in classical weakly nonlinear-dispersive Boussinesq models is reported. This expression can be also recovered from that presented by Veeramony and Svendsen (1999) by neglecting the terms involving vorticity. u' can be expressed as a function of quantities measured at different levels in the water column or in terms of averaged or integrated quantities. For example either the horizontal velocity at the bottom u'_0, or the velocity at a specific level z_α, or the depth-integrated velocity $u^* = \frac{1}{(h^*+\delta\zeta^*)}\int_{-h^*}^{\delta\zeta} u'^*\, dz$ can be used as variable. A widely used expression relates u'^* to u^* and reads

$$u'^* = u^* + \mu^2\left(\frac{\Delta_1}{2} - z^*\right)(h^*u^*)_{x^*x^*} + \frac{\mu^2}{2}\left(\frac{\Delta_2}{3} - z^{*2}\right)u^*_{x^*x^*} \tag{2.1.16}$$

where $\Delta_1 = \delta\zeta^* - h^*$ and $\Delta_2 = \delta^2\zeta^{*2} - \delta\zeta^*h^* + h^{*2}$. Equation (2.1.16) represents the classical parabolic velocity profile of BTE. It is evident that if wave dispersiveness is neglected (i.e. $\mu = O(0)$), the horizontal velocity is constant over the depth and, of course, is equal to the depth-integrated velocity.

2.1.6 The final equations

The approximate expression for the velocity (2.1.16) can be used to evaluate the integrals appearing in the non-dimensional form of (2.1.7) and in (2.1.15). During the algebraic procedure terms of high order in δ and μ appear. Therefore a specified degree of accuracy is chosen and only terms consistent with this accuracy are retained. Nevertheless the depth-integrated continuity equation is not affected by the truncation in μ and δ. This equation is, under the hypotesis summarized in section 2.1.2, exact and its final form reads

$$\zeta^*_{t^*} + \left[(h^* + \zeta^*)\, u^*\right]_{x^*} = 0. \tag{2.1.17}$$

Let us now discuss the influence of the scaling parameters on the final depth-integrated momentum equations. If the final equations are to be used to simulate nonlinear waves in very

shallow water, the effect of frequency dispersion is neglected, since in these conditions the order of magnitude of the scaling parameters is

$$\delta = O(1), \qquad \mu^2 = O(0). \tag{2.1.18}$$

The final form of the depth-integrated momentum equation, if all terms of orderμ^2 and smaller are neglected, reads

$$u^*{}_{t^*} + \delta u^* u^*{}_{x^*} + \zeta^*{}_{x^*} = 0 \tag{2.1.19}$$

which is the well known momentum equation of the NSWE.

Extending the NSWE to the intermediate depths involves retaining terms of higher order inμ. Weakly nonlinear waves in intermediate water can be simulated by chosing the following order of magnitude of the parameters:

$$\frac{\delta}{\mu^2} = O(1), \qquad \mu^2 << O(1). \tag{2.1.20}$$

This choice leads to the classic weakly dispersive, weakly nonlinear BTE momentum equations that read

$$u^*{}_{t^*} + \delta u^* u^*_{x^*} + \zeta^*{}_{x^*} + \mu^2 \left[-\frac{1}{3} h^{*2} u^*_{x^* x^* t^*} - \frac{1}{2} h^* h^*{}_{x^* x^*} u^*{}_{t^*} - h^* h^*{}_{x^*} u^*{}_{x^* t^*} \right] = 0. \tag{2.1.21}$$

The NSWE (2.1.19) and the BTE (2.1.21) are the most widely used nonlinear depth-integrated models for the nearshore hydrodynamics. Each of these equations presents some advantages and some drawbacks, which we discuss in this final part of the section.

Any model application, aimed at studying nearshore waves and currents, consists of simulating wave transformations from the offshore to the inshore, where knowledge of flow conditions is usually required. Input wave conditions are usually known, with a certain degree of accuracy, in deep water, where the influence of the bottom is small. This information can be obtained for example by buoys, hindcasting or forecasting models, etc. Neverthless, waves in very deep water are characterized by high values of the dispersiveness parameter μ, and the assumptions (2.1.18) and (2.1.20) are clearly in contrast with this feature of the waves to be simulated. It is therefore clear that a very important limitation characterizes the application of the model discussed in this section: the offshore boundary of the computational domain is to be carefully selected in order to impose, as boundary conditions, waves consistent with the assumptions that are at the basis of the models.

In other words these models are *shallow water* models and can be applied in regions where waves are strongly influenced by the bottom (shallow and intermediate areas). Wave transformation from offshore areas to the intermediate or shallow areas, where accurate modelling can be performed with NSWE and BTE, are to be taken into account using alternative techniques. NSWE suffer greatly from this limitation if compared to BTE. Due to their non-dispersive nature, NSWE cannot propagate waves of constant form. Being purely amplitude-dispersive, NSWE simulate waveforms that evolve in time, since the higher parts of the waves propagates faster than the lowers, inducing to steepening of the wave profile. This leads to vertical wave fronts which, in some sense, model the physical process of wave-breaking. The problem with NSWE is that the steepening process is only partially influenced by the bottom: also very long waves, propagating over a horizontal bottom would unrealistically break after a few wavelengths. Indeed it is to be noted that once the shoreward part of the wave profile has become vertical, if a suitable numerical method is employed

to solve the equations, a bore-like solution would be obtained, simulating the dissipative effects of wave-breaking. Furthermore NSWE are usually conveniently solved by means of numerical methods that allow a very effective treatment of the swash zone. It can be concluded that NSWE can be applied with good results in the surf and in the swash zone, but they can not accurately predict where the waves start breaking. Moreover wave-breaking effects are simulated by means of a purely numerical treatment and no representation of the physical phenomena is generally incorporated into the equations.

On the contrary BTE can accurately simulate wave propagation before wave-breaking occurs: in the last ten years great efforts have been spent in order to extend to intermediate and deep waters the BTE (Madsen and Schäffer 1998). Very recently Madsen et al. (2001) presented a very advanced form of the equations that allows an accurate representation of wave propagation from almost deep waters to the surf zone. In general these new form of BTE are achieved relaxing the assumptions (2.1.20) and retaining high order terms both in μ and δ. Wave-breaking in BTE models is simulated by introducing additional terms in the equations, which appear when the wave front has reached a certain slope. BTE, if compared to NSWE are a very complete and advanced model, but mainly two drawbacks limit their application. First the computational times needed to solve the equations are very large if compared to those required for solving the NSWE. By retaining high order terms, very complicated governing equations are obtained. These are characterized by high order derivatives of the dependent variables which, in order to be evaluated numerically, need very fine space and time grids. Furthermore the flow in the swash zone is represented using ad hoc techniques (see chapter 3), which limit the accuracy of the results.

2.2 A numerical model for solving the BTE

This section is dedicated to a brief description of the numerical model for solving the BTE that was coded in order to verify the boundary conditions described in chapter 3 and the wave-breaking criterion presented in chapter 4. We have chosen to adopt and code the model derived by Veeramony and Svendsen (1999), because of its effectiveness in representing nearshore flows.

The basic model equations are both the mass conservation equation

$$\zeta_t + \left[(h+\zeta)\,u\right]_x = 0 \tag{2.2.22}$$

and the momentum conservation equation

$$\begin{array}{c} u_t + uu_x + g\zeta_x + \left(\mathcal{B} - \frac{1}{3}\right) h^2 u_{xxt} - \frac{1}{2} h h_{xx} u_t - h h_x u_{xt} + \mathcal{B} g h^2 \zeta_{xxx} - \frac{1}{3} h^2 u u_{xxx} \\ + \frac{1}{3} h^2 u_x u_{xx} - \frac{3}{2} h h_{xx} u u_x - \frac{1}{2} h h_{xxx} u^2 - h h_x u u_{xx} + \mathcal{B} h^2 \left(u u_x\right)_{xx} - \frac{1}{3} h \zeta u_x u_{xx} \\ - \frac{1}{3} h u_{xx} \left(\zeta u\right)_x + h \left(\zeta u_x^2\right)_x - \frac{2}{3} h \left(\zeta u u_{xx}\right)_x - \zeta_x h_{xx} u^2 - \zeta h_x u u_{xx} - \frac{1}{2} \zeta h_{xxx} u^2 \\ - \frac{3}{2} \zeta h_{xx} u u_x - \zeta_x h_x u u_x - \frac{1}{3} \zeta^2 u u_{xxx} - \zeta \zeta_x u u_{xx} + \zeta \zeta_x u_x^2 + \frac{1}{3} \zeta^2 u_x u_{xx} - h \zeta_x u_{tx} \\ - \frac{2}{3} h \zeta \left(u_t\right)_{xx} + \zeta h_x \left(u_t\right)_x - h_x \zeta_x u_t - \frac{1}{2} \zeta h_{xx} u_t + \frac{1}{6} \zeta^2 \left(u_t\right)_{xx} - \frac{1}{2} \left(\zeta^2 \left(u_t\right)_x\right)_x = 0 \end{array} \tag{2.2.23}$$

with improved dispersion characteristics (here $\mathcal{B} = -\frac{1}{15}$). Good dispersion properties, which make this model suitable for accurate flow predictions from the 'intermediate' to the 'shallow waters', have been obtained by retaining terms of order up to $O(\delta^3\mu^2)$ inclusive.

Notice that, although the original form of equation (2.2.23) includes additional terms which model energy dissipations caused by wave breaking, these are here neglected for simplicity. They will be re-introduced in chapter 4. A second note of caution is highlighted in section 2.3 and for the

reason discussed there we coded the equivalent (but written in terms of the water depth d instead of the surface elevation ζ) momentum equation 2.3.53 which is reported here for convenience (notice that here $\mathcal{B}$ has been set to zero for simplicity sake):

$$\begin{gathered} u_t + uu_x + g\zeta_x - \tfrac{1}{3}d^2u_{xxt} + \tfrac{1}{2}dh_{xx}u_t + dh_xu_{xt} \\ -\tfrac{1}{3}d^2uu_{xxx} - \tfrac{1}{3}d^2u_xu_{xx} + \tfrac{3}{2}dh_{xx}uu_x + \tfrac{1}{2}dh_{xxx}u^2 + dh_xuu_{xx} + d\zeta_xu_{xt} + h_x\zeta_xu_t \\ -d\zeta_xuu_{xx} - d\zeta_xu_x^2 + \zeta_xh_{xx}u^2 + \zeta_xh_xuu_x = 0. \end{gathered} \tag{2.2.24}$$

The governing equations (2.2.22) and (2.2.24) are solved adopting a 4th-order Adam-Bashfort-Moulton scheme (ABM hereinafter) to step the model forward in time and a five-point finite difference scheme to evaluate the spatial derivatives. The resulting model scheme is widely adopted with good results to solve the Boussinesq equations (see for example Wei et al. 1995) and the short-wave-averaged NSWE (Sancho and Svendsen 1997).

In order to apply the ABM scheme the governing equations are written in a more convenient way:

$$\zeta_t = E, \tag{2.2.25}$$

$$\upsilon_t = F \tag{2.2.26}$$

where

$$E = -\left[(h+\zeta)\,u\right]_x, \tag{2.2.27}$$

$$\begin{gathered} F = uu_x + g\zeta_x \\ -\tfrac{1}{3}d^2uu_{xxx} - \tfrac{1}{3}d^2u_xu_{xx} + \tfrac{3}{2}dh_{xx}uu_x + \tfrac{1}{2}dh_{xxx}u^2 + dh_xuu_{xx} + d\zeta_xu_{xt} + h_x\zeta_xu_t \\ -d\zeta_xuu_{xx} - d\zeta_xu_x^2 + \zeta_xh_{xx}u^2 + \zeta_xh_xuu_x = 0 \end{gathered} \tag{2.2.28}$$

and

$$\upsilon = \frac{1}{3}d^2u_{xx} - \frac{1}{2}dh_{xx}u - dh_xu_x. \tag{2.2.29}$$

The independent variables x and t are discretized over an unstaggered grid by defining $x_i = (i-1)\Delta x$, $(i = 1, 2, ..., nx-1, N)$ and $t_n = (n-1)\Delta t$, $(n = 1, 2, ..., T-1, T)$, where N is the number of nodes of the computational domain and T is the number of time-steps.

If initial conditions are specified, i.e. if the values of ζ and u at the time levels n, $n-1$, $n-2$ are available, the solution at the subsequent time level $n+1$ can be obtained by means of the following procedure:

1. evaluation of the right-hand sides of equations (2.2.25) and (2.2.26) at the time level n, $n-1$, $n-2$;
2. integration in time of equations (2.2.25) and (2.2.26) by means of the predictor stage of the ABM scheme;
3. evaluation of right-hand sides of equations (2.2.25) and (2.2.26) at the time level $n+1$;
4. integration in time of equations (2.2.25) and (2.2.26) by means of the corrector stage of the ABM scheme;
5. evaluation of u_i^{n+1} at all interior grid points by means of the solution of the tridiagonal system resulting from the discretizing of (2.2.29).

Steps from 4 to 5 are iterated in order to improve the accuracy of the convergence.

The ABM time stepping scheme and the finite-differences expressions for the spatial derivatives are detailed in the following sections.

2.2.1 The Adam-Bashfort-Moulton time stepping scheme

Once the right-hand sides of equations (2.2.25) and (2.2.26) are computed at time-steps n, $n-1$ and $n-2$, estimates of quantities ζ and υ at the following time-step $n+1$ can be obtained by applying the ABM scheme which at the predictor stage reads:

$$\zeta_i^{n+1} = \zeta_i^n + \frac{\Delta t}{12}\left[23E_i^n - 16E_i^{n-1} + 5E_i^{n-2}\right], \tag{2.2.30}$$

$$\upsilon_i^{n+1} = \upsilon_i^n + \frac{\Delta t}{12}\left[23F_i^n - 16F_i^{n-1} + 5F_i^{n-2}\right]. \tag{2.2.31}$$

All values at the right hand sides of equations (2.2.30) and (2.2.31) are known from previous calculations. The values of ζ_i^{n+1} are thus straightforward to obtain. The evaluation of horizontal velocities, u, at the new time level, however, requires solution of the tridiagonal system resulting from the discretizing of (2.2.29) as detailed in section 2.2.4.

Once ζ_i^{n+1} and u_i^{n+1} are estimated, the quantities E and F can be evaluated at the time-step $n+1$ and the corrector stage of the ABM scheme can be applied:

$$\zeta_i^{n+1} = \zeta_i^n + \frac{\Delta t}{24}\left[9E_i^{n+1} + 19E_i^n - 5E_i^{n-1} + E_i^{n-2}\right], \tag{2.2.32}$$

$$\upsilon_i^{n+1} = \upsilon_i^n + \frac{\Delta t}{24}\left[9F_i^{n+1} + 19F_i^n - 5F_i^{n-1} + F_i^{n-2}\right]. \tag{2.2.33}$$

The time-stepping scheme is accurate up to $O(\Delta t)^3$ at the predictor stage and up to $O(\Delta t)^4$ at the corrector stage. As introduced before, by applying repeatidly the corrector stage, very accurate estimates of the dependent variable can be obtained. More specifically, the corrector step is iterated until the error between two successive results reaches a required limit. The error is computed for each of the two dependent variables ζ and u and is defined as:

$$\Delta f \;=\; \frac{\sum_{i=1}^{i=N} |f_i' - f_i|}{\sum_{i=1}^{i=N} |f_i'|} \tag{2.2.34}$$

where $f = \{\zeta, u\}$, while f', and f respectively denote the solution at successive iterations.

2.2.2 Time differencing

The quantity F, defined by (2.2.28) includes time derivatives of the dependent variable u. These derivatives are evaluated employing time-differencing expressions consistent with the accuracy of the selected ABM scheme. As far as the predictor stage is concerned, we apply the following expressions

$$(u_t)_i^n = \frac{1}{2\Delta t}\left[3u_i^n - 4u_i^{n-1} + u_i^{n-2}\right] + O(\Delta t^2), \tag{2.2.35}$$

$$(u_t)_i^{n-1} = \frac{1}{2\Delta t}\left[u_i^n - u_i^{n-2}\right] + O(\Delta t^2), \tag{2.2.36}$$

$$(u_t)_i^{n-2} = -\frac{1}{2\Delta t}\left[3u_i^n - 4u_i^{n-1} + u_i^{n-2}\right] + O(\Delta t^2). \tag{2.2.37}$$

For the corrector stage, we evaluate u_t according to

$$(u_t)_i^{n+1} = \frac{1}{6\Delta t}\left[11u_i^{n+1} - 18u_i^n + 9u_i^{n-1} - 2u_i^{n-2}\right] + O(\Delta t^2), \tag{2.2.38}$$

$$(u_t)_i^{n} = \frac{1}{6\Delta t}\left[2u_i^{n+1} - 3u_i^n + 6u_i^{n-1} - u_i^{n-2}\right] + O(\Delta t^2), \tag{2.2.39}$$

$$(u_t)_i^{n-1} = -\frac{1}{6\Delta t}\left[2u_i^{n+1} - 3u_i^n + 6u_i^{n-1} - u_i^{n-2}\right] + O(\Delta t^2), \tag{2.2.40}$$

$$(u_t)_i^{n-2} = -\frac{1}{6\Delta t}\left[11u_i^{n+1} - 18u_i^n + 9u_i^{n-1} - 2u_i^{n-2}\right] + O(\Delta t^2). \tag{2.2.41}$$

Notice that the expressions reported above use the value of u at the time level $n+1$; this implies that during the iterative application of the corrector stage, the value of u_t, and therefore F at the four time levels has to be computed repeatidily. In order to speed up the computation we found useful storing at each time step the terms in F not containing time derivatives of u and adding to them the terms containing u_t at each iteration of the corrector expression.

2.2.3 Spatial differencing

The spatial derivatives appearing in E and F are computed by means of high order finite difference schemes in order to obtain estimates with truncation errors lower than the highest order dispersive terms in the governing equations. In the interior region of the domain central schemes can be applied while one-sided schemes are used to evaluate derivatives at the boundaries.

These scheme reads, for first order derivatives with respect to x,

$$(w_x)_1 = \frac{1}{12\Delta x}\left(-25w_1 + 48w_2 - 36w_3 + 16w_4 - 3w_5\right), \tag{2.2.42}$$

$$(w_x)_2 = \frac{1}{12\Delta x}\left(-3w_1 - 10w_2 + 18w_3 - 6w_4 + w_5\right), \tag{2.2.43}$$

$$(w_x)_i = \tfrac{1}{12\Delta x}\left[8\left(w_{i+1} - w_{i-1}\right) - \left(w_{i+2} - w_{i-2}\right)\right] \qquad (i = 3, 4, ..., N-2), \tag{2.2.44}$$

$$(w_x)_{N-1} = \frac{1}{12\Delta x}\left(3w_N + 10w_{N-1} - 18_{N-2} + 6w_{N-3} - w_{N-4}\right), \tag{2.2.45}$$

$$(w_x)_N = -\frac{1}{12\Delta x}\left(25w_N - 48w_{N-1} + 36_{N-2} - 16w_{N-3} + 3w_{N-4}\right) \tag{2.2.46}$$

where w is the variable to be differenced.

For second order derivatives, a three-point difference schemes is used:

$$(w_{xx})_i = \frac{w_{i+1} - 2w_i + w_{i-1}}{(\Delta x)^2}, \qquad (i = 2, 3, 4, ..., N-1) \tag{2.2.47}$$

2.2.4 Evaluation of u from the computed v

Once the value of v_i^{n+1} has been determined at each grid node ($i = 2, 3, ..., N-2, N-1$), a technique to solve the ordinary differential equation (2.2.29) is needed to compute the water velocity.

Equation (2.2.29) can be discretized using a three-point finite difference scheme for the second derivative of u and a simple two-point central finite difference scheme for the first derivatives to give:

$$v_i^{n+1} = A_i u_{i-1}^{n+1} + B_i u_i^{n+1} + C_i u_{i+1}^{n+1} \qquad \text{for} \qquad i = 2, 3, ..., N-2, N-1. \tag{2.2.48}$$

In which A, B, C are defined by:

$$\begin{aligned} A_i &= -\frac{d_i^2}{3\Delta x^2} + \frac{d_i (h_x)_i}{2\Delta x}, \\ B_i &= \left[1 - \frac{1}{2} d_i (h_{xx})_i\right] + \frac{2 d_i^2}{3\Delta x^2}, \\ C_i &= -\frac{d_i^2}{3\Delta x^2} - \frac{d_i (h_x)_i}{2\Delta x}. \end{aligned} \tag{2.2.49}$$

These $N-2$ equations form a tridiagonal system that can be solved to obtain u_i^{n+1} at all the grid points if u_1^{n+1} and u_N^{n+1} are specified. It is to be stressed that the velocity at the boundaries at the time step $n+1$ are requested by the numerical scheme and are the boundary conditions needed to solve the governing system of partial differential equations.

2.3 On using the Boussinesq equations in the swash zone: a note of caution

The behaviour of BTE models at the shoreward boundary of the domain of interest i.e. in the swash zone is discussed in this section. In order to illustrate problems and proposed solutions we make use of the high-order BTE model given by equations (2.2.22) and (2.2.23) (Veeramony and Svendsen 1999). As already mentioned we set to zero the parameter $\mathcal{B}$ and do not include additional terms which model energy dissipations caused by wave breaking.

In our firsts attempts of using these equations from intermediate waters up to the shoreline (see chapter 3) we run into numerical troubles when reaching the run-up region i.e. $x > 0$. These problems were essentially related to numerical instabilities due to the uncontrolled growth of the dispersive contributions (i.e. $O(\mu^2)-$terms). Such contributions govern the three-points central difference scheme used to solve the tridiagonal system obtained when adopting the numerical scheme described in the previous section, to advance the solution at the $i-$th node from the instant n to the instant $n+1$ (see section 2.2.4 for more details):

$$v_i^{n+1} = A_{i-1} u_{i-1}^{n+1} + B_i u_i^{n+1} + A_{i+1} u_{i+1}^{n+1} \tag{2.3.50}$$

where, if the original formulation (2.2.23) is used instead of (2.2.24)

$$\begin{aligned} A_i &= -\frac{h_i^2}{3\Delta x^2} + \frac{h_i (h_x)_i}{2\Delta x}, \\ B_i &= \left[1 - \frac{1}{2} h_i (h_{xx})_i\right] + \frac{2 h_i^2}{3\Delta x^2}, \\ C_i &= -\frac{h_i^2}{3\Delta x^2} - \frac{h_i (h_x)_i}{2\Delta x} \end{aligned} \tag{2.3.51}$$

are the equivalents of (2.2.49).

Since all the three coefficients contain h_i, the solution of this tridiagonal system depends on the size of h_i which is shoreward decreasing until the still shoreline is reached. Then, for $x > 0$ i.e. in the run-up region, h_i grows to reach a maximum value at the actual shoreline. This spurious behavior (we would expect pure dispersion to be zero in very shallow waters) makes the solution unstable. It is correct mentioning we were not the first to encounter difficulties in using BTE models in the swash. For example, Madsen et al. (1997) report: *"However, to make this technique* (i.e. the 'slot technique' for moving the shoreline) *operational in connection with Boussinesq type models a couple of problems call for special attention."*. They, however, took the following very pragmatic view: *"Firstly the Boussinesq terms are switched off at the still water shoreline, where their relative importance is extremely small anyway. Hence in this region the equations simplify to the nonlinear shallow water equations..."*.

On the other hand, we tried to solve the same problem in a different way i.e. forcing the dispersive terms which appear in the tridiagonal system of (2.3.50) to identically vanish at the shoreline. It is therefore obvious that the reference-dependent variable h had to be replaced by the more physically important total water depth d. With this aim in mind we re-wrote the model equations in the following slightly different but equivalent form:

$$\zeta_t + [du]_x = 0, \tag{2.3.52}$$

$$u_t + uu_x + g\zeta_x - \underbrace{\left[\frac{1}{3}d^2u_{xxt} + \frac{1}{2}dh_{xx}u_t + dh_xu_{xt}\right]}_{(I)}$$
$$- \underbrace{\left[\frac{1}{3}d^2uu_{xxx} - \frac{1}{3}d^2u_xu_{xx} + \frac{3}{2}dh_{xx}uu_x + \frac{1}{2}dh_{xxx}u^2 + dh_xuu_{xx} + d\zeta_xu_{xt} + h_x\zeta_xu_t\right]}_{(II)}$$
$$- \underbrace{\left[d\zeta_xuu_{xx} - d\zeta_xu_x^2 + \zeta_xh_{xx}u^2 + \zeta_xh_xuu_x\right]}_{(III)} = 0. \tag{2.3.53}$$

With this choice the coefficients A_i and C_i in (2.3.51) of the tridiagonal system (2.3.50), which for these new equations are given by (2.2.49), identically vanish at the actual shoreline hence allowing for a much more stable numerical solution while the coefficients B_i reduces to unity. Some very small spurious oscillations were still detectable due to the non-zero high-order dispersive-nonlinear terms. In order to better illustrate the role of dispersive and dispersive-nonlinear contributions near the shoreline we have performed a simple analysis which is presented in the next section.

2.3.1 Analysis and Discussion

The adopted BTE model contains contributions of order $O(\mu^2)$, $O(\delta\mu^2)$, $O(\delta^2\mu^2)$ and $O(\delta^3\mu^2)$. In order to illustrate the role of each term near the shoreline we have computed such contributions on the basis of a reference solution i.e. the only available analytical solution for periodic waves in the swash zone. This is the solution of (Carrier and Greenspan 1958). With this solution we do not have to rely on numerical computations of each contribution of equations governing equations. Such computations would always carry with them the uncertainties due to numerical errors and instabilities which could obscure the results. Rather, the Carrier and Greenspan analytical solution allows to directly and reliably estimate contributions to BTE equations under investigation.

We have performed a few computations but, to highlight what happens in the swash zone, we choose to show only that concerning the motion of a wave of dimensionless amplitude (hereafter stars characterize dimensionless quantities) $a_0^* = 0.5$ and dimensionless frequency $\omega^* = 1$. This non-breaking wave allows for a sufficiently wide swash zone the width of which being of $a_0^*\omega^*/2 = 0.25$ (see Brocchini and Peregrine 1996).

Before discussing the results we want to clarify that, due to the dimensionless definition of the total water depth:

$$d^* = h^* + \delta\zeta^* \tag{2.3.54}$$

the dimensionless form of the first bracket of equation (2.3.53), i.e. that denoted by (I), not only contains $O(\mu^2)$ terms but also $O(\delta\mu^2)$. Similarly, the second bracket [i.e. (II)] of the same equation contains both $O(\delta\mu^2)$ and $O(\delta^2\mu^2)$ terms, while the third [i.e. (III)] contains both $O(\delta^2\mu^2)$ and $O(\delta^3\mu^2)$ contributions. Notwithstanding this mixture of contributions we found it useful to compare the spatial distribution of the terms of the three brackets of equation (2.3.53) respectively with that of the $O(\mu^2)$, $O(\delta\mu^2)$ and $O(\delta^2\mu^2) + O(\delta^3\mu^2)$ terms of equation (2.2.23). These are reported, with the same order, in figures 2.3, 2.4 and 2.5, while figure 2.2 shows, for reference, the free surface position (i.e. the phase of the wave) and the sloping beach. The wave run-up/run-down motion is illustrated for the four following dimensionless times $t^* = 0, \pi/5, 3\pi/5, 4\pi/5$ on the panels (from left to right) of each figure. In each panel of figures 2.3, 2.4 and 2.5, the contributions coming from equation (2.3.53) are plotted with solid lines while those relative to equation (2.2.23) with dashed lines.

Notice that the comparison of the mixed-ordered brackets with the different order contributions to (2.2.23) is even more reasonable when considering that δ and μ are built with scales (still water depth, wave amplitude and wavelength) of the flow in the offshore region of the domain of interest. Hence, they are typical of shallow but *finite* water depths and are not suitable for describing the order of magnitude of the various contributions in the swash zone which is characterized by very thin sheets of water. To be more precise this inadequacy starts from the region in which h is a small contribution to d.

At a first glance (see figure 2.3) it is evident how the contributions of bracket (I) of equation (2.3.53) are almost equivalent to the $O(\mu^2)$ terms of equation (2.2.23). The largest discrepancies occur inside the swash zone. At the shoreline the $O(\mu^2)$ terms can be positive or negative depending on run-up/run-down phase. On the contrary the (I) contribution is always zero at the shoreline. As for the high-order contributions (see figures 2.4 and 2.5) the redistribution operated to get equation (2.3.53) is such that contributions (II) and (III) are characterized by smaller oscillations than the $O(\delta\mu^2)$ and $O(\delta^2\mu^2) + O(\delta^3\mu^2)$ terms. In order to fully illustrate the behaviour of these terms their spatial distribution has been shown over a larger distance from the shoreline (about one and a half wavelengths). It is clear that dispersive-nonlinear contributions are increasingly important while approaching the shoreline. Hence, in principle, they cannot be neglected. In particular the highest order term of figure 2.5 are almost zero at a distance of one wavelength from the undisturbed shoreline and abruptly grow to reach their maximum in the swash zone. This behaviour in the swash zone is such to require much care when computing dispersive-nonlinear terms up to the shoreline: high-order spatial derivative may easily introduce numerical instabilities and suitable techniques must be adopted to handle them (see chapter 3).

In summary we have shown one significant practical result: using d instead of h in the equations of BTE models leads to re-grouping terms in the form of equation (2.3.53). This is equivalent to equation (2.2.23) but better tractable from a numerical point of view. Notice that, though based

on a specific BTE model, most of the observations we have made are valid for a large number of high-order BTE models (also for the fully nonlinear models like those of Wei et al. 1995 and Madsen and Schäffer 1998). In fact all of them have to face the problem of treating high-order terms in the run-up region (i.e. for $x > 0$). Moreover, most of the available and currently used BTE models are numerically solved by the ABM scheme mentioned above (e.g. Wei et al. 1995; Skotner and Apelt 1999; Veeramony and Svendsen 2000 and others) which carries with it the problem of dealing with the coefficients of the tridiagonal system (2.3.50) for$x > 0$. One second result concerns quntification and illustration of the importance of the various dispersive-nonlinear contributions in very shallow waters on the basis of an analytical model solution.

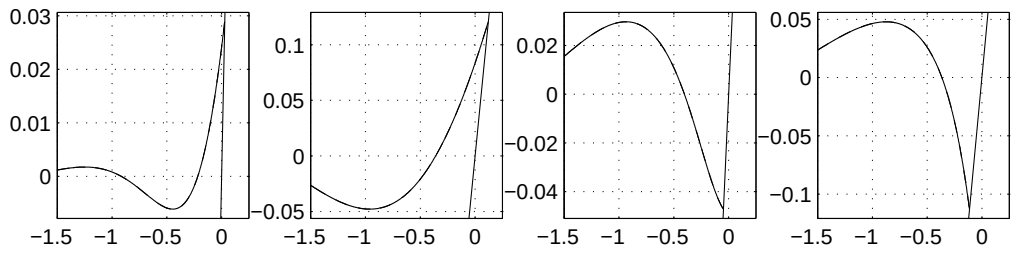

Figure 2.2: Free surface elevation plotted at different nondimensional times$t^* = 0, \pi/5, 3\pi/5, 4\pi/5$ versus the $x-$coordinate. The straight line represents the sloping beach.

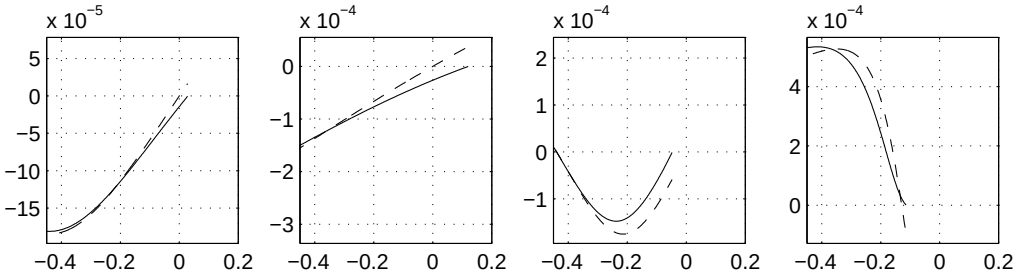

Figure 2.3: For the same times of figure 2.2 contributions of$O(\mu^2)$ to equation (2.2.23) are plotted with dashed lines versus the $x-$coordinate. Superposed with a solid line are the (I) contributions to equation (2.3.53).

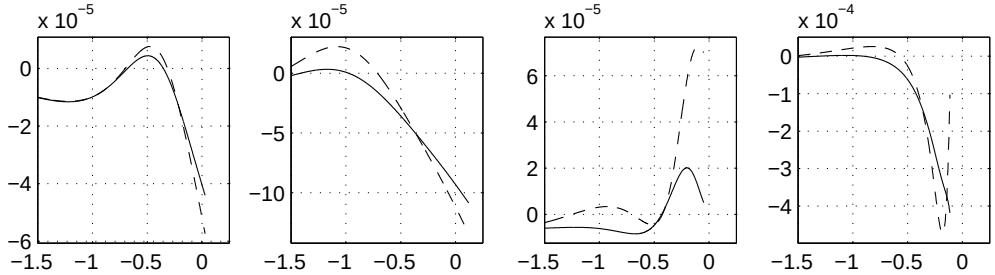

Figure 2.4: For the same times of figure 2.2 contributions of$O(\delta\mu^2)$ to equation (2.2.23) are plotted with dashed lines versus the $x-$coordinate. Superposed with a solid line are the (II) contributions to equation (2.3.53).

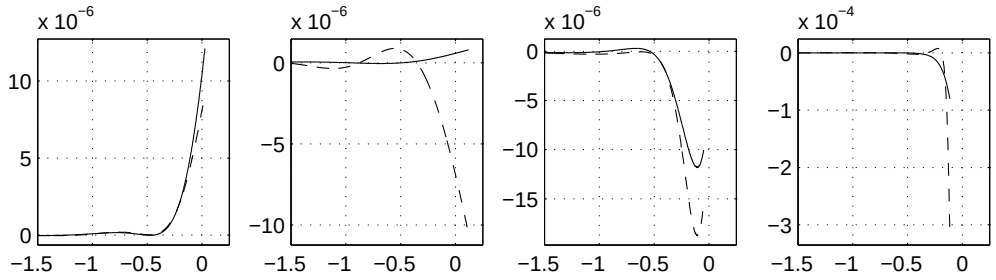

Figure 2.5: For the same times of figure 2.2 contributions of$O(\delta^2\mu^2)+O(\delta^3\mu^2)$ to equation (2.2.23) are plotted with dashed lines versus the $x-$coordinate. Superposed with a solid line are the (III) contributions to equation (2.3.53).

Chapter 3

A new shoreline boundary condition for Boussinesq-type models

3.1 Introduction

As already mentioned the most favoured approximate model equations for studying nearshore hydrodynamics are both the NSWE and the many available BTE which all stem from the work of Peregrine (1967).

BTE became very popular when it was proved they could model fairly well breaking waves (Brocchini et al. 1992; Schäffer et al. 1993). Subsequently, in order to make such equations more suitable for coastal engineering practice, dispersive characteristics were greatly improved extending their seaward limit to reach the so-called 'intermediate depths' (see Madsen and Schäffer 1998 and references therein).

Notwithstanding these important improvements, which recently made BTE models 'the models' for coastal engineering, flow solvers based on those equations suffer of a major problem. This is related to the mathematical/numerical treatment of both the swash motions and the delicate shoreline boundary conditions (Brocchini and Peregrine 1996).

To our knowledge no available solver based on BTE correctly models the shoreline motions and often *ad-hoc* artificial techniques are used to model wave run-up and run-down (see for example the 'slot technique' used by Madsen et al. 1997). The quest for good shoreline boundary conditions (SBCs hereinafter) to be implemented in BTE models is currently being pushed in a number of different directions. Recently new SBCs are being developed (Özkan-Haller and Kirby 1997) with the use of coordinate transformations which map the irregular shoreline to a straight line. Although a few examples are given which testify good performances some doubts can be reasonably raised on the effectiveness of such techniques in the case of heavily breaking waves which require strongly distorted transformations. This is more true for breaking waves which interact in the swash zone (e.g. backwash bores) as they generate cusps-like indentations at the shoreline which seem hardly representable by a smooth coordinate transformation. No artificial techniques are required when using the NSWE as model equations. NSWE are typically solved by means of the method of characteristics and the shoreline is a characteristic itself!

It is now becoming clear that better modelling is required of the SBCs employed in BTE models. To this purpose a number of methods can be applied a short list of which is here given as reference.

BTE-NSWE matching

This method, currently applied by some researchers, does not directly address the real problems concerning the definition of suitable SBCs. Rather, a pragmatic view is taken according to which purely dispersive BTE (i.e. with no extra nonlinear contributions, see section 2.3 for a discussion) reduce to NSWE in very shallow waters. Consequently a matching is imposed (depending on the local Ursell number) between BTE and NSWE solvers (Giarrusso 1998; Dodd and Giarrusso 2001). With this technique swash zone motions are always modelled by the NSWE module which properly handles the motion of the shoreline.

Extension of the NSWE to include dispersion

It is based on the view that NSWE are most suitable for modelling the swash zone motions and track the shoreline position. In order to extend the range of validity of the NSWE to the 'intermediate depths' suitable nonlinear-dispersive contributions can be included either into the flux term $\mathbf{F}_x$ or into the source term $\mathbf{S}$ of the model equation:

$$\mathbf{U}_t + \mathbf{F}_x = \mathbf{S} \tag{3.1.1}$$

used to cast the 1DH-NSWE in a typical conservation form to be solved for the variable$\mathbf{U}$ (Brocchini et al. 2001).

Characteristic-type SBCs for BTE

A third approach is here followed which is believed to both provide a close description of what actually happens at the point (line) where the water meets the beach face and to be easily implemented in any type of numerical models based on BTE. Analysis is underway to define the most suitable form of the SBCs (1DH flow propagation):

$$\frac{dx_s}{dt} = u_s, \qquad\qquad d_s = 0 \tag{3.1.2}$$

[x_s being the shoreline position, d_s and u_s respectively the water depth and the flow speed at the shore].

This chapter is organized as follows. A description of the problem to be solved and of the schematization adopted is given in section 3.2. A detailed analysis of the celerity at which the shoreline moves is given in section 3.3, where the 'shoreline Riemann problem' is introduced. The description and the implementation of the new shoreline boundary conditions in the model described in section 2.2 is detailed in section 3.4. Section 2.2 illustrates the specific BTE model which has been developed in order to evaluate the performance of the new SBCs. In section 3.5 the performances of the new SBCs and their implementation is verified by means of the comparison against well known analytical solutions. Some concluding remarks are given in the final section 3.6 along with a short description of ongoing research on this topic.

3.2 Problem statement

Our objective here is to derive a shoreline boundary condition suitable to be implemented in most commonly used numerical schemes for solving the Boussinesq type equations, i.e. finite differences schemes, working on fixed computational grids. In order to proceed a careful definition of the problem to be solved is needed. With reference to Figure 3.1, it can be noted that in the swash zone the water depth gradually decreases up to a point where it becomes zero. This point is commonly referred to as *the shoreline*. Notice that in the sketch reported in the figure it is assumed that a very smooth transition in the solution, i.e. in water depth and velocity, verifies. This is not the case when a bore is propagating on the beach or when a strong interaction between two waves, one running-up and one running-down the slope, occurs. Nevertheless the essence of the problem is not altered: it can always be recognized that there is a point where the transition between wet and dry conditions occurs: that point is *the shoreline*.

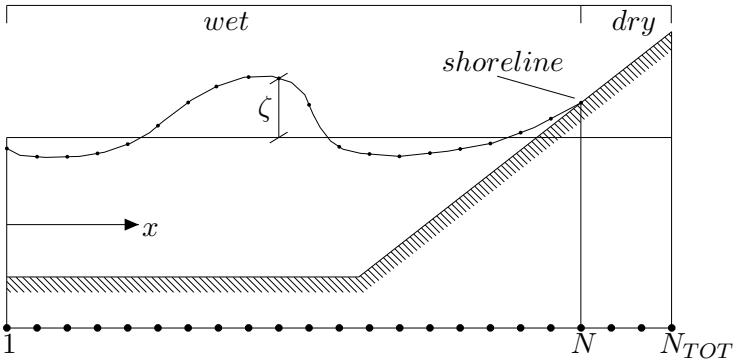

Figure 3.1: The computational domain.

If we look at the problem from a numerical point of view, a discrete representation of the physical conditions described above results. The solution, i.e. the value of both water depth and velocity, can be known only at the computational points and it is clear that an exact definition of the shoreline is no longer available. The shoreline is hence somewhere between the last wet node (N in the Figure) and the first dry node ($N+1$). In this work we assumed that if a small spacing between the nodes Δx is adopted, the shoreline can reasonably be considered to lay in the middle of the region $[x_N, x_{N+1}]$, where x_N and x_{N+1} are the abscissa of the two nodes N and $N+1$. The position of the shoreline x_s is hence defined as $x_s = x_N + \frac{\Delta x}{2}$.

By taking this view the computational domain is divided into two sub-domains as depicted in Figure 3.1. From node 1 to node N the nodes are wet and the governing equations are solved by means of a finite differences scheme as detailed in section 2.2. From node$N+1$ to node N_{tot} the nodes are dry. At the first and last wet nodes (i.e. 1 and N), suitable boundary conditions are to be specified in order to solve the problem (see section 2.2.4). Furthermore, by changing the value of N, i.e. by inundating and drying the nodes, the movements of the shoreline can be simulated.

It is now becoming clear that any swash zone modelling based on the conceptual scheme described above has to deal with two problems. The first one is the specification of water depth and velocity at the last wet node. These two values are the boundary conditions needed to solve

the system of partial differential equations. The second problem deals with the simulation of the shoreline movements: a technique is needed capable of deciding whether the wet region of the computational domain is to be enlarged (thus increasing the value of N simulating run-up) or restricted (decreasing N simulating run-down).

3.3 The shoreline Riemann problem

Different approaches can be used to model the motion of the shoreline on a beach. Until recently one of the most used was the “thin film approach" in which the whole computational domain is considered as “wet" but the thickness of the water is defined as “very small" in the region of the beach not reached by the motion of the waves. However, it can be demonstrated that such an approach leads both to a theoretically wrong solution and to great numerical inaccuracies. Hence we prefer to define and solve the motion of a genuine wet-dry interface.

In this section the ‘shoreline Riemann problem’ is introduced with the aim of investigating the celerity at which, according to the Boussinesq equation, the shoreline moves. As detailed in the previous section at the shoreline a transition occurs between a finite and a null value of the water depth. Hence a discontinuity of the solution verifies. A suitable theoretical approach for dealing with such a discontinuity originates from the method of the characteristics and is based on the solution of the so called Riemann problem (Toro 1997). In the following the conservative form of BTE, the generic and the *shoreline* Riemann problems are introduced. Finally the solution in the BTE framework is derived.

Let us first of all recognize that for small enough water depth most dispersive-nonlinear terms D which characterize BTE from NSWE become negligible. Hence near the shoreline we can write the 1DH version of any BTEs as:

$$d_t + (ud)_x = 0 \tag{3.3.3a}$$

$$u_t + uu_x + gd_x = gh_x - \tau_b + D, \tag{3.3.3b}$$

where $d = h + \zeta$ (see figure 3.2) is the total water depth, u is a depth-averaged velocity, τ_b is the seabed friction and subscripts are used to represent partial derivatives.

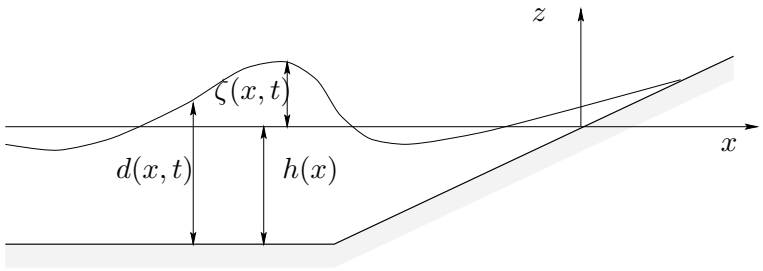

Figure 3.2: Sketch of typical problem geometry

These can be cast in suitable conservative vectorial form which is typically used in shock-capturing numerical solvers:

$$\mathbf{U}_t + \mathbf{F}(\mathbf{U})_x = \mathbf{S}(\mathbf{U}) \tag{3.3.4}$$

$\mathbf{U}$ being the vector of the unknowns, $\mathbf{F}$ the flux term and $\mathbf{S}$ the source term

$$\mathbf{U} = \begin{bmatrix} d \\ ud \end{bmatrix}, \qquad \mathbf{F}(\mathbf{U}) = \begin{bmatrix} ud \\ u^2 d + \frac{gd^2}{2} \end{bmatrix}, \qquad \mathbf{S}(\mathbf{U}) = \begin{bmatrix} 0 \\ gdh_x - d\tau_b + dD \end{bmatrix} \tag{3.3.5}$$

which also includes all dispersive-nonlinear contributions D which characterize each specific BTE.

The above mentioned Riemann problem is defined by equations (3.3.4), (3.3.5) and constant initial conditions (see figure 3.3a) such that:

$$\mathbf{U}(x,0) = \mathbf{U}_0(x) = \begin{cases} \mathbf{U}^L & \text{if } x < 0 \\ \mathbf{U}^R & \text{if } x > 0. \end{cases} \tag{3.3.6}$$

A very specific Riemann problem is the one in which the right constant state is dry. This helps to formulate and solve the transition which occurs at the shoreline (see figure 3.3b). A similar description was given by Stoker (1957) of the 'retreating piston' or 'retreating wave paddle' problem. We call the specific Riemann problem of figure 3.3b as the 'shoreline Riemann problem'.

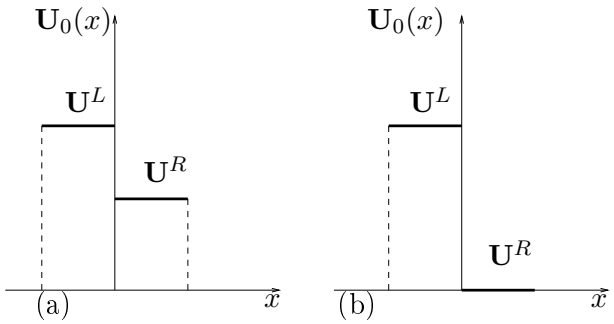

Figure 3.3: The Riemann problem. Illustration of the initial data for: (a) a generic Riemann problem, (b) the 'shoreline Riemann problem'.

In figure 3.4 the solution structure of a typical Riemann problem is shown. This is the well known 'dam break on a wet bed'. On the upper panel the initial configuration (time $t = 0$) of the free surface is shown; it can be noted that an abrupt variation of the water depth occurs at $x = x_0$. The velocity of the fluid is in this case equal to zero. At a generic time $t^\dagger > 0$ from the point $x = x_0$ two wave families emanate (see lower panel). For the specific case at hand the left wave family is a *rarefaction wave* and the right one is a *shock wave*.

Rarefaction waves, also indicated as *depressions*, connect two data states through a smooth transition. At any fixed time all flow quantities vary continuously across the wave. As depicted in the figure the wave has a fan like structure, centered at the origin. Rarefaction waves propagate in the deep water region (left in the figure) reducing the water depth. Shock waves, also known as *bores*, connect, through a single jump discontinuity, two constant data states. For the case reported in figure the shock wave propagates in the shallow water region (right) rising the water depth abruptly.

A simple, intuitive method for determining what kind of waves (weather rarefaction or shock) emanates from the original discontinuity is given here below, provided that an exact description of this mathematical problem can be found in a number of books (see for example Toro 1997). Given that the governing system of equations is hyperbolic, it can always be recognized that some

information on fluid motion travels along the characteristics curves. Two characteristics originate from each point in the $x-t$ space, one is termed *positive* or *advancing* characteristic (C_+) and one is termed *negative* or *receding* (C_-). In very shallow water the characteristic curves C_- and C_+ of (3.3.4) are:

$$\frac{dx}{dt} = \lambda_1 = u - c \qquad (C_-), \qquad\qquad \frac{dx}{dt} = \lambda_2 = u + c \qquad (C_+) \tag{3.3.7}$$

where $c = \sqrt{gd}$.

Subcritical flow states are characterized by the fact that the signs of λ_1 and λ_2 are discordant. The contrary occurs for supercritical flows, where the sign of λ_1 and λ_2 is equal. Now, compare the magnitude of the quantities λ_1^L and λ_1^R, where the superscripts indicate if the quantity refers to left (L) or right (R) states. It can be stated that left rarefaction waves are generated if $\lambda_1^L < \lambda_1^R$ and that left shock waves are generated if $\lambda_1^L > \lambda_1^R$. Furthermore right rarefaction waves are generated if $\lambda_2^L < \lambda_2^R$ and right shock waves are generated if $\lambda_2^L > \lambda_2^R$.

In the typical case shown in figure 3.4 the negative characteristics (notice that in this case $\lambda_1^L < \lambda_1^R$) originating from the left and from the right of the initial discontinuity, bound the left*fan* region. On the contrary the positive characteristics ($\lambda_2^L > \lambda_2^R$) collapse into a right shock waves.

In principle there are four possible wave patterns for a generic Riemann problem. These are depicted in the figure 3.5 where thick lines represent shock waves and the fans represent rarefactions. Case (a) is characterized by a left rarefaction wave and a right shock wave, case (b) by a left shock and a right rarefaction, case (c) by a left and right rarefaction and finally case (d) by left and right shock waves. The waves that originates from the initial discontinuity separate three constant states, indicated in figure 3.5 by $\mathbf{U}^L$, $\mathbf{U}^*$ and $\mathbf{U}^R$. The left ($\mathbf{U}^L$) and right ($\mathbf{U}^R$) states are known, being equal to the initial left and right initial conditions. The region in the middle of the wave families is indicated as the *cross region*. Water depth and velocity ($d^\dagger$ and $u^\dagger$) can be calculated by means of exact or approximate Riemann solvers (Toro 1997).

The 'shoreline Riemann problem' is in principle very similar. In this case (indicated in the NSWE framework as 'dry bed Riemann problem') only the left wave family originates from the initial discontinuity, being no medium in which the right wave can propagate. It can be demonstrated that this left wave is a rarefaction and the rightmost wave of the fan coincides with the instantaneous position of the shoreline (see figure 3.6).

The characteristic curves C_+ and C_- (Figure 3.6) are used to represent the solution structure for the problem of figure 3.3b) meet at the shoreline which can be considered as a C_--type characteristic such that:

$$\frac{dx}{dt} = \lambda_{1_s} = u_s - c_s, \qquad (C_-). \tag{3.3.8}$$

In this case the (x,t)-plane is subdivided into three regions which characterize the solution of the shoreline Riemann problem: region II is made of an expansion fan of C_--type characteristics connecting conditions of region I of left constant conditions $\mathbf{U}^L = (d^L, u^L d^L)$ with the dry conditions $\mathbf{U}^R = (d^R, u^R d^R) = (0,0)$ of region III.

Notice that along the C_- and C_+ characteristics Riemann variables $(\mathcal{R}_1, \mathcal{R}_2) = (u - 2c, u + 2c)$ are not conserved (as in the case of inviscid NSWE) because of the presence of non-zero source terms which also include dispersive-nonlinear contributions. On the contrary the following is valid:

$$\frac{d\mathcal{R}_1}{dt} = \mathcal{S} \quad \text{along} \quad C_-, \qquad\qquad \frac{d\mathcal{R}_2}{dt} = \mathcal{S} \quad \text{along} \quad C_+ \tag{3.3.9}$$

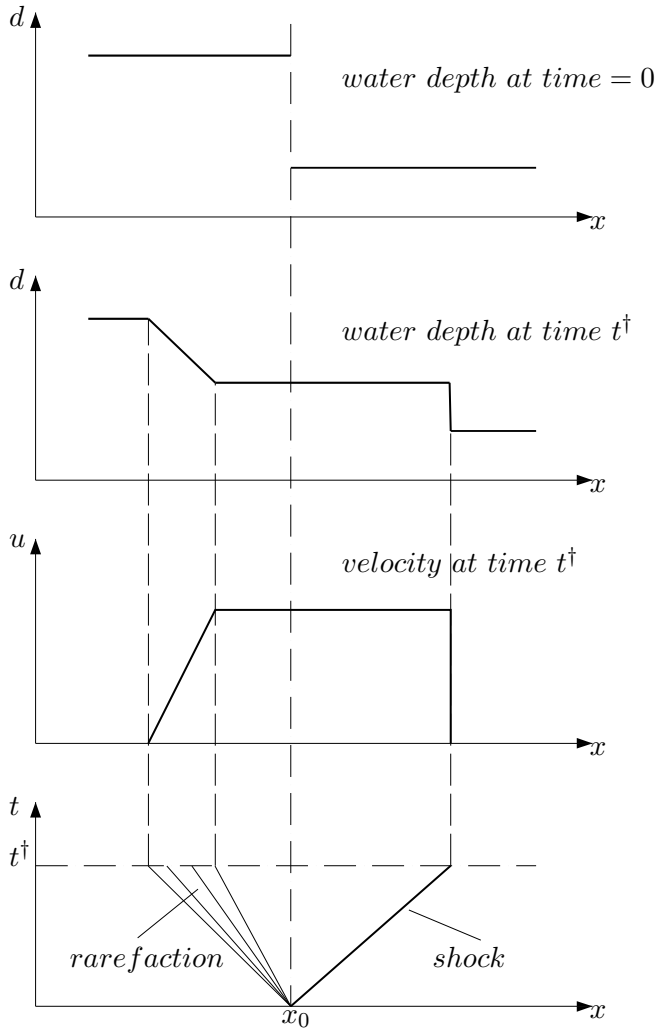

Figure 3.4: The generic Riemann problem.

where $\mathcal{S} = S_2/d = gh_x - \tau_b + D$.

It is, finally, essential to notice that SBCs are only a simplified version of:

$$\frac{dx_s}{dt} = u_s, \quad \text{or} \quad x_s = \int u_s \, dt, \tag{3.3.10a}$$

$$d_s = 0 \tag{3.3.10b}$$

and the purpose of any analyses dealing with SBCs is to suitably defineu_s which appears in (3.3.10a) by obeying the constraint (3.3.10b).

Following Brocchini et al. (2001) we compute u_s using conditions (3.3.9) in which $d_s = 0 \Longrightarrow$

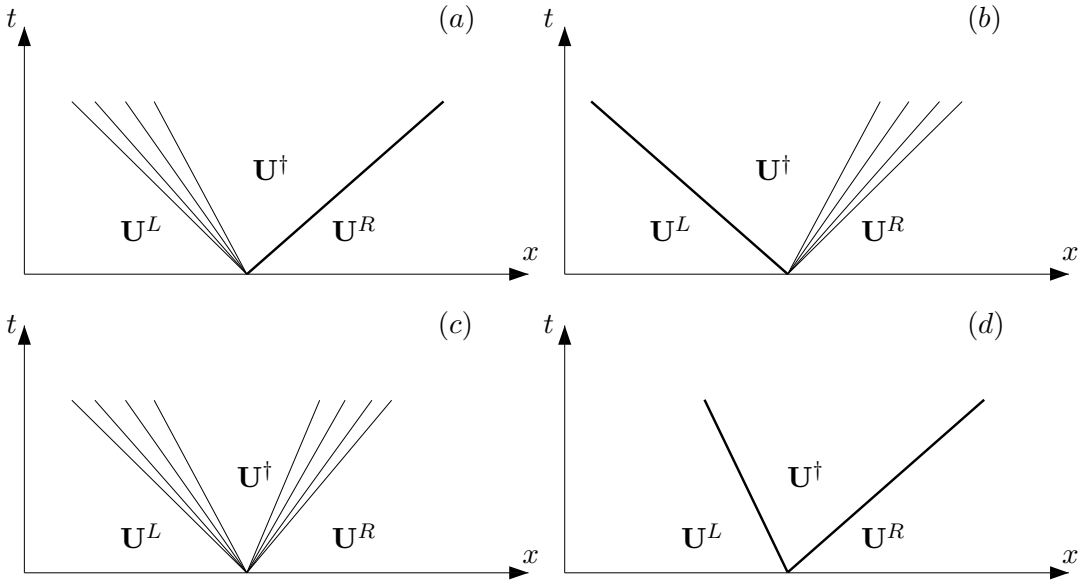

Figure 3.5: Possible wave patterns in the solution of the Riemann problem.

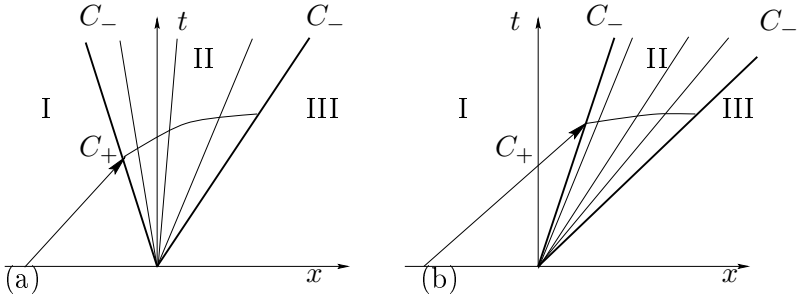

Figure 3.6: C_+ and C_- characteristic patterns used to solve the Riemann problem at the shoreline: (a) subcritical flow, (b) supercritical flow.

$c_s = \sqrt{gd_s} = 0$ is used on the C_- characteristic which represents the shoreline:

$$\frac{d\mathcal{R}_1}{dt} = \mathcal{S} \quad \text{along} \quad \frac{dx_s}{dt} = u_s, \tag{3.3.11a}$$

$$\frac{d\mathcal{R}_2}{dt} = \mathcal{S} \quad \text{along} \quad \frac{dx_s}{dt} = u^L + c^L. \tag{3.3.11b}$$

Integration of these gives

$$\mathcal{R}_1(t+\Delta t) = \mathcal{R}_1(t) + \int_t^{t+\Delta t} \mathcal{S}dt \quad \text{along} \quad \frac{dx_s}{dt} = u_s, \tag{3.3.12a}$$

$$\mathcal{R}_2(t+\Delta t) = \mathcal{R}_2(t) + \int_t^{t+\Delta t} \mathcal{S}dt \quad \text{along} \quad \frac{dx_s}{dt} = u^L + c^L \tag{3.3.12b}$$

where in this case $[\mathcal{R}_1(t), \mathcal{R}_2(t)] = [u_s - 2c_s, u^L + 2c^L] = [u_s, u^L + 2c^L]$.

Substitution into equations (3.3.12) and knowledge of the integration path gives

$$\mathcal{R}_1(t+\Delta t) = u_s(t) + \int_{x/u_s}^{(x+\Delta x)/u_s} \frac{\mathcal{S}}{u_s}\, dx, \tag{3.3.13a}$$

$$\mathcal{R}_2(t+\Delta t) = u^L(t) + 2c^L(t) + \int_{x/(u^L+2c^L)}^{(x+\Delta x)/(u^L+2c^L)} \frac{\mathcal{S}}{u^L+2c^L}\, dx. \tag{3.3.13b}$$

Notice that particular attention should be taken to evaluate integral contributions for small velocity values. At the shoreline this only occurs when at the maximum run-up and run-down locations.

At the shoreline the above conditions are simultaneously valid (see figure 3.6) hence giving the final result

$$u_s(t) = u^L(t) + 2c^L(t) + \int_{x/(u^L+2c^L)}^{(x+\Delta x)/(u^L+2c^L)} \frac{\mathcal{S}}{u^L+2c^L}\, dx - \int_{x/u_s}^{(x+\Delta x)/u_s} \frac{\mathcal{S}}{u_s}\, dx \tag{3.3.14}$$

which replaces the condition

$$u_s(t+\Delta t) = u^L(t) + 2c^L(t) \tag{3.3.15}$$

valid for NSWE.

In the case of inviscid BTEs (i.e. with no seabed friction included) with purely dispersive extra contributions, $D \to 0$ in very shallow depths and the source term reduces to the acceleration due to the beach slope. Therefore (3.3.15) can suitably be used to evolve the shoreline positionx_s in time through (3.3.10a) if either a splitting technique is used for such term (Brocchini et al. 2001) or the coordinate transformation by Watson et al. (1992) is adopted. On the other hand, if$D$ also contains nonlinear-dispersive terms (see section 2.3 for proper treatment of these terms) equation (3.3.14) replaces (3.3.15).

3.4 Implementation of characteristic type SBCs

In section 3.3 the fluid velocity u_s^{n+1} at the interface between wet and dry states was obtained by solving the 'shoreline Riemann problem'. Now, in order to employ this solution as a boundary condition for the BTE model, it should clarified what is the difference (if any) betweenu_s^{n+1} and u_N^{n+1}, that is the boundary condition for the BTE model.

We can state that by assuming $u_N^{n+1} = u_s^{n+1}$ unrealistic and numerically unstable solutions are obtained by the BTE model. The reason is that u_s is the velocity of the fluid at a specific point (the shoreline) of the computational domain, whileu_N^{n+1} should be representative of flow conditions in the region $[x_N - \frac{\Delta x}{2}, x_N + \frac{\Delta x}{2}]$.

A numerical technique to evaluate u_N^{n+1} from u_s^{n+1} is therefore needed. The basic assumption we start from is that u and ζ are piece-wise constant over the three regions $[x_i - \frac{\Delta x}{2}, x_i + \frac{\Delta x}{2}]$, $i = N-1, N, N+1$, hereinafter referred to as 'computational cells'. The quantitiesu_{N-1}^n, u_N^n and u_{N+1}^n can therefore be viewed as integral averages of the solution$u(x)^n$, namely

$$u_i^n = \frac{1}{\Delta x} \int_{x_{i-\frac{1}{2}}}^{x_{i+\frac{1}{2}}} u(x)^n dx. \tag{3.4.16}$$

Now a suitable numerical method is to be chosen in order to evaluate u_N^{n+1} starting from piece-wise constant initial conditions as depicted in figure 3.8. It is necessary that the method can adequately deal with solution discontinuities (between cells $N-1$ and N) and treat the wet-dry interface between cells N and $N+1$ by taking the most from the accurate analysis performed in section 3.3. Brocchini and co-workers (Brocchini et al. 2001) showed that a NSWE nearshore flow solver based on the WAF (Weighted Averaged Flux) method can accurately simulate swash zone flows and shoreline motions. The WAF method is therefore adopted in the present study as the numerical tool to evaluate u_N^{n+1}, i.e. the boundary condition of the BTE model. It is to be stressed that this method is here merely used to convert the 'real' velocity value u_s into the 'numerical' value u_N^{n+1}.

3.4.1 A WAF technique to move the shoreline

The WAF method is used to solve the conservative form of the NSWE. First, concentrate on the homogenous form of equations (3.3.4) which is identical to the NSWE homogeneous problem for horizontal bottom

$$\mathbf{U}_t + \mathbf{F}(\mathbf{U})_x = 0. \tag{3.4.17}$$

These equations can be integrated in a rectangular region of the $x-t$ space (see figure 3.7) in order to obtain a weak form. Using Green's theorem:

$$\oint [\mathbf{U}dx - \mathbf{F}(\mathbf{U})dt] = 0. \tag{3.4.18}$$

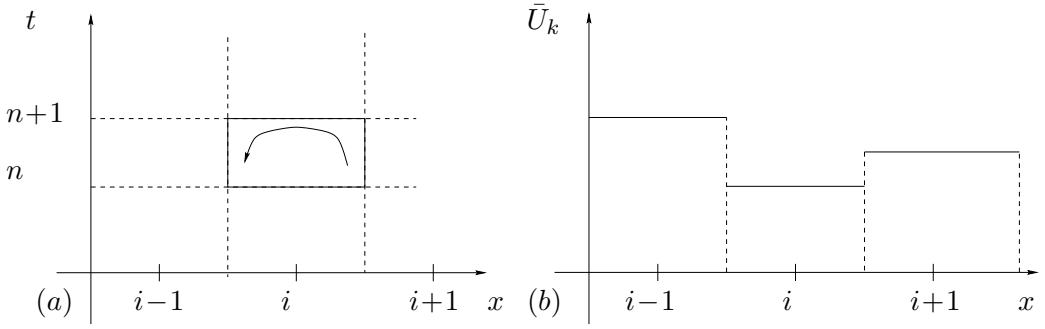

Figure 3.7: Variables representation on a discretized domain: anticlockwise integration of (3.4.18) on a discretized $x-t$ space, (b) discrete solution behaviour.

These equations can be solved on a staggered grid as depicted in figure 3.7 if written in the following discrete form:

$$U_{k_N}^{n+1} = U_{k_N}^{n} + \frac{\Delta t}{\Delta x}\left[F_{k_{N-\frac{1}{2}}}^{n+\frac{1}{2}} - F_{k_{N+\frac{1}{2}}}^{n+\frac{1}{2}}\right],\ k = 1, 2 \tag{3.4.19}$$

where $F_{k_{N-\frac{1}{2}}}^{n+\frac{1}{2}}$ and $F_{k_{i+\frac{1}{2}}}^{n+\frac{1}{2}}$ are the intercell fluxes at the time level $n+\frac{1}{2}$.

u_N^{n+1} can be obtained by time-stepping the solution applying equation (3.4.19) once the fluxes between cells given by

$$F_{k_{N-\frac{1}{2}}}^{n+\frac{1}{2}} = \frac{1}{\Delta x}\int_{x_{N-1}}^{x_N} F_k\left(\mathbf{U}^{n+\frac{1}{2}}(x)\right)dx,\quad F_{k_{N+\frac{1}{2}}}^{n+\frac{1}{2}} = \frac{1}{\Delta x}\int_{x_N}^{x_{N+1}} F_k\left(\mathbf{U}^{n+\frac{1}{2}}(x)\right)dx,\quad k = 1,\ 2 \tag{3.4.20}$$

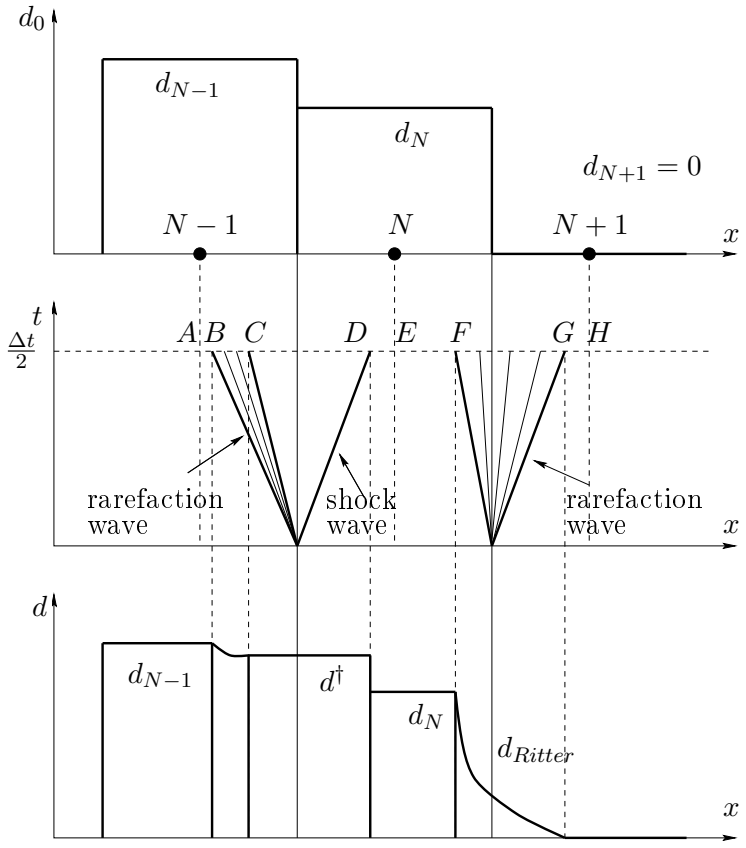

Figure 3.8: Example of solution of the 'shoreline Riemann problem'. Only the problem for the $U_1 = d$ component is illustrated. Top: the piece-wise initial condition. Middle: the solution structure in the $(x,t)-$plane. Bottom: solution of the Riemann problem in the physical space.

have been suitably evaluated (e.g. Toro 1992; Toro 1997). Notice that (3.4.20) coincide with averages of the fluxes over the regions around the boundaries of each cell. From a practical point of view, the fluxes are evaluated by performing a weighted average, from which the name of the present method.

In order to evaluate the integrals in equation (3.4.20), a technique to estimate the value of the variables at time level $n+1/2$ is required. This technique is entirely based on the solution of the Riemann problem, detailed in the previous section. In particular, at any given time level the variables U_k have a piece-wise constant distribution and a Riemann problem in which the initial data is made of a pair of constant states can be formulated. The value of$U_k(x, t^{n+1/2})$ over the whole computational cell is therefore preliminarily calculated and then the fluxes between cells are obtained by means of equation (3.4.20).

Once the Riemann problems are solved, i.e. the state$\mathbf{U}^\dagger$ and the speed of the waves are known, the fluxes between the computational cells can be evaluated by means of following procedure (the WAF method). The first step is to decompose the two regions of widthΔx between nodes $N-1$ and N and between nodes N and $N+1$ in a number of segments, namely AB, BC, CD, DE, EF,

FG and GH (refer to middle panel of figure 3.8). For the specific case shown in figure 3.8, which consist of a left rarefaction wave and a right shock wave emanating from the wet-wet interfaces, the length of the segments can be evaluated by means of the following expressions:

$$\begin{aligned}
\overline{AB} &= \tfrac{\Delta x}{2} + \tfrac{\Delta t}{2}\lambda_h^l, \\
\overline{BC} &= \tfrac{\Delta t}{2}\left(\lambda_h^l - \lambda_t^l\right), \\
\overline{CD} &= \tfrac{\Delta t}{2}\left(\lambda^r - \lambda_t^l\right), \\
\overline{DE} &= \tfrac{\Delta x}{2} - \tfrac{\Delta t}{2}\lambda^r, \\
\overline{EF} &= \tfrac{\Delta x}{2} + \tfrac{\Delta t}{2}\lambda_1, \\
\overline{FG} &= \tfrac{\Delta t}{2}\left(\lambda^s - \lambda_t^s\right).
\end{aligned} \tag{3.4.21}$$

Where λ_h^l and λ_t^l are respectively the celerity of the head and of the tail of the fan of the left rarefaction wave. Since the right wave is a shock, a single speed $\lambda^r \equiv \lambda_h^r \equiv \lambda_t^r$ has been used for the right wave, but the generalization to the case in which the right wave is a rarefaction or the left one is a shock is straightforward. Notice that in the case under investigation (see figure 3.8) the speeds λ_h^l and λ_t^l are negative. Definitions (3.4.20) can therefore be approximated by

$$F_{k_{N-\frac{1}{2}}}^{n+\frac{1}{2}} = \frac{1}{\Delta x}\left[F_k(\mathbf{U}_{N-1})\overline{AB} + F_k(\mathbf{U}_{rarefact})\overline{BC} + F_k\left(\mathbf{U}^\dagger\right)\overline{CD} + F_k(\mathbf{U}_N)\overline{DE}\right] \tag{3.4.22}$$

$$F_{k_{N+\frac{1}{2}}}^{n+\frac{1}{2}} = \frac{1}{\Delta x}\left[F_k\left(\mathbf{U}_N\right)\overline{EF} + F_k\left(\mathbf{U}_{Ritter}\right)\overline{FG}\right] \tag{3.4.23}$$

where $\mathbf{U}_{rarefact}$ is a state representative of the value of the variables within the head and the tail of the rarefaction wave and $\mathbf{U}_{Ritter}$ is Ritter's solution (see Stoker 1957). Equation (3.4.22) is found to be accurate even if a rough estimate of $\mathbf{U}_{rarefact}$ is provided, for example by assuming $\mathbf{U}_{rarefact} = (\mathbf{U}_{N-1} + \mathbf{U}^\dagger)/2$ (Toro 1997). This is due to the fact that the segment BC is usually much smaller than AB, CD and DE.

Numerical tests have revealed that the flux given by equation (3.4.23) is very sensitive to the definition of $\mathbf{U}_{Ritter}$. The integral average over the segment FG should therefore be performed adopting a more accurate integration method on the basis of Ritter's solution. It turns out that the trapezoidal rule provides satisfactory estimate of the exact integral; the final expression adopted for $F_{k_{N+\frac{1}{2}}}^{n+\frac{1}{2}}$, $k = 1,\ 2$ reads

$$F_{k_{N+\frac{1}{2}}}^{n+\frac{1}{2}} = \frac{1}{\Delta x}\left[F_k\left(\mathbf{U}_N\right)\overline{EF} + F_k^b\overline{FG}\right] \tag{3.4.24}$$

where F_k^b is given by

$$F_k^b = \frac{1}{4}F_k\left(d^L, u^L\right) + \frac{1}{2}F_k\left(d_r, u_r\right) + \frac{1}{4}F_k\left(0, u_s\right) \tag{3.4.25}$$

in which d_r and u_r are the fluid depth and velocity at the center of the rarefaction fan. Note that equation (3.4.25) is the expression of the trapezoidal rule adopted for the integration in the region where Ritter's solution holds.

In order to solve equations (3.3.4), which differ from (3.4.17) because of the presence of the source terms, we follow the approach of Watson et al. (1992). These authors proposed a technique based on the incorporation of the source terms into the Riemann problem. The idea is to transform

the problem into a reference frame with horizontal acceleration equal to $g\alpha - D$, where α is the bottom slope assumed to be constant in each cell and D are the dispersive-nonlinears terms. This transformation gives a set of homogenous equations that can be solved as described before. Then, by means of a reverse transformation, the solution is obtained in the original reference frame. Note however that D, unlike $g\alpha$, is not constant over each cell since its value depends on both the water depth and the velocity. To overcome this undetermination, D is assumed to be constant over Δt, given that this value is computed at the beginning of the time step.

The new variables in the accelerating reference frame are

$$\begin{aligned} \xi &= x + \tfrac{1}{2}(g\alpha - D)\,t^2, \qquad & \tau &= t, \\ v &= u + (g\alpha - D)\,t, & \varsigma &= d. \end{aligned} \tag{3.4.26}$$

If these new variables are substituted into (3.3.4) a set of homogenous equations, formally identical to (3.4.17) is obtained. Once the solution is found in the accelerating frame, the reverse transformation yields the following relations between (3.4.26) and the original variables

$$\begin{aligned} u(x,t) &= v\left[x + \tfrac{1}{2}(g\alpha - D)\,t^2, t\right] - (g\alpha - D)\,t, \\ d(x,t) &= \varsigma\left[x + \tfrac{1}{2}(g\alpha - D)\,t^2, t\right]. \end{aligned} \tag{3.4.27}$$

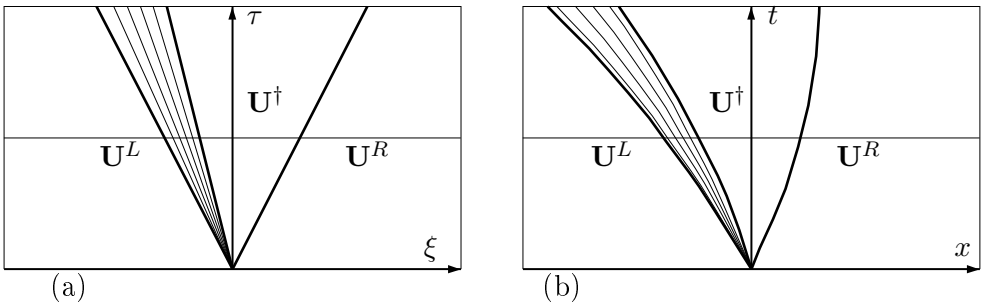

Figure 3.9: Riemann problem solution in the accelerating (a) and in the stationary (b) reference frames.

The structure of the solution of the Riemann problem in the case of a left rarefaction and a right shock wave is shown in figure 3.9. The solution in the accelerating (panel a) reference frame is identical to the solution of equations (3.4.17) while in the stationary frame (panel b) the trajectory of each wave is no longer a straight line but turns into a parabola.

From a practical point of view, in order to apply the WAF method, the quantity $\frac{1}{2}(g\alpha - D)\,\Delta t$ must be subtracted from all the velocities and, in evaluating the weights of each flux, it is to be considered that the solution is shifted in x by a constant amount $\frac{1}{2}(g\alpha - D)\left(\frac{1}{2}\Delta t\right)^2$.

Equation (3.4.19), modified to take into account source terms effects reads

$$U_{k_N}^{n+1} = U_{k_N}^{n} + \frac{\Delta t}{\Delta x}\left[F_{k_{N-\frac{1}{2}}}^{n+\frac{1}{2}} - F_{k_{N+\frac{1}{2}}}^{n+\frac{1}{2}}\right] + S_N^{n+\frac{1}{2}}\Delta t, \quad k = 1, 2 \tag{3.4.28}$$

where

$$\mathbf{S}(\mathbf{U}) = \begin{bmatrix} 0 \\ -gd\alpha + dD \end{bmatrix}. \tag{3.4.29}$$

[Notice that in the original work (Watson et al. 1992) because of a typographical error an incorrect expression for $\mathbf{S}(\mathbf{U})$ is reported on equation 3.4.29.]

Finally, the technique to change the value of N during the run-up phase is based on the volume of fluid entering the dry cell $N+1$ at each time step. An estimate of this volume can be obtained by applying the WAF method to the cell $N+1$. The expression (3.4.28) reads in this case:

$$U_{k_{N+1}}^{n+1} = \frac{\Delta t}{\Delta x}\left[F_{k_{N+\frac{1}{2}}}^{n+\frac{1}{2}}\right] + S_{N+1}^{n+\frac{1}{2}}\Delta t, \quad k = 1,2 \tag{3.4.30}$$

since $U_{k_{N+1}}^{n} = 0,\ k = 1,2$ and $F_{k_{N+\frac{3}{2}}}^{n+\frac{1}{2}} = 0\ , k = 1,2.$

If $d_{N+1}^{n+1}\Delta x$ is greater than a threshold value the cell is inundated and at the following time step the new value of $N = N+1$ is employed.

During the run-down phase a simpler technique provides good results. This is based on the use of the water depth at node N: if d_N^{n+1} is lower than a threshold value at the following time step the new value of $N = N-1$ is employed.

Note that in this work run-up and run-down phases were defined on the basis of flow direction at node $N-1$ at the time level n: $u_{N-1}^n > 0$ defines run-up, $u_{N-1}^n < 0$ run-down.

3.4.2 The basic steps of the proposed procedure

Let us now briefly summarize the basic steps required to apply the proposed procedure. Assume that the dependent variable d and u are known over the computational grid at time level n. The objective is to compute u_N^{n+1} and d_N^{n+1} which are the boundary conditions for the wave solver. The first step is to solve the Riemann problems at the interfaces between cells $N-1$, N and $N+1$. On the basis of the solution of the Riemann problems the fluxes at the interfaces of the cell N are estimated by means of equations (3.4.22) and (3.4.24). Once the fluxes are known, the solution at node N is updated by applying equation (3.4.28). At this point, the model checks if at the subsequent time step the value of N is to be changed, i.e. if the shoreline is to be moved. This can occur either in the form of run-up when the volume of water in the cell $N+1$ is larger than the chosen threshold and the same cell is inundated becoming part of the computational domain or in form of run-down when the depth in the cell N is lower than the threshold and the cell is removed from the computational domain becoming a dry cell.

3.5 Performance evaluation of the BTE model with the new SBCs

A number of tests are here reported to help the reader evaluate the performances of the implementation of the new SBCs (section 3.4) in the BTE model described in section 2.2.

Analytical solutions are the most suitable for evaluating the performances of the implemented SBCs as they represent an exact benchmark. We here consider three important analytical solutions for waves propagating over a uniform sloping beach. They respectively model the run-up due to a depression of the water level (the fluid held motionless) which is suddenly released (the 'Carrier and Greenspan's run-up solution', Carrier and Greenspan 1958), the run-up and run-down characteristic of a periodic wave travelling shoreward and being reflected out to sea (the 'Carrier and Greenspan's standing wave solution', Carrier and Greenspan 1958) and the run-up of a solitary wave (the 'Synolakis run-up solution', Synolakis 1987).

3.5.1 The Carrier and Greenspan run-up solution

This test corresponds to the physical problem in which the water level at the coastline of a plane uniform beach is depressed, the fluid held motionless and then released. It also represents the most classical test conditions for assessing the quality of any run-up solver.

Carrier & Greenspan (1958) used a hodograph transformation to solve the NSWE and obtained an analytical solution of this problem. The transformation makes use of two dimensionless variables (σ^* ıless ordinary
var s:

$(3.5.31a)$

$(3.5.31b)$

wh roblem under
inv

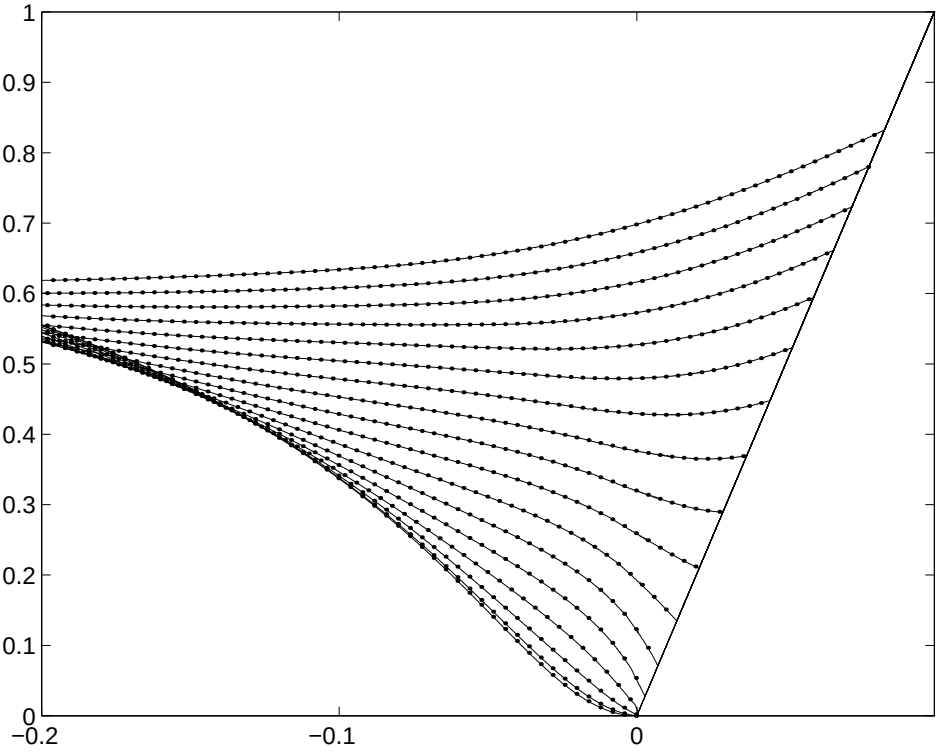

Figure 3.10: The 'Carrier & Greenspan run-up test' on a uniform plane beach. Dimensionless, scaled, analytical (dotted lines) and numerical (solid lines) profiles of water elevationζ^* are plotted versus the dimensionless onshore coordinate x^* at dimensionless times increasing of $\Delta t^* = 0.05$ from $t^* = 0.00$ (bottom curves) to $t^* = 0.80$ (top curves).

The 'run-up solution' is specified by the following initial conditions at $t^* = 0$

$$\zeta^* = \epsilon \left[1 - \frac{5}{2} \frac{a^3}{(a^2 + \sigma^{*2})^{3/2}} + \frac{3}{2} \frac{a^5}{(a^2 + \sigma^{*2})^{5/2}} \right], \tag{3.5.32a}$$

$$u^* = 0, \tag{3.5.32b}$$

$$x^* = -\frac{\sigma^*}{16} + \epsilon \left[1 - \frac{5}{2} \frac{a^3}{(a^2 + \sigma^{*2})^{3/2}} + \frac{3}{2} \frac{a^5}{(a^2 + \sigma^{*2})^{5/2}} \right] \tag{3.5.32c}$$

where $a = 3/2(1 + 0.9\epsilon)^{1/2}$ and ϵ is a nonlinearity parameter.

Further details on both initial conditions and the analytical solution can be found in the original work of Carrier & Greenspan.

In figure 3.10, which is the equivalent of figure 7 of (Carrier and Greenspan 1958), the analytical solution ζ^*/ϵ versus the onshore coordinate x^* is shown by means of dotted lines for different adimensional times. On the other hand, solid lines pertain to the numerical results while the thicker line represents the sloping seabed. It is evident that an excellent matching exists between the analytical and the numerical solution. It is also worth underlying that no spurious oscillations are present near the shoreline. Any oscillatory behaviours would reveal two possible sources of errors:

- a bad implementation of the SBCs in the chosen BTE model;
- a bad implementation of the 'wetting-drying' procedure.

On the contrary, the smooth behaviour of the elevation profiles of figure 3.10 testifies the absence of such problems.

3.5.2 The Carrier and Greenspan standing wave solution

This solution of the NSWE represents the motion of a wave of dimensionless amplitude A^* and dimensionless frequency ω^* travelling shoreward and being reflected out to sea generating a standing wave (Carrier and Greenspan 1958). In the past it has been widely used to analyze the dynamics of water waves approaching a coast or a continental shelf (Carrier 1966; Carrier 1971).

Such a solution can be specified by means of the following potential function:

$$\phi^*(\sigma^*, \lambda^*) = A^* J_0(\omega^* \sigma^*) \cos(\omega^* \lambda^*) \tag{3.5.33}$$

where J_0 is the Bessel function of the first kind.

Once (3.5.33) is substituted into (3.5.31) a solution can be found for all the flow properties of interest in the ordinary $(x^*, t^*)-$space. Such a solution has been obtained both analytically and numerically for the case $A^* = 0.6$ and $\omega^* = 1$ (non-breaking wave).

In figure 3.11 both profiles of the numerically-computed free surface elevation and the envelope of the analytically-derived surface elevations are reported. The figure reveals an almost perfect agreement between analytical and numerical solutions. Again, the absence of any oscillations in the numerical solution is particularly satisfying.

The comparison can also be pushed forward to analyze any possible differences in the horizontal motion of the shoreline. This is reported in figure 3.12 in which a dotted line is used to represent the analytical solution while the solid line gives the numerical shoreline. Apart from a very

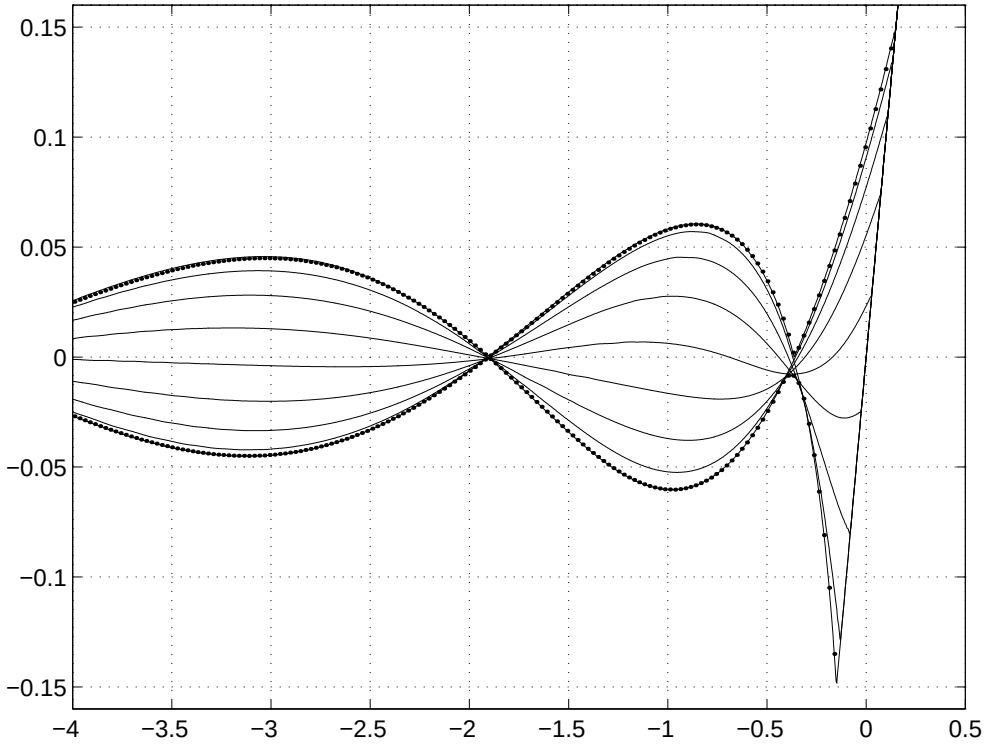

Figure 3.11: The 'Carrier & Greenspan standing wave test' on a uniform plane beach: envelope of surface elevations. Envelope of the dimensionless, analytical solution by Carrier & Greenspan (dotted lines) and numerical (solid lines) profiles of water elevation ζ^* are plotted versus the dimensionless onshore coordinate x^*.

small underestimation at the peak of the run-up (which could be fixed by increasing the spatial discretization) the numerical solution perfectly matches the analytical one. This does not happen when employing artificial techniques like the slot-technique (Madsen et al. 1997) which always introduce a loss of mass (revealed by a reduced swash amplitude). The agreement is even more remarkable in view of the structure of the proposed SBCs which does not depend on any calibration parameters.

3.5.3 The Synolakis run-up solution

Synolakis' solution (Synolakis 1987) is one of the very few available analytical solutions for the run-up of a solitary wave (a similar solution is also available for the interactions of solitary waves in shallow waters, see Brocchini 1998). Such an equations has been obtained in the framework of the NSWE but has been shown to model very well beach inundation conditions caused by solitary waves.

In Synolakis' solution a solitary wave of dimensionless height H^* centered at a distance X_1^* from

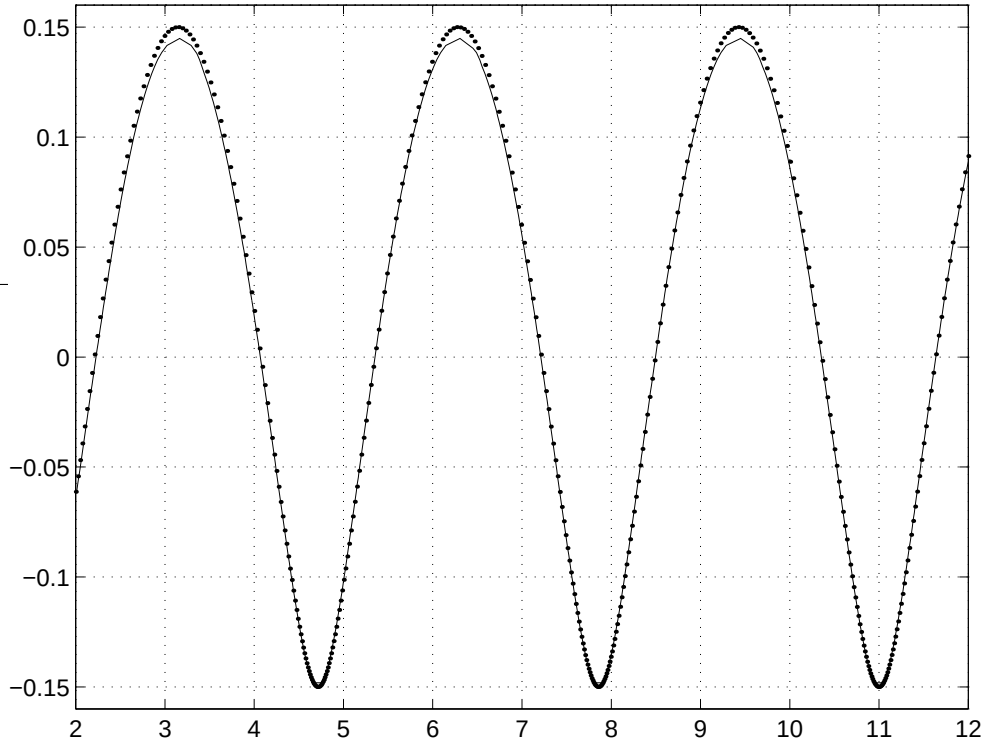

Figure 3.12: The 'Carrier & Greenspan standing wave test' on a uniform plane beach: horizontal motion of the shoreline. Incident wave of dimensionless amplitude $A^* = 0.6$ and dimensionless frequency $\omega^* = 1$. Dimensionless analytical shoreline path as from Carrier and Greenspan (1958) (dotted line) and numerical shoreline path (shoreline line) in time.

the shore at time $t^* = 0$:

$$\zeta^* = \frac{H^*}{d^*}\mathrm{sech}^2[\gamma(x^* - X_1^*)], \quad \text{where} \quad \gamma = \sqrt{3H^*/4d^*} \tag{3.5.34}$$

is propagated over a combined topography made of a plateau of depthd^* and a plane sloping beach of slope β; matching of the two regions occurs at $x^* = X_0^* = \cot\beta$ (see figure 3.13) .

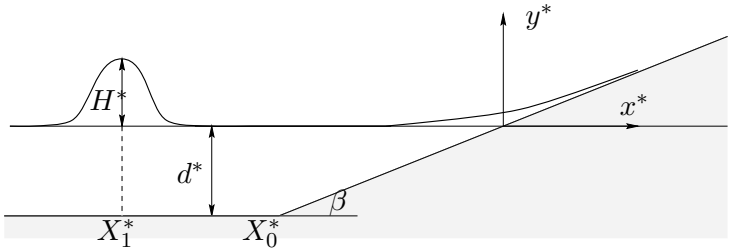

Figure 3.13: Definition sketch for the initial condition of Synolakis' run-up solution.

Propagation of the above signal by means of the NSWE is more easily modelled if Carrier

& Greenspan's (Carrier and Greenspan 1958) hodograph transformation and a Fourier transform technique are used in combination. This brings to the following definition forϕ^*:

$$\phi^*(\sigma^*,\lambda^*) = -\frac{32i}{3}\int_{-\infty}^{\infty} \mathrm{cosech}(\xi k^*)\frac{J_0(k^*\sigma^* X_0^*/2)e^{ik^*\theta}}{J_0(2k^*X_0^*) - iJ_1(2k^*X_0^*)}dk^* \tag{3.5.35}$$

where $\xi = \pi/2\gamma$ and $\theta = X_1^* - X_0^* + \lambda^* X_0^*/2$ is the pulse phase.

We refer the reader to Synolakis (1987) for a detailed description of the solution.

We used such a solution to illustrate the model performances to reproduce the run-up of a solitary wave. More specifically we have tried to reproduce Synolakis' results given in his figure 6. This summarizes the comparison of the analytical solution and experimental data in the case of solitary wave of $H^*/d^* = 0.019$ climbing up a $1 : 19.85$ beach. Cross-shore profiles of the free surface elevation at different stages of the run-up process are reported on figure 3.14. Notice that instead of centering the initial wave profile at $X_1^* = 37.35$ we used $X_1^* = 40$. This only introduces a small shift in the origin of the times.

A very good matching exists between the numerical solution provided by the BTE model (solid lines) and Synolakis' analytical solution (dotted lines). The matching is almost perfect during most of the run-up. However, when the wave is just to reach the maximum run-up small discrepancies can be found far from the shore (i.e. $x^* > 10$), the numerical solution being slightly smaller than the analytical one. This discrepancy can be ascribed to two connected reasons:

1. being obtained within the NSWE framework Synolakis' solution best represents flow conditions near the shoreline;

2. Synolakis' solution was seen to slightly overestimate experimental data far from the shore.

However, near the shoreline (i.e for $x^* < 4$) matching of the two solutions is always excellent, again suggesting a good implementation of the SBCs in the chosen BTE model.

3.6 Conclusions

A novel type of SBCs has been proposed for Boussinesq-type models. This is derived by using the characteristic form of the NSWE and is shown to properly model the shoreline motion. The methodology used to implement such SBCs in a specific BTE model is illustrated and its effectiveness verified by means of three different analytical solutions. The illustrated model represents an efficient tool for modelling nearshore flows and analysis is underway to compare it with a shock-capturing version of the same BTE model in which nonlinear-dispersive terms are regarded as forcings of the classical NSWE.

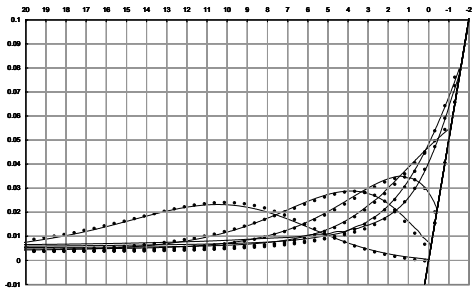

Figure 3.14: The 'Synolakis run-up solution'. Dimensionless free surface elevationζ^* as functions of the dimensionless x^* coordinate at different adimensional times $t^* = 20, 30, 35, 40, 45, 50$ (from left to right and from top to bottom). The solid line represents computed data while solid circles are used for Synolakis analytical solution.

Chapter 4

A new treatment of wave-breaking in Boussinesq-type models

4.1 Introduction

An attempt at improving wave-breaking modelling in fully nonlinear Boussinesq-type models is here described. The approach extends the work of Veeramony and Svendsen (2000) to give a more flexible and accurate description of the turbulence due to a breaking wave. Turbulent stresses are handled by means of the Boussinesq hypothesis and the eddy viscosity is assumed to be constant in time but varying in space, in particular over the water depth. The model is described in detail and its performances are evaluated both against an available semi-analytical solution and against experimental data of regular waves breaking over a slope. Prediction of the wave height decay is comparable to that of given by the solution of Veeramony and Svendsen (2000). Four different vertical profiles of eddy viscosity are considered and the differences in terms of hydrodynamic features are discussed. The model allows to estimate the velocity fields under a breaking wave, which is fundamental to describe the hydrodynamics in the vicinity of low-crested structures.

4.2 Overview

Modelling the flow inside the surf zone is crucial in order to understand and predict the complex hydrodynamics in the vicinity of low-crested structures. The present study aims at improving the treatment of wave breaking in Boussinesq-type models. Although Boussinesq models can handle most of wave phenomena occurring in the nearshore (like refraction, diffraction, shoaling, dispersion and nonlinear interaction) they cannot predict where and when a wave breaks. Therefore the effects of wave breaking (e.g. the energy dissipation and the momentum transfer to long waves) are not described by these models. Since wave breaking cannot be intrinsically handled by the model itself it is necessary to detect the location of the breaking point and to describe the energy dissipation due to breaking with additional terms in the Boussinesq equations which represent the excess of momentum related to breaking.

In the last decade many approaches have been followed, here a brief description of each is given. A very simple approach is that of Zelt (1991) which adds turbulent stresses to the momentum equation to model the dissipation of energy, by conserving the overall momentum. The breaking

criterion was based on a critical ratio between the local wave height and the water depth (H/h) and on a critical value of the velocity gradient in the cross-shore direction u_x. Karambas and Koutitas (1992) used an eddy viscosity approach too, but their model assumes that breaking can be treated as an unresolved turbulent motion. By using the mixing length hypothesis, they determined the eddy viscosity by integrating the turbulent transport equation. The breaking criterion which they used was based on the ratio between the crest elevation at the breaking point, ζ_{cb} and the wave length in deep waters L_0. Also Chen et al. (1999) and Kennedy et al. (2000) used Zelt's approach for both 1DH and 2DH Boussinesq models. In these studies the breaking criterion was related to the value of the variation in time of the surface elevation. A similar approach has been proposed by Schäffer et al. (1993): the breaking starts when the slope of the water surface α exceeds a critical value α_b and the breaking stops if $\alpha < \alpha_0$. Both α_b and α_0 are calibrated using experimental observations. Once breaking has started, an exponential decrease in time of α is assumed

$$\tan\alpha = \tan\alpha_0 + (\tan\alpha_b - \tan\alpha_0)\exp\left[-\ln\left(2\frac{t-t_0}{T_b}\right)\right] \tag{4.2.1}$$

where t_b is the time at which breaking starts and T_b is a characteristic duration of breaking.

Another approach to wave breaking modelling is based on the roller model. The roller is the region in a spilling breaker in which an air-water mixture recirculates near the front of a breaking wave while translating at approximatively the same speed of the wave. The idea of the roller was first introduced by Svendsen (1984) while Brocchini et al. (1992) and Schäffer et al. (1993) used this approach to incorporate the effects of breaking in their Boussinesq model. In the former study the contribution of the roller was taken into account only through an added pressure term in the momentum equation the roller being considered as a rigid body which does not participate in the fluid motion. In Schäffer et al. (1993), the horizontal velocity was assumed uniform below the roller and equal to the wave celerity within the roller region. In all the aforementioned works the flow motion in the wave body is assumed to be irrotational. However, as the breaking process begins vorticity is advected and diffused inside the fluid (e.g. Ting and Kirby 1996; Chang and Liu 1999), hence the assumption of irrotational flow is only valid as a first approximation in the case of breaking waves (this is especially true for breaking in shallow waters). Moreover, the assumption of irrotational flow is such that important phenomena like the undertow cannot be suitably modelled by using a Boussinesq-type model.

The most recent Boussinesq-type models attempt at removing the assumption of irrotational flow and regard the injection of vorticity due to the roller as the fundamental ingredient for a physically-based description of the energy dissipation (Veeramony and Svendsen 2000; VS hereinafter). VS used the similarity between the flow of a spilling breaker and that typical of a hydraulic jump to derive boundary conditions describing vorticity injection at the lower edge of the roller. Hence, a fully nonlinear Boussinesq-type model, in which the breaking terms are derived directly by a decomposition of the velocity into a potential and a rotational part, is coupled with the vorticity transport equation (VTE hereinafter) which is used to evolve the horizontal component of the vorticity needed to compute the rotational contribution to the flow velocity. This approach is the starting point of the present work, hence it is discussed in detail in the next session.

4.3 A fully nonlinear Boussinesq-type model

The Boussinesq equations have been introduced in section 2.1; for the reader's convenience brief remarks are reported herebelow posing emphasis on wave-breaking inclusion into the model equations. In VS, the Boussinesq equations have been derived by integrating the Reynolds equations over the depth and by applying the kinematic and dynamic boundary conditions at the bottom and at the free surface. In particular (see 4.1) by assuming a cartesian reference frame (x, z) and by taking (u, w) as the horizontal and vertical velocity components respectively, the surface elevation, ζ, and the depth-averaged velocity, $\bar{u}$, can be used as the dependent variables of the Boussinesq-type equations. These are made dimensionless with the following scales: the wavenumber k, the local water depth h and the wave amplitude a. The following equations are thus obtained which are characterized by two dimensionless parameter $\mu = kh$ (measuring the frequency dispersion) and $\delta = a/h$ (measuring the nonlinearities):

$$\zeta_t + \left[\bar{u}\left(h + \delta\zeta\right)\right]_x = 0 \tag{4.3.2}$$

$$\begin{aligned}
&\bar{u}_t + \delta\bar{u}\bar{u}_x + \zeta_x + \mu^2\left[\left(B - \tfrac{1}{3}\right)h^2\bar{u}_{xxt} - \tfrac{1}{2}hh_{xx}\bar{u}_t - hh_x\bar{u}_{xt}\right] + B\mu^2h^2\zeta_{xxx} \\
&+\delta\mu^2\left[-\tfrac{1}{3}h^2\bar{u}\bar{u}_{xxx} - h\zeta_x\bar{u}_{xt} + \tfrac{1}{3}h^2\bar{u}_x\bar{u}_{xx} - \tfrac{2}{3}h\zeta\bar{u}_{xxt} - \tfrac{3}{2}hh_{xx}\bar{u}\bar{u}_{xx}\right. \\
&\left.-\tfrac{1}{2}hh_{xxx}\bar{u}^2 - hh_x\bar{u}\bar{u}_{xx} - \zeta h_x\bar{u}_{xt} - h_x\zeta_x\bar{u}_t - \tfrac{1}{2}\zeta h_{xx}\bar{u}_t + Bh^2\left(\bar{u}\bar{u}_x\right)_{xx}\right] \\
&+\delta^2\mu^2\left[\tfrac{1}{6}\zeta^2\bar{u}_{xxt} - \tfrac{1}{3}h\zeta\bar{u}_x\bar{u}_{xx} - \tfrac{1}{3}h\bar{u}_{xx}\left(\zeta\bar{u}\right)_x + h\left(\zeta\bar{u}_x^2\right)_x - \tfrac{1}{2}\left(\zeta^2\bar{u}_{xt}\right)_x\right. \\
&\left.-\tfrac{2}{3}h\left(\zeta\bar{u}\bar{u}_{xx}\right)_x - \zeta_x h_{xx}\bar{u}^2 - \zeta h_x\bar{u}\bar{u}_{xx} - \tfrac{1}{2}\zeta h_{xxx}\bar{u}^2 - \tfrac{3}{2}\zeta h_{xx}\bar{u}\bar{u}_x - \zeta_x h_x\bar{u}\bar{u}_x\right] \\
&+\delta^3\mu^2\left[-\tfrac{1}{3}\zeta^2\bar{u}\bar{u}_{xxx} - \zeta\zeta_x\bar{u}\bar{u}_{xx} + \zeta\zeta_x\bar{u}_x^2 - \tfrac{1}{3}\zeta^2u_x\bar{u}_{xx}\right] \\
&+\left[\delta\left(\Delta M\right)_x + \mu^2\left(\left(\Delta P\right)_{xxt} - D_s\right) + \delta\mu^2\left(\left(\Delta M_1\right)_x + D_w + D_{uw}\right)\right]\left(h + \delta\zeta\right)^{-1} = 0
\end{aligned} \tag{4.3.3}$$

where subscripts are used to denote partial differentiation and the linear operator

$$L = 1 + B\mu^2h^2\frac{\partial^2}{\partial x^2} \tag{4.3.4}$$

introduced by Madsen et al. (1991) to improve the dispersion characteristics has also been applied (the value of the free parameter B is chosen so that the model's dispersive characteristics better mimic the linear theory in deep waters). In equations (4.3.2) and (4.3.3), the flow velocity is computed by differentiating the streamfunction ψ which, in turn, can be obtained by integrating in space the equation which defines ω in terms of ψ.

It is worth stressing that the assumption of irrotational flow has been removed here. Indeed the velocity turns out equal to:

$$u = u_p + u_r \tag{4.3.5}$$

where u_p, representing the potential flow velocity, is equivalent to the velocity of typical potential flow formulations, while u_r, i.e. the rotational velocity component, is assumed to be only due to the vorticity caused by the breaking. Thus the terms inside the square bracket of the last line of equation (4.3.3), which are only due to u_r, are called *"breaking terms"*. In particular, D_s is related to the shear stress inside the fluid, $(\Delta M)_x$ and $(\Delta M_1)_x$ give the excess of momentum flux due to

the vertical variation of the rotational velocity, $(\Delta P)_{xxt}$ is the contribution to the pressure due to the vertical motion, D_w is the excess of momentum due to the vertical motion and D_{uw} represents the interaction between the waves and the mean flow. For more details on such classification please refer to VS.

All the expressions of the breaking terms are here omitted, suffice it to say that they all require knowledge of the rotational velocity which is a further unknown of the problem. Hence, to close the problem it is necessary to introduce a further equation for the u_r. It is possible to show that:

$$u_r \equiv \int_{-h}^{z} \omega dz - \mu^2 \int_{-h}^{z}\int_{-h}^{z}\int_{-h}^{z} \omega_{xx} dz dz dz + O\left(\mu^4\right) \tag{4.3.6}$$

i.e. that it is possible to compute the rotational velocity by an integration of functions of the vorticity ω only. This is the means by which the Boussinesq model is coupled with the VTE. Figure 4.1 shows the most important parameters involved in the problem.

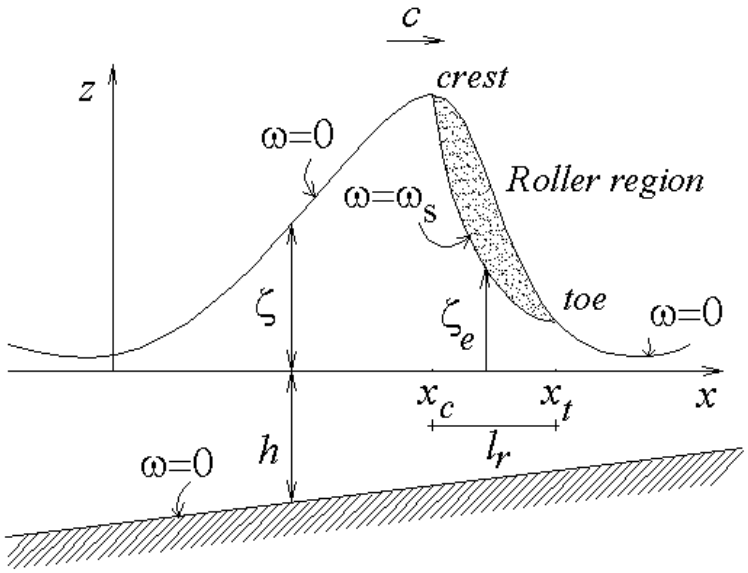

Figure 4.1: Schetch of flow characteristics and notation.

With the same scales used for the Boussinesq model this equation may be written in the dimensionless form:

$$\omega_t + \delta u \omega_x + \delta w \omega_z = \nu_t \omega_{zz} + 2\nu_{t_z}\omega_z + \nu_{t_{zz}}\omega + O(\mu^2, h_x) \tag{4.3.7}$$

where the eddy viscosity ν_t is here taken to be variable within the fluid i.e. $\nu_t = \nu_t(x, z)$.

In VS this quantity has been considered uniform over the water column i.e. $\nu_t = \nu_t(x)$. The latter assumption leads to the possibility of an analytic solution to be found for the problem which is determined by a suitable set of boundary conditions:

$$\omega\left(z = \zeta_e, t\right) = \omega_s\left(x, t\right) \tag{4.3.8}$$

$$\omega\left(z=-h,t\right)=0. \tag{4.3.9}$$

Although the assumption of depth-independence of ν_t can be useful to derive VS's analytical solution the turbulence structure of breaking waves is such that much of the turbulence generated at the free surface penetrates into the water body by vertical advection and diffusion (e.g. Ting and Kirby 1996; Chang and Liu 1999). It is, thus, clear that the assumption $\nu_{t_z}=0$ is theoretically rather crude and many experimental studies reveal the need for an adequate description of the vertical structure of ν_t (e.g. Cox et al. 1995). We here attempt at such description which can only be possible if a suitable procedure is used to solve the VTE with $\nu_t=\nu_t(x,z)$. The first step is to introduce a change of variables (also used by VS) which allows for an easier treatment of the equation. Since the lower edge of the roller is considered the upper boundary of the computational domain and since it is not parallel to a line *z=cost* it would be difficult to assign there boundary condition. Transformation of both equations and boundary conditions into sigma-coordinates avoids this problem. The variable transformation reads:

$$x=x,\quad t=t,\quad \sigma=\frac{h+z}{h+\delta\zeta_e}. \tag{4.3.10}$$

As σ itself is a function of time and space, in the VTE new terms due to the coordinate variation in time and space appear. The final form of (4.3.7) in $\sigma-$coordinate and accurate up to $O\left(\mu^2,h_x,\right)$ reads:

$$\begin{aligned}&\frac{\partial\omega}{\partial t}-\delta\left[\frac{\sigma}{h+\delta\zeta_e}\frac{\partial\zeta_e}{\partial t}\right]\frac{\partial\omega}{\partial\sigma}+\delta u\frac{\partial\omega}{\partial x}-\delta\left[\frac{u\sigma}{h+\delta\zeta_e}\frac{\partial\zeta_e}{\partial x}\right]\frac{\partial\omega}{\partial\sigma}+\delta\left[\frac{w}{h+\delta\zeta_e}\right]\frac{\partial\omega}{\partial\sigma}=\\&+\left[\frac{\nu_t}{(h+\delta\zeta_e)^2}\right]\frac{\partial^2\omega}{\partial\sigma^2}+\left[\frac{\omega}{(h+\delta\zeta_e)^2}\right]\frac{\partial^2\nu_t}{\partial\sigma^2}+\left[\frac{1}{(h+\delta\zeta_e)^2}\frac{\partial\nu_t}{\partial\sigma}\right]\frac{\partial\omega}{\partial\sigma}\end{aligned} \tag{4.3.11}$$

where, for the sake of clarity, we reverted to the standard notation for differentiation.

The associated boundary conditions are given along iso-σ lines and read:

$$\omega\left(\sigma=1,t\right)=\omega_s\left(x,t\right) \tag{4.3.12}$$

$$\omega\left(\sigma=0,t\right)=0. \tag{4.3.13}$$

Equation (4.3.11) together with boundary condition (4.3.12), (4.3.13) can be coupled with the 1DH Boussinesq model equations in which the breaking terms are accounted for.

4.4 A numerical solution of the VTE

SV solved (4.3.11) using a spectral method. Retaining terms of $O\left(\mu^2\right)$ and assuming the eddy viscosity to vary only with x, the vorticity is given by a series expansion:

$$\omega=\sigma\omega_s+\sum_{n=1}^{\infty}G_n\sin\left(n\pi\sigma\right). \tag{4.4.14}$$

In the present study to allow for a vertical variation of the turbulence (i.e. $\nu_t=\nu_t(x,z)$) a numerical approach is used to solve (4.3.11) by means of a finite-difference technique.

An Adams-Bashforth-Moulton (ABM hereinafter; Press 1992) predictor-corrector method is used to integrate both the Boussinesq model and the VTE. In particular for the Boussinesq model the scheme is of the third order in time at the predictor stage and of the fourth order at the corrector stage. As the order of derivatives in the VTE is lower than in the Boussinesq equations the order of the scheme used to solve the VTE may be lowered without affecting the accuracy of the solution and with the advantage of increasing the stability of the model. The ABM scheme that we use to solve the VTE is of the second order in time at the predictor stage and of the third order at the corrector stage.

In order to calculate the rotational velocity and all the breaking terms the vorticity field is obtained at each time step of the Boussinesq model in each point of the domain. The VTE integration module needs as input data both the boundary values ω_s, the roller thickness and the depth-averaged velocity $\bar{u}$. Boundary conditions for the vorticity are given by the following empirical relation derived by VS:

$$\omega_s = 15.75\left(1-\frac{x-x_t}{l_r}\right)\left(1-e^{-40\frac{x-x_t}{l_r}}\right) \tag{4.4.15}$$

which shows that the vorticity is maximum at the toe of the breaker. The roller thickness is also given by an empirical relation.

Finally, the local value of the velocity component u is evaluated by the expression:

$$u = \bar{u}_p + \mu^2\left(h\bar{u}_p\right)_{xx}\left(\frac{\Delta_1}{2}-z\right) + \frac{\mu^2}{2}\bar{u}_{pxx}\left(\frac{\Delta_1}{3}-z^2\right) + u_r + O\left(\mu^4\right) \tag{4.4.16}$$

where:

$$\Delta_1 = (\delta\zeta - z) \tag{4.4.17}$$

and the rotational velocity is given by (4.3.6). The component w is obtained by using the continuity equation $u_x + w_z = 0$.

Since the stability condition of the Boussinesq model is different and less restrictive than that for the VTE a coupled integration in time should be run by using the small time step required for the VTE hence dramatically reducing the computational efficiency. To avoid this problem a "mode splitting" technique has been used. A number of time steps of the VTE integration model (internal module) are carried out for each time step of the Boussinesq model (external module). Since the boundary conditions, the free surface elevation and and the depth-averaged velocity are calculated by the Boussinesq model a data reconstruction by linear interpolation has been carried out to obtain values of these variables in the internal module. This technique is common in problems in which the free surface has to be resolved together with a scalar quantity that diffuses in the fluid (Blumberg and Mellor 1987).

In the roller region the vorticity distribution is not calculated. Nevertheless, the contribution of this region to the breaking terms is of great importance; therefore a linear distribution of ω in this region has been *a priori* assumed. Once the quantity ω has been calculated, the breaking terms in (4.3.3) may be calculated. The eddy viscosity distribution over the water column $N(z)$ is assumed such that its maximum value is located at the water surface except at the roller where the maximum is located at the lower edge of the roller. This values is estimated by a mixing length hypothesis:

$$\nu_t = \nu_{t0} h(x)\sqrt{g h(x)} N(z) \tag{4.4.18}$$

where ν_{t0} is a constant which assumes values in the range $0.01 - 0.04$.

4.5 Comparison with experimental data

The performances of the present model have been compared with two sets of experimental data from Hansen and Svendsen (1979) (HS hereinafter), Cox et al. (1995) and Cox and Kobayashi (1997) (CK hereinafter). The tests mainly aim at gaining information on the features of the numerical solution of the VTE by comparing the results with those which are obtained with VS's analytical solution. We also try to assess the differences between various possible profiles $N(z)$ for the eddy viscosity profiles. To this purpose the data of CCox et al. (1995) are the most valuable as velocity profiles are available in conjunction with other synthetic data like the wave height decay.

The experimental studies of Cox et al. (1995) on the propagation of regular waves over a uniformly sloping beach have been carried out at the Ocean Engineering Laboratory of the University of Delaware. The experimental flume was 33m long, 0.6m wide and 1.5m deep, the steepness of the sloping part was of $1:35$. The bottom was made of concrete and it was made rough by gluing natural sand to the bottom ($d_{50} = 1.0$mm). The water depth on the horizontal bottom was of0.4m. A schematic view of the experiment is given in figure (4.2).

Six measuring lines, $L1, L2, L3, L4, L5, L6$, were located along the slope. The position of the lines was chosen in order to have $L1$ in the shoaling region, $L2$ at the breaking point (defined in the experiments as the onset of aeration in the tip of the wave crest) $L3$ was in the transition region (where the wave evolves towards a bore), $L4$, $L5$ and $L6$ were all in the inner surf zone. In correspondence of the six measuring lines, surface elevation measurements were obtained by using six capacitance wave gauges and the velocities were measured over the the water column by using a Laser Doppler Velocimeter (LDV). Due to the dropout of the LDV the velocities are significant only under the level of the wave trough. Cox and co-workers simulated only one wave condition ($H = 0.115$m, $T = 2.2$s) obtaining spilling breakers. The same experimental setup has been used in CK for the measurement of the undertow current.

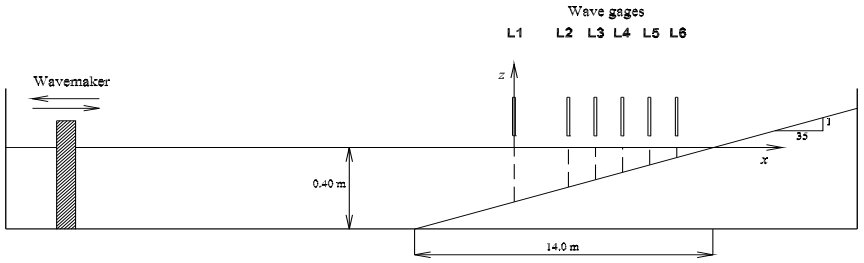

Figure 4.2: Experimental setup of Cox *et al.* (1995)

The numerical flume differs from the real one as it is not necessary to model the whole length of the uniform-depth region of the flume. The total length of the computational domain is of18m, where the horizontal bottom is 1m long, with a water depth of $h_0 = 0.4$m. At the onshore boundary a sponge layer is used, the onshore shelf is 5.65m long with a depth of 0.04m. Cnoidal waves have been generated at the offshore boundary using a generating-absorbing condition (Van Dongeren and Svendsen 1997).

The experimental setup used in Hansen and Svendsen (1979) is quite similar to that above described. The flume was 0.6m wide, 32m long, the slope of the beach was $1:34.26$ and its toe

was 14.78m far from the wavemaker. Being the primary object of the experiments the evaluation of the wave height decay, wave heights were accurately measured by using a wave gauge mounted on a movable carriage. Unfortunately surface profile measurements are available only seaward of the breaking point, while no measurements were made of the flow velocities.

Among the 18 wave conditions simulated in the experiments two cases of spilling breakers were chosen for the comparison. The first test (named "test Q") has the following characteristics: $H = 0.0375$m, $T = 2.0$s. While the second test (named "test O") had: $H = 0.0399$m, $T = 2.5$s.

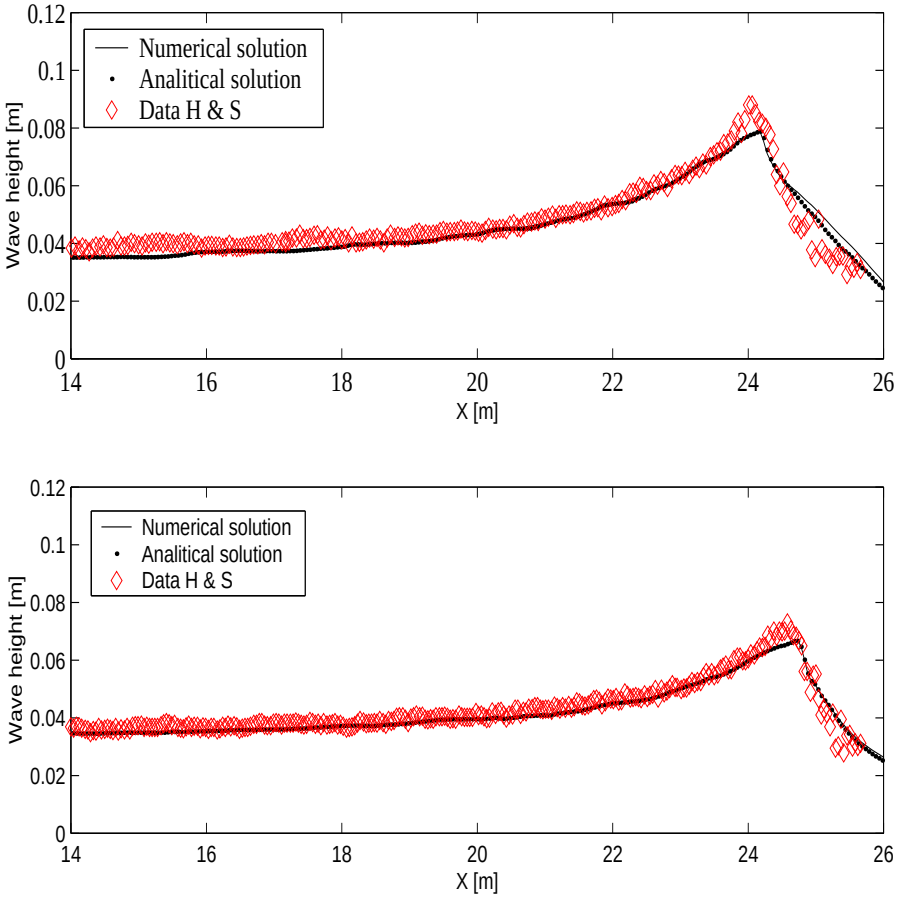

Figure 4.3: Wave height comparison. Red diamonds represent experimental results from Hansen & Svendsen (1979), black circles results from VS numerical simulations. Solid black line, present model.

The first set of results here shown aims at comparing the numerical solution of the problem (VTE+Boussinesq) and the semi-analytical approach by VS (analytical VTE + numerical Boussinesq), both using a uniform profile of eddy viscosity over the water column. The value of ν_{t0} in these simulations has been kept equal to 0.01 a value also prescribed in Cox et al. (1995). The critical value (for breaking) of the free surface slope has been fixed to $\alpha_b = 26°$. All the tests were run with a spatial and temporal discretization equivalent to those used in VS and Musumeci et al. (2003).

Figure 4.3 shows the comparison of the wave heights along the flume and obtained with the

mathematical models and from the experiments. The wave height in the shoaling region is the result of the interaction between the flow coming from offshore and the waves reflected off the beach. Only the latter contribution can be different in dependence of the approach (analytical or numerical) used to solve the VTE over the surf zone. For the case at hand this is negligible. Moreover, both models underestimate the wave height at breaking. In the transition region, both models predict almost the same wave height dissipation rate, which is different from that typical of the inner surf zone. The most important evidence which is brought up by this figure is the difference between the model of VS and the present model in predicting is the wave height distribution in the inner surf zone: where the numerical solution of the VTE seems to give a lower dissipation. The source of this differences becomes more clear when looking at the velocity profiles predicted by the models and those coming from the experiments of Cox et al. (1995).

From the comparison of the evolution in time of the profiles of the vorticity (figure 4.4 and 4.7, each figure shows surface profiles, the roller area and vorticity profiles over a wave period at each of the six gauges used in the experiment: from top panel L1 to bottom panel L6) it is clear that both models represent in a similar way the vorticity dynamics under the breaking wave. However, several remarkable differences require discussion. For example, it is clear that in the present model vorticity does not penetrate down in the water body as rapidly as predicted by the model of VS. Moreover, the model of VS predicts a rather intense vorticity much downstream of the wave crest.

These differences largely influence the computation of the rotational velocities. Smaller absolute values of u_r are computed by means of the numerical solver of the VTE (figure 4.5 and figure 4.8). However, from a qualitative point of view the profiles of u_r computed from the fully numerical solution of the problem seem closer to the experimental profiles over much of the water column (clearly no sensible comparison can be made between flow velocities near the bed). This is particularly clear when analyzing the flow region downstream the wave crest (see fourth and fifth panels of figures 4.5 and 4.8): the profiles of u_r computed from the analytical solution are characterized by stronger vertical gradients than both the numerical and the experimental solutions.

Both models show a similar sensitivity to the size ν_{t0} of the eddy viscosity. As it increases from 0.01 to 0.03 the diffusion of vorticity in the fluid is more rapid and also vorticity dissipation is faster (compare 4.4 with 4.7 and 4.5 with 4.8). Also the comparison with data from Cox et al. (1995) shows that the dissipation in the inner surf zone (L5 and L6) is higher in VS model rather than in the present one. In both models waves begin to break a little bit upstream of $L3$, where, as shown in the experiments, breaking has already occurred. This has been obtained by setting the critical value of surface slope at $\alpha_b = 26°$.

The comparison of the profiles of the velocity component u shows that this is overestimated by both models in correspondence of the crest. Since VS's solution predicts a rotational flow with strong vertical gradients a similar feature can be seen in the total velocity which is found to differ much from the measured profile in the upper part of the water column. On the other hand, the present model predicts a larger velocity because of a reduced energy dissipation, however, the profiles seems to be qualitatively similar in shape to the measured ones. This is particularly true away from the wave crest where velocities predicted by the present solver because of the smaller vorticity generation fit better the experimental data than VS's solution. The above considerations hold true for both values of ν_{t0} used in the comparison.

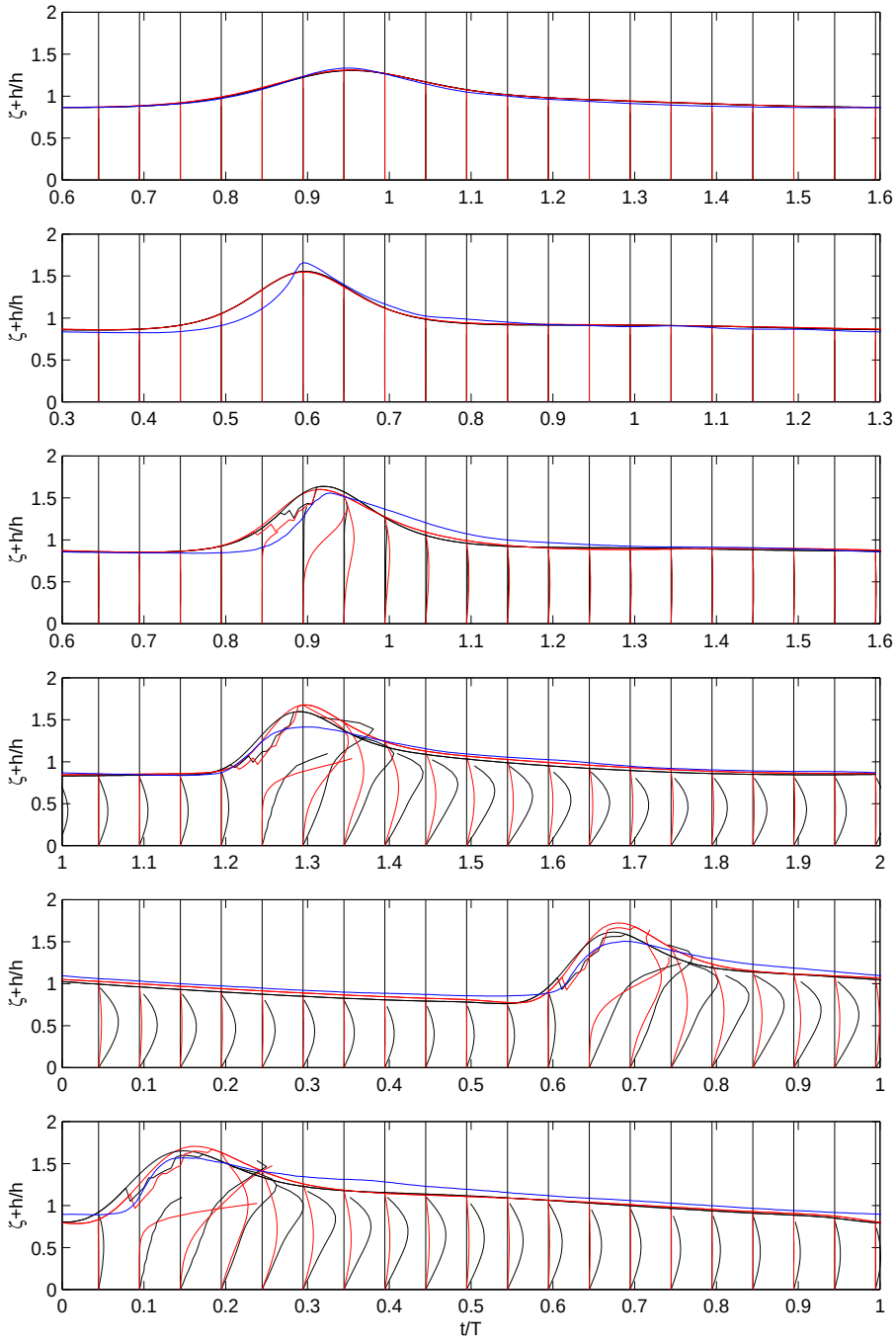

Figure 4.4: Time evolution of the vorticity profiles at the six locations (from top L1 to bottom L6) of the gauges of Cox et al. (1995). Blue solid line, experimental results, red solid line, results from the present model (the roller area is also shown below the crest). Black solid line results from VS. $\nu_{t0} = 0.01$.

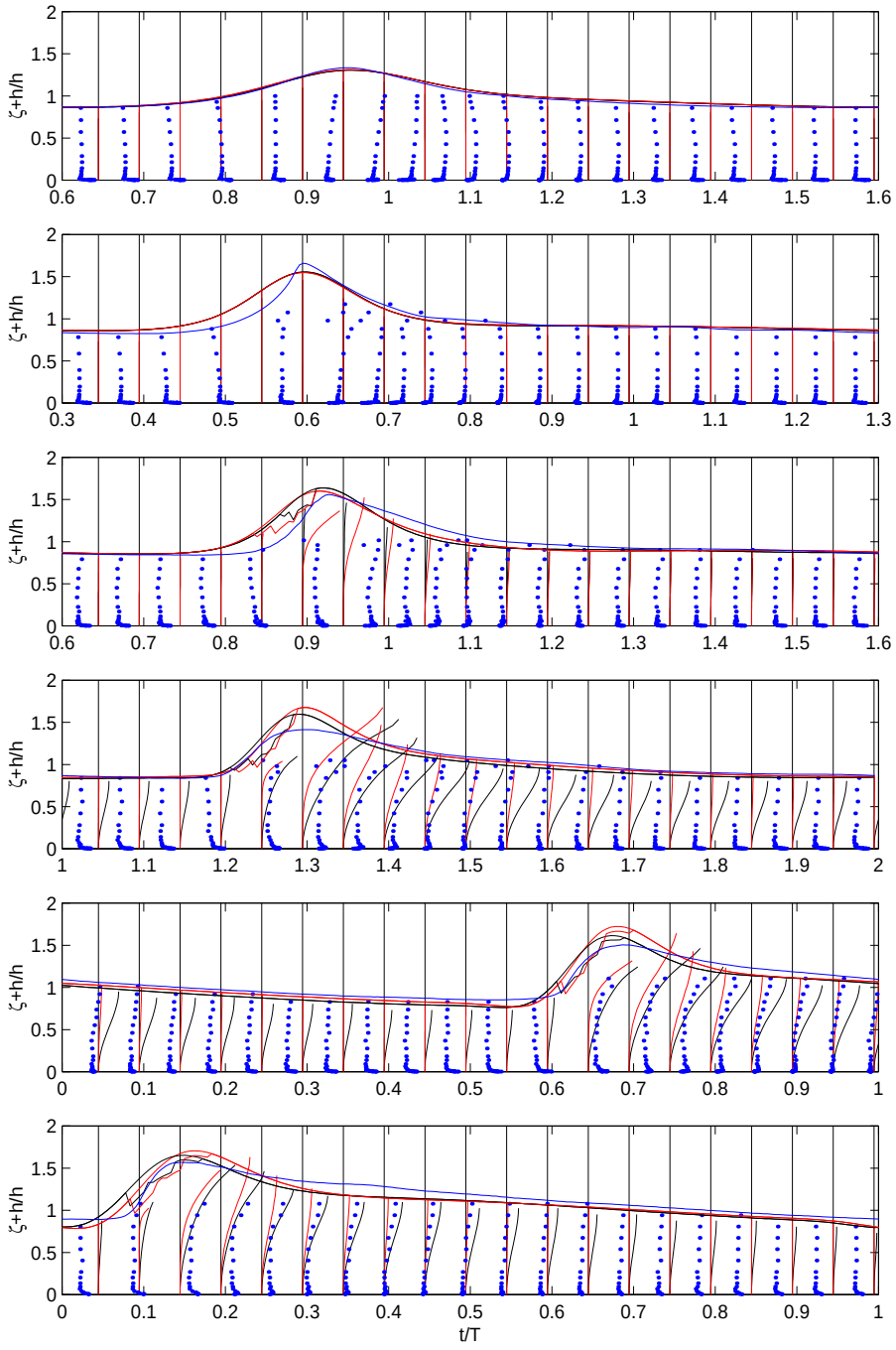

Figure 4.5: Time evolution of the profiles of the rotational velocity at the six locations (from top L1 to bottom L6) of the gauges of Cox et al. (1995). Blue solid line, experimental results, red solid line, results from the present model (the roller area is also shown below the crest). Black solid line, results from VS. Blue dots, experimental results from LDV measurements of velocity. $\nu_{t0} = 0.01$.

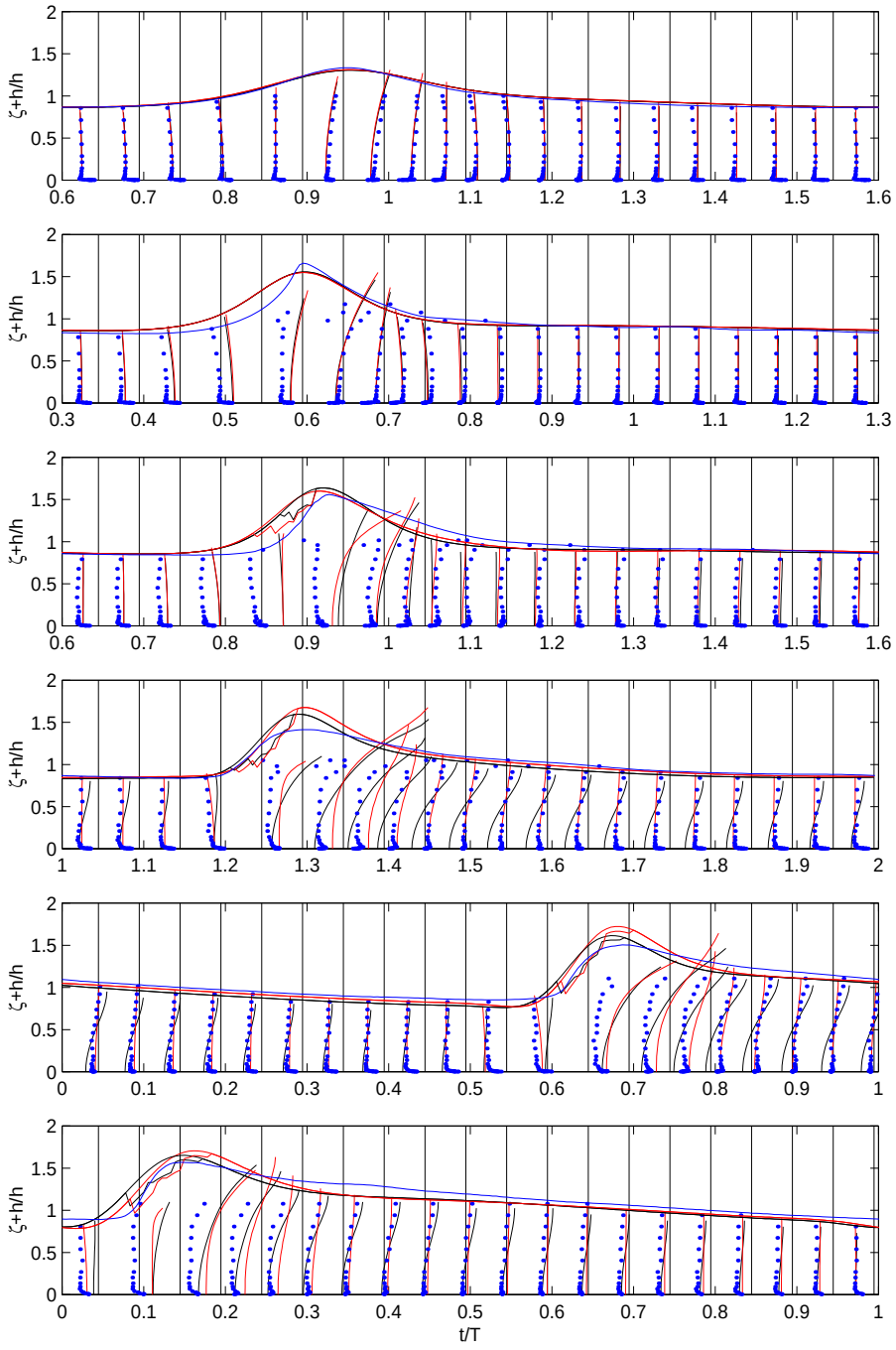

Figure 4.6: Time evolution of the profiles of the total velocity at the six locations (from top L1 to bottom L6) of the gauges of Cox et al. (1995). Blue solid line, experimental results, red solid line, results from the present model (the roller area is also shown below the crest). Black solid line, results from VS. Blue dots, experimental results from LDV measurements of velocity. $\nu_{t0} = 0.01$.

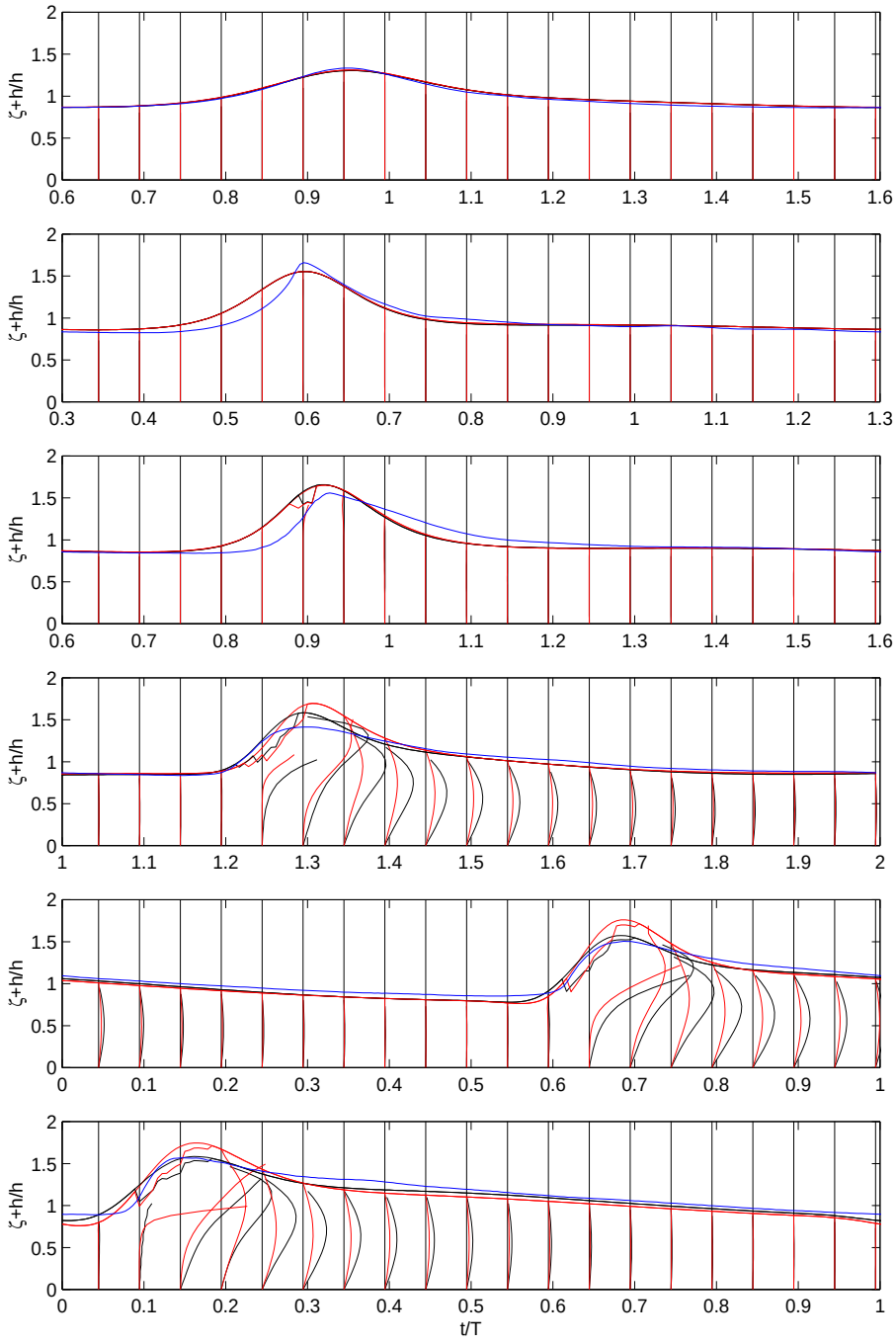

Figure 4.7: Time evolution of the profiles of the vorticity at the six locations (from top L1 to bottom L6) of the gauges of Cox et al. (1995). Blue solid line, experimental results, red solid line, results from the present model (the roller area is also shown below the crest). Black solid line results from VS. $\nu_{t0} = 0.03$.

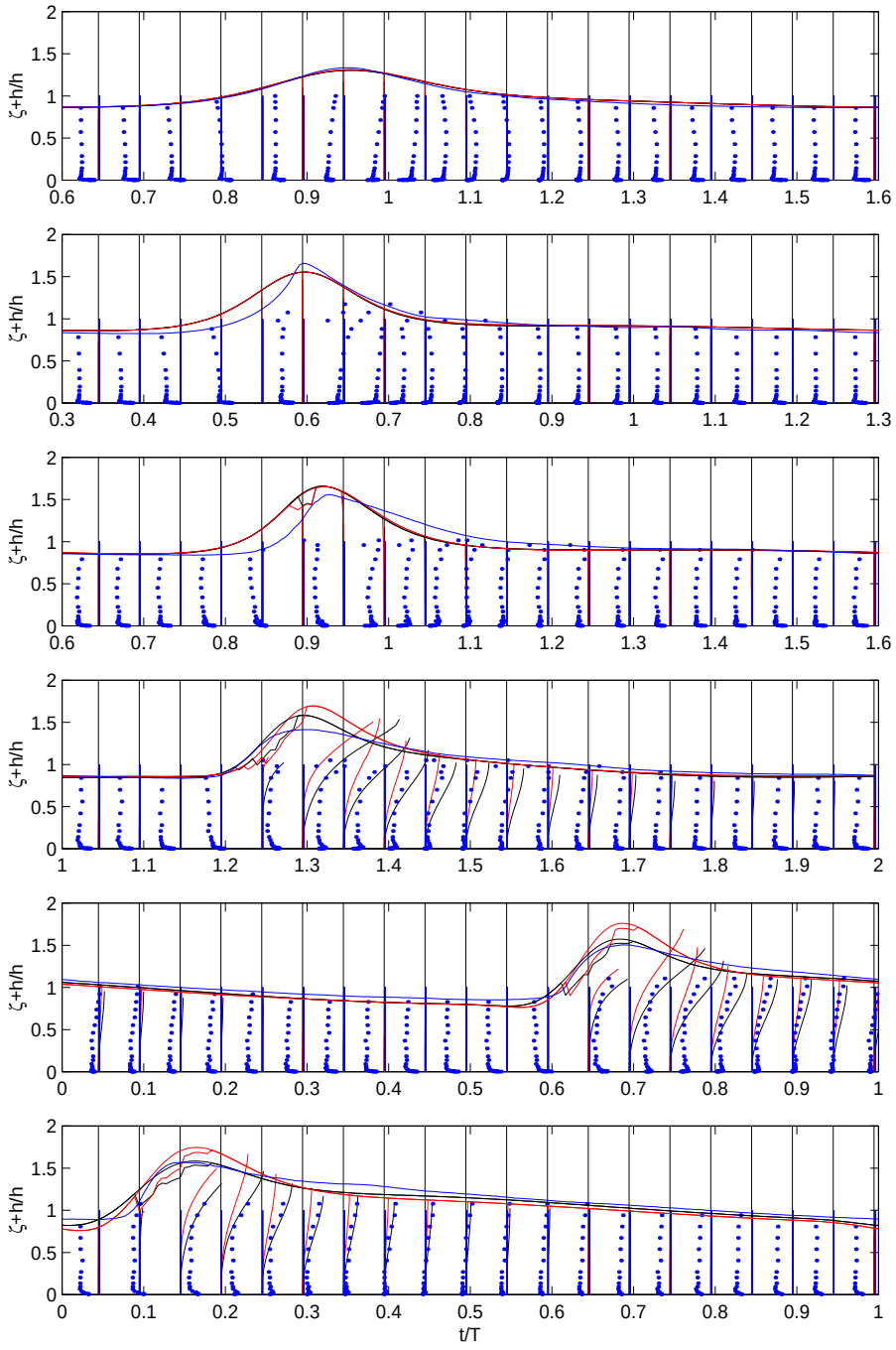

Figure 4.8: Time evolution of the profiles of the rotational velocity at the six locations (from top L1 to bottom L6) of the gauges of Cox et al. (1995). Blue solid line, experimental results, red solid line, results from the present model (the roller area is also shown below the crest). Black solid line, results from VS. Blue dots, experimental results from LDV measurements of velocity. $\nu_{t0} = 0.03$.

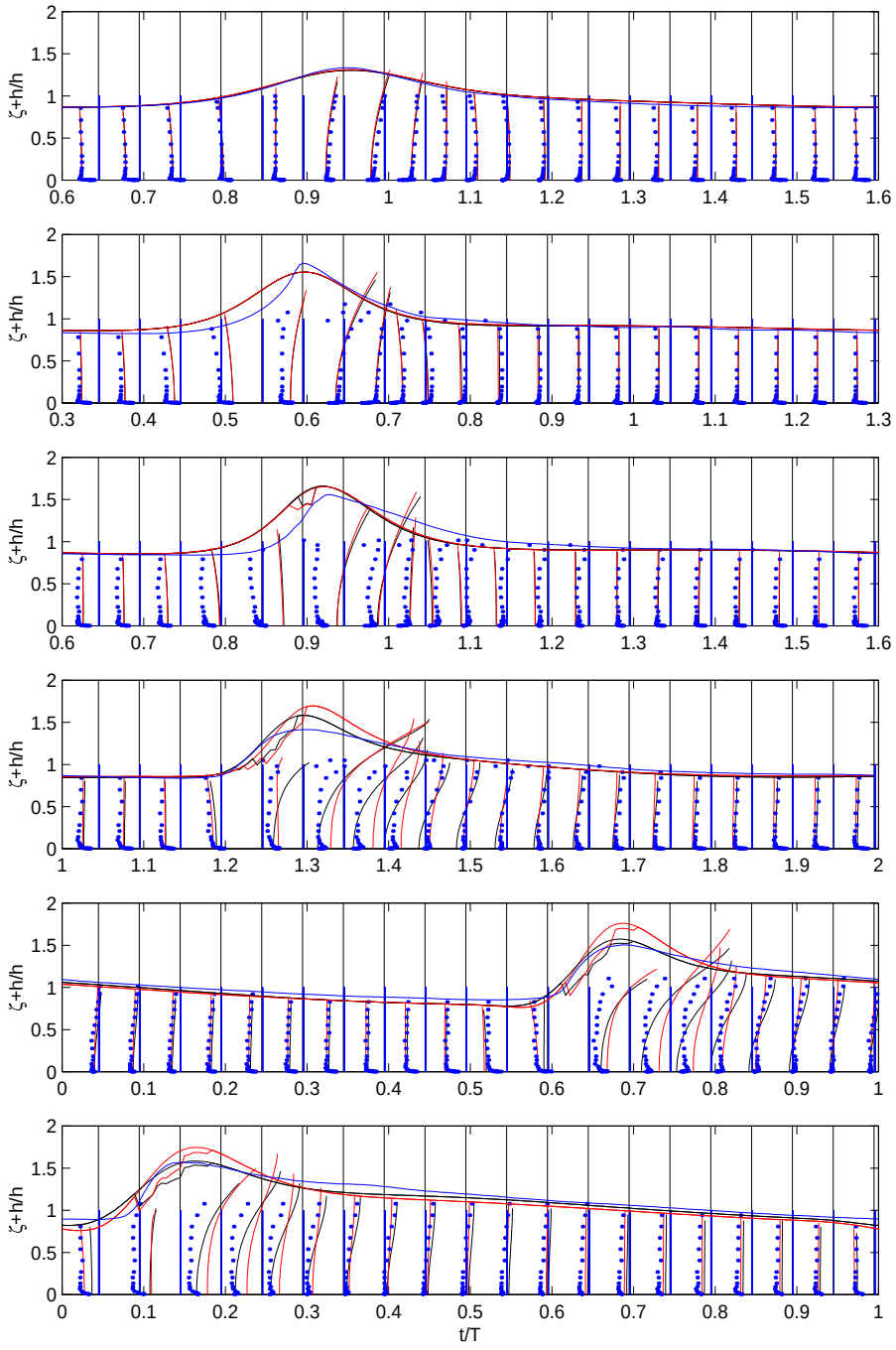

Figure 4.9: Time evolution of the profiles of the total velocity at the six locations (from top L1 to bottom L6) of the gauges of Cox et al. (1995). Blue solid line, experimental results, red solid line, results from the present model (the roller area is also shown below the crest). Black solid line, results from VS. Blue dots, experimental results from LDV measurements of velocity. $\nu_{t0} = 0.03$.

4.6 Sensitivity analysis on different profiles $N(z)$

In order to estimate the importance of the eddy viscosity distribution$N(z)$ over the water column, four possible test profiles have been chosen. Figure 4.10 shows the shape such profiles$N_0(z)$ being the uniform profile for which results have already been shown in the previous section. The other three profiles are possible parametrization of the turbulence structure all stemming from the observation that much of the vorticity and turbulence is introduced in the water body by the breaking wave near the surface. Hence, profiles $N_1(z)$ and $N_3(z)$ embody the assumption that turbulent stresses are non-zero only in the region of the water column directly influenced by the wave motion i.e. approximately the upper half of the normalized water column. This approach seems to be supported by experimental evidence of turbulence in hydraulic jumps (e.g. Svendsen et al. 2000). Profile $N_2(z)$ is the one suggested by Cox et al. (1995). In summary $N_0(z)$ and $N_2(z)$ are representative of turbulent stresses distributed over the whole water column while $N_1(z)$ and $N_3(z)$ represent turbulence localized near the surface. It is obvious that the choice of the profiles is completely arbitrary and other possible profiles can be used. However, sensitivity analysis on these profiles can shed light on the structure of the most appropriate one to adequately represent the natural flow dynamics.

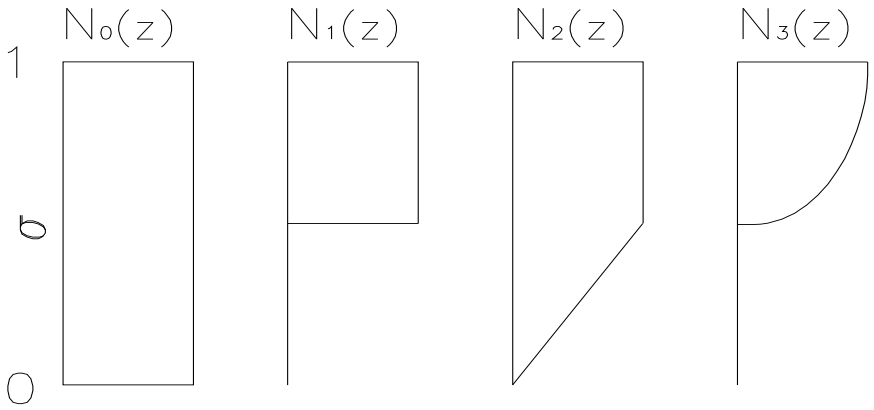

Figure 4.10: Eddy viscosity profiles chosen for the numerical simulations. The water column is normalised through the $\sigma-$coordinates transformation of equation (4.3.10).

Figures 4.11, 4.12, 4.13 show the evolution in time of the vorticity and velocity profiles as computed by the present model with the four different eddy viscosity profiles of figure 4.10 and with $\nu_{t0} = 0.03$. The largest differences induced by the various eddy viscosity distributions can be found in the profiles of the vorticity (figure 4.11). It is clear that the two profiles$N_1(z)$ and $N_3(z)$, which prescribe a region with zero eddy viscosity, induce rather different vorticity distributions especially downstream of the wave crest i.e. over the so-called 'wake region'. Over the roller region, which is interested by the beginning of vorticity transport in the fluid, differences seem to reduce due to the fact that vorticity is confined in a vertically narrow region over which all profiles prescribe approximately the same value of eddy viscosity. Also, the dissipation of vorticity is different, in particular, the parabolic eddy viscosity profile shows a reduced dissipation due to the fact that vorticity dissipation is locally proportional to the value of the eddy viscosity. In this profile the

Solver	L4	L5	L6
Analytical	Crest $\epsilon \leq 1$ Wake $\epsilon \approx 3$	Crest $\epsilon \leq 1$ Wake $\epsilon \approx 3.5$	Crest $\epsilon \leq 1$ Wake $\epsilon \approx 4.5$
Numerical $N_0(z)$	Crest $\epsilon \leq 1$ Wake $\epsilon \approx 0.5$	Crest $\epsilon \leq 2$ Wake $\epsilon \approx 1$	Crest $\epsilon \leq 2$ Wake $\epsilon \approx 1$
Numerical $N_1(z)$	Crest $\epsilon \leq 1$ Wake $\epsilon \approx 3$	Crest $\epsilon \approx 1$ Wake $\epsilon \leq 1$	Crest $\epsilon \approx 1$ Wake $\epsilon \leq 3$
Numerical $N_2(z)$	Crest $\epsilon \leq 1$ Wake $\epsilon \leq 1$	Crest $\epsilon \leq 2$ Wake $\epsilon \leq 1$	Crest $\epsilon \leq 2$ Wake $\epsilon \approx 2$
Numerical $N_3(z)$	Crest $\epsilon \leq 1$ Wake $\epsilon \approx 3$	Crest $\epsilon \leq 1$ Wake $\epsilon \approx 1$	Crest $\epsilon \leq 3.5$ Wake $\epsilon \approx 1$

Table 4.1: Summary of the quadratic error for four representative solvers over the transition region ($L4$) and the inner surf zone ($L5, L6$).

eddy viscosity value decreases gradually towards zero. This induces higher values of vorticity in the wake which are more evident at the L5 an L6 locations (inner surf zone).

Analysis of the velocity profiles reveals that differences among the various profiles of the rotational velocity are more evident over the 'wake regions' than over the the crest area due to the aforementioned reasons. Hence, at L5 and L6 the velocity away from the crest is well approximated by the simulations carried out with the parabolic eddy viscosity profile. The analysis also shows that the profile $N_1(z)$ leads to unreal spiky profiles of vorticity and velocity and, hence, cannot be considered as a good candidate for our modeling purposes. For this reason it is not analyzed in more detail in the following.

In order to quantitatively discuss the differences among the various approaches we have decided to measure the distance between the computed u_n^C and the experimental u_n^M velocity profiles (n gives the discrete vertical level) in terms of the quadratic error:

$$\epsilon = \frac{\sum_{n=n_0}^{N} \left(u_n^C - u_n^M\right)^2}{\sum_{n=n_0}^{N} \left(u_n^M\right)^2}. \tag{4.6.19}$$

Note that the lowest level n_0 has been taken to coincide with the top of the bottom boundary layer, while N is the level of the water surface.

We report errors only of four representative cases which are the VS' s solution (figure 4.14), the fully numerical solution with $N_0(z)$ (figure 4.15), with $N_2(z)$ (figure 4.16) and with $N_3(z)$ (figure 4.17). Inspection of the figures reveals that a rather large error characterizes the analytical solution over the "wake region" for propagation in the transition region ($L4$) and in the inner surf zone ($L5$, $L6$). On the contrary good performances are achieved by this method in the crest region. The overall best performances seem to be those of the numerical solution with either uniform ($N_0(z)$) or linear-uniform eddy viscosity ($N_2(z)$) while a worse comparison characterizes the numerical solution obtained with the parabolic profile $N_3(z)$. A synthetic description of the quadratic error is given in table 4.1.

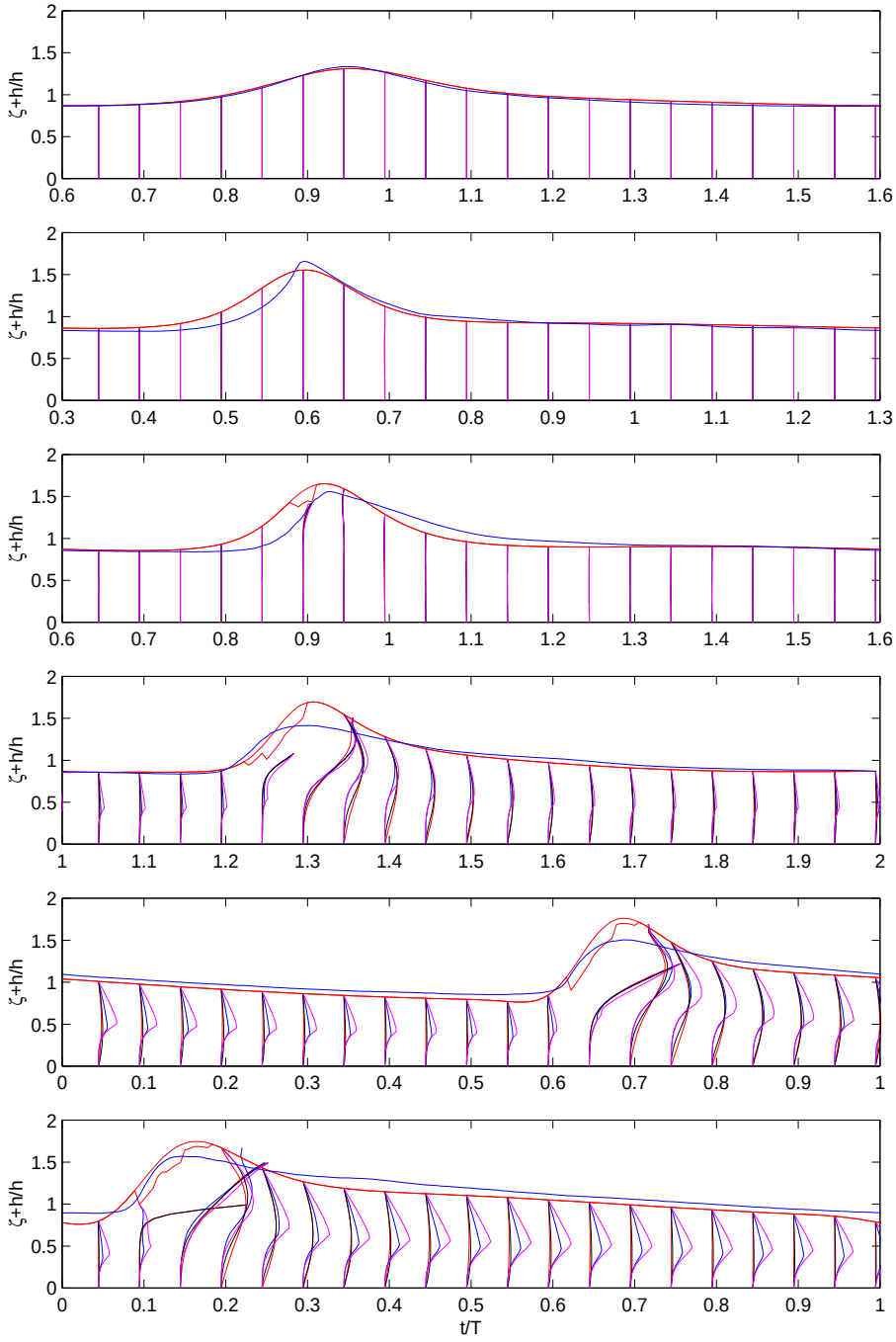

Figure 4.11: Time evolution of vorticity profiles at the six locations from top L1 to bottom L6) of the gauges of Cox *et al.* (1995). Red solid line, $N_0(z)$ (with water surface and roller area), blue solid line, $N_1(z)$, black solid line, $N_2(z)$, magenta solid line, $N_3(z)$. Blue dots and blue solid line wave profile, experimental results from Cox *et al.* (1995).

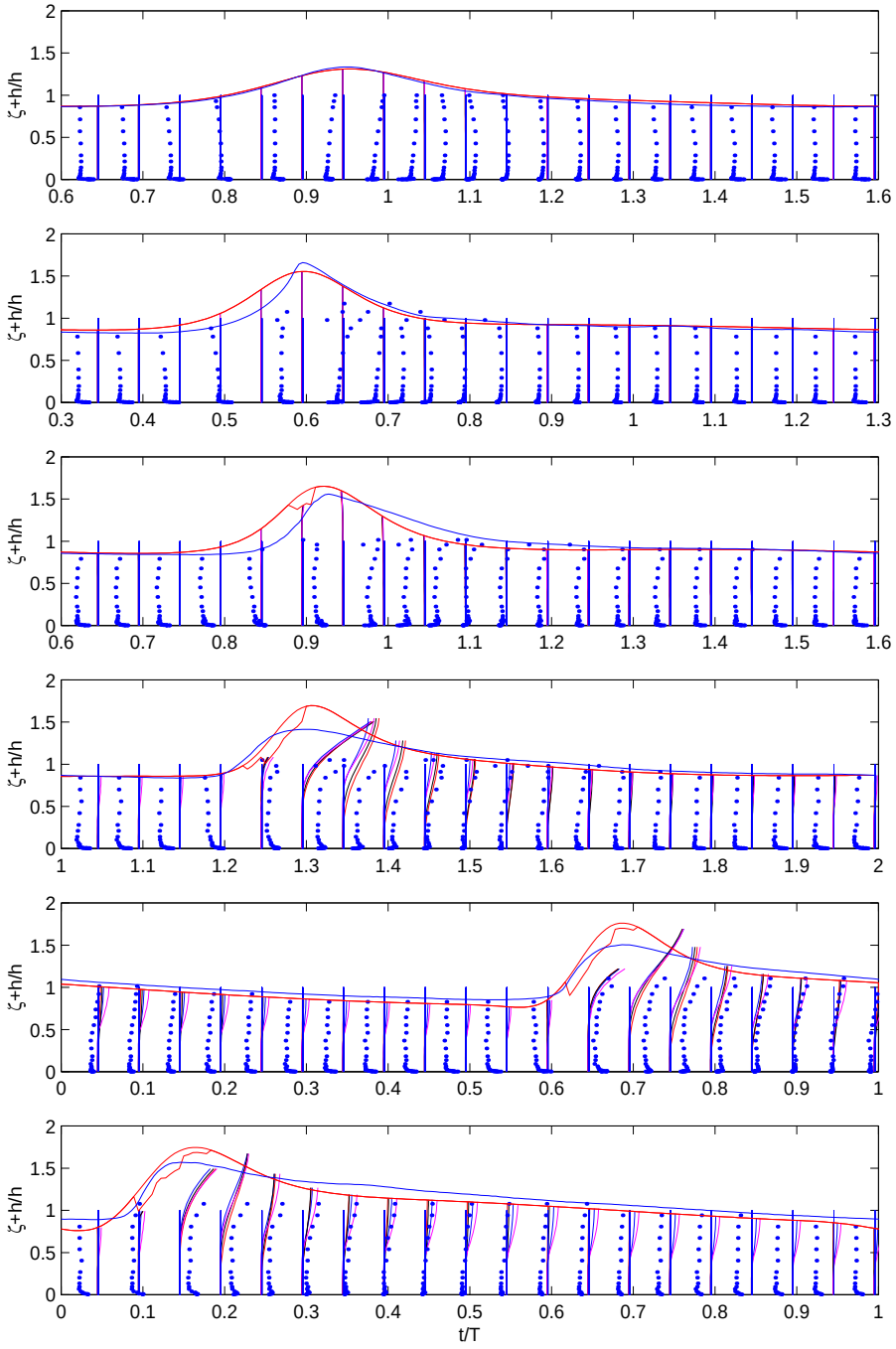

Figure 4.12: Time evolution of the profiles of the rotational velocity at the six locations from top L1 to bottom L6) of the gauges of Cox *et al.* (1995). Red solid line, $N_0(z)$ (with water surface and roller area), blue solid line, $N_1(z)$, black solid line, $N_2(z)$, magenta solid line, $N_3(z)$. Blue dots and blue solid line wave profile, experimental results from Cox *et al.* (1995).

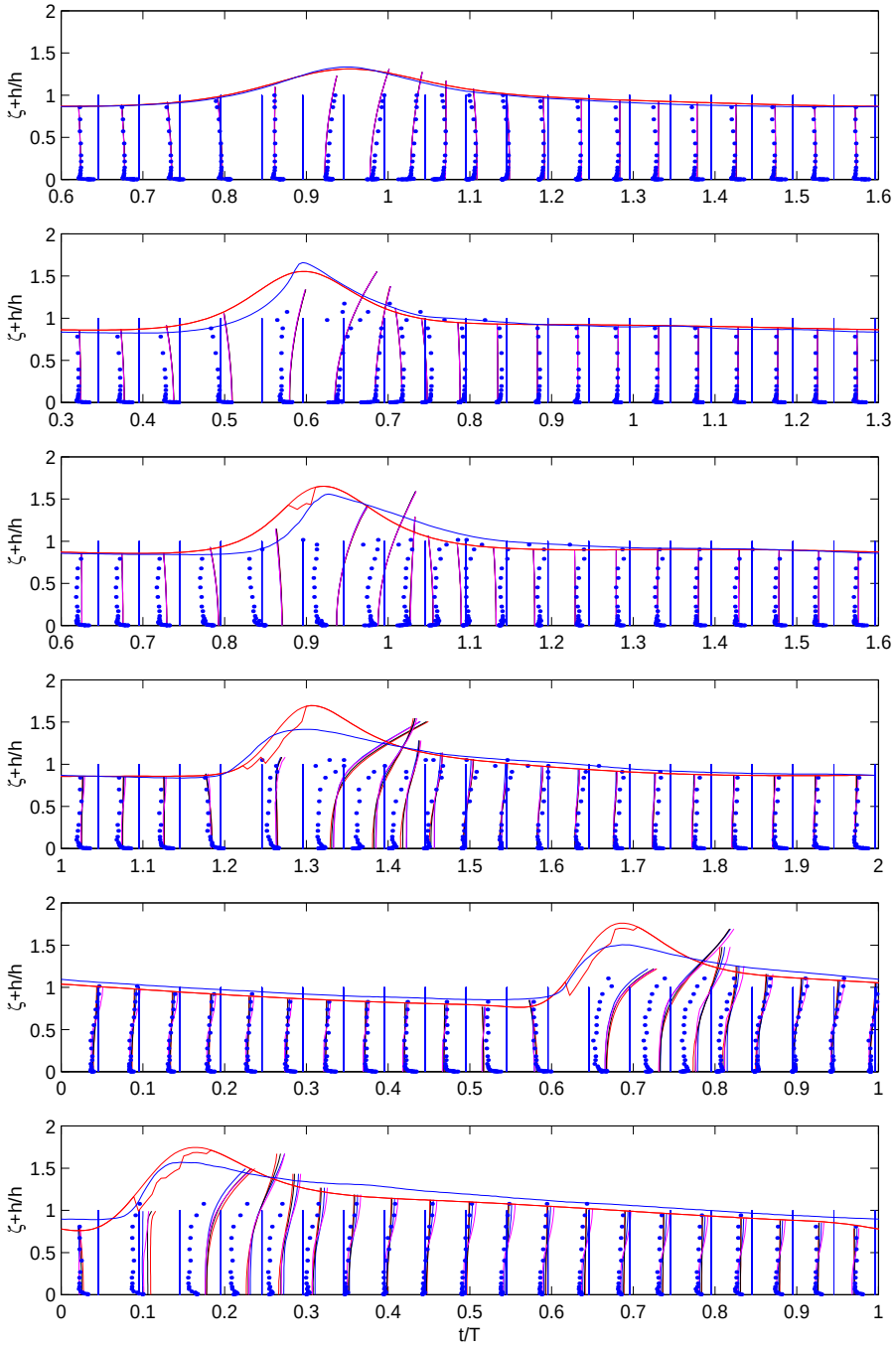

Figure 4.13: Time evolution of the profiles of the total velocity at the six locations from top L1 to bottom L6) of the gauges of Cox *et al.* (1995). Red solid line, $N_0(z)$ (with water surface and roller area), blue solid line, $N_1(z)$, black solid line, $N_2(z)$, magenta solid line, $N_3(z)$. Blue dots and blue solid line wave profile, experimental results from Cox *et al.* (1995).

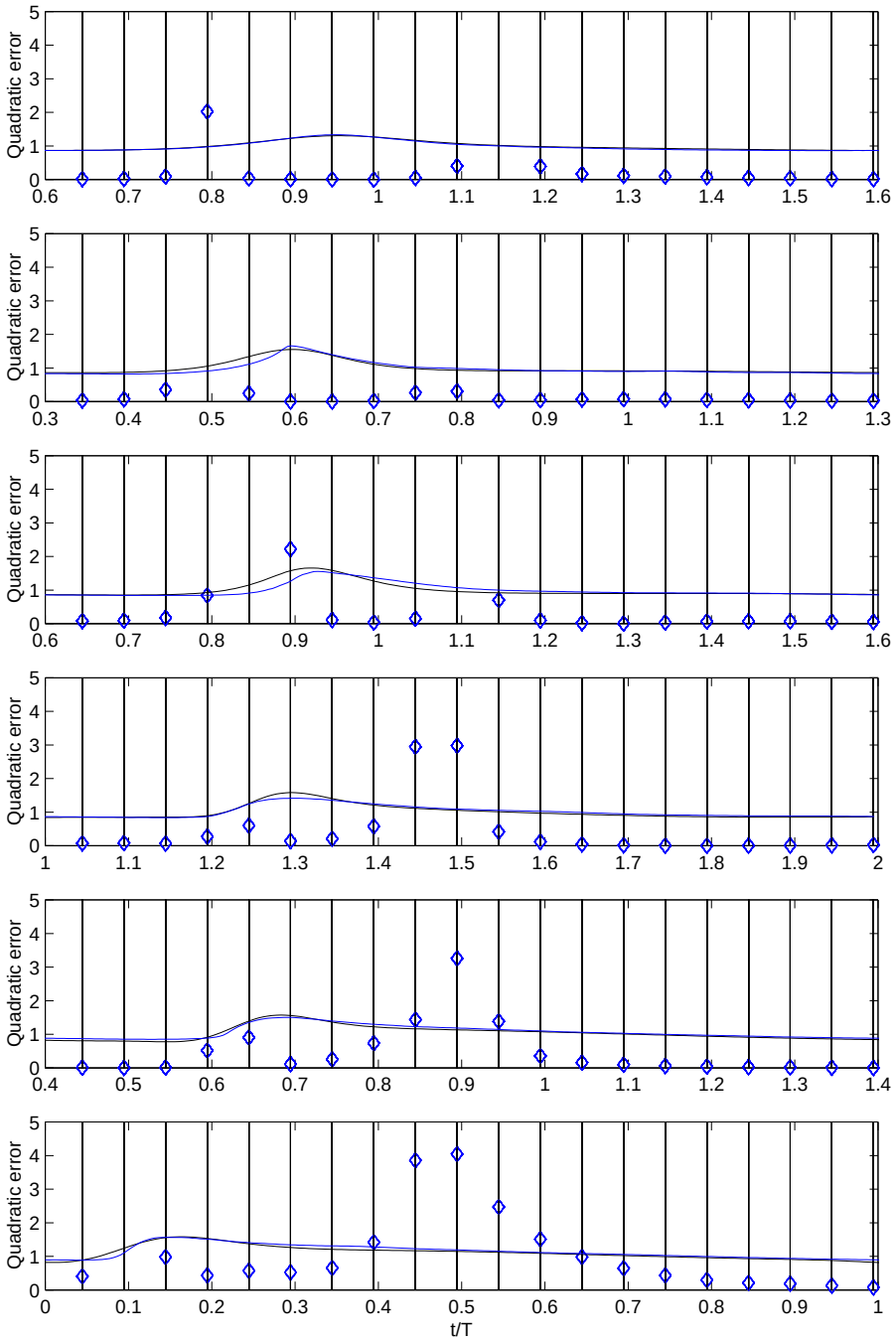

Figure 4.14: Quadratic error between the experimental and the computed velocity profiles over a wave period. The computed profile comes from VS's solution. The blue line and the black line respectively give the experimental water surface from Cox *et al.* (1995) and the computed one.

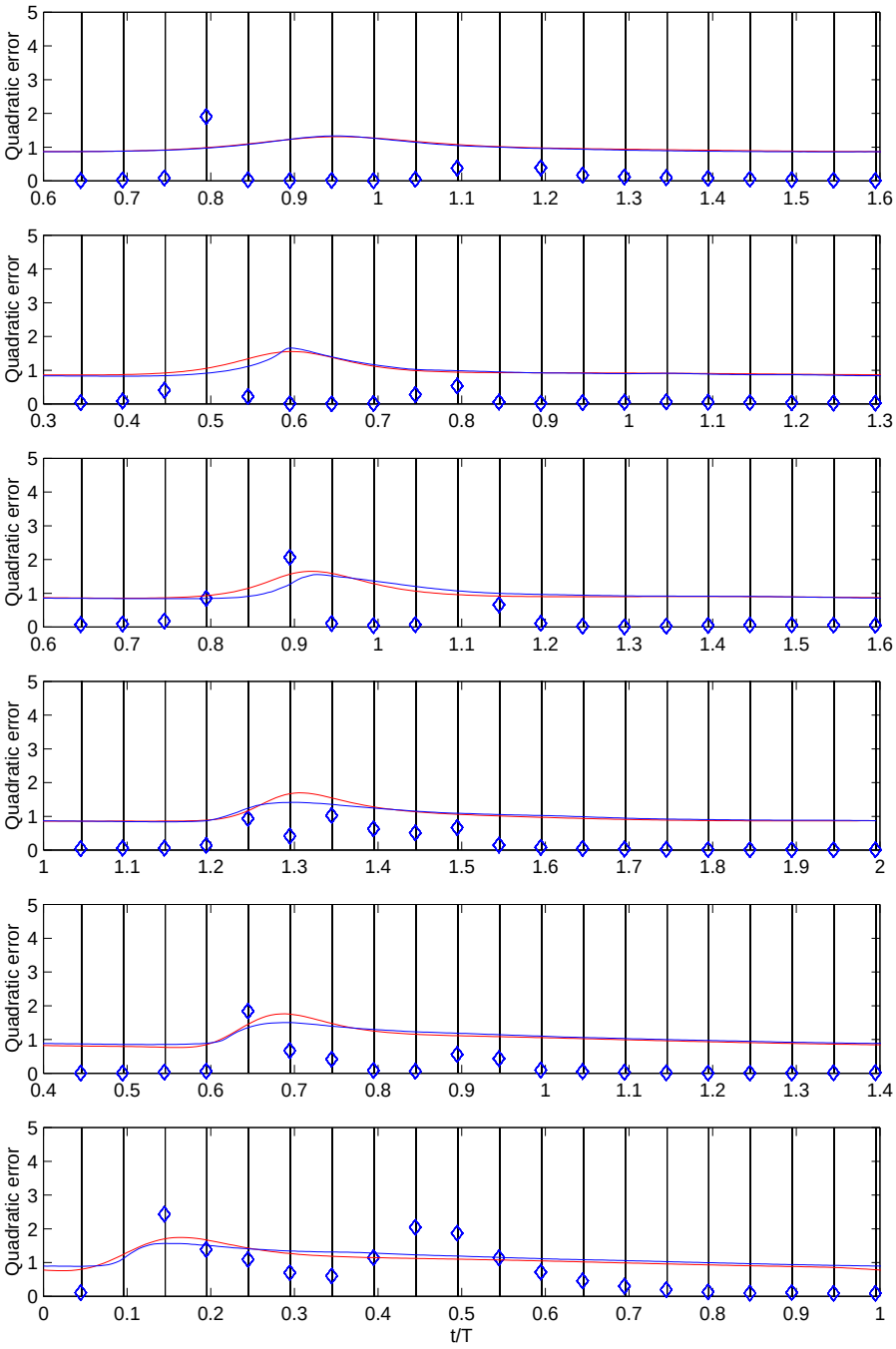

Figure 4.15: Quadratic error between the experimental and the computed velocity profiles over a wave period. The computed profile comes from the present model with$N_0(z)$. The blue line and the red line respectively give the experimental water surface from Cox *et al.* (1995) and the computed one.

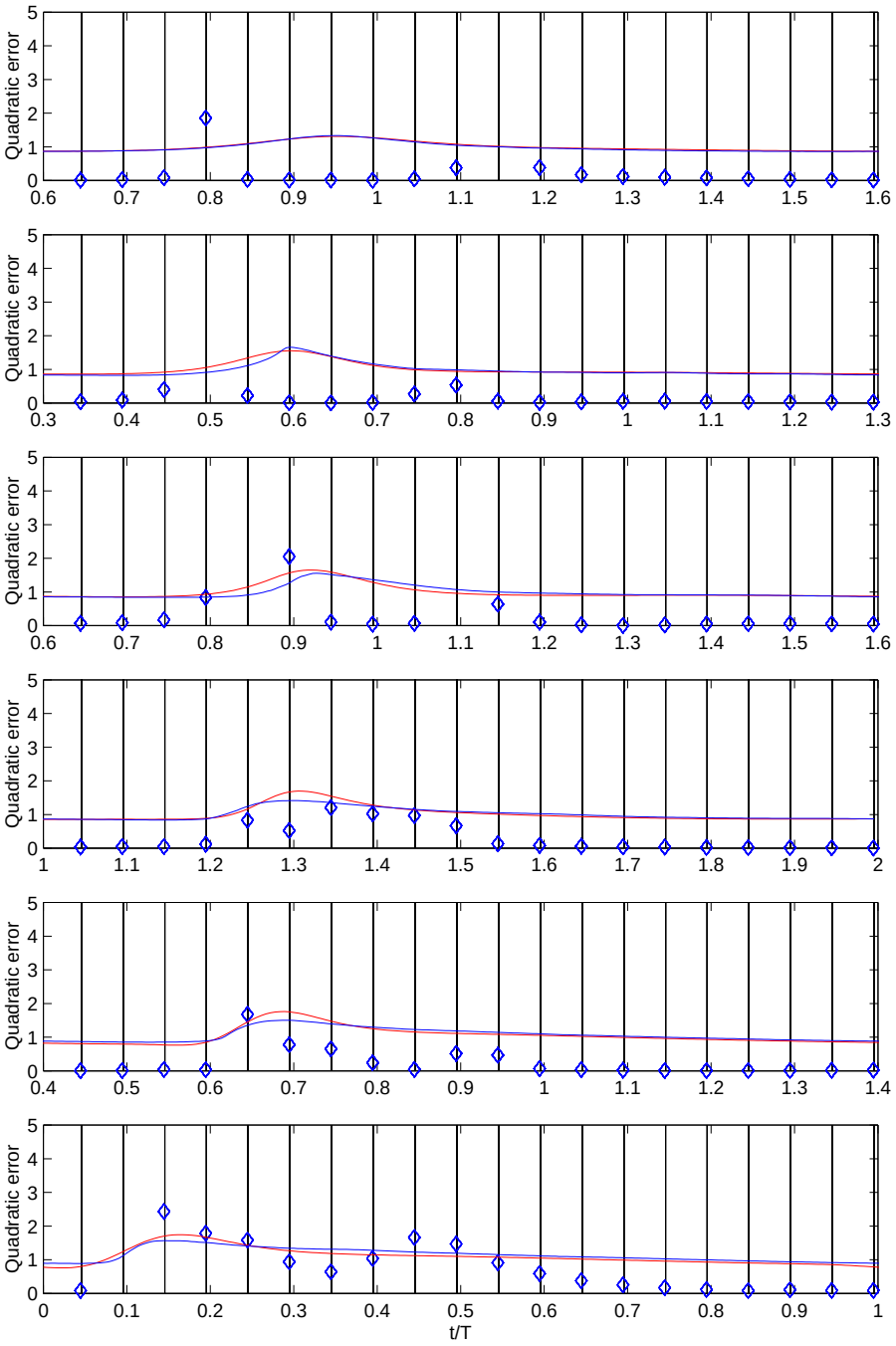

Figure 4.16: Quadratic error between the experimental and the computed velocity profiles over a wave period. The computed profile comes from the present model with$N_2(z)$. The blue line and the red line respectively give the experimental water surface from Cox *et al.* (1995) and the computed one.

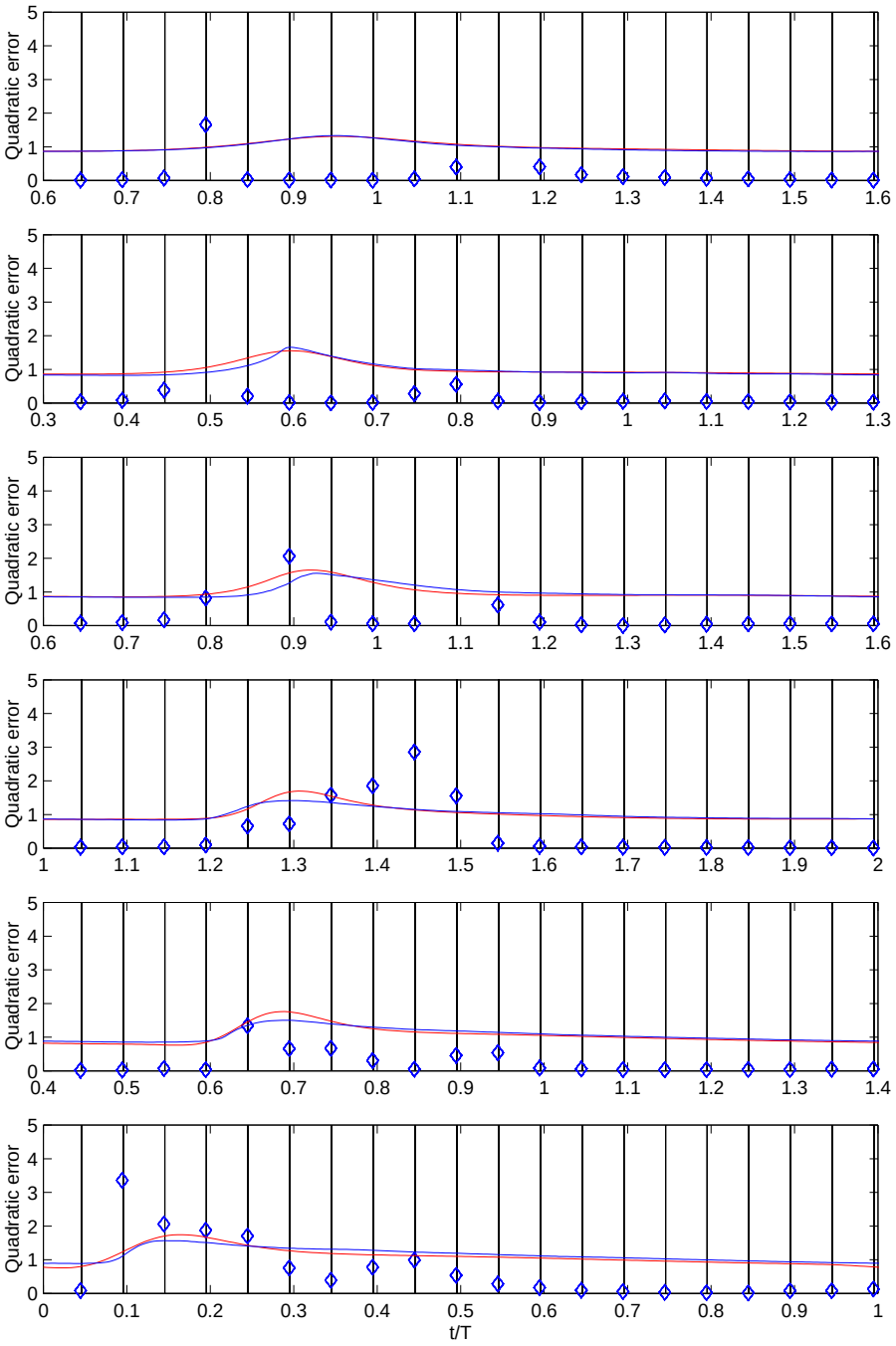

Figure 4.17: Quadratic error between the experimental and the computed velocity profiles over a wave period. The computed profile comes from the present model with$N_3(z)$. The blue line and the red line respectively give the experimental water surface from Cox *et al.* (1995) and the computed one.

Solver	L4	L5	L6
Analytical	0.1033	0.2079	0.0286
Numerical $N_0(z)$	0.0395	0.0198	0.0632
Numerical $N_1(z)$	0.0774	0.0299	0.0408
Numerical $N_2(z)$	0.0427	0.0227	0.0546
Numerical $N_3(z)$	0.0571	0.0820	0.1541

Table 4.2: Summary of the quadratic error for four representative solvers in undertow estimation over the transition region ($L4$) and the inner surf zone ($L5, L6$).

4.7 Undertow profiles

The 'undertow current' plays a key role in the sediment transport processes within the nearshore region and, consequently, in the morphodynamics of the beach profile. Boussinesq-type models, in general, cannot predict the undertow profiles, because they do not consider the roller effect on the velocity field. The present model, being derived from VS's one, drops the hypothesis of irrotational flow and takes in account the roller effects. Hence, the undertow current may be evaluated according to the relation:

$$u_{undertow}(z) = u_{mean}(z) - \frac{\bar{Q}}{h_0 + \bar{\zeta}} \tag{4.7.20}$$

in which the first term at the right hand side is the mean horizontal velocity (properly defined for $-h_0 < z < \zeta_t$, h_0 being the offshore water depth and ζ_t being the surface elevation at the trough level). The second term represents the correction for the sloshing in the experimental wave tank. $\bar{Q}$ is defined as:

$$\bar{Q} = \frac{1}{T} \int_t^{t+T} \int_{-h}^{\zeta_t} u dz dt. \tag{4.7.21}$$

Results the models have been compared with the measurements of CK collected at six sections over the slope, which coincide with those of Cox *et al.*. Undertow profiles estimated with VS's model and the present one with $N_0(z)$ are shown in figures 4.18 and 4.19 respectively.

The comparison between the two models shows that also for the undertow results are comparable even if the profiles at $L4$ and $L5$ seem to be better represented by the fully numerical solver. Also results obtained with $N_2(z)$ and $N_3(z)$ are shown respectively on figures 4.20 and 4.21. Quadratic errors have been summarized in table 4.2 from which it is clear that the overall best performances have been obtained using the fully numerical solver with the $N_0(z)$ and $N_2(z)$ profiles. Even the profile $N_3(z)$ performs better than VS's solution especially for data of sections $L4$ and $L5$. In $L6$ performances are worse than those of the other models, this is probably due to the differences, already pointed out in the previous sections, in the velocity profiles and in the estimate of the free surface.

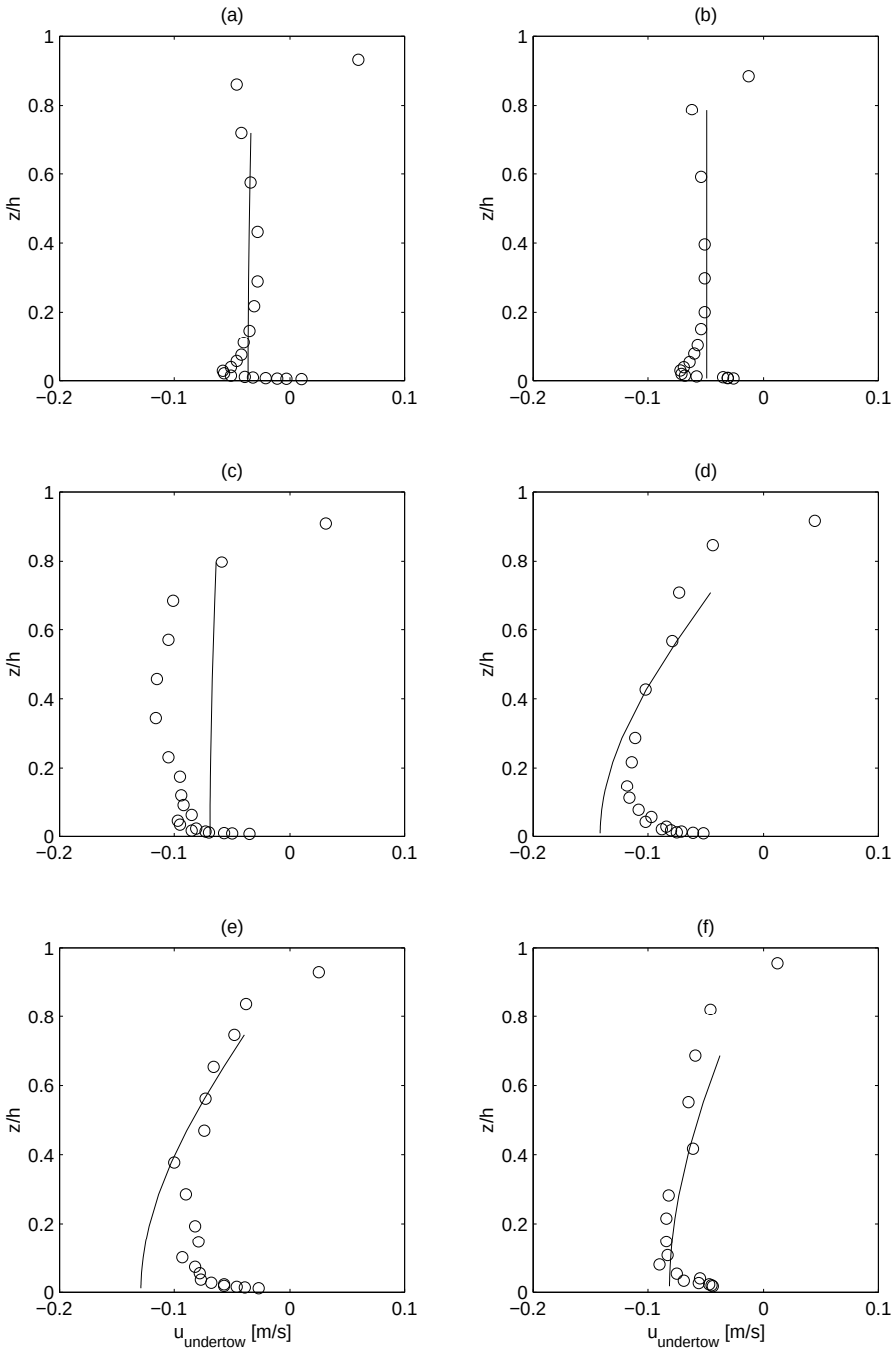

Figure 4.18: Undertow profiles: circles data from CK, solid line results from VS' s model. Panel (a) section L1, (b) section L2, (c) section L3, (d) section L4, (e) section L5, (f) section L6.

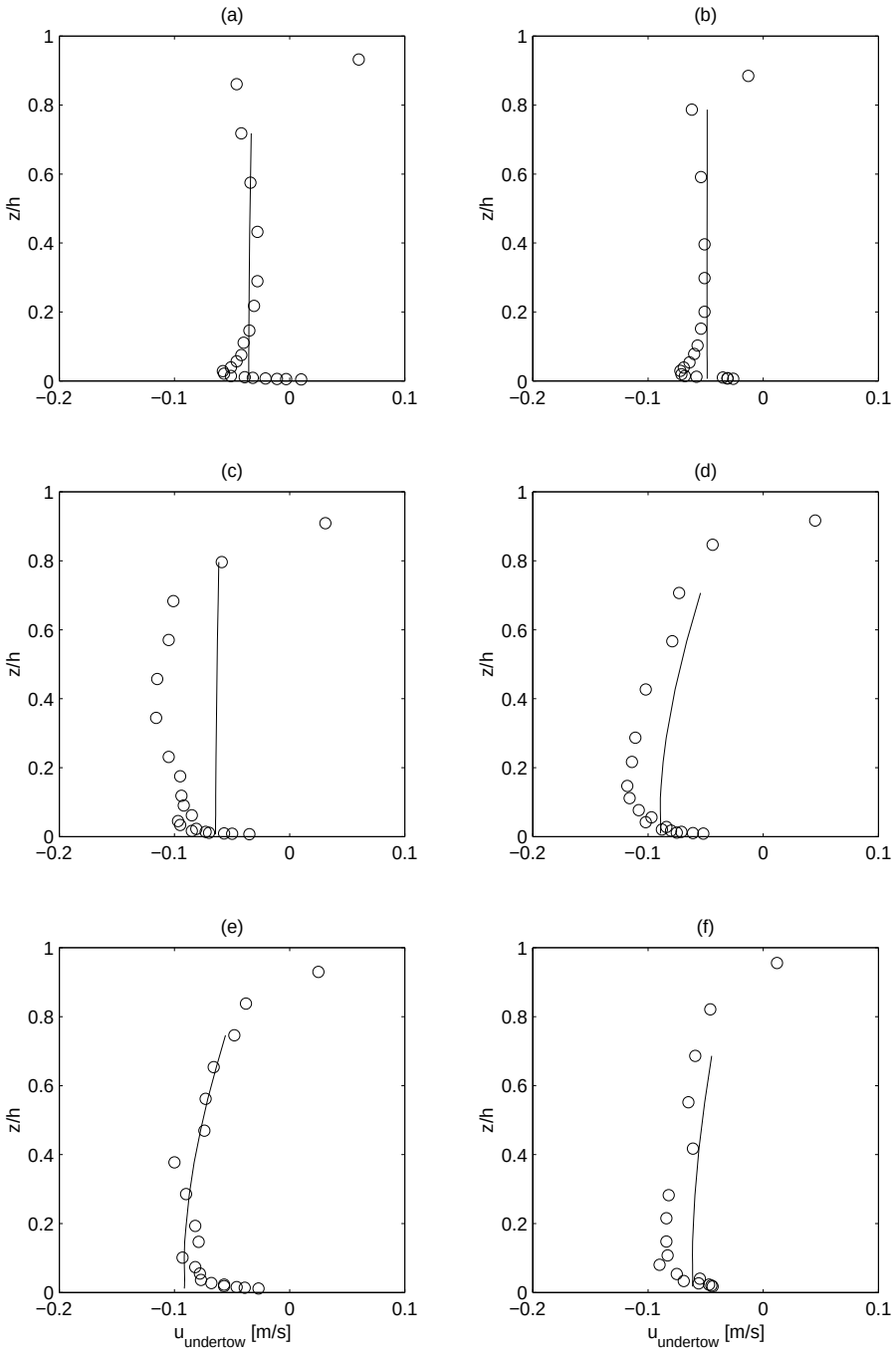

Figure 4.19: Undertow profiles: circles data from CK, solid line results from $N_0(z)$ solver. Panel (a) section L1, (b) section L2, (c) section L3, (d) section L4, (e) section L5, (f) section L6.

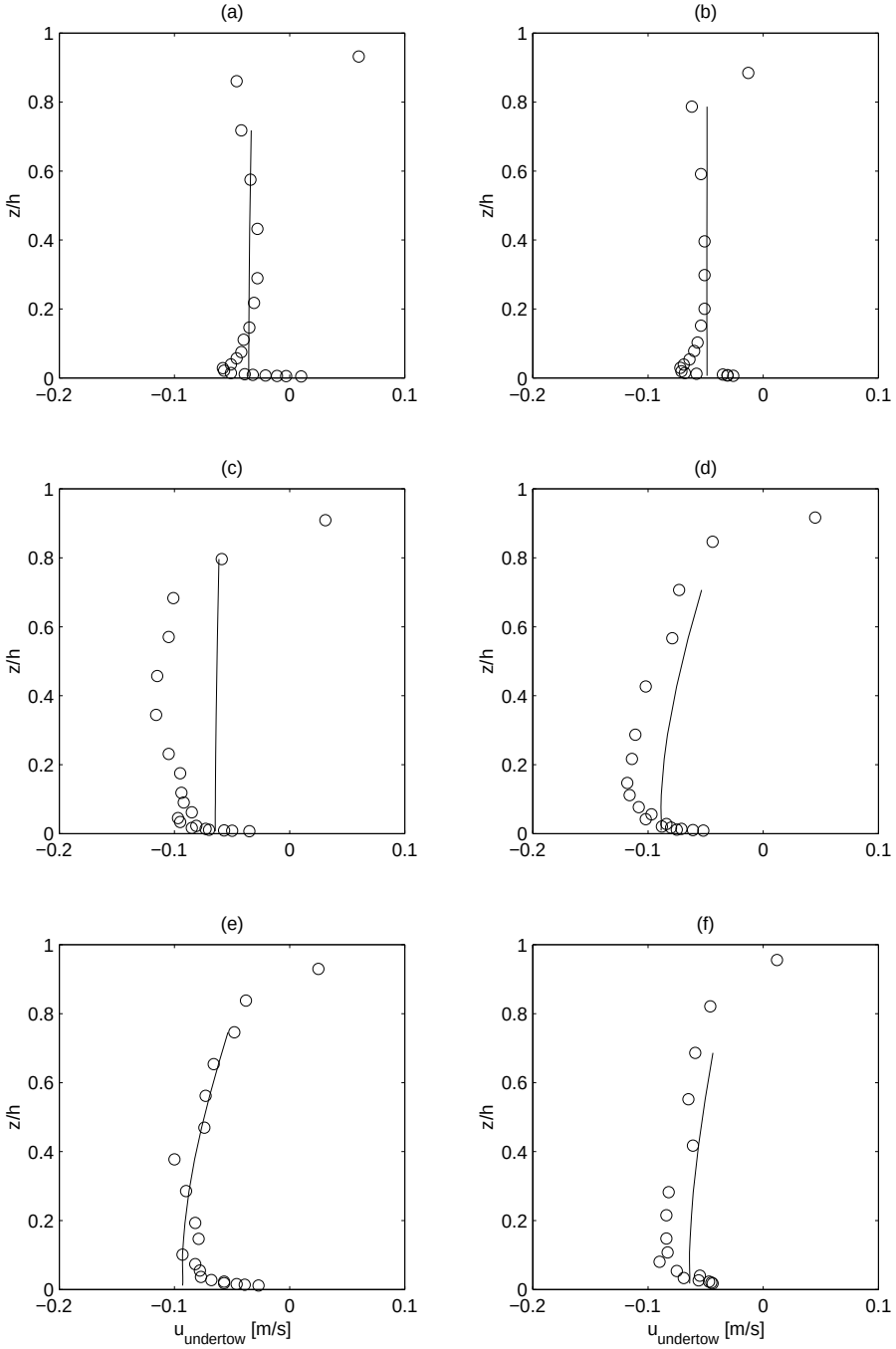

Figure 4.20: Undertow profiles: circles data from CK, solid line results from $N_2(z)$ solver. Panel (a) section L1, (b) section L2, (c) section L3, (d) section L4, (e) section L5, (f) section L6.

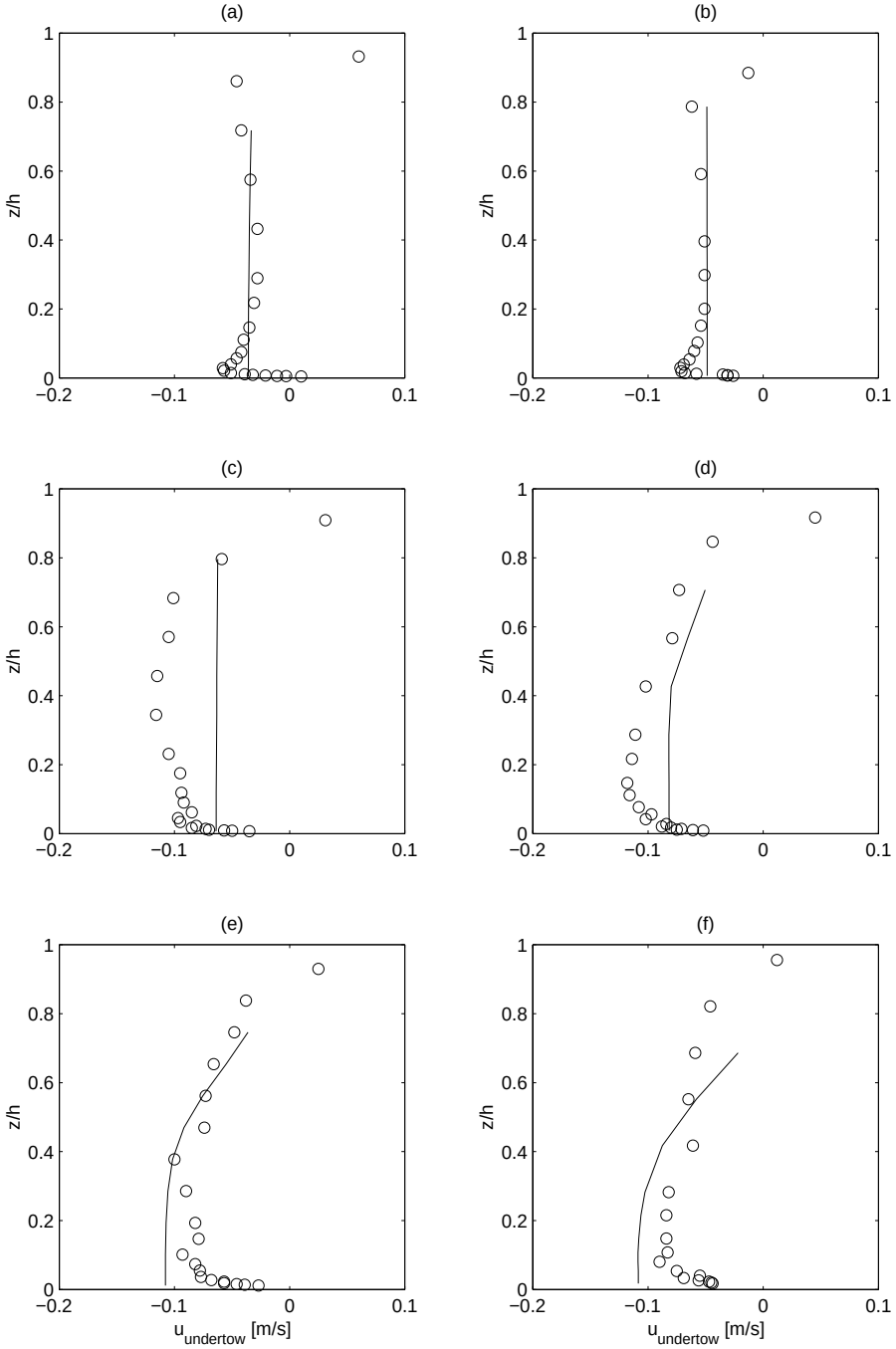

Figure 4.21: Undertow profiles: circles data from CK, solid line results from $N_3(z)$ solver. Panel (a) section L1, (b) section L2, (c) section L3, (d) section L4, (e) section L5, (f) section L6.

4.8 Conclusions

Accurate knowledge of the flow velocity over the entire water column is essential for any analysis aimed at computing wave loads on and sediment transport in the vicinity of maritime structures. This is particularly true for low-crested structures.

The Boussinesq-type model of VS for long waves breaking in shallow waters has been extended to give a more flexible and accurate description of the turbulence due to breaking waves. This has been achieved by allowing the eddy viscosity, used to represent turbulent stresses, to vary along the water column.

A vertically-varying eddy viscosity, in turn, requires a fully numerical solution of the VTE to be coupled with the Boussinesq solver. Hence, a numerical solver based on the ABM predictor-corrector scheme has been implemented to solve the VTE. This scheme has been chosen as it allows for an adequate accuracy and for an optimal interlacing with the Boussinesq-type solver (the data-structure is basically the same). In order to improve the computational efficiency a "mode splitting" technique has been used such that a number of time steps of the VTE integration model (internal module) are carried out for each time step of the Boussinesq model (external module).

The flow solutions of the fully numerical solver with uniform eddy viscosity profile have been compared both with the semi-analytical VS's solution and with experimental data. The data sets used for the comparison are those of Hansen and Svendsen (1979) and of Cox et al. (1995). Analysis of the results reveals that the fully numerical solver injects in the flow less vorticity than that predicted by VS's solution. Moreover, the vorticity seems to remain more confined in the upper half of the water column, never reaching the bottom as predicted by VS's solution. As a consequence of the reduced energy decay we find that within the inner surf zone wave crests are less rounded and the wave height decay is weaker. On the other hand, the profiles of the velocity (both rotational and total) seem to be qualitatively well predicted especially away from the wave crests the major dicrepancy being caused by a shift, also characterizing the VS solution, in the velocity profile with respect to the experimental data. We believe this shift is mainly due to an incorrect prediction of the bottom boundary condition i.e. of the flow velocity at the top of the bottom boundary layer.

We pushed forward our analysis to gain some knowledge on the most suitable profiles of eddy viscosity to be used for modelling. Hence, a sensitivity analisys has been carried out aimed at comparing four possible profiles. Rather surprisingly we found that the profiles which lead to the best overall comparison between experimental and computed velocity profiles are given either by a uniform or by a linear-uniform eddy viscosity over the whole water column. Although these results are in line with the analysis of Cox et al. (1995) there is a contradictory experimental evidence (see Svendsen et al. 2000) for which turbulence should be better represented by a non-vanishing eddy viscosity only over the top half of the water column. Analysis is underway to evaluate such different behavior as depending on the different flow conditions (i.e. hydraulic jump vs. propagating bores).

Chapter 5

Conclusions

In this report the range of validity of solutions provided by depth-integrated numerical models for studying the nearshore hydrodynamics has been extended to cover swash zone motions and improve the description of surf zone flows. Three innovative results were achieved. These are here below summarized.

- The applicability of BTE in the swash zone and the role of dispersive and dispersive-nonlinear terms was studied (section 2.3).
- A new SBC for BTE was derived and verified against well-known analytical solution (chapter 3).
- A new technique for simulating wave-breaking into BTE models was proposed and verified against available experimental data (chapter 4).

As far as the BTE are concerned, we have shown that if not properly handled, dispersive and dispersive-nonlinear terms of these equations, can unrealistically grow in the swash zone. A modified form of the BTE, written in terms of the total water depth and not in terms of the undisturbed water depth was therefore introduced. According to this new form of the equations, dispersive terms naturally tend to vanish at the shoreline, where the water depth tends to zero.

A new technique for specifying SBC and tracking the movements of the instantaneous shoreline was subsequently derived for numerical models based on the BTE. This technique is based on the use of a specific shock-capturing method for dealing with the discontinuity occurring at the shoreline, where a transition between wet and dry conditions occur. A numerical model based on the scheme proposed by Wei and Kirby (1995) was coded in order to implement and verify the new SBC. The comparison of the numerical model results against well-known analytical solutions suggested that using the new SBC can lead to very accurate and physically-based simulations of swash zone flows.

A novel procedure for solving the coupled set of BTE+VTE has been implemented which allows to extend the method of VS to the case of vertically-nonuniform eddy viscosities. This is a fundamental step towards the choice and implementation of the profiles which most suitable represent the vertical turbulence structure caused by a spilling breaker either far or close to a submerged structure. Preliminary results carried out over uniformly sloping beaches show that the most suitable profiles are either the uniform profile (hence conforming the validity of VS analysis) or the linear-uniform profile of eddy viscosity. Analysis is still ongoing which aims at: (1) improving

the computation of the flow velocity just outside the bottom boundary layer, (2) verifying what the turbulence structure is in the vicinity of sudden topographic changes, (3) calibrating the model once the most suitable profile of eddy viscosity is definitevely chosen.

It is clear that the above improvements, which deeply influence the computation of sediment transport in the vicinity of low-crested structures, are fully in line with the aims of UR3 contributions to DELOS Project.

Bibliography

Aagaard, T. and B. Greenwood. 1994. "Suspended sediment transport and the role of infragravity waves in a barred surf zone." *Mar. Geol.* 118:23–48.

Baldock, T.E., P. Holmes, and D.P. Horn. 1997. "Low frequency swash motion induced by wave grouping." *Coast. Engng.* 32:197–222.

Beach, R.A. and R.W. Sternberg. 1991. "Infragravity driven suspended sediment transport in the swash, inner and outer surf zone." *Proc. Coastal Sed.'91-ASCE*, Volume 1. 114–128.

Blumberg, A. F. and G. L. Mellor. 1987. "A description of a three-dimentional coastal ocean circulation models." *In N-Heaps (Ed.), Three-Dimensional Coastal Ocean Models, American Geophysical Union, Washington, DC*, pp. 1–16.

Brocchini, M. 1998. "The run-up of weakly two-dimensional solitary pulses." *Nonlin. Proc. In Geophys.* 5:27–38.

Brocchini, M. and D.H. Peregrine. 1996. "Integral flow properties of the swash zone and averaging." *J. Fluid Mech.* 317:241–273.

Brocchini, M, R. Bernetti, A. Mancinelli, and G. Albertini. 2001. "An efficient solver for nearshore flows based on the WAF method." *Coastal Engng.* 43:105–129.

Brocchini, M., M. Drago, and L. Iovenitti. 1992. "The modelling of short waves in shallow waters. Comparison of numerical models based on Boussinesq and Serre equations." *Proc. of 23rd ICCE, ASCE*, Volume 23. 76–88.

Carrier, G.F. 1966. "Gravity waves on water of variable depth." *J. Fluid Mech.* 24:641–659.

Carrier, G.F. 1971. "Dynamics of tsunamis." *in Mathematical problems in the geophysical sciences*, vol. 1.

Carrier, G.F. and H. P. Greenspan. 1958. "Water waves of finite amplitude on a sloping beach." *J. Fluid Mech.* 4:97–109.

Chang and Liu. 1999. "Experimental investigation of turbulence generated by breaking waves in water of intermediate depths." *Phys. Fluids* 11:3390–3400.

Chang, K.A., T.J. Hsu, and P.L.-F. Liu. 2001. "Vortex generation and evolution in water waves propagating over a submerged rectangular obstacle. Part I. Solitary waves." *Coast. Engng.* 44:13–36.

Chen, Q., R. A. Dalrymple, J. T. Kirby, A. B. Kennedy, and M. C. Haller. 1999. "Boussinesq modelling of a rip current system." *Journal of Geophysical Research* 104 (c9):20,617–20,637.

Cox, D. T. and N. Kobayashi. 1997. "Kinematc undertow model with logarithmic boundary layer." *J. Waterway Port Coast. and Ocean Engng. - ASCE* 123:354–360.

Cox, D. T., N. Kobayashi, and A. Okayasu. 1995. "Experimental and numerical modeling of surf-zone hydrodynamics." Technical Report Technical Report CACR-95-07, Center for Applied Coastal Research, University of Delaware.

Dodd, N. and C. Giarrusso. 2001. "ANEMONE: Otto 1-d, A user manual." Technical Report 87, HR Wallingford.

Fredsoe, J. and B. M. Sumer. 1997. "Scour at the round head of a rubble-mound breakwater." *Coastal Engng.* 29:231–262.

Giarrusso, C. 1998. "Studio numerico del moto ondoso su fondali intermedi e bassi." Ph.D. diss., Università degli studi della Calabria, Cosenza.

Hansen, J.B. and I.A. Svendsen. 1979. "Regular waves in shoaling water: epxerimental data." Technical Report Technical Report, ISVA Series, 21, ISVA.

Holman, R.A. and A.J. Bowen. 1982. "Bar, bumps and holes: models for the generation of complex beach topography." *J. Geophys. Res.-Oceans* 87:457–468.

Karambas, T. K. and C. Koutitas. 1992. "A breaking wave propagation model based on the Boussinesq equations." *Coastal Engng.* 18:1–19.

Kennedy, A. B., Q. Chen, J. T. Kirby, and Dalrymple R. A. 2000. "Boussinesq modeling of wave transformation, breaking and run-up. I: One dimension." *ASCE J. Waterway, Port, Coastal and Ocean Engng.* 126(1):48–56.

Lynnet, P.J., T.R. Wu, and P.L.-F. Liu. 2002. "Modeling wave runup with depth-averaged equations." *Coast. Engng.* 46:89–107.

Madsen, P. A. and H. A. Schäffer. 1998. "Higher order Boussinesq-type equations for surface gravity waves: derivation and analysis." *Phil. Trans. R. Soc. Lond., Series A.* 356:3123–3184.

Madsen, P., B. Bingham, and H. Liu. 2001. "Nonlinear wave dynamics and breaking waves modeled by the use of a highly accurate Boussinesq formulation." *Proc. of WAVES 2001, ASCE.*

Madsen, P. A., R. Murray, and O. R. Sorensen. 1991. "A new form of Boussinesq equations with improved dispersion characteristics." *Coastal Engng.* 15:371–388.

Madsen, P. A., O. R. Sørensen, and H. A. Schäffer. 1997. "Surf zone dynamics simulated by a Boussinesq type model. Part I: Model description and cross-shore motion of regular waves." *Coastal Engng.* 32:255–287.

Mase, H. 1995. "Frequency down-shift on swash oscillations compared to incident waves." *J. Hydr. Res.* 33:397–411.

Musumeci, R., Svendsen, I.A., and E. Foti. 2003. "A fully nonlinear Boussinesq model for breaking waves." Technical Report CACR-03-05, University of Delaware, Center for Applied Coastal Research.

O'Hare, T.J. and D.A. Huntley. 1994. "Bar formation due to wave groups and associated long waves." *Mar. Geol.* 116:313–325.

Ozanne, F., A. J. Chadwick, D. A. Huntley, D. J. Simmonds, and J. Lawrence. 2000. "Velocity predictions for shoaling and breaking waves with a Boussinesq-type model." *Coastal Engng.* 41:361–397.

Özkan-Haller, H. and J. T. Kirby. 1997. "A Fourier-Chebyshev collocation method for the shallow water equations including shoreline runup." *Applied ocean research* 19:21–34.

Peregrine, D. H. 1967. "Long waves on a beach." *J. Fluid Mech.* 27:815–827.

Press, W. H. et al. 1992. *Numerical recipes in FORTRAN, the art of scientific computing. 2nd Edition.* Cambdridge University Press, Cambridge, 963 pp.

Rakha, K.A., R. Deigaard, and I. Broker. 1997. "A phase-resolving cross shore sediment transport model for beach profile evolution." *Coast. Engng.* 31:321–261.

Rego, V., J. Kirby, and D. Thompson. 2001. "Boussinesq Waves on Flows with Arbitrary Vorticity." *Proceedings of Waves 2001-ASCE, in print*

Sancho, F. E. and I. A. Svendsen. 1997. "Unsteady nearshore currents on longshore varying topographies." Technical Report CACR-97-10, Center for Applied Coastal Research, University of Delaware.

Schäffer, H. A., P. A. Madsen, and R. Deigaard. 1993. "A Boussinesq model for wave breaking in shallow water." *Coastal Engng.* 20:185–202.

Skotner, C. and CJ. Apelt. 1999. "Application of a Boussinesq model for the computation of breaking waves Part 1: Development and verification." *Ocean Engng.* 26 (10):905–925.

Stoker, J. J. 1957. *Water waves.* Interscience: New York.

Svendsen, I. A. 1984. "Wave height and set-up in a surf zone." *Coast. Engng.* 8:303–329.

Svendsen, I. A., J. Veeramony, J. Bakunin, and J. Kirby. 2000. "The flow in weak turbulent hydraulic jumps." *J. Fluid Mech.* 418:25–57.

Synolakis, C. E. 1987. "The runup of solitary waves." *J. Fluid Mech.* 185:523–545.

Ting and Kirby. 1996. "Dynamics of surf-zone turbulence in a spilling breaker." *Coast. Engng.* 27:131–160.

Toro, E. F. 1992. "Riemann problems and the WAF method for solving twodimensaional shallow water equations." *Phil. Trans. of the Roy. Soc. London A* 338:43–68.

Toro, E. F. 1997. *Riemann solvers and numerical methods for fluid dynamics.* Springer, Berlin.

Van Dongeren, A. R. and I. A. Svendsen. 1997. "Absorbing-generating boundary conditions for shallow water models." *ASCE J. Waterway, Port, Coastal and Ocean Engng.* 123 (6):303–313.

Veeramony, J. and I. A. Svendsen. 1999. "Modeling the flow in surf zone waves." Technical Report CACR-99-04, Center for Applied Coastal Research, University of Delaware.

Veeramony, J. and I. A. Svendsen. 2000. "The flow in surf zone waves." *Coastal Engng.* 39:93–122.

Watson, G., T.C.D. Barnes, and D.H. Peregrine. 1994. "The generation of low frequency waves by a single group incident on a beach." *24th Int. Conf. Coastal Engng.-ASCE.* 776–790.

Watson, G., D. H. Peregrine, and E.F. Toro. 1992. "Numerical solution of the shallow-water equations on a beach using the weighted average flux method." *Computational Fluid Dynamics '92.*

Wei, G., J. T. Kirby, S. T. Grilli, and R. Subramanya. 1995. "A fully nonlinear Boussinesq model for surface waves. I. Highly nonlinear, unsteady waves." *J. Fluid Mech.* 294:71–92.

Zelt, J. A. 1991. "The run-up of nonbreaking and breaking solitary waves." *Coastal Engng.* 15:205–246.